Immersed Discontinuous Galerkin Methods for Acoustic Wave Propagation in Inhomogeneous Media

Kihyo Moon

Dissertation submitted to the Faculty of the
Virginia Polytechnic Institute and State University
in partial fulfillment of the requirements for the degree of

Doctor of Philosophy
in
Mathematics

Slimane Adjerid, Chair
Tao Lin
Yuriko Renardy
Jeffrey T. Borggaard

March 29, 2016
Blacksburg, Virginia

Keywords: Immersed Finite Element, Discontinuous Galerkin Method, Hyperbolic PDEs, Acoustic Wave Propagation, Inhomogeneous Media, Interface Problems

Immersed Discontinuous Galerkin Methods for Acoustic Wave Propagation in Inhomogeneous Media

Kihyo Moon

(ABSTRACT)

We present immersed discontinuous Galerkin finite element methods for one and two dimensional acoustic wave propagation problems in inhomogeneous media where elements are allowed to be cut by the material interface. The proposed methods use the standard discontinuous Galerkin finite element formulation with polynomial approximation on elements that contain one fluid while on interface elements containing more than one fluid they use specially-built piecewise polynomial shape functions that satisfy appropriate interface jump conditions. The finite element spaces on interface elements satisfy physical interface conditions from the acoustic problem in addition to extended conditions derived from the system of partial differential equations. Additional curl-free and consistency conditions are added to generate bilinear and biquadratic piecewise shape functions for two dimensional problems. We established the existence and uniqueness of one dimensional immersed finite element shape functions and existence of two dimensional bilinear immersed finite element shape functions for the velocity.

The proposed methods are tested on one dimensional problems and are extended to two dimensional problems where the problem is defined on a domain split by an interface into two different media. Our methods exhibit optimal $O(h^{p+1})$ convergence rates for one and two dimensional problems. However it is observed that one of the proposed methods is not stable for two dimensional interface problems with high contrast media such as water/air. We performed an analysis to prove that our immersed Petrov-Galerkin method is stable for interface problems with high jumps across the interface. Local time-stepping and parallel algorithms are used to speed up computation.

Several realistic interface problems such as ether/glycerol, water/methyl-alcohol and water/air with a circular interface are solved to show the stability and robustness of our methods.

This work received support from National Science Foundation (Grant Number DMS1016313).

Dedication

To my parents and family.

Acknowledgments

I would love to express my gratitude sincerely to my advisor Prof. Slimane Adjerid for the support of my Ph.D research for his patience and deep knowledge. I could not finish the research and this dissertation without his guidance. I have learned his integrity and passion for the research as a scholar.

I would like to thank my dissertation committee: Prof. Tao Lin, Prof. Yuriko Renardy, and Prof. Jeffrey T. Borggaard, for their insightful comments and encouragement. Their help inspired me to widen my research from various perspectives.

I wish to express my sincerest gratitude to my parents and family for their support and love.

Contents

List of Figures

List of Tables

Chapter 1

Introduction

We start with a brief discussion of wave propagation and then provide a history of discontinuous Galerkin methods and recently developed immersed finite element method and their advantages. We present our main achievements in this work which include a stable and efficient immersed Petrov-Galerkin method. We implement our method using a parallel-local time-stepping algorithm to solve acoustic wave propagation problems in inhomogeneous media. Finally, we review each chapter briefly for one and two dimensional problems.

1.1 Wave Propagation

In classical physics, the wave equation is a linear partial differential equation in which the second derivative in position is proportional to the second derivative in time. Hence the wave equation has the following general form:

$$\frac{\partial^2 \omega}{\partial t^2} = c^2 \Delta \omega, \tag{1.1.1}$$

which was discovered by Jean-Baptiste le Rond d'Alembert by studying vibrating string. Daniel Bernoulli showed that the solution can be represented by trigonometric functions. This equation plays an important role in many modern physical phenomena in science and engineering such as acoustics, elasticity, electromagnetism, particle physics and gravitational waves. Wave propagation in inhomogeneous media is ubiquitous in nature, appearing in acoustics, elasticity and electromagnetism. Each variable satisfies the wave property (1.1.1) and is modeled by hyperbolic partial differential equations with discontinuous coefficients which reflect the fact that waves travel a different speeds in different media.

1.1.1 Acoustic Wave Propagation in Inhomogeneous Media

The acoustic wave equation describes how the acoustic waves propagate in fluids. Acoustic waves are longitudinal waves which are reflected and transmitted when they hit an interface of two different media. Acoustic wave propagation in inhomogeneous media were studied, for instance, by Lombard, Piraux, Monk and Richter [87, 89, 92] with the governing equation

$$\begin{cases} \frac{\partial p}{\partial t} + \rho c^2 \nabla \cdot \mathbf{v} &= 0, \\ \frac{\partial \mathbf{v}}{\partial t} + \frac{1}{\rho} \nabla p &= 0, \end{cases} \tag{1.1.2}$$

where p is the pressure, $\mathbf{v}$ is the velocity, c is the speed of sound and ρ is the density. Both p and $\mathbf{v}$ satisfy the second-order wave equation (1.1.1).

An interface is the line separating the two media. When the incident wave hits the interface, it splits into reflected and transmitted waves.

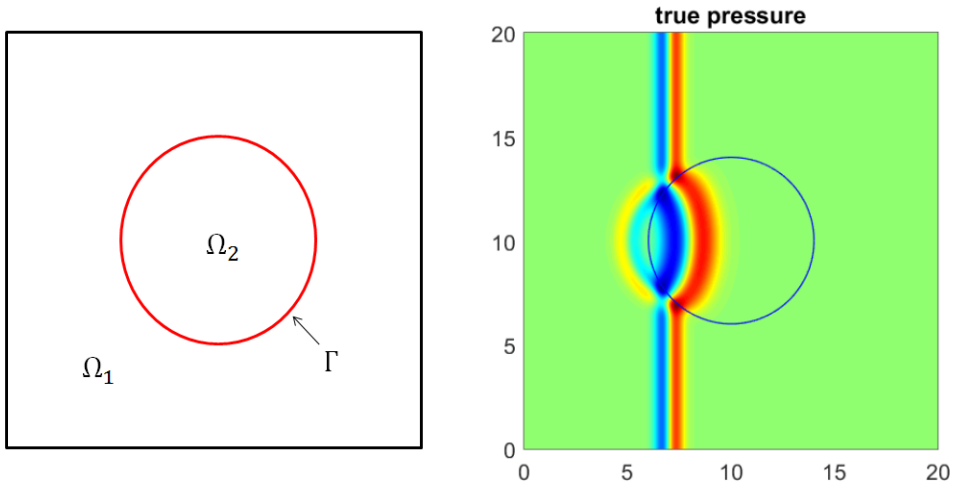

Figure 1.1.1: A domain containing two media separated by an interface Γ and an example of wave propagation for acoustic pressure.

As illustrated in Figure 1.1.1, pressure wave propagates faster in the interior of the circle.

1.2 Discontinuous Galerkin Methods

The discontinuous Galerkin (DG) method is a conservative, stable and high-order accurate finite element method for solving partial differential equations. The DG method is a finite element method obtained from a weak formulation of partial differential equations and

constructed over piecewise continuous trial spaces of polynomial functions. It has been successfully applied hyperbolic [5, 44, 58, 71, 94], parabolic [99] and elliptic [12, 25, 29, 48] partial differential equations for the past several decades.

First, we look at a brief history of the DG method which was introduced to solve the neutron transport equation by Reed and Hill in 1973 [93]. Error estimation of the DG method was first analyzed by Lesaint and Raviant in 1974 [73]. They showed an L^2 convergence rate $O(h^p)$ for an arbitrary triangulation and $O(h^{p+1})$ for Cartesian meshes where h is the mesh size and p is the polynomial degree. TVB (total variation bounded) DG finite element methods were developed for solving conservation laws by Bourgeat, Cockburn, Shu, Hou and Lin in 1988, 1989 and 1990 [22, 30, 33, 34]. Later Runge-Kutta discontinuous Galerkin methods [36, 37] and the local discontinuous Galerkin methods [23, 25, 31, 32, 35] were developed. Convergence of the weak solution assuming that the exact solution is in $H^{1/2}(\Omega)$ was proved by Lin and Zhou in 1993 [80]. Discontinuous Galerkin methods for partial differential equations with third or higher order derivatives were developed in [28, 55, 63, 70, 106, 107]. Spectral element methods for partial differential equations were developed by Kopriva [68]. The reader may consult the book by Hesthaven and Warburton [56] and Rivière [95] for more details.

The DG methods were used with *hp*-adaptive methods by Baumann and Oden which supports any type of meshes including non-matching grids [16, 17]. They also provided a priori error estimates. Other *hp*-versions of DG methods are developed with error analysis in [19, 91]. Higher order accurate DG methods were introduced to solve compressible Navier Stokes equations and Euler equations by Bassi and Rebay [14, 15]. They combined two key ideas of the finite volume and finite element methods. A priori error estimates have been developed for local DG methods for elliptic problems and convection diffusion problems in [26]. A posteriori error estimates were analyzed for locally conservative methods for subsurface flow and DG approximations of elliptic problems [5, 18, 96].

The advantages of DG methods can be summarized as follows: (*i*) easy handling of complicated and irregular geometries and boundary conditions, (*ii*) high-order accuracy on unstructured and irregular grids which make it well suited for large-scale time-dependent computations, (*iii*) communication occurs only with immediate neighbors and solution is computed element by element which implies easy parallelization, (*iv*) a posteriori estimates of discretization errors may be obtained for reasonable costs for hyperbolic system and (*v*) a conservative method and small dispersion (or phase) errors. Even though the DG method has good advantages, it has some disadvantages if used on fitted meshes for moving interface problems which means that it is hard to use uniform meshes. Furthermore, the mesh has to be regenerated when the interface moves to a new location during a numerical simulation which can be an expensive task. For this reason, several immersed methods have been proposed since 1990s.

1.3 Immersed Methods

The immersed interface method was developed by LeVeque and Li in 1994 [74, 75] to solve partial differential equations that have discontinuities or singularities in the coefficients. They used uniform rectangular grids for irregular interfaces which means that the mesh does not need to be regenerated when the interface moves to a new location.

Immersed interface methods have been applied to solve time dependent problems such as moving interface problems by Li [77] who solved a one dimensional nonlinear moving interface problem. The interface $\alpha(t)$ for $t > 0$ partitions the solution domain into two subdomains $[0, \alpha(t))$ and $(\alpha(t), 1]$. The solution is smooth in each subdomains and coupled with the solution on each side by the interface jump conditions. Other moving interface problems have been investigated in [57, 103]. Immersed interface methods were extended to three dimensional problems by Li in 1996 [76]. Li solved elliptic equations with a finite difference method on the domain that has irregular interface with a uniform Cartesian grid. Convergence and stability of the immersed interface method were analyzed by Huang and Li [59] where the authors calculated error bounds for elliptic problems with discontinuities and singularities.

Immersed boundary methods are widely used to solve interface problems with complex geometries and moving interface problems [43, 66, 72, 100, 104]. They solved two or three dimensional incompressible fluid and Navier-Stokes problems using finite volume and finite difference methods. Adaptive and penalty immersed boundary methods were developed to solve these problems [47, 60, 61, 67, 97].

Since Li has developed immersed interface finite element (IFE) method for interface problems in 1998 [78], it has been successfully applied to many problems in the past decade for elliptic problems [6, 7, 8, 46, 49, 50, 51, 52, 64, 81, 105]. IFE methods have been applied to other problems such as elasticity [82, 85], Stokes [3, 4] and parabolic [27, 54] problems. Three dimensional IFE methods have been introduced by Kafafy, T. Lin, Y. Lin and Wang [64]. They solved elliptic interface problems arising from electric field simulation with two different IFE methods. IFE methods also have been extended to higher order approximations by Adjerid, Lin and Romdhane in 2007, 2009, 2013 and 2014 [1, 2, 6, 7]. Partially penalized IFE methods for parabolic interface problems were developed by Lin, Yang and Zhang in 2015 [83]. They analyzed a priori error estimates for discontinuous Galerkin IFE methods in 2015 [84].

Nonconforming rotated IFE shape functions are developed [108]. Both conforming and nonconforming IFE shape functions are introduced on triangular meshes [79]. Other nonconforming immersed interface methods have also been developed [46]. The bilinear IFE spaces and their approximation capability were investigated [49, 81] and the immersed DG method using bilinear IFE spaces was introduced in [52, 53]. The quadratic IFE spaces and its approximation capability were developed by Camp, T. Lin, Y. Lin and Sun [24]. They showed that quadratic IFE shape functions cannot be uniquely determined by nodal values and interface jump conditions unlike the linear IFE shape functions.

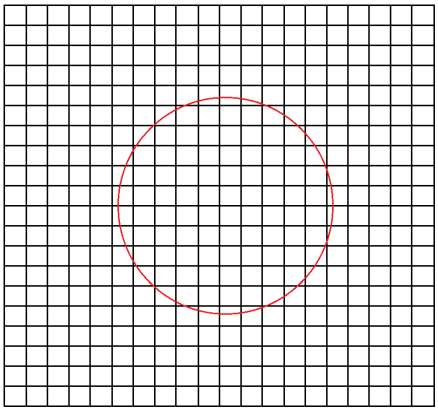

Figure 1.3.1: Partition of domain by a circular interface.

Immersed DG method inherits the advantages of both conventional DG method and immersed finite element method. Conventional DG method uses meshes that are tailored to the interface in such a way that each element contains only one fluid. For immersed finite element methods, meshes do not need to be regenerated with changing interface. Interface elements contain more than one fluid whereas non interface elements contain one fluid. Specially designed piecewise polynomial shape functions which satisfy appropriate jump conditions are used on interface element while on non interface elements standard polynomial shape functions are used.

The advantages of immersed DG methods are that the mesh does not need to be regenerated when the interface moves to a new location which implies that mesh generation is greatly simplified (uniform mesh) as shown in Figure 1.3.1. Immersed DG methods inherit the following properties of DG method: (i) it can be easily parallelized and (ii) has small dissipation and dispersion errors.

1.4 Research Goals

In this dissertation, we focus on constructing stable DG formulations with IFE spaces in order to solve one and two dimensional acoustic interface problems with high contrast media such as water/air interface problems.

1.4.1 IFE Spaces for Acoustic Interface Problems

In order to solve two dimensional acoustic interface problems (1.1.2), we construct IFE spaces using physical jump condition

$$\begin{cases} [p]_\Gamma & = 0, \\ [\mathbf{v} \cdot \nu]_\Gamma & = 0, \end{cases} \tag{1.4.1}$$

where $[\omega] = \omega_1 - \omega_2$ denotes the jump across the interface and extended conditions which are derived from the problem (1.1.2), curl-free for irrotational fluid as

$$[\nabla \times \mathbf{v}] = 0, \tag{1.4.2}$$

in addition to other consistency conditions. An instance of Lagrange type IFE shape functions shown in Figure 1.4.1.

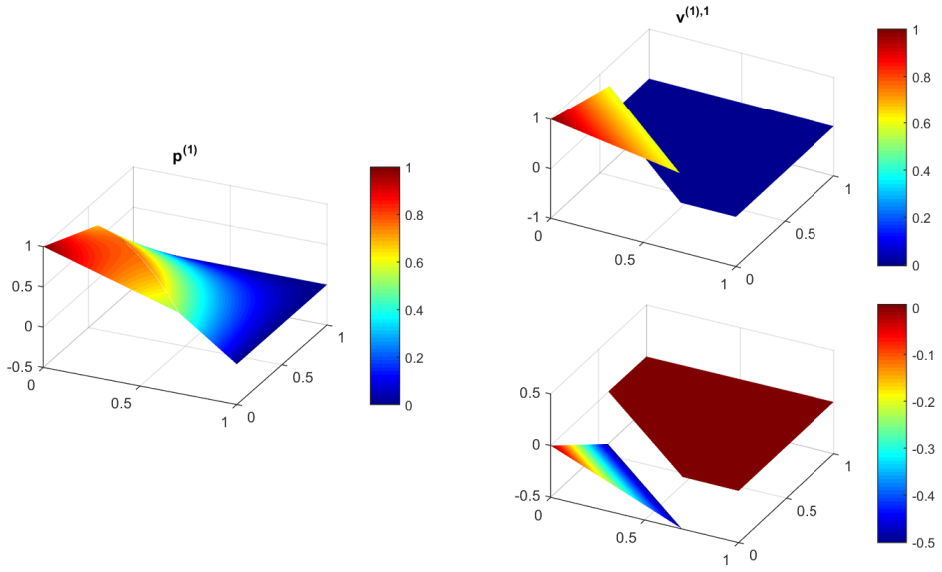

Figure 1.4.1: Piecewise bilinear IFE shape function for pressure (left) and velocity (right).

The IFE shape functions are constructed on an interface element T by taking a piecewise polynomial on each $T \cup \Omega_i$ that satisfy the jump conditions such as (1.4.1) and (1.4.2). We study their existence and uniqueness as well as their approximation capability.

1.4.2 Immersed Discontinuous Galerkin Methods

The Petrov-Galerkin method is a weak formulation of partial differential equations where the test and trial functions belong to different spaces. For instance, Petrov-Galerkin methods

have been applied to solve Navier-Stokes equations [10, 38, 98], Stokes problems [13] and convection-dominated problems [11, 42, 45]. The reader may consult [40, 41, 109, 39] for more details about discontinuous Petrov-Galerkin methods.

In this dissertation, we show that the DG method is not stable for two dimensional acoustic interface problems with high contrast media. To remedy this, we apply DG method to a scaled acoustic interface problem which yields a stable method with a small stability region. For this reason we introduce a stable discontinuous Petrov-Galerkin (DPG) method for acoustic interface problems.

1.4.3 Stability

Since hyperbolic systems are discretized in space using DG method combined with an explicit time integration scheme, stability becomes important. Numerical computations show that the standard DG method is unstable for high-jumps in speed of sound and density. However, we proved that the DG method applied to a scaled problem is stable but has a small stability region. Finally, the stability of discontinuous Petrov-Galerkin solution is established for one and two dimensional acoustic interface problems with a family of numerical fluxes. Computational results confirm the stability of our last two methods and show that extra penalty terms add more dissipation. We further show that the stability region of our immersed discontinuous Petrov-Galerkin finite element is comparable to that of the fitted mesh DG method.

1.4.4 Time Stepping

For simulations of acoustic wave propagation in inhomogeneous media on uniform meshes, the time step size is dictated by the largest CFL condition which causes a waste of computational resources. For instance, for a problem where the subregion with high sound speed is smaller than the subregion with low speed, using global time step by satisfying the CFL condition on the region with high speed is not efficient. In order to remedy this issue, we use local time-stepping that uses different time step size on each subregion by satisfying its own CFL condition.

Local time-stepping has been applied to DG methods to solve many problems such as Maxwell equations [90, 101], unsteady diffusion equations [88] and shallow-water equations [102]. We propose local time-stepping with cubic interpolation for fourth-order Runge-Kutta time integration and analyze its efficiency.

In order to further speed up computation we implement a parallel version of our C code using MPI (message passing interface) on a cluster of processors. We followed ideas in [20, 21, 62, 65] to minimize communication and achieve reasonable speed up.

Computational results show optimal convergence rates for one and two dimensional acoustic interface problems with linear and curved interfaces. We show the true and immersed Petrov-Galerkin solutions in Figure 1.4.2 for the water/air acoustic problem on a 200^2-element uniform rectangular mesh.

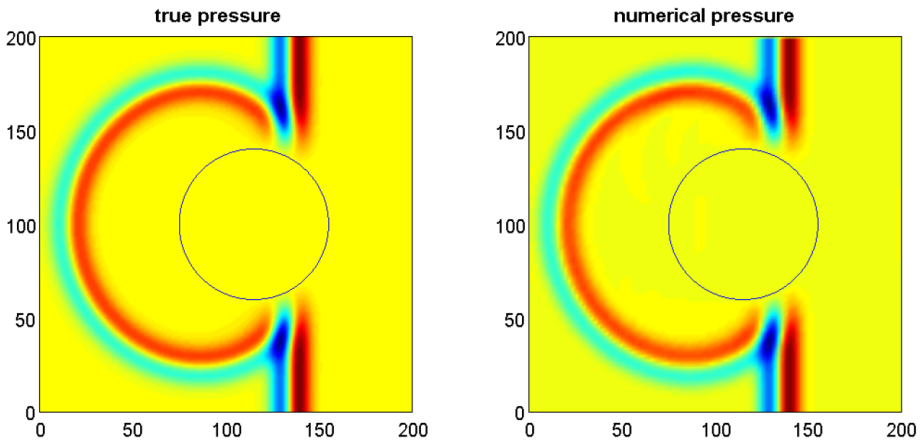

Figure 1.4.2: True and numerical pressures using 200^2 uniform square elements with bilinear IFE spaces for a two dimensional water/air interface problem.

1.5 Outline of the Dissertation

In this dissertation, we focus on higher order IFE spaces and stable immersed DG methods for solving acoustic interface problems with high jumps across the interface. The rest of the chapters are organized as follows.

In Chapter 2, we construct linear, quadratic, cubic and quartic IFE spaces for one dimensional acoustic interface problems. We develop standard Galerkin method, Galerkin method applied to a scaled problem and Petrov-Galerkin method. The existence and uniqueness of linear, quadratic, cubic and quartic IFE shape functions are proved. For the stability analysis, we prove the stability of true and discontinuous Petrov-Galerkin solutions for the one dimensional acoustic interface problem. Computational experiments for the three methods are carried out and their advantages and disadvantages are discussed.

In Chapter 3, we construct Lagrange and non Lagrange type bilinear and biquadratic IFE spaces for two dimensional acoustic problems. Several computational examples are provided

to demonstrate the approximation capability of IFE spaces and compare the IFE spaces with and without the curl-free condition. The existence of bilinear IFE shape functions for the velocity is proved.

In Chapter 4, we introduce standard Galerkin method, Galerkin method applied to the scaled problem and Petrov-Galerkin method for two dimensional acoustic interface problems and explain why we introduce three methods and the reason that penalty term is need. A local time-stepping and parallel algorithm is provided. L^2 errors and their orders of convergence are presented for several computational examples including realistic interface problems such as water/air.

In Chapter 5, we establish stability results for both immersed DG applied to a scaled problem and the immersed discontinuous Petrov-Galerkin method. Numerical results are in agreement with theory and show that the immersed DG method is unstable for the water/air interface problem. Advantages and disadvantages of the three methods are discussed for problems with a circular interface.

In Chapter 6, we briefly discuss our results and conclude with future works.

Chapter 2

One Dimensional Acoustic Problem

In this chapter, we investigate immersed discontinuous Galerkin methods for the acoustic interface problem in one dimension. We first start by stating the problem.

2.1 Problem Statement

Let p and u, respectively, be the pressure and velocity defined on the interval $I = (a, b)$ which is split into $I_1 = (a, \alpha)$ and $I_2 = (\alpha, b)$ such that $\bar{I} = \overline{I_1 \cup I_2}$. Now we consider the acoustic interface problem on I where $\mathbf{U} = [p, u]^T$ satisfies

$$\frac{\partial \mathbf{U}}{\partial t} + \mathbf{A}\frac{\partial \mathbf{U}}{\partial x} = 0 \qquad x \in I \setminus \{\alpha\}, \qquad t > t_0, \tag{2.1.1a}$$

$$\mathbf{A}_i = \mathbf{A}|_{I_i} = \begin{pmatrix} 0 & \rho_i c_i^2 \\ \frac{1}{\rho_i} & 0 \end{pmatrix}, \qquad i \ = \ 1, 2, \tag{2.1.1b}$$

with $\rho_i,\ c_i$, respectively, being the densities and sound speeds in I_i. The matrix $\mathbf{A}$ can be split as $\mathbf{A} = \mathbf{A}^+ + \mathbf{A}^-$ such that $\mathbf{A}^+$ and $\mathbf{A}^-$, respectively, have non negative and non positive eigenvalues, *i.e.*, if $A = X\Lambda X^{-1}$ with $\Lambda = diag(\lambda_1, \cdots, \lambda_n)$, then $\Lambda^{\pm} = \frac{\Lambda \pm |\Lambda|}{2}$ and $A^{\pm} = X\Lambda^{\pm}X^{-1}$.

In this problem,

$$\mathbf{A}_i^+ = \mathbf{A}^+|_{I_i} = \begin{pmatrix} \frac{c_i}{2} & \frac{\rho_i c_i^2}{2} \\ \frac{1}{2\rho_i} & \frac{c_i}{2} \end{pmatrix}, \ \mathbf{A}_i^- = \mathbf{A}^-|_{I_i} = \begin{pmatrix} -\frac{c_i}{2} & \frac{\rho_i c_i^2}{2} \\ \frac{1}{2\rho_i} & -\frac{c_i}{2} \end{pmatrix}, \qquad i \ = \ 1, 2, \tag{2.1.1c}$$

and the eigenvalues of $\mathbf{A}_i^+$ and $\mathbf{A}_i^-$ are $c_i, 0$ and $-c_i, 0$ for $i = 1, 2$, respectively. Let $\Lambda_i = \Lambda_i^+ + \Lambda_i^-$ and $X_i = X|_i$ be the matrix of eigenvectors corresponding to eigenvalues c_i, given

by

$$\Lambda_i = \Lambda|_{I_i} = \begin{pmatrix} c_i & 0 \\ 0 & -c_i, \end{pmatrix}, \; X_i = X|_{I_i} = \begin{pmatrix} c_i & c_i \\ \frac{1}{\rho_i} & -\frac{1}{\rho_i}, \end{pmatrix}, \tag{2.1.1d}$$

$$\Lambda_i^+ = \Lambda^+|_{I_i} = \begin{pmatrix} c_i & 0 \\ 0 & 0, \end{pmatrix}, \; \Lambda_i^- = \Lambda^-|_{I_i} = \begin{pmatrix} 0 & 0 \\ 0 & -c_i, \end{pmatrix}, \tag{2.1.1e}$$

for $i = 1, 2$.

This problem is further subjected to the inflow boundary conditions

$$\mathbf{A}_1^+ \mathbf{U}|_{x=a} = \mathbf{g}_a, \qquad \mathbf{A}_2^- \mathbf{U}|_{x=b} = \mathbf{g}_b, \tag{2.1.1f}$$

initial conditions

$$\mathbf{U}(x, t_0) = \mathbf{U}_0(x), \; x \in I, \tag{2.1.1g}$$

and interface conditions

$$\begin{cases} [p]|_{x=\alpha} = 0 \\ [u]|_{x=\alpha} = 0 \end{cases}, \tag{2.1.1h}$$

where $[\omega]|_{x=\alpha} = \omega(\alpha^+, t) - \omega(\alpha^-, t)$, is the jump of ω across the interface $x = \alpha$.

2.2 Immersed Finite Element Spaces

2.2.1 Construction of IFE Shape Functions

Applying the physical interface conditions (2.1.1h) all immersed shape functions must be continuous at the interface. To uniquely define high-degree immersed shape functions we need additional jump conditions (referred to as "extended jump conditions") derived in [86] from the acoustic equations (2.1.1a) as

$$\begin{aligned} &\frac{\partial^{2k}}{\partial t^{2k}} \mathbf{U} = c^{2k} \frac{\partial^{2k}}{\partial x^{2k}} \mathbf{U}, \\ &\frac{\partial^{2k+1}}{\partial t^{2k+1}} \mathbf{U} = -c^{2k} \mathbf{A} \frac{\partial^{2k+1}}{\partial x^{2k+1}} \mathbf{U}, \qquad \text{for} \quad k \geq 0. \end{aligned}$$

The continuity of $\mathbf{U}$ and its time derivatives at the interface yields the jump conditions

$$\frac{\partial^{2k}}{\partial x^{2k}} \mathbf{U}(\alpha^+, t) = \begin{pmatrix} \left(\frac{c_1}{c_2}\right)^{2k} & 0 \\ 0 & \left(\frac{c_1}{c_2}\right)^{2k} \end{pmatrix} \frac{\partial^{2k}}{\partial x^{2k}} \mathbf{U}(\alpha^-, t), \tag{2.2.1a}$$

$$\frac{\partial^{2k+1}}{\partial x^{2k+1}} \mathbf{U}(\alpha^+, t) = \begin{pmatrix} \left(\frac{\rho_2}{\rho_1}\right)\left(\frac{c_1}{c_2}\right)^{2k} & 0 \\ 0 & \left(\frac{\rho_1}{\rho_2}\right)\left(\frac{c_1}{c_2}\right)^{2k+2} \end{pmatrix} \frac{\partial^{2k+1}}{\partial x^{2k+1}} \mathbf{U}(\alpha^-, t), \tag{2.2.1b}$$

for $k \geq 0$.

Now let us consider the reference interface element $(-1, 1)$ containing an interface $\xi = \hat{\alpha}$ and the set of points $X = \{\xi_0, \xi_1, \cdots, \xi_q\}$ such that $-1 = \xi_0 < \xi_1 < \cdots < \xi_{i-1} < \hat{\alpha} < \xi_i < \cdots < \xi_q = 1$ and let $L_j,\ j = 0, 1, \cdots, q$ be the standard Lagrange polynomials such that $L_j(\xi_l) = \delta_{jl}$ given by $L_j(\xi) = \prod_{i=0, i\neq j}^{q} \frac{\xi - \xi_i}{\xi_j - \xi_i}$.

Without loss of generality we assume that $\xi_j \neq \hat{\alpha}$ and let $\mathscr{I}_1 = \{0, 1, \cdots, i-1\}$ and $\mathscr{I}_2 = \{i, i+1, \cdots, q\}$ and $\mathscr{I} = \mathscr{I}_1 \cup \mathscr{I}_2$. We express the q^{th}-degree immersed shape functions in terms of L_j as

$$\phi_i^{(q)} = \begin{cases} \phi_i^{(q),1} & = L_i + \sum\limits_{j \in \mathscr{I} \setminus \mathscr{I}_s} c_j L_j, \quad \text{on } (-1, \hat{\alpha}), \\ \phi_i^{(q),2} & = \sum\limits_{j \in \mathscr{I}_s} c_j L_j, \qquad\qquad \text{on } (\hat{\alpha}, 1), \end{cases} \qquad i \in \mathscr{I}_s, s = 1, 2. \tag{2.2.2}$$

We note that these immersed shape functions are of Lagrange type, *i.e.*, $\phi_i^{(q)}(\xi_j) = \delta_{ij}$ and the constants c_j for the pressure are determined by the jump conditions

$$\phi_i^{(q),1}(\hat{\alpha}^-) = \phi_i^{(q),2}(\hat{\alpha}^+), \tag{2.2.3a}$$

$$\frac{\partial^k \phi_i^{(q),1}(\hat{\alpha}^-)}{\partial \xi^k} = r_k \frac{\partial^k \phi_i^{(q),2}(\hat{\alpha}^+)}{\partial \xi^k}, \qquad k = 1, 2, \cdots, q, \tag{2.2.3b}$$

where for $k = 2l(\text{even})$ and $k = 2l+1(\text{odd})$

$$r_{2l} = \left(\frac{c_1}{c_2}\right)^{2l}, \qquad r_{2l+1} = \left(\frac{\rho_2}{\rho_1}\right)\left(\frac{c_1}{c_2}\right)^{2l}. \tag{2.2.3c}$$

The immersed shape functions for the velocity are obtained in a similar manner with r_{2l+1} replaced by

$$r_{2l+1} = \left(\frac{\rho_1}{\rho_2}\right)\left(\frac{c_1}{c_2}\right)^{2l+2}. \tag{2.2.3d}$$

2.2.2 Existence and Uniqueness

Here we prove the existence and uniqueness of the linear, quadratic, cubic and quartic IFE shape functions on $(-1, 1)$ which can be mapped onto a physical interface element (x_l, x_{l+1}) by linear mapping. Since the only difference between pressure and velocity IFE shape functions is r_k in (2.2.3b), we only consider the pressure IFE shape functions.

Theorem 2.2.1. *The linear IFE shape functions $\phi_i^{(1)}$, $i = 0, 1$ of the form (2.2.2) satisfying the jump conditions (2.2.3) uniquely exist on the reference element $(-1, 1)$ with $-1 < \hat{\alpha} < 1$.*

Proof. From (2.2.2), the linear IFE shape function has the form:

$$\phi_0^{(1)} = \begin{cases} \phi_0^{(1),1} & = L_0 + c_1 L_1, \quad \text{on } (-1, \hat{\alpha}), \\ \phi_0^{(1),2} & = c_0 L_0, \quad \text{on } (\hat{\alpha}, 1). \end{cases} \tag{2.2.4}$$

By the jump condition (2.2.3a) and (2.2.3b) for the linear IFE shape function, we have

$$\begin{cases} \phi_0^{(1),1}(\hat{\alpha}^-) = \phi_0^{(1),2}(\hat{\alpha}^+), \\ \frac{\partial \phi_0^{(1),1}(\hat{\alpha}^-)}{\partial \xi} = r_1 \frac{\partial \phi_0^{(1),2}(\hat{\alpha}^+)}{\partial \xi}. \end{cases} \tag{2.2.5}$$

Applying (2.2.5), we get

$$\begin{cases} L_0(\hat{\alpha}^-) + c_1 L_1(\hat{\alpha}^-) = c_0 L_0(\hat{\alpha}^+), \\ \frac{\partial L_0(\hat{\alpha}^-)}{\partial \xi} + c_1 \frac{\partial L_1(\hat{\alpha}^-)}{\partial \xi} = c_0 r_1 \frac{\partial L_0(\hat{\alpha}^+)}{\partial \xi}, \end{cases} \tag{2.2.6}$$

where matrix is

$$\begin{pmatrix} L_0(\hat{\alpha}^+) & -L_1(\hat{\alpha}^-) \\ r_1 \frac{\partial L_0(\hat{\alpha}^+)}{\partial \xi} & -\frac{\partial L_1(\hat{\alpha}^-)}{\partial \xi} \end{pmatrix} \begin{pmatrix} c_0 \\ c_1 \end{pmatrix} = \begin{pmatrix} L_0(\hat{\alpha}^-) \\ \frac{\partial L_0(\hat{\alpha}^-)}{\partial \xi} \end{pmatrix}. \tag{2.2.7}$$

Thus it is enough to show that the matrix

$$\mathbf{M} = \begin{pmatrix} L_0(\hat{\alpha}^+) & -L_1(\hat{\alpha}^-) \\ r_1 \frac{\partial L_0(\hat{\alpha}^+)}{\partial \xi} & -\frac{\partial L_1(\hat{\alpha}^-)}{\partial \xi} \end{pmatrix} \tag{2.2.8}$$

is invertible for $-1 < \hat{\alpha} < 1$ in order to show the existence and uniqueness of the linear IFE shape function (2.2.4).

Since the linear Lagrange shape functions L_j, $j = 0, 1$ are continuous on $(-1, 1)$, the matrix is

$$\mathbf{M} = \begin{pmatrix} L_0(\hat{\alpha}) & -L_1(\hat{\alpha}) \\ r_1 L_0'(\hat{\alpha}) & -L_1'(\hat{\alpha}) \end{pmatrix}. \tag{2.2.9}$$

Using L_j, $j = 0, 1$ where $\xi_0 = -1$ and $\xi_1 = 1$, the determinant of $\mathbf{M}$ is

$$\det(\mathbf{M}) = \left(\frac{-(\hat{\alpha} + 1)}{4} \right) r_1 + \left(\frac{\hat{\alpha} - 1}{4} \right). \tag{2.2.10}$$

For $-1 < \hat{\alpha} < 1$, since $\hat{\alpha} + 1 > 0$, $\hat{\alpha} - 1 < 0$ and $r_1 > 0$, we get $\det(\mathbf{M}) < 0$. Thus the linear IFE shape function $\phi_0^{(1)}$ uniquely exists. For $\phi_1^{(1)}$, we obtain the same matrix $\mathbf{M}$. Thus $\phi_1^{(1)}$ uniquely exists. □

Theorem 2.2.2. *The quadratic IFE shape functions $\phi_i^{(2)}$, $i = 0, 1, 2$ of the form (2.2.2) satisfying the jump conditions (2.2.3) uniquely exist on the reference element $(-1, 1)$ with $-1 < \hat{\alpha} < 1$.*

Proof. For the quadratic IFE shape function, we use the three points $X = \{-1, 0, 1\}$ to construct L_j on $(-1, 1)$. Thus there are two cases depending on the position of the interface: $-1 < \hat{\alpha} \leq 0$ and $0 < \hat{\alpha} < 1$. Since the proof for all shape functions are the same, we consider one shape function in each case.

Case 1: $-1 < \hat{\alpha} \leq 0$.
We consider the IFE shape function which is

$$\phi_0^{(2)} = \begin{cases} \phi_0^{(2),1} & = L_0 + c_1 L_1 + c_2 L_2, \quad \text{on } (-1, \hat{\alpha}), \\ \phi_0^{(2),2} & = c_0 L_0, \qquad\qquad\quad \text{on } (\hat{\alpha}, 1). \end{cases} \tag{2.2.11}$$

Applying (2.2.3), we obtain

$$\begin{cases} L_0(\hat{\alpha}^-) + c_1 L_1(\hat{\alpha}^-) + c_2 L_2(\hat{\alpha}^-) = c_0 L_0(\hat{\alpha}^+), \\ \frac{\partial L_0(\hat{\alpha}^-)}{\partial \xi} + c_1 \frac{\partial L_1(\hat{\alpha}^-)}{\partial \xi} + c_2 \frac{\partial L_2(\hat{\alpha}^-)}{\partial \xi} = c_0 r_1 \frac{\partial L_0(\hat{\alpha}^+)}{\partial \xi}, \\ \frac{\partial^2 L_0(\hat{\alpha}^-)}{\partial \xi^2} + c_1 \frac{\partial^2 L_1(\hat{\alpha}^-)}{\partial \xi^2} + c_2 \frac{\partial^2 L_2(\hat{\alpha}^-)}{\partial \xi^2} = c_0 r_2 \frac{\partial^2 L_0(\hat{\alpha}^+)}{\partial^2 \xi}. \end{cases} \tag{2.2.12}$$

Using the same argument of Theorem 2.2.1, it is enough to show that the matrix

$$\mathbf{M} = \begin{pmatrix} L_0(\hat{\alpha}) & -L_1(\hat{\alpha}) & -L_2(\hat{\alpha}) \\ r_1 L_0'(\hat{\alpha}) & -L_1'(\hat{\alpha}) & -L_2'(\hat{\alpha}) \\ r_2 L_0''(\hat{\alpha}) & -L_1''(\hat{\alpha}) & -L_2''(\hat{\alpha}) \end{pmatrix} \tag{2.2.13}$$

is invertible for $-1 < \hat{\alpha} < 1$. Using the quadratic Lagrange shape functions L_j, $j = 0, 1, 2$ where $\xi_0 = -1$, $\xi_1 = 0$ and $\xi_2 = 1$, the determinant of $\mathbf{M}$ is

$$\det(\mathbf{M}) = \left(\frac{-(\hat{\alpha} + 1)(2\hat{\alpha} - 1)}{2} \right) r_1 + \left(\frac{(\hat{\alpha} + 1)^2}{2} \right) r_2 + \left(\frac{\hat{\alpha}(\hat{\alpha} - 1)}{2} \right). \tag{2.2.14}$$

We note that $\hat{\alpha}+1 > 0$, $2\hat{\alpha}-1 < 0$, $\hat{\alpha}-1 < 0$, $\hat{\alpha} \leq 0$ and r_1, r_2 are positive, thus $\det(\mathbf{M}) > 0$ and the quadratic IFE shape function $\phi_0^{(2)}$ for $-1 < \hat{\alpha} \leq 0$ is uniquely determined.

Case 2: $0 < \hat{\alpha} < 1$.
The IFE shape function has the form:

$$\phi_0^{(2)} = \begin{cases} \phi_0^{(2),1} & = L_0 + c_2 L_2, \qquad \text{on } (-1, \hat{\alpha}), \\ \phi_0^{(2),2} & = c_0 L_0 + c_1 L_1, \quad \text{on } (\hat{\alpha}, 1), \end{cases} \tag{2.2.15}$$

where associated matrix

$$\mathbf{M} = \begin{pmatrix} L_0(\hat{\alpha}) & L_1(\hat{\alpha}) & -L_2(\hat{\alpha}) \\ r_1 L_0'(\hat{\alpha}) & r_1 L_1'(\hat{\alpha}) & -L_2'(\hat{\alpha}) \\ r_2 L_0''(\hat{\alpha}) & r_2 L_1''(\hat{\alpha}) & -L_2''(\hat{\alpha}) \end{pmatrix}, \tag{2.2.16}$$

and

$$\det(\mathbf{M}) = \left(\frac{-(\hat{\alpha} - 1)^2}{2} \right) r_1 + \left(\frac{(\hat{\alpha} - 1)(2\hat{\alpha} + 1)}{2} \right) r_2 + \left(\frac{-\hat{\alpha}(\hat{\alpha} + 1)}{2} \right) r_1 r_2. \tag{2.2.17}$$

We note that $\hat{\alpha}-1<0$, $2\hat{\alpha}+1>0$, $\hat{\alpha}>0$, $\hat{\alpha}+1>0$, and r_1, r_2 are positive, thus $\det(\mathbf{M})<0$ and the quadratic IFE shape function $\phi_0^{(2)}$ for $0<\hat{\alpha}<1$ uniquely exists.

Combining cases 1 and 2 for $-1<\hat{\alpha}<1$, we conclude that the quadratic IFE shape function $\phi_0^{(2)}$ uniquely exists on $(-1,1)$. Since we obtain the same matrix $\mathbf{M}$ for $\phi_1^{(2)}$ and $\phi_2^{(2)}$, the quadratic IFE basis $\phi_1^{(2)}$ and $\phi_2^{(2)}$ also exist uniquely. □

Theorem 2.2.3. *The cubic IFE shape functions $\phi_i^{(3)}$, $i=0,1,2,3$ of the form (2.2.2) satisfying the jump conditions (2.2.3) uniquely exist on the reference element $(-1,1)$ with $-1<\hat{\alpha}<1$.*

Proof. For the cubic IFE shape functions, we consider four points $X=\{-1,-\frac{1}{\sqrt{3}},\frac{1}{\sqrt{3}},1\}$ on $(-1,1)$ but other points may also be used. Here, we consider three cases: $-1<\hat{\alpha}\le-\frac{1}{\sqrt{3}}$, $-\frac{1}{\sqrt{3}}<\hat{\alpha}\le\frac{1}{\sqrt{3}}$ and $\frac{1}{\sqrt{3}}<\hat{\alpha}<1$.

Case 1: $-1<\hat{\alpha}\le-\frac{1}{\sqrt{3}}$.
The first IFE cubic shape function has the form:

$$\phi_0^{(3)}=\begin{cases}\phi_0^{(3),1} & =L_0+c_1L_1+c_2L_2+c_3L_3, \quad \text{on } (-1,\hat{\alpha}),\\ \phi_0^{(3),2} & =c_0L_0, \quad \text{on } (\hat{\alpha},1).\end{cases} \tag{2.2.18}$$

Applying (2.2.3), we get

$$\begin{cases} L_0(\hat{\alpha}^-)+c_1L_1(\hat{\alpha}^-)+c_2L_2(\hat{\alpha}^-)+c_3L_3(\hat{\alpha}^-)=c_0L_0(\hat{\alpha}^+),\\ \frac{\partial L_0(\hat{\alpha}^-)}{\partial\xi}+c_1\frac{\partial L_1(\hat{\alpha}^-)}{\partial\xi}+c_2\frac{\partial L_2(\hat{\alpha}^-)}{\partial\xi}+c_3\frac{\partial L_3(\hat{\alpha}^-)}{\partial\xi}=c_0r_1\frac{\partial L_0(\hat{\alpha}^+)}{\partial\xi},\\ \frac{\partial^2 L_0(\hat{\alpha}^-)}{\partial\xi^2}+c_1\frac{\partial^2 L_1(\hat{\alpha}^-)}{\partial\xi^2}+c_2\frac{\partial^2 L_2(\hat{\alpha}^-)}{\partial\xi^2}+c_3\frac{\partial^2 L_3(\hat{\alpha}^-)}{\partial\xi^2}=c_0r_2\frac{\partial^2 L_0(\hat{\alpha}^+)}{\partial^2\xi},\\ \frac{\partial^3 L_0(\hat{\alpha}^-)}{\partial\xi^3}+c_1\frac{\partial^3 L_1(\hat{\alpha}^-)}{\partial\xi^3}+c_2\frac{\partial^3 L_2(\hat{\alpha}^-)}{\partial\xi^3}+c_3\frac{\partial^3 L_3(\hat{\alpha}^-)}{\partial\xi^3}=c_0r_3\frac{\partial^3 L_0(\hat{\alpha}^+)}{\partial^3\xi}, \end{cases} \tag{2.2.19}$$

for $-1<\hat{\alpha}\le-\frac{1}{\sqrt{3}}$. By the same argument used for Theorem 2.2.1, it is enough to show that the matrix

$$\mathbf{M}=\begin{pmatrix} L_0(\hat{\alpha}) & -L_1(\hat{\alpha}) & -L_2(\hat{\alpha}) & -L_3(\hat{\alpha})\\ r_1L_0'(\hat{\alpha}) & -L_1'(\hat{\alpha}) & -L_2'(\hat{\alpha}) & -L_3'(\hat{\alpha})\\ r_2L_0''(\hat{\alpha}) & -L_1''(\hat{\alpha}) & -L_2''(\hat{\alpha}) & -L_3''(\hat{\alpha})\\ r_3L_0'''(\hat{\alpha}) & -L_1'''(\hat{\alpha}) & -L_2'''(\hat{\alpha}) & -L_3'''(\hat{\alpha}) \end{pmatrix} \tag{2.2.20}$$

is invertible for $-1<\hat{\alpha}\le\frac{1}{\sqrt{3}}$. By the cubic Lagrange shape functions L_j, $j=0,1,2,3$ where $\xi_0=-1$, $\xi_1=-\sqrt{\frac{1}{3}}$, $\xi_2=\sqrt{\frac{1}{3}}$ and $\xi_3=1$,

$$\begin{aligned}\det(\mathbf{M})=&\left(\frac{-27\sqrt{3}(\hat{\alpha}+1)(9\hat{\alpha}^2-6\hat{\alpha}-1)}{16}\right)r_1+\left(\frac{81\sqrt{3}(3\hat{\alpha}-1)(\hat{\alpha}+1)^2}{16}\right)r_2\\ &+\left(\frac{-81\sqrt{3}(\hat{\alpha}+1)^3}{16}\right)r_3+\left(\frac{27\sqrt{3}(\hat{\alpha}-1)(3\hat{\alpha}^2-1)}{16}\right).\end{aligned} \tag{2.2.21}$$

The quadratic function $9\hat{\alpha}^2 - 6\hat{\alpha} - 1 > 0$ for $-1 < \hat{\alpha} \leq -\frac{1}{\sqrt{3}}$ and $\hat{\alpha} + 1 > 0$ which yields that the coefficient of r_1 is negative.

Noting that $3\hat{\alpha} - 1 < 0$ and $\hat{\alpha} + 1 > 0$ shows that the coefficients of r_2 and r_3 are negative. For $\hat{\alpha} - 1 < 0$ and $3\hat{\alpha}^2 - 1 \geq 0$, we know the coefficient of r_4 is non positive.

Since all the terms are negative or non positive and r_1, r_2 ,r_3 are positive, the determinant of $\mathbf{M}$ is negative. Thus the cubic IFE shape function $\phi_0^{(3)}$ uniquely exists for $-1 < \hat{\alpha} \leq -\frac{1}{\sqrt{3}}$.

Case 2: $-\frac{1}{\sqrt{3}} < \hat{\alpha} \leq \frac{1}{\sqrt{3}}$.
The IFE shape function $\phi_0^{(3)}$ can be written as

$$\phi_0^{(3)} = \begin{cases} \phi_0^{(3),1} & = L_0 + c_2 L_2 + c_3 L_3, \quad \text{on } (-1, \hat{\alpha}), \\ \phi_0^{(3),2} & = c_0 L_0 + c_1 L_1, \quad \text{on } (\hat{\alpha}, 1). \end{cases} \tag{2.2.22}$$

Similarly, the matrix $\mathbf{M}$ is

$$\mathbf{M} = \begin{pmatrix} L_0(\hat{\alpha}) & L_1(\hat{\alpha}) & -L_2(\hat{\alpha}) & -L_3(\hat{\alpha}) \\ r_1 L_0'(\hat{\alpha}) & r_1 L_1'(\hat{\alpha}) & -L_2'(\hat{\alpha}) & -L_3'(\hat{\alpha}) \\ r_2 L_0''(\hat{\alpha}) & r_2 L_1''(\hat{\alpha}) & -L_2''(\hat{\alpha}) & -L_3''(\hat{\alpha}) \\ r_3 L_0'''(\hat{\alpha}) & r_3 L_1'''(\hat{\alpha}) & -L_2'''(\hat{\alpha}) & -L_3'''(\hat{\alpha}) \end{pmatrix}. \tag{2.2.23}$$

A direct computation shows that

$$\begin{aligned} \det(\mathbf{M}) = & \left(\frac{81(2-\sqrt{3})(\hat{\alpha}-1)^2(\sqrt{3}\hat{\alpha}-1)^2}{32} \right) r_1 \\ & + \left(\frac{-9\sqrt{3}(2-\sqrt{3})(\hat{\alpha}-1)(\sqrt{3}\hat{\alpha}-1)(6\hat{\alpha}+\sqrt{3}+3)(6\hat{\alpha}-\sqrt{3}-3)}{32} \right) r_2 \\ & + \left(\frac{27\sqrt{3}(2-\sqrt{3})(\hat{\alpha}-1)(\sqrt{3}\hat{\alpha}-1)(9\hat{\alpha}^2+3\sqrt{3}\hat{\alpha}+9\hat{\alpha}+\sqrt{3}+4)}{32} \right) r_3 \\ & + \left(\frac{27\sqrt{3}(2-\sqrt{3})(\hat{\alpha}+1)(\sqrt{3}\hat{\alpha}+1)(9\hat{\alpha}^2-3\sqrt{3}\hat{\alpha}-9\hat{\alpha}+\sqrt{3}+4)}{32} \right) r_1 r_2 \\ & + \left(\frac{-9\sqrt{3}(2-\sqrt{3})(\hat{\alpha}+1)(\sqrt{3}\hat{\alpha}+1)(6\hat{\alpha}+\sqrt{3}+3)(6\hat{\alpha}-\sqrt{3}-3)}{32} \right) r_1 r_3 \\ & + \left(\frac{81(2-\sqrt{3})(\hat{\alpha}+1)^2(\sqrt{3}\hat{\alpha}+1)^2}{32} \right) r_2 r_3. \end{aligned} \tag{2.2.24}$$

One can immediately note that the coefficient of r_1 is non negative. Since $\hat{\alpha} - 1 < 0$, $\sqrt{3}\hat{\alpha} - 1 \leq 0$, $6\hat{\alpha} + \sqrt{3} + 3 > 0$ and $6\hat{\alpha} - \sqrt{3} - 3 < 0$, we show that the coefficient of r_2 is non negative. The quadratic function $9\hat{\alpha}^2 + 3\sqrt{3}\hat{\alpha} + 9\hat{\alpha} + \sqrt{3} + 4 > 0$ and we know $\hat{\alpha} - 1 < 0$, $\sqrt{3}\hat{\alpha} - 1 \leq 0$, we know that the coefficient of r_3 is non negative.

Next, we have $\hat{\alpha}+1>0$, $\sqrt{3}\hat{\alpha}+1>0$ and $9\hat{\alpha}^2-3\sqrt{3}\hat{\alpha}-9\hat{\alpha}+\sqrt{3}+4>0$. Thus coefficient of r_1r_2 is positive. Noting that $\hat{\alpha}+1>0$, $\sqrt{3}\hat{\alpha}+1>0$, $6\hat{\alpha}+\sqrt{3}+3>0$ and $6\hat{\alpha}-\sqrt{3}-3<0$, we obtain that the coefficient of r_1r_3 is positive. Finally we observe that the coefficient of r_2r_3 is positive.

Since all coefficients are positive or non negative and r_1, r_2 ,r_3 are positive, the determinant of $\mathbf{M}$ is positive. Thus, the cubic IFE shape function $\phi_0^{(3)}$ for $-\frac{1}{\sqrt{3}}<\hat{\alpha}\leq\frac{1}{\sqrt{3}}$ uniquely exists.

Case 3: $\frac{1}{\sqrt{3}}<\hat{\alpha}<1$.
The IFE shape function $\phi_0^{(3)}$ is

$$\phi_0^{(3)}=\begin{cases}\phi_0^{(3),1} & =L_0+c_3L_3, \qquad \text{on } (-1,\hat{\alpha}),\\ \phi_0^{(3),2} & =c_0L_0+c_1L_1+c_2L_2, \qquad \text{on } (\hat{\alpha},1).\end{cases} \tag{2.2.25}$$

Similarly, the corresponding matrix $\mathbf{M}$ is

$$\mathbf{M}=\begin{pmatrix} L_0(\hat{\alpha}) & L_1(\hat{\alpha}) & L_2(\hat{\alpha}) & -L_3(\hat{\alpha})\\ r_1L_0'(\hat{\alpha}) & r_1L_1'(\hat{\alpha}) & r_1L_2'(\hat{\alpha}) & -L_3'(\hat{\alpha})\\ r_2L_0''(\hat{\alpha}) & r_2L_1''(\hat{\alpha}) & r_2L_2''(\hat{\alpha}) & -L_3''(\hat{\alpha})\\ r_3L_0'''(\hat{\alpha}) & r_3L_1'''(\hat{\alpha}) & r_3L_2'''(\hat{\alpha}) & -L_3'''(\hat{\alpha}) \end{pmatrix}, \tag{2.2.26}$$

with

$$\begin{aligned}\det(\mathbf{M})=&\left(\frac{81\sqrt{3}(\hat{\alpha}-1)^3}{16}\right)r_1r_2+\left(\frac{-81\sqrt{3}(3\hat{\alpha}+1)(\hat{\alpha}-1)^2}{16}\right)r_1r_3 \\ &+\left(\frac{27\sqrt{3}(\hat{\alpha}-1)(9\hat{\alpha}^2+6\hat{\alpha}-1)}{16}\right)r_2r_3+\left(\frac{-27\sqrt{3}(\hat{\alpha}+1)(3\hat{\alpha}^2-1)}{16}\right)r_1r_2r_3.\end{aligned} \tag{2.2.27}$$

Since $\hat{\alpha}-1<0$, the coefficient of r_1r_2 is negative. Again since $3\hat{\alpha}+1>0$ and the coefficient of r_1r_3 is negative. Additionally, by the fact that $\hat{\alpha}-1<0$ and $9\hat{\alpha}^2+6\hat{\alpha}-1>0$, we show that the coefficient of r_2r_3 is negative. Lastly, since $\hat{\alpha}+1>0$ and $3\hat{\alpha}^2-1>0$, the coefficient of $r_1r_2r_3$ is negative.

Since all terms are negative and r_1, r_2, r_3 are positive, the determinant of $\mathbf{M}$ is negative. This implies that the cubic IFE shape function $\phi_0^{(3)}$ uniquely exists for $\frac{1}{\sqrt{3}}<\hat{\alpha}<1$.

Combining cases 1, 2 and 3 for $-1<\hat{\alpha}<1$, we conclude that the cubic IFE shape function $\phi_0^{(3)}$ uniquely exists on $(-1,1)$. For $\phi_1^{(3)}$, $\phi_2^{(3)}$ and $\phi_3^{(3)}$, the matrix $\mathbf{M}$ is the same. Thus $\phi_1^{(3)}$, $\phi_2^{(3)}$ and $\phi_3^{(3)}$ uniquely exist. □

Theorem 2.2.4. *The quartic IFE shape functions $\phi_i^{(4)}$, $i=0,1,2,3,4$ of the form (2.2.2) satisfying the jump conditions (2.2.3) uniquely exist on the reference element $(-1,1)$ with $-1<\hat{\alpha}<1$.*

Proof. For the quartic IFE shape function, we use five points $X = \{-1, -\sqrt{\frac{3}{5}}, 0, \sqrt{\frac{3}{5}}, 1\}$ on $(-1, 1)$ but other points may also be used. Without loss of generality, we consider the four cases: $-1 < \hat{\alpha} \leq -\sqrt{\frac{3}{5}}$, $-\sqrt{\frac{3}{5}} < \hat{\alpha} \leq 0$, $0 < \hat{\alpha} \leq \sqrt{\frac{3}{5}}$ and $\sqrt{\frac{3}{5}} < \hat{\alpha} < 1$.

Case 1: $-1 < \hat{\alpha} \leq -\sqrt{\frac{3}{5}}$.
The quartic IFE shape function has the form:

$$\phi_0^{(4)} = \begin{cases} \phi_0^{(4),1} & = L_0 + c_1 L_1 + c_2 L_2 + c_3 L_3 + c_4 L_4, \quad \text{on } (-1, \hat{\alpha}), \\ \phi_0^{(4),2} & = c_0 L_0, \quad \text{on } (\hat{\alpha}, 1). \end{cases} \tag{2.2.28}$$

Applying (2.2.3) yields

$$\begin{cases} L_0(\hat{\alpha}^-) + c_1 L_1(\hat{\alpha}^-) + c_2 L_2(\hat{\alpha}^-) + c_3 L_3(\hat{\alpha}^-) + c_4 L_4(\hat{\alpha}^-) = c_0 L_0(\hat{\alpha}^+), \\ \frac{\partial L_0(\hat{\alpha}^-)}{\partial \xi} + c_1 \frac{\partial L_1(\hat{\alpha}^-)}{\partial \xi} + c_2 \frac{\partial L_2(\hat{\alpha}^-)}{\partial \xi} + c_3 \frac{\partial L_3(\hat{\alpha}^-)}{\partial \xi} + c_4 \frac{\partial L_4(\hat{\alpha}^-)}{\partial \xi} = c_0 r_1 \frac{\partial L_0(\hat{\alpha}^+)}{\partial \xi}, \\ \frac{\partial^2 L_0(\hat{\alpha}^-)}{\partial \xi^2} + c_1 \frac{\partial^2 L_1(\hat{\alpha}^-)}{\partial \xi^2} + c_2 \frac{\partial^2 L_2(\hat{\alpha}^-)}{\partial \xi^2} + c_3 \frac{\partial^2 L_3(\hat{\alpha}^-)}{\partial \xi^2} + c_4 \frac{\partial^2 L_4(\hat{\alpha}^-)}{\partial \xi^2} = c_0 r_2 \frac{\partial^2 L_0(\hat{\alpha}^+)}{\partial^2 \xi}, \\ \frac{\partial^3 L_0(\hat{\alpha}^-)}{\partial \xi^3} + c_1 \frac{\partial^3 L_1(\hat{\alpha}^-)}{\partial \xi^3} + c_2 \frac{\partial^3 L_2(\hat{\alpha}^-)}{\partial \xi^3} + c_3 \frac{\partial^3 L_3(\hat{\alpha}^-)}{\partial \xi^3} + c_4 \frac{\partial^3 L_4(\hat{\alpha}^-)}{\partial \xi^3} = c_0 r_3 \frac{\partial^3 L_0(\hat{\alpha}^+)}{\partial^3 \xi}, \\ \frac{\partial^4 L_0(\hat{\alpha}^-)}{\partial \xi^4} + c_1 \frac{\partial^4 L_1(\hat{\alpha}^-)}{\partial \xi^4} + c_2 \frac{\partial^4 L_2(\hat{\alpha}^-)}{\partial \xi^4} + c_3 \frac{\partial^4 L_3(\hat{\alpha}^-)}{\partial \xi^4} + c_4 \frac{\partial^4 L_4(\hat{\alpha}^-)}{\partial \xi^4} = c_0 r_4 \frac{\partial^4 L_0(\hat{\alpha}^+)}{\partial^4 \xi}, \end{cases} \tag{2.2.29}$$

for $-1 < \hat{\alpha} \leq -\sqrt{\frac{3}{5}}$. By the same argument of Theorem 2.2.1, it suffices to show that the matrix

$$\mathbf{M} = \begin{pmatrix} L_0(\hat{\alpha}) & -L_1(\hat{\alpha}) & -L_2(\hat{\alpha}) & -L_3(\hat{\alpha})) & -L_4(\hat{\alpha}) \\ r_1 L_0'(\hat{\alpha}) & -L_1'(\hat{\alpha}) & -L_2'(\hat{\alpha}) & -L_3'(\hat{\alpha}) & -L_4'(\hat{\alpha}) \\ r_2 L_0''(\hat{\alpha}) & -L_1''(\hat{\alpha}) & -L_2''(\hat{\alpha}) & -L_3''(\hat{\alpha}) & -L_4''(\hat{\alpha}) \\ r_3 L_0'''(\hat{\alpha}) & -L_1'''(\hat{\alpha}) & -L_2'''(\hat{\alpha}) & -L_3'''(\hat{\alpha}) & -L_4'''(\hat{\alpha}) \\ r_4 L_0''''(\hat{\alpha}) & -L_1''''(\hat{\alpha}) & -L_2''''(\hat{\alpha}) & -L_3''''(\hat{\alpha}) & -L_4''''(\hat{\alpha}) \end{pmatrix}. \tag{2.2.30}$$

is invertible for $-1 < \hat{\alpha} \leq -\sqrt{\frac{3}{5}}$. Using the quartic Lagrange shape functions L_j, $j = 0, 1, 2, 3, 4$ where $\xi_0 = -1$, $\xi_1 = -\sqrt{\frac{3}{5}}$, $\xi_2 = 0$, $\xi_3 = \sqrt{\frac{3}{5}}$ and $\xi_4 = 1$, the determinant of $\mathbf{M}$ is

$$\begin{aligned} \det(\mathbf{M}) = & \left(\frac{-125\sqrt{15}(\hat{\alpha}+1)(20\hat{\alpha}^3 - 15\hat{\alpha}^2 - 6\hat{\alpha} + 3)}{2} \right) r_1 \\ & + \left(\frac{375\sqrt{15}(\hat{\alpha}+1)^2(10\hat{\alpha}^2 - 5\hat{\alpha} - 1)}{2} \right) r_2 + \left(\frac{-625\sqrt{15}(4\hat{\alpha}-1)(\hat{\alpha}+1)^3}{2} \right) r_3 \\ & + \left(\frac{625\sqrt{15}(\hat{\alpha}+1)^4}{2} \right) r_4 + \left(\frac{125\sqrt{15}\hat{\alpha}(\hat{\alpha}-1)(5\hat{\alpha}^2 - 3)}{2} \right). \end{aligned} \tag{2.2.31}$$

Using $20\hat{\alpha}^3 - 15\hat{\alpha}^2 - 6\hat{\alpha} + 3 < 0$ for $-1 < \hat{\alpha} \leq -\sqrt{\frac{3}{5}}$ and $\hat{\alpha} + 1 > 0$, we show that the coefficient of r_1 is positive. Next we note that $10\hat{\alpha}^2 - 5\hat{\alpha} - 1 > 0$, thus the coefficient of r_2 is positive.

Since $4\hat{\alpha}-1<0$ and $\hat{\alpha}+1>0$, the coefficient of r_3 is positive. The coefficient of r_4 is also positive and using the fact that $\hat{\alpha}<0$, $\hat{\alpha}-1<0$ and $5\hat{\alpha}^2-3\geq 0$, the last coefficient is non negative.

Since all terms are positive or non negative and r_1, r_2, r_3, r_4 are positive, the determinant of $\mathbf{M}$ is also positive and the quartic IFE shape function $\phi_0^{(4)}$ uniquely exists for $-1<\hat{\alpha}\leq -\sqrt{\frac{3}{5}}$.

Case 2: $-\sqrt{\frac{3}{5}}<\hat{\alpha}\leq 0$.

The IFE shape function $\phi_0^{(4)}$ is

$$\phi_0^{(4)}=\begin{cases}\phi_0^{(4),1} & =L_0+c_2L_2+c_3L_3+c_4L_4, \quad \text{on } (-1,\hat{\alpha}),\\ \phi_0^{(4),2} & =c_0L_0+c_1L_1, \qquad\qquad\qquad\quad \text{on } (\hat{\alpha},1),\end{cases} \tag{2.2.32}$$

with matrix

$$\mathbf{M}=\begin{pmatrix} L_0(\hat{\alpha}) & L_1(\hat{\alpha}) & -L_2(\hat{\alpha}) & -L_3(\hat{\alpha})) & -L_4(\hat{\alpha})\\ r_1L_0'(\hat{\alpha}) & r_1L_1'(\hat{\alpha}) & -L_2'(\hat{\alpha}) & -L_3'(\hat{\alpha}) & -L_4'(\hat{\alpha})\\ r_2L_0''(\hat{\alpha}) & r_2L_1''(\hat{\alpha}) & -L_2''(\hat{\alpha}) & -L_3''(\hat{\alpha}) & -L_4''(\hat{\alpha})\\ r_3L_0'''(\hat{\alpha}) & r_3L_1'''(\hat{\alpha}) & -L_2'''(\hat{\alpha}) & -L_3'''(\hat{\alpha}) & -L_4'''(\hat{\alpha})\\ r_4L_0''''(\hat{\alpha}) & r_4L_1''''(\hat{\alpha}) & -L_2''''(\hat{\alpha}) & -L_3''''(\hat{\alpha}) & -L_4''''(\hat{\alpha}) \end{pmatrix}. \tag{2.2.33}$$

The determinant of $\mathbf{M}$ is

$$\begin{aligned}
\det(\mathbf{M}) &= \left(\frac{-125(4\sqrt{15}-15)\hat{\alpha}^2(\hat{\alpha}-1)^2(5\hat{\alpha}-\sqrt{15})^2}{12}\right)r_1\\
&+\left(\frac{25(4\sqrt{15}-15)\hat{\alpha}(\hat{\alpha}-1)(5\hat{\alpha}-\sqrt{15})(10\hat{\alpha}+5+\sqrt{15})(15\hat{\alpha}^2-(10+2\sqrt{15})\hat{\alpha}+\sqrt{15})}{12}\right)r_2\\
&+\left(\frac{-25(4\sqrt{15}-15)\hat{\alpha}(\hat{\alpha}-1)(5\hat{\alpha}-\sqrt{15})(15\hat{\alpha}-5-\sqrt{15})(15\hat{\alpha}^2+(15+3\sqrt{15})\hat{\alpha}+8+\sqrt{15})}{12}\right)r_3\\
&+\left(\frac{25(4\sqrt{15}-15)\hat{\alpha}(\hat{\alpha}-1)(5\hat{\alpha}-\sqrt{15})(10\hat{\alpha}+5+\sqrt{15})(5\hat{\alpha}^2+(5+\sqrt{15})\hat{\alpha}+4)}{6}\right)r_4\\
&+\left(\frac{-625(\hat{\alpha}+1)(\sqrt{15}\hat{\alpha}+3)(30(4-\sqrt{15})\hat{\alpha}^4-8(5-\sqrt{15})\hat{\alpha}^3+(12\sqrt{15}-39)\hat{\alpha}^2-3(\sqrt{15}-3)\hat{\alpha}+3(4-\sqrt{15}))}{12}\right)r_1r_2\\
&+\left(\frac{5(4\sqrt{15}-15)(2\hat{\alpha}-1)(\hat{\alpha}+1)(5\hat{\alpha}+\sqrt{15})(10\hat{\alpha}-\sqrt{15})(10\hat{\alpha}-5-\sqrt{15})(10\hat{\alpha}+5+\sqrt{15})}{12}\right)r_1r_3\\
&+\left(\frac{-25(4-\sqrt{15})(\hat{\alpha}+1)(\sqrt{15}\hat{\alpha}+3)(15\hat{\alpha}+\sqrt{40-5\sqrt{15}}-\sqrt{15}-5)(15\hat{\alpha}-\sqrt{40-5\sqrt{15}}-\sqrt{15}-5)(15\hat{\alpha}^2+(15+3\sqrt{15})\hat{\alpha}+\sqrt{15}+8)}{36}\right)r_1r_4\\
&+\left(\frac{-25(\hat{\alpha}+1)^2(5\hat{\alpha}+\sqrt{15})^2((-450+120\sqrt{15})\hat{\alpha}^2+(60-20\sqrt{15})\hat{\alpha}-60+17\sqrt{15})}{12}\right)r_2r_3\\
&+\left(\frac{5(4\sqrt{15}-15)(\hat{\alpha}+1)^2(10\hat{\alpha}+5+\sqrt{15})(15\hat{\alpha}-5-\sqrt{15})(5\hat{\alpha}+\sqrt{15})^2}{12}\right)r_2r_4\\
&+\left(\frac{-25(4\sqrt{15}-15)(\hat{\alpha}+1)^3(5\hat{\alpha}+\sqrt{15})^3}{12}\right)r_3r_4.
\end{aligned} \tag{2.2.34}$$

For $-\sqrt{\frac{3}{5}}<\hat{\alpha}\leq 0$, the coefficient of r_1 is non positive. Since $\hat{\alpha}\leq 0$, $\hat{\alpha}-1<0$, $5\hat{\alpha}-\sqrt{15}<0$, $10\hat{\alpha}+5+\sqrt{15}>0$ and $15\hat{\alpha}^2-(10+2\sqrt{15})\hat{\alpha}+\sqrt{15}>0$, the coefficient of r_2 is non positive. Moreover, $15\hat{\alpha}-5-\sqrt{15}<0$ and $15\hat{\alpha}^2+(15+3\sqrt{15})\hat{\alpha}+8+\sqrt{15}>0$, we obtain that the coefficient of r_3 is non positive. The coefficient of r_4 is non positive because $15\hat{\alpha}^2+(15+3\sqrt{15})\hat{\alpha}+8+\sqrt{15}>0$ and the sign of the other terms is already established.

Next one can immediately see that $30(4-\sqrt{15})\hat{\alpha}^4-8(5-\sqrt{15})\hat{\alpha}^3+(12\sqrt{15}-39)\hat{\alpha}^2-3(\sqrt{15}-3)\hat{\alpha}+3(4-\sqrt{15})>0$ because $\hat{\alpha}$ is non positive with all other coefficients being positive. We also have $\hat{\alpha}+1>0$, $\sqrt{15}\hat{\alpha}+3>0$ which shows that the coefficient of r_1r_2 is negative.

Since $2\hat{\alpha}-1<0$, $\hat{\alpha}+1>0$, $5\hat{\alpha}+\sqrt{15}>0$, $10\hat{\alpha}-\sqrt{15}<0$, $10\hat{\alpha}-5-\sqrt{15}<0$ and $10\hat{\alpha}+5+\sqrt{15}>0$, the coefficient of r_1r_3 is negative.

Also the linear and quadratic terms are $\hat{\alpha}+1>0$, $\sqrt{15}\hat{\alpha}+3>0$, $15\hat{\alpha}+\sqrt{40-5\sqrt{15}}-\sqrt{15}-5<0$, $15\hat{\alpha}-\sqrt{40-5\sqrt{15}}-\sqrt{15}-5<0$ and $15\hat{\alpha}^2+(15+3\sqrt{15})\hat{\alpha}+\sqrt{15}+8>0$. Thus coefficient of r_1r_4 is negative.

Since the quadratic term is $(-450+120\sqrt{15})\hat{\alpha}^2+(60-20\sqrt{15})\hat{\alpha}-60+17\sqrt{15})>0$, the coefficient of r_2r_3 is negative.

Similarly, noting that $10\hat{\alpha}+5+\sqrt{15}>0$ and $15\hat{\alpha}-5-\sqrt{15}<0$, we show that the coefficient of r_2r_4 is negative. Finally, since $\hat{\alpha}+1>0$ and $5\hat{\alpha}+\sqrt{15}>0$, the coefficient of r_3r_4 is nonnegative.

Since all terms are negative or non positive and r_1, r_2, r_3, r_4 are positive, the determinant of $\mathbf{M}$ is negative and the quartic IFE shape function $\phi_0^{(4)}$ uniquely exists for $-\sqrt{\frac{3}{5}}<\hat{\alpha}\leq 0$.

Case 3: $0<\hat{\alpha}\leq\sqrt{\frac{3}{5}}$.
The first shape function is

$$\phi_0^{(4)}=\begin{cases}\phi_0^{(4),1} & =L_0+c_3L_3+c_4L_4, \qquad \text{on } (-1,\hat{\alpha}),\\ \phi_0^{(4),2} & =c_0L_0+c_1L_1+c_2L_2, \quad \text{on } (\hat{\alpha},1),\end{cases} \tag{2.2.35}$$

with matrix

$$\mathbf{M}=\begin{pmatrix} L_0(\hat{\alpha}) & L_1(\hat{\alpha}) & L_2(\hat{\alpha}) & -L_3(\hat{\alpha})) & -L_4(\hat{\alpha})\\ r_1L_0'(\hat{\alpha}) & r_1L_1'(\hat{\alpha}) & r_1L_2'(\hat{\alpha}) & -L_3'(\hat{\alpha}) & -L_4'(\hat{\alpha})\\ r_2L_0''(\hat{\alpha}) & r_2L_1''(\hat{\alpha}) & r_2L_2''(\hat{\alpha}) & -L_3''(\hat{\alpha}) & -L_4''(\hat{\alpha})\\ r_3L_0'''(\hat{\alpha}) & r_3L_1'''(\hat{\alpha}) & r_3L_2'''(\hat{\alpha}) & -L_3'''(\hat{\alpha}) & -L_4'''(\hat{\alpha})\\ r_4L_0''''(\hat{\alpha}) & r_4L_1''''(\hat{\alpha}) & r_4L_2''''(\hat{\alpha}) & -L_3''''(\hat{\alpha}) & -L_4''''(\hat{\alpha}) \end{pmatrix}. \tag{2.2.36}$$

The determinant of $\mathbf{M}$ is

$$\begin{aligned}
\det(\mathbf{M}) = &\left(\frac{25(4\sqrt{15}-15)(\hat{\alpha}-1)^3(5\hat{\alpha}-\sqrt{15})^3}{12}\right) r_1r_2 \\
&+\left(\frac{-5(4\sqrt{15}-15)(\hat{\alpha}-1)^2(10\hat{\alpha}-5-\sqrt{15})(15\hat{\alpha}+5+\sqrt{15})(5\hat{\alpha}-\sqrt{15})^2}{12}\right) r_1r_3 \\
&+\left(\frac{25(\hat{\alpha}-1)^2(5\hat{\alpha}-\sqrt{15})^2((-450+120\sqrt{15})\hat{\alpha}^2+(-60+20\sqrt{15})\hat{\alpha}-60+17\sqrt{15})}{12}\right) r_1r_4 \\
&+\left(\frac{25(4-\sqrt{15})(\hat{\alpha}-1)(\sqrt{15}\hat{\alpha}+3)(15\hat{\alpha}+\sqrt{40-5\sqrt{15}}+\sqrt{15}+5)(15\hat{\alpha}-\sqrt{40-5\sqrt{15}}+\sqrt{15}+5)(15\hat{\alpha}^2-(15+3\sqrt{15})\hat{\alpha}+\sqrt{15}+8)}{36}\right) r_2r_3 \\
&+\left(\frac{-5(4\sqrt{15}-15)(2\hat{\alpha}+1)(\hat{\alpha}-1)(5\hat{\alpha}-\sqrt{15})(10\hat{\alpha}+\sqrt{15})(10\hat{\alpha}-5-\sqrt{15})(10\hat{\alpha}+5+\sqrt{15})}{12}\right) r_2r_4 \\
&+\left(\frac{625(\hat{\alpha}-1)(\sqrt{15}\hat{\alpha}-3)(30(4-\sqrt{15})\hat{\alpha}^4+8(5-\sqrt{15})\hat{\alpha}^3+(12\sqrt{15}-39)\hat{\alpha}^2+3(\sqrt{15}-3)\hat{\alpha}+3(4-\sqrt{15}))}{12}\right) r_3r_4 \\
&+\left(\frac{-25(4\sqrt{15}-15)\hat{\alpha}(\hat{\alpha}+1)(5\hat{\alpha}+\sqrt{15})(10\hat{\alpha}-5-\sqrt{15})(5\hat{\alpha}^2-(5+\sqrt{15})\hat{\alpha}+4)}{6}\right) r_1r_2r_3 \\
&+\left(\frac{25(4\sqrt{15}-15)\hat{\alpha}(\hat{\alpha}+1)(5\hat{\alpha}+\sqrt{15})(15\hat{\alpha}+5+\sqrt{15})(15\hat{\alpha}^2-(15+3\sqrt{15})\hat{\alpha}+8+\sqrt{15})}{12}\right) r_1r_2r_4 \\
&+\left(\frac{-25(4\sqrt{15}-15)\hat{\alpha}(\hat{\alpha}+1)(5\hat{\alpha}+\sqrt{15})(10\hat{\alpha}-5-\sqrt{15})(15\hat{\alpha}^2+(10+2\sqrt{15})\hat{\alpha}+\sqrt{15})}{12}\right) r_1r_3r_4 \\
&+\left(\frac{125(4\sqrt{15}-15)\hat{\alpha}^2(\hat{\alpha}+1)^2(5\hat{\alpha}+\sqrt{15})^2}{12}\right) r_2r_3r_4. \qquad (2.2.37)
\end{aligned}$$

For $0 < \hat{\alpha} \leq \sqrt{\frac{3}{5}}$, since $\hat{\alpha} - 1 < 0$ and $5\hat{\alpha} - \sqrt{15} \leq 0$, the coefficient of r_1r_2 is non negative. Additionally, since we know $10\hat{\alpha} - 5 - \sqrt{15} < 0$ and $15\hat{\alpha} + 5 + \sqrt{15} > 0$, the coefficient of r_1r_3 is non negative.

Additionally, $\sqrt{5}\hat{\alpha} - \sqrt{15} \leq 0$ and noting that the quadratic term $(-450 + 120\sqrt{15})\hat{\alpha}^2 + (-60 + 20\sqrt{15})\hat{\alpha} - 60 + 17\sqrt{15} > 0$ (because all coefficients and $\hat{\alpha}$ are positive), we show that the coefficient of r_1r_4 is non negative.

Next $\hat{\alpha} - 1 < 0$, $\sqrt{15}\hat{\alpha} + 3 > 0$, $15\hat{\alpha} + \sqrt{40 - 5\sqrt{15}} + \sqrt{15} + 5 > 0$, $15\hat{\alpha} - \sqrt{40 - 5\sqrt{15}} + \sqrt{15} + 5 > 0$ and $15\hat{\alpha}^2 - (15 + 3\sqrt{15})\hat{\alpha} + \sqrt{15} + 8 < 0$ yield that the coefficient of r_2r_3 is positive.

Since we have $2\hat{\alpha} + 1 > 0$, $\hat{\alpha} - 1 < 0$, $5\hat{\alpha} - \sqrt{15} \leq 0$, $10\hat{\alpha} + \sqrt{15} > 0$, $10\hat{\alpha} - 5 - \sqrt{15} < 0$ and $10\hat{\alpha} + 5 + \sqrt{15} > 0$, we obtain that the coefficient of r_2r_4 is non negative.

One can check that all the coefficients of $30(4 - \sqrt{15})\hat{\alpha}^4 + 8(5 - \sqrt{15})\hat{\alpha}^3 + (12\sqrt{15} - 39)\hat{\alpha}^2 + 3(\sqrt{15} - 3)\hat{\alpha} + 3(4 - \sqrt{15})$ are positive and $\hat{\alpha}$ is positive, thus, this term is positive. We further know that $\hat{\alpha} - 1 < 0$ and $\sqrt{15}\alpha - 3 \leq 0$ to show that the coefficient of r_3r_4 is non negative.

Since $\hat{\alpha} > 0$, $\hat{\alpha} + 1 > 0$, $5\hat{\alpha} + \sqrt{15} > 0$, $10\hat{\alpha} - 5 - \sqrt{15} < 0$ and $5\hat{\alpha}^2 - (5 + \sqrt{15})\hat{\alpha} + 4 > 0$, we see that the coefficient of $r_1r_2r_3$ is positive.

Next, $5\hat{\alpha} + \sqrt{15} > 0$, $15\hat{\alpha} + 5 + \sqrt{15} > 0$ and $15\hat{\alpha}^2 - (15 + 3\sqrt{15})\hat{\alpha} + 8 + \sqrt{15} > 0$ show that the coefficient of $r_1r_2r_4$ is positive.

Since all the coefficients of $15\hat{\alpha}^2 + (10 + 2\sqrt{15})\hat{\alpha} + \sqrt{15}$ are positive and $\hat{\alpha}$ are positive, $15\hat{\alpha}^2 + (10 + 2\sqrt{15})\hat{\alpha} + \sqrt{15} > 0$ for $0 < \hat{\alpha} \leq \sqrt{\frac{3}{5}}$. Also we already know $\hat{\alpha} > 0$, $\hat{\alpha} + 1 > 0$,

$5\hat{\alpha}+\sqrt{15}>0$ and $10\hat{\alpha}-5-\sqrt{15}<0$ which yield that the coefficient of $r_1r_3r_4$ is positive. Finally, one can know easily that the coefficient of $r_2r_2r_4$ is positive.

Since all terms are positive or non negative and r_1, r_2, r_3, r_4 are also positive, the determinant of $\mathbf{M}$ are positive and the quartic IFE shape function $\phi_0^{(4)}$ uniquely exists for $0<\hat{\alpha}\leq\sqrt{\frac{3}{5}}$.

Case 4: $\sqrt{\frac{3}{5}}<\hat{\alpha}<1$.
The first shape function is

$$\phi_0^{(4)}=\begin{cases}\phi_0^{(4),1} & =L_0+c_4L_4, & \text{on } (-1,\hat{\alpha}),\\ \phi_0^{(4),2} & =c_0L_0+c_1L_1+c_2L_2+c_3L_3, & \text{on } (\hat{\alpha},1),\end{cases} \tag{2.2.38}$$

with matrix

$$\mathbf{M}=\begin{pmatrix} L_0(\hat{\alpha}) & L_1(\hat{\alpha}) & L_2(\hat{\alpha}) & L_3(\hat{\alpha})) & -L_4(\hat{\alpha})\\ r_1L_0'(\hat{\alpha}) & r_1L_1'(\hat{\alpha}) & r_1L_2'(\hat{\alpha}) & r_1L_3'(\hat{\alpha}) & -L_4'(\hat{\alpha})\\ r_2L_0''(\hat{\alpha}) & r_2L_1''(\hat{\alpha}) & r_2L_2''(\hat{\alpha}) & r_2L_3''(\hat{\alpha}) & -L_4''(\hat{\alpha})\\ r_3L_0'''(\hat{\alpha}) & r_3L_1'''(\hat{\alpha}) & r_3L_2'''(\hat{\alpha}) & r_3L_3'''(\hat{\alpha}) & -L_4'''(\hat{\alpha})\\ r_4L_0''''(\hat{\alpha}) & r_4L_1''''(\hat{\alpha}) & r_4L_2''''(\hat{\alpha}) & r_4L_3''''(\hat{\alpha}) & -L_4''''(\hat{\alpha}) \end{pmatrix}. \tag{2.2.39}$$

The determinant of $\mathbf{M}$ is

$$\begin{aligned}\det(\mathbf{M})&=\left(\frac{-625\sqrt{15}(\hat{\alpha}-1)^4}{2}\right)r_1r_2r_3+\left(\frac{625\sqrt{15}(4\hat{\alpha}+1)(\hat{\alpha}-1)^3}{2}\right)r_1r_2r_4\\&+\left(\frac{-375\sqrt{15}(\hat{\alpha}-1)^2(10\hat{\alpha}^2+5\hat{\alpha}-1)}{2}\right)r_1r_3r_4+\left(\frac{125\sqrt{15}(\hat{\alpha}-1)(20\hat{\alpha}^3+15\hat{\alpha}^2-6\hat{\alpha}-3)}{2}\right)r_2r_3r_4\\&+\left(\frac{-125\sqrt{15}\hat{\alpha}(\hat{\alpha}+1)(5\hat{\alpha}^2-3)}{2}\right)r_1r_2r_3r_4.\end{aligned} \tag{2.2.40}$$

Since all coefficients are negative and r_1, r_2, r_3, r_4 are positive, the determinant of $\mathbf{M}$ is negative and the quadratic IFE shape function $\phi_0^{(4)}$ uniquely exists for $\sqrt{\frac{3}{5}}<\hat{\alpha}<1$.

Combining cases 1, 2, 3 and 4, we conclude that the quartic IFE shape function $\phi_0^{(4)}$ uniquely exists for $-1<\hat{\alpha}<1$. For other quartic IFE shape functions $\phi_1^{(4)}$, $\phi_2^{(4)}$, $\phi_3^{(4)}$ and $\phi_4^{(4)}$, the matrix $\mathbf{M}$ is the same. Thus we conclude that $\phi_1^{(4)}$, $\phi_2^{(4)}$, $\phi_3^{(4)}$ and $\phi_4^{(4)}$ exist uniquely. □

The following properties can be verified by a direct computation:

- The IFE shape functions form a partition of unity.
- The IFE shape functions reduce to the standard shape functions when $\rho_1=\rho_2$ and $c_1=c_2$.

- The IFE shape functions converge to the standard shape functions when the interface leaves the element.

We present instances of q^{th}-degree immersed shape functions on the reference interface element $(-1, 1)$ constructed using jump conditions (2.2.3), for $\hat{\alpha} = 0.4$, $c_1 = 1$, $\rho_1 = 2$, $c_2 = 2$, $\rho_2 = 4$ and $q = 1, 2, 3, 4$, for the pressure and velocity, respectively, in Figures 2.2.1 and 2.2.2.

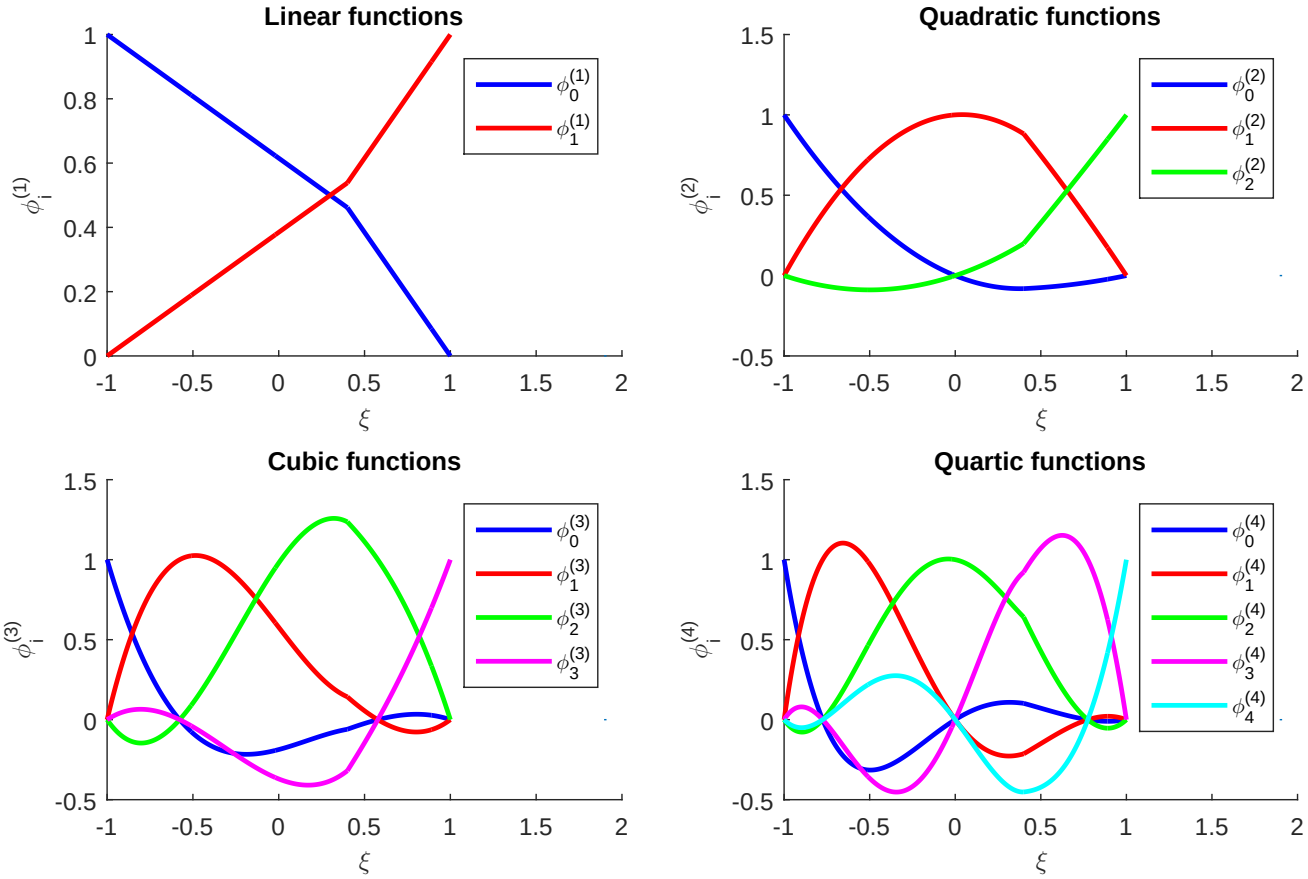

Figure 2.2.1: Immersed shape functions for the pressure with $c_1 = 1$, $\rho_1 = 2$, $c_2 = 2$, $\rho_2 = 4$ and $\hat{\alpha} = 0.4$.

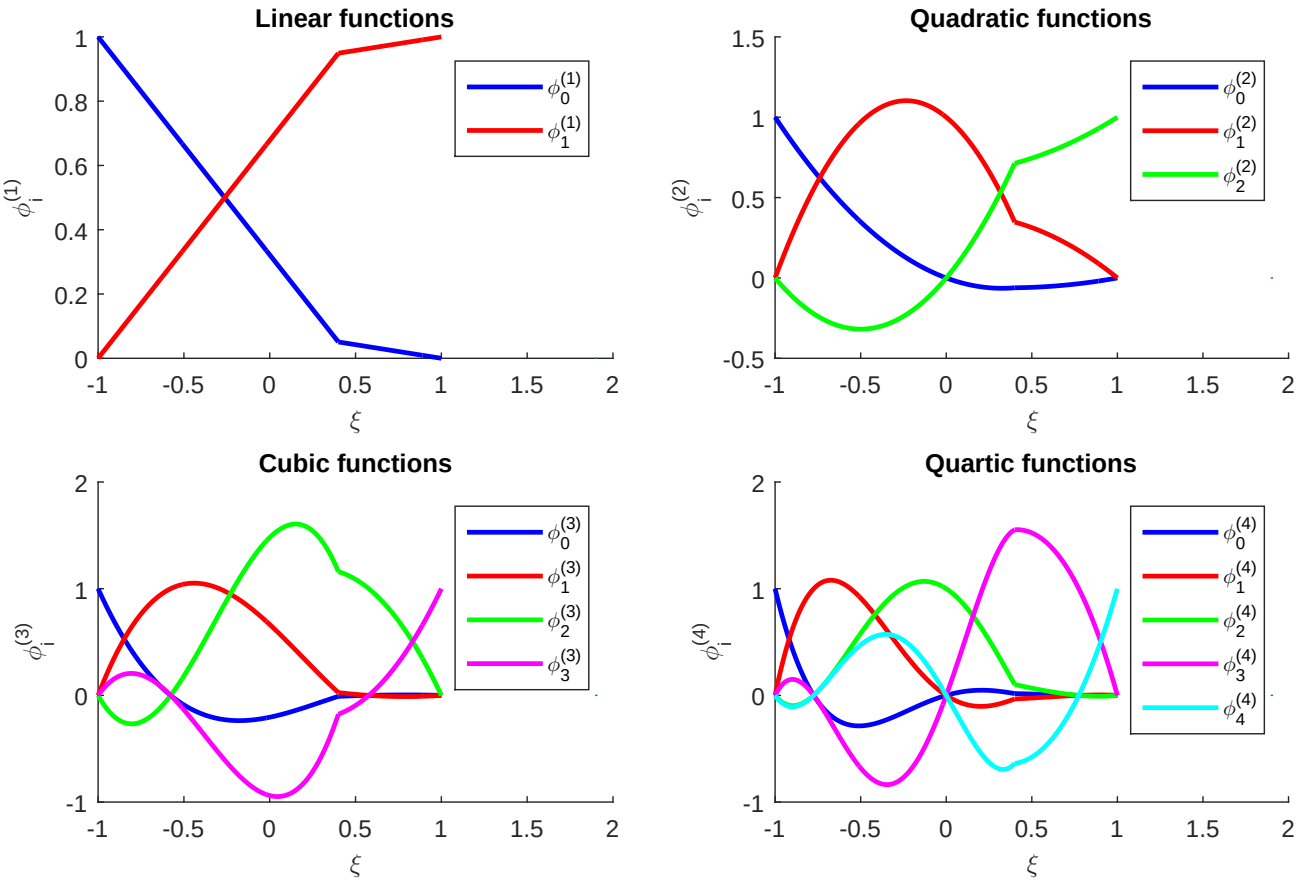

Figure 2.2.2: Immersed shape functions for the velocity with $c_1 = 1$, $\rho_1 = 2$, $c_2 = 2$, $\rho_2 = 4$ and $\hat{\alpha} = 0.4$.

In Figures 2.2.3 and 2.2.4 we show the IFE shape functions for water/air interface problem. The parameters and the interface are $c_1 = 1450$, $\rho_1 = 1000$, $c_2 = 340$, $\rho_2 = 1.3$ and $\hat{\alpha} = 0.4$.

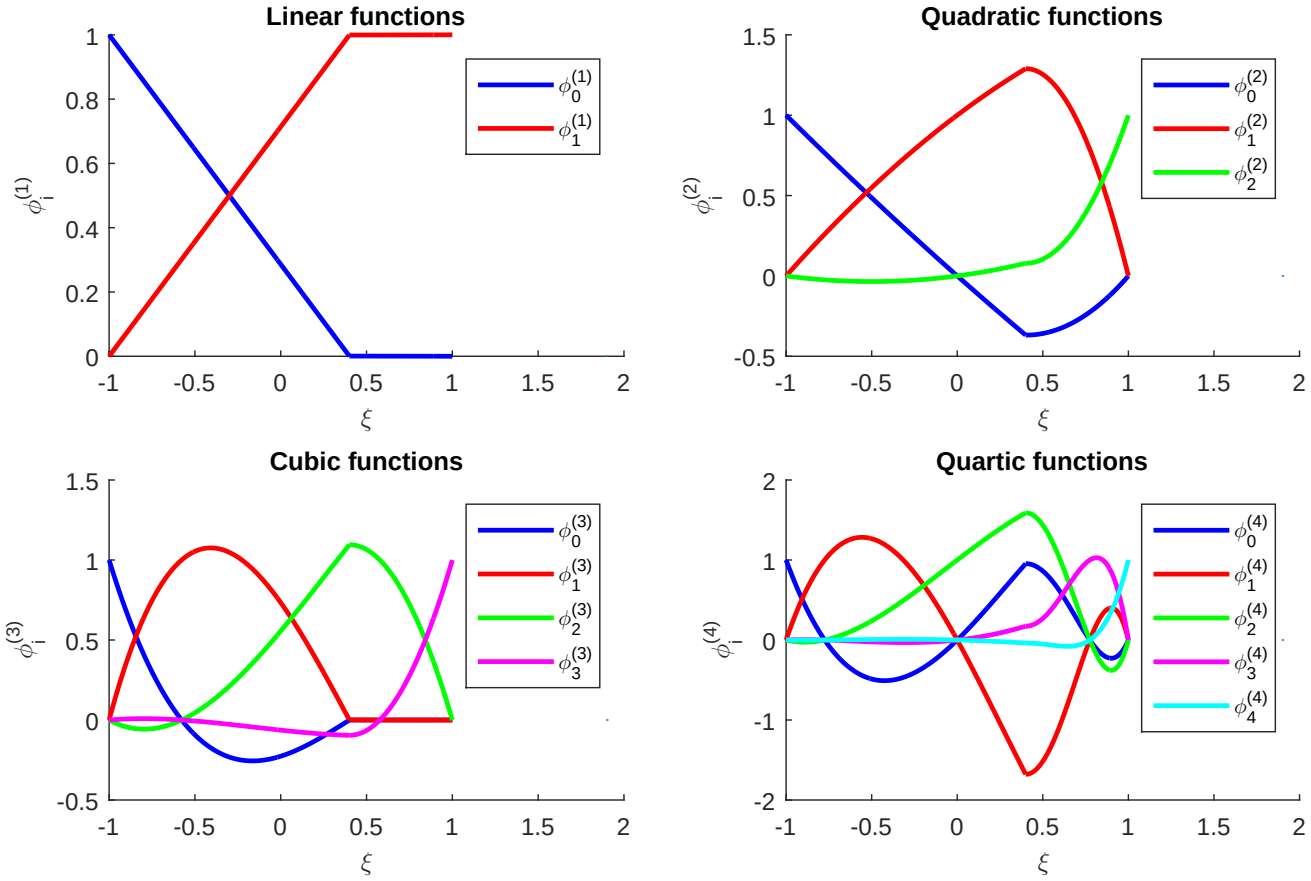

Figure 2.2.3: Immersed shape functions for the pressure for water/air problem with $\hat{\alpha} = 0.4$.

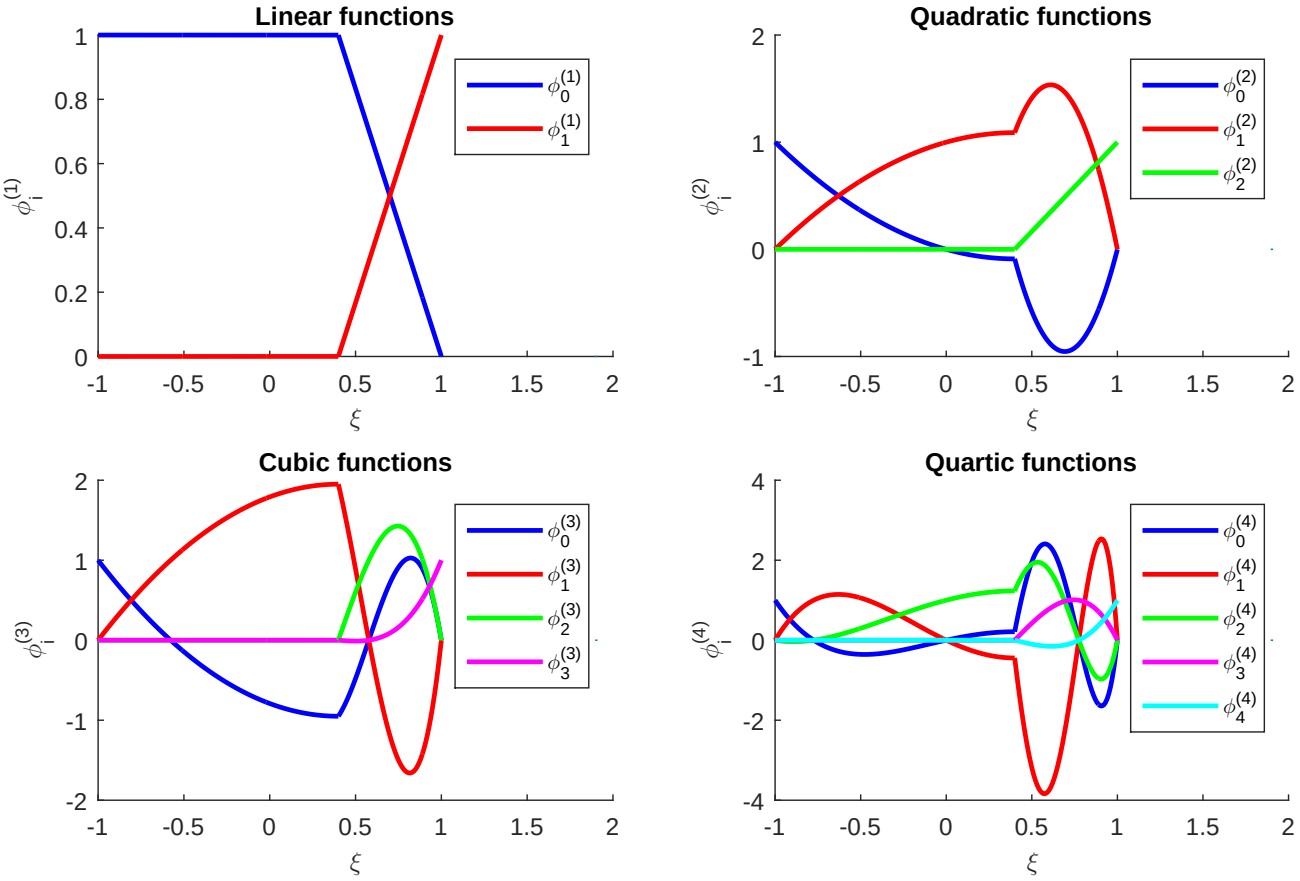

Figure 2.2.4: Immersed shape functions for the velocity for water/air problem with $\hat{\alpha} = 0.4$.

Each IFE shape function has a singularity at the interface $\hat{\alpha}$. If the interface $\hat{\alpha}$ moves, the IFE shape function changes its shape. This function satisfies Lagrange condition and jump conditions (2.2.1) at the interface $\hat{\alpha}$.

We note that the IFE shape functions are only C^0 at the interface $x = \hat{\alpha}$.

2.3 Immersed Finite Element Methods

We consider three discontinuous finite element methods. The first method is the standard DG formulation applied to the problem (2.1.1). The second method is based on the DG formulation applied to a scaled version of problem (2.1.1). The third method is based on a Petrov-Galerkin (PG) formulation.

We partition the interval I into N subintervals $a = x_0 < x_1 < x_2 < \cdots < x_N = b$ and use standard Lagrange shape functions on non interface elements and IFE shape functions on

the interface element.

2.3.1 Standard Discontinuous Galerkin Formulation

We use the standard DG weak formulation on a non interface element (x_l, x_{l+1}) by multiplying (2.1.1a) by a test function $\mathbf{V}$, integrating over the element and integrating by parts, we get

$$\int_{x_l}^{x_{l+1}} \mathbf{V}^T \frac{\partial \mathbf{U}}{\partial t} dx + \mathbf{V}^T \mathbf{A}\mathbf{U} \mid_{x_l}^{x_{l+1}} - \int_{x_l}^{x_{l+1}} \frac{\partial \mathbf{V}^T}{\partial x} \mathbf{A}\mathbf{U} dx = 0. \tag{2.3.1}$$

Applying the numerical flux, we obtain

$$\begin{aligned} &\int_{x_l}^{x_{l+1}} \mathbf{V}^T \frac{\partial \mathbf{U}}{\partial t} dx + \mathbf{V}^{-T} \mathbf{F}(\mathbf{U}^+, \mathbf{U}^-)|_{x=x_{l+1}} - \mathbf{V}^{+T} \mathbf{F}(\mathbf{U}^+, \mathbf{U}^-)|_{x=x_l} \\ &- \int_{x_l}^{x_{l+1}} \frac{\partial \mathbf{V}^T}{\partial x} \mathbf{A}\mathbf{U} dx = 0, \end{aligned} \tag{2.3.2}$$

where

$$\mathbf{F}(\mathbf{U}^+, \mathbf{U}^-) = \mathbf{A}^+ \mathbf{U}^- + \mathbf{A}^- \mathbf{U}^+, \tag{2.3.3}$$

and $\mathbf{A}$ is the matrix in (2.1.1b).

Then we define the DG formulation to find $\mathbf{U}_h \in \mathcal{P}_q$, the space of polynomials of degree not exceeding q, such that

$$\begin{aligned} &\int_{x_l}^{x_{l+1}} \mathbf{V}_h^T \frac{\partial \mathbf{U}_h}{\partial t} dx + \mathbf{V}_h^{-T} \mathbf{A}^+ \mathbf{U}_h^- \mid_{x=x_{l+1}} + \mathbf{V}_h^{-T} \mathbf{A}^- \mathbf{U}_h^+ \mid_{x=x_{l+1}} \\ &- \mathbf{V}_h^{+T} \mathbf{A}^+ \mathbf{U}_h^- \mid_{x=x_l} - \mathbf{V}_h^{+T} \mathbf{A}^- \mathbf{U}_h^+ \mid_{x=x_l} - \int_{x_l}^{x_{l+1}} \frac{\partial \mathbf{V}_h^T}{\partial x} \mathbf{A}\mathbf{U}_h dx = 0, \ \forall \ \mathbf{V}_h \in \mathcal{P}_q. \end{aligned} \tag{2.3.4}$$

On an interface element (x_l, x_{l+1}) containing an interface point $x = \alpha$, let $\mathcal{V}_{h,IFE}$ be the space spanned by the IFE shape functions $\psi_i^{(q)}, \ i = 0, 1, \cdots, q$ obtained from $\phi_i^{(q)}$ through the affine mapping $x(\xi) = x_l \frac{1-\xi}{2} + x_{l+1} \frac{1+\xi}{2}$ from $(-1, 1) \to (x_l, x_{l+1})$.

We multiply (2.1.1a) by a test function $\mathbf{V}_h \in \mathcal{V}_{h,IFE}$, integrate over the element. We integrate by parts on (x_l, α) and (α, x_{l+1}). The discrete DG formulation is obtained by approximating $\mathbf{U}$ on (x_l, x_{l+1}) by $\mathbf{U}_h \in \mathcal{V}_{h,IFE}$ and the boundary terms at x_l and x_{l+1} are approximated using numerical fluxes. We note that the resulting immersed discontinuous Galerkin finite element (IDGFE) formulation contains a penalty term at the interface $x = \alpha$ as shown below.

Multiplying (2.1.1a) by $\mathbf{V}$ and integrating over (x_l, α), we get

$$\int_{x_l}^{\alpha} \mathbf{V}_1^T \frac{\partial \mathbf{U}_1}{\partial x} dx + \mathbf{V}_1^T \mathbf{A}_1 \mathbf{U}_1 \mid_{x=\alpha} - \mathbf{V}_1^T \mathbf{A}_1 \mathbf{U}_1 \mid_{x=x_l} - \int_{x_l}^{\alpha} \frac{\partial \mathbf{V}_1}{\partial x}^T \mathbf{A}_1 \mathbf{U}_1 dx = 0. \tag{2.3.5}$$

Similarly, integrating over (α, x_{l+1}) and integrating by parts, we get

$$\int_{\alpha}^{x_{l+1}} \mathbf{V}_2^T \frac{\partial \mathbf{U}_2}{\partial t} dx + \mathbf{V}_2^T \mathbf{A}_2 \mathbf{U}_2 \mid_{x=x_{l+1}} - \mathbf{V}_2^T \mathbf{A}_2 \mathbf{U}_2 \mid_{x=\alpha} - \int_{\alpha}^{x_{l+1}} \frac{\partial \mathbf{V}_2}{\partial x}^T \mathbf{A}_2 \mathbf{U}_2 dx = 0. \tag{2.3.6}$$

Combining the previous two equations and applying the flux splitting (2.3.3) at $x = x_l$ and $x = x_{l+1}$ yield the DG formulation on the interface element (x_l, x_{l+1}) which consists of determining $\mathbf{U}_h \in \mathcal{V}_{h,IFE}$ such that

$$\begin{aligned}
&\int_{x_l}^{\alpha} \mathbf{V}_{1,h}^T \frac{\partial \mathbf{U}_{1,h}}{\partial t} dx + \int_{\alpha}^{x_{l+1}} \mathbf{V}_{2,h}^T \frac{\partial \mathbf{U}_{2,h}}{\partial t} dx + \mathbf{V}_{2,h}^{-}{}^T \mathbf{A}_2^+ \mathbf{U}_{2,h}^- \mid_{x=x_{l+1}} + \mathbf{V}_{2,h}^{-}{}^T \mathbf{A}_2^- \mathbf{U}_{2,h}^+ \mid_{x=x_{l+1}} \\
&- \mathbf{V}_{1,h}^{+}{}^T \mathbf{A}_1^+ \mathbf{U}_{1,h}^- \mid_{x=x_l} - \mathbf{V}_{1,h}^{+}{}^T \mathbf{A}_1^- \mathbf{U}_{1,h}^+ \mid_{x=x_l} + \mathbf{V}_{1,h}^T \mathbf{A}_1 \mathbf{U}_{1,h} \mid_{x=\alpha} - \mathbf{V}_{2,h}^T \mathbf{A}_2 \mathbf{U}_{2,h} \mid_{x=\alpha} \\
&- \int_{x_l}^{\alpha} \frac{\partial \mathbf{V}_{1,h}^T}{\partial x} \mathbf{A}_1 \mathbf{U}_{1,h} dx - \int_{\alpha}^{x_{l+1}} \frac{\partial \mathbf{V}_{2,h}^T}{\partial x} \mathbf{A}_2 \mathbf{U}_{2,h} dx = 0, \qquad \forall\ \mathbf{V}_h \in \mathcal{V}_{h,IFE},
\end{aligned} \tag{2.3.7}$$

where $\mathbf{V}_{i,h} = \mathbf{V}_h \mid_{I_i \cap (x_l, x_{l+1})}$ and $\mathbf{U}_{i,h} = \mathbf{U}_h \mid_{I_i \cap (x_l, x_{l+1})}$ for $i = 1, 2$.

Combining the previous equation on the interface element and the DG formulation on non interface elements we obtain IDGFE method for solving the acoustic problem on non fitted meshes and the system of ordinary differential equation

$$\frac{d\mathbf{C}}{dt} = \mathbf{A}_{h,q}^G \mathbf{C}, \tag{2.3.8}$$

where $\mathbf{C}$ is a global solution vector and $\mathbf{A}_{h,q}^G$ is a global matrix.

2.3.2 Galerkin Formulation for Scaled Problem

Since standard immersed discontinuous Galerkin formulation is not stable for two dimensional acoustic problems with high contrast media, we derive a stable formulation obtained by first multiplying (2.1.1a) by

$$\mathbf{S}_i = \mathbf{S}|_{I_i} = \begin{pmatrix} \frac{1}{\rho_i c_i^2} & 0 \\ 0 & \rho_i \end{pmatrix}, \text{ for } i = 1, 2 \tag{2.3.9a}$$

to obtain the scaled problem

$$\mathbf{S} \frac{\partial \mathbf{U}}{\partial t} + \tilde{\mathbf{A}} \frac{\partial \mathbf{U}}{\partial x} = 0, \tag{2.3.9b}$$

where

$$\tilde{\mathbf{A}} = \mathbf{S}\mathbf{A} = \begin{pmatrix} 0 & 1 \\ 1 & 0 \end{pmatrix}. \tag{2.3.9c}$$

Multiplying (2.3.9b) by a test function $\mathbf{V}$ and integrating over the element (x_l, x_{l+1}), we get

$$\int_{x_l}^{x_{l+1}} \mathbf{V}^T \mathbf{S} \frac{\partial \mathbf{U}}{\partial t} dx + \int_{x_l}^{x_{l+1}} \mathbf{V}^T \tilde{\mathbf{A}} \frac{\partial \mathbf{U}}{\partial x} dx = 0. \tag{2.3.10}$$

Integrating (2.3.10) by parts, we obtain

$$\int_{x_l}^{x_{l+1}} \mathbf{V}^T \mathbf{S} \frac{\partial \mathbf{U}}{\partial t} dx + \mathbf{V}^T \tilde{\mathbf{A}} \mathbf{U} \mid_{x_l}^{x_{l+1}} - \int_{x_l}^{x_{l+1}} \frac{\partial \mathbf{V}^T}{\partial x} \tilde{\mathbf{A}} \mathbf{U} dx = 0. \tag{2.3.11}$$

Using the numerical flux, we obtain

$$\begin{aligned} &\int_{x_l}^{x_{l+1}} \mathbf{V}^T \mathbf{S} \frac{\partial \mathbf{U}}{\partial t} dx + \mathbf{V}^{-T} \mathbf{F}(\mathbf{U}^+, \mathbf{U}^-) \mid_{x=x_{l+1}} - \mathbf{V}^{+T} \mathbf{F}(\mathbf{U}^+, \mathbf{U}^-) \mid_{x=x_l} \\ &- \int_{x_l}^{x_{l+1}} \frac{\partial \mathbf{V}^T}{\partial x} \tilde{\mathbf{A}} \mathbf{U} dx = 0, \end{aligned} \tag{2.3.12}$$

where

$$\mathbf{F}(\mathbf{U}^+, \mathbf{U}^-) = \tilde{\mathbf{A}}^+ \mathbf{U}^- + \tilde{\mathbf{A}}^- \mathbf{U}^+ = (\mathbf{SA})^+ \mathbf{U}^- + (\mathbf{SA})^- \mathbf{U}^+. \tag{2.3.13}$$

The DG formulation becomes

$$\begin{aligned} &\int_{x_l}^{x_{l+1}} \mathbf{V}_h^T \mathbf{S} \frac{\partial \mathbf{U}_h}{\partial t} dx + \mathbf{V}_h^{-T} \tilde{\mathbf{A}}^+ \mathbf{U}_h^- \mid_{x=x_{l+1}} + \mathbf{V}_h^{-T} \tilde{\mathbf{A}}^- \mathbf{U}_h^+ \mid_{x=x_{l+1}} \\ &- \mathbf{V}_h^{+T} \tilde{\mathbf{A}}^+ \mathbf{U}_h^- \mid_{x=x_l} - \mathbf{V}_h^{+T} \tilde{\mathbf{A}}^- \mathbf{U}_h^+ \mid_{x=x_l} - \int_{x_l}^{x_{l+1}} \frac{\partial \mathbf{V}_h^T}{\partial x} \tilde{\mathbf{A}} \mathbf{U}_h dx = 0, \ \forall \ \mathbf{V}_h \in \mathcal{P}_q, \end{aligned} \tag{2.3.14}$$

where $\mathbf{U}_h \in \mathcal{P}_q$ on a non interface element.

On the interface element (x_l, x_{l+1}) containing an interface point $x = \alpha$, multiplying (2.3.9b) by $\mathbf{V}$, integrating over (x_l, α) and integrating by parts, we write

$$\int_{x_l}^{\alpha} \mathbf{V}_1^T \mathbf{S}_1 \frac{\partial \mathbf{U}_1}{\partial x} dx + \mathbf{V}_1^T \tilde{\mathbf{A}} \mathbf{U}_1 \mid_{x=\alpha} - \mathbf{V}_1^T \tilde{\mathbf{A}} \mathbf{U}_1 \mid_{x=x_l} - \int_{x_l}^{\alpha} \frac{\partial \mathbf{V}_1}{\partial x}^T \tilde{\mathbf{A}} \mathbf{U}_1 dx = 0 \tag{2.3.15}$$

Similarly, on (α, x_{l+1}), we write

$$\int_{\alpha}^{x_{l+1}} \mathbf{V}_2^T \mathbf{S}_2 \frac{\partial \mathbf{U}_2}{\partial t} dx + \mathbf{V}_2^T \tilde{\mathbf{A}} \mathbf{U}_2 \mid_{x=x_{l+1}} - \mathbf{V}_2^T \tilde{\mathbf{A}} \mathbf{U}_2 \mid_{x=\alpha} - \int_{\alpha}^{x_{l+1}} \frac{\partial \mathbf{V}_2}{\partial x}^T \tilde{\mathbf{A}} \mathbf{U}_2 dx = 0. \tag{2.3.16}$$

Combining the previous two equations and applying the flux splitting (2.3.13) at $x = x_l$ and $x = x_{l+1}$, the DG formulation on the interface element (x_l, x_{l+1}) consists of finding

$\mathbf{U}_h \in \mathcal{V}_{h,IFE}$ such that

$$\int_{x_l}^{\alpha} \mathbf{V}_{1,h}^T \mathbf{S}_1 \frac{\partial \mathbf{U}_{1,h}}{\partial t} dx + \int_{\alpha}^{x_{l+1}} \mathbf{V}_{2,h}^T \mathbf{S}_2 \frac{\partial \mathbf{U}_{2,h}}{\partial t} dx$$
$$+ {\mathbf{V}_{2,h}^-}^T \tilde{\mathbf{A}}^+ \mathbf{U}_{2,h}^- \mid_{x=x_{l+1}} + {\mathbf{V}_{2,h}^-}^T \tilde{\mathbf{A}}^- \mathbf{U}_{2,h}^+ \mid_{x=x_{l+1}} - {\mathbf{V}_{1,h}^+}^T \tilde{\mathbf{A}}^+ \mathbf{U}_{1,h}^- \mid_{x=x_l} - {\mathbf{V}_{1,h}^+}^T \tilde{\mathbf{A}}^- \mathbf{U}_{1,h}^+ \mid_{x=x_l}$$
$$- \int_{x_l}^{\alpha} \frac{\partial \mathbf{V}_{1,h}^T}{\partial x} \tilde{\mathbf{A}} \mathbf{U}_{1,h} dx - \int_{\alpha}^{x_{l+1}} \frac{\partial \mathbf{V}_{2,h}^T}{\partial x} \tilde{\mathbf{A}} \mathbf{U}_{2,h} dx = 0, \qquad \forall\ \mathbf{V}_h \in \mathcal{V}_{h,IFE}, \tag{2.3.17}$$

where $\mathbf{V}_{i,h} = \mathbf{V}_h \mid_{I_i \cap (x_l, x_{l+1})}$ and $\mathbf{U}_{i,h} = \mathbf{U}_h \mid_{I_i \cap (x_l, x_{l+1})}$ for $i = 1, 2$. Due to the interface jump conditions, the previous equation has no penalty terms at $x = \alpha$.

Combining the previous equation on the interface element and the DG formulation on non interface elements for the scaled problem, we get the immersed discontinuous Galerkin (IDG) method for solving the scaled acoustic problem on non fitted meshes and the system of ordinary differential equation

$$\frac{d\mathbf{C}}{dt} = \mathbf{A}_{h,q}^{GS} \mathbf{C}, \tag{2.3.18}$$

where $\mathbf{C}$ is a global solution vector and $\mathbf{A}_{h,q}^{GS}$ is a global matrix.

As the numerical results show Figures 2.5.4 and 2.5.9, the stability region of this method is much smaller than that for the IDGFE method for homogeneous acoustic problem which leads us to investigate the following Petrov-Galerkin method.

2.3.3 Discontinuous Petrov-Galerkin Formulation

Since the IDG formulation for the scaled acoustic problem has a small stability region compared to the standard IDGFE formulation for homogeneous problems, we introduce a more efficient Petrov-Galerkin formulation.

In order to get the formulation on a non interface element (x_l, x_{l+1}) we multiply (2.1.1a) by a test function $\mathbf{SV}$, integrate over the element and integrate by parts to obtain

$$\int_{x_l}^{x_{l+1}} \mathbf{V}^T \mathbf{S} \frac{\partial \mathbf{U}}{\partial t} dx + \mathbf{V}^T \mathbf{S} \mathbf{A} \mathbf{U} \mid_{x_l}^{x_{l+1}} - \int_{x_l}^{x_{l+1}} \frac{\partial \mathbf{V}^T}{\partial x} \tilde{\mathbf{A}} \mathbf{U} dx = 0, \tag{2.3.19}$$

where $\tilde{\mathbf{A}}$ is defined in (2.3.9c).

Applying the numerical flux, we obtain

$$\int_{x_l}^{x_{l+1}} \mathbf{V}^T \mathbf{S} \frac{\partial \mathbf{U}}{\partial t} dx + {\mathbf{V}^-}^T \mathbf{S} \mathbf{F}(\mathbf{U}^+, \mathbf{U}^-) \mid_{x=x_{l+1}} - {\mathbf{V}^+}^T \mathbf{S} \mathbf{F}(\mathbf{U}^+, \mathbf{U}^-) \mid_{x=x_l}$$
$$- \int_{x_l}^{x_{l+1}} \frac{\partial \mathbf{V}^T}{\partial x} \tilde{\mathbf{A}} \mathbf{U} dx = 0, \tag{2.3.20}$$

where

$$\mathbf{F}(\mathbf{U}^+,\mathbf{U}^-)=\mathbf{A}^+\mathbf{U}^-+\mathbf{A}^-\mathbf{U}^+. \tag{2.3.21}$$

The DPG formulation on a non interface element (x_l,x_{l+1}) consists of finding $\mathbf{U}_h\in\mathcal{P}_q$ such that

$$\begin{aligned}&\int_{x_l}^{x_{l+1}}\mathbf{V}_h^T\mathbf{S}\frac{\partial\mathbf{U}_h}{\partial t}dx+\mathbf{V}_h^{-T}\mathbf{S}\mathbf{A}^+\mathbf{U}_h^-\mid_{x=x_{l+1}}+\mathbf{V}_h^{-T}\mathbf{S}\mathbf{A}^-\mathbf{U}_h^+\mid_{x=x_{l+1}}\\&-\mathbf{V}_h^{+T}\mathbf{S}\mathbf{A}^+\mathbf{U}_h^-\mid_{x=x_l}-\mathbf{V}_h^{+T}\mathbf{S}\mathbf{A}^-\mathbf{U}_h^+\mid_{x=x_l}-\int_{x_l}^{x_{l+1}}\frac{\partial\mathbf{V}_h^T}{\partial x}\tilde{\mathbf{A}}\mathbf{U}_h dx=0,\\&\forall\ \mathbf{V}_h\in\mathcal{P}_q.\end{aligned} \tag{2.3.22}$$

On an interface element (x_l,x_{l+1}) containing an interface point $x=\alpha$, we multiply (2.1.1a) by a test function $\mathbf{SV}$, integrate over (x_l,α) to obtain

$$\int_{x_l}^{\alpha}\mathbf{V}_1^T\mathbf{S}_1\frac{\partial\mathbf{U}_1}{\partial x}dx+\mathbf{V}_1^T\mathbf{S}_1\mathbf{A}_1\mathbf{U}_1\mid_{x=\alpha}-\mathbf{V}_1^T\mathbf{S}_1\mathbf{A}_1\mathbf{U}_1\mid_{x=x_l}-\int_{x_l}^{\alpha}\frac{\partial\mathbf{V}_1}{\partial x}^T\tilde{\mathbf{A}}\mathbf{U}_1dx=0. \tag{2.3.23}$$

Similarly, integrating over (α,x_{l+1}) and integrating by parts, we get

$$\int_{\alpha}^{x_{l+1}}\mathbf{V}_2^T\mathbf{S}_2\frac{\partial\mathbf{U}_2}{\partial t}dx+\mathbf{V}_2^T\mathbf{S}_2\mathbf{A}_2\mathbf{U}_2\mid_{x=x_{l+1}}-\mathbf{V}_2^T\mathbf{S}_2\mathbf{A}_2\mathbf{U}_2\mid_{x=\alpha}-\int_{\alpha}^{x_{l+1}}\frac{\partial\mathbf{V}_2}{\partial x}^T\tilde{\mathbf{A}}\mathbf{U}_2dx=0. \tag{2.3.24}$$

Combining the previous two equations and applying the flux splitting (2.3.21) at $x=x_l$ and $x=x_{l+1}$, the DPG formulation consists of finding $\mathbf{U}_h\in\mathcal{V}_{h,IFE}$ such that

$$\begin{aligned}&\int_{x_l}^{\alpha}\mathbf{V}_{1,h}^T\mathbf{S}_1\frac{\partial\mathbf{U}_{1,h}}{\partial t}dx+\int_{\alpha}^{x_{l+1}}\mathbf{V}_{2,h}^T\mathbf{S}_2\frac{\partial\mathbf{U}_{2,h}}{\partial t}dx+\mathbf{V}_{2,h}^-{}^T\mathbf{S}_2\mathbf{A}_2^+\mathbf{U}_{2,h}^-\mid_{x=x_{l+1}}\\&+\mathbf{V}_{2,h}^-{}^T\mathbf{S}_2\mathbf{A}_2^-\mathbf{U}_{2,h}^+\mid_{x=x_{l+1}}-\mathbf{V}_{1,h}^+{}^T\mathbf{S}_1\mathbf{A}_1^+\mathbf{U}_{1,h}^-\mid_{x=x_l}-\mathbf{V}_{1,h}^+{}^T\mathbf{S}_1\mathbf{A}_1^-\mathbf{U}_{1,h}^+\mid_{x=x_l}\\&-\int_{x_l}^{\alpha}\frac{\partial\mathbf{V}_{1,h}^T}{\partial x}\tilde{\mathbf{A}}\mathbf{U}_{1,h}dx-\int_{\alpha}^{x_{l+1}}\frac{\partial\mathbf{V}_{2,h}^T}{\partial x}\tilde{\mathbf{A}}\mathbf{U}_{2,h}dx=0,\qquad\forall\ \mathbf{V}_h\in\mathcal{V}_{h,IFE},\end{aligned} \tag{2.3.25}$$

where $\mathbf{V}_{i,h}=\mathbf{V}_h\mid_{I_i\cap(x_l,x_{l+1})}$ and $\mathbf{U}_{i,h}=\mathbf{U}_h\mid_{I_i\cap(x_l,x_{l+1})}$ for $i=1,2$.

Combining the previous equation on interface element and DPG formulation on non interface elements, we obtain the immersed discontinuous Petrov-Galerkin finite element (IDPGFE) method for solving the acoustic interface problem on non fitted meshes.

Here we know that the only difference between IDG formulation applied to the scaled problem and IDPGFE formulation is the numerical flux. IDG formulation applied to the scaled

problem uses the numerical flux $\tilde{\mathbf{A}} = \tilde{\mathbf{A}}^+ + \tilde{\mathbf{A}}^- = (\mathbf{SA})^+ + (\mathbf{SA})^-$ while IDPGFE method uses the numerical flux $\tilde{\mathbf{A}} = \mathbf{SA}^+ + \mathbf{SA}^-$ ($\mathbf{A} = \mathbf{A}^+ + \mathbf{A}^-$) where matrices are

$$(\mathbf{SA})^+ = \begin{pmatrix} \frac{1}{2} & \frac{1}{2} \\ \frac{1}{2} & \frac{1}{2} \end{pmatrix}, \ (\mathbf{SA})^- = \begin{pmatrix} -\frac{1}{2} & \frac{1}{2} \\ \frac{1}{2} & -\frac{1}{2} \end{pmatrix}, \tag{2.3.26a}$$

$$\mathbf{SA}^+ = \begin{pmatrix} \frac{1}{2\rho c} & \frac{1}{2} \\ \frac{1}{2} & \frac{\rho c}{2} \end{pmatrix}, \ \mathbf{SA}^- = \begin{pmatrix} -\frac{1}{2\rho c} & \frac{1}{2} \\ \frac{1}{2} & -\frac{\rho c}{2} \end{pmatrix}, \tag{2.3.26b}$$

with ρ, c being the density and speed of sound.

On the boundary, we apply inflow boundary conditions in the numerical flux as

$$\mathbf{F}(\mathbf{U}^+, \mathbf{U}^-) = \mathbf{F}(\mathbf{U}^+(a), \mathbf{U}(a)) \mid_{x=a}, \tag{2.3.27a}$$

$$\mathbf{F}(\mathbf{U}^+, \mathbf{U}^-) = \mathbf{F}(\mathbf{U}(b), \mathbf{U}^-(b)) \mid_{x=b} \tag{2.3.27b}$$

and periodic boundary conditions as

$$\mathbf{F}(\mathbf{U}^+, \mathbf{U}^-) = \mathbf{F}(\mathbf{U}^+(a), \mathbf{U}^-(b)) \mid_{x=a}, \tag{2.3.28a}$$

$$\mathbf{F}(\mathbf{U}^+, \mathbf{U}^-) = \mathbf{F}(\mathbf{U}^+(a), \mathbf{U}^-(b)) \mid_{x=b} . \tag{2.3.28b}$$

Projecting initial values $\mathbf{C}(0) = \mathbf{C}_0$ using L^2 projection we obtain an initial value problem for the finite element coefficients. The resulting system of ordinary differential equation is

$$\frac{d\mathbf{C}}{dt} = \mathbf{A}_{h,q}^{PG}\mathbf{C}, \tag{2.3.29}$$

where $\mathbf{C}$ is a solution vector and $\mathbf{A}_{h,q}^{PG}$ is a global matrix which is solved using fourth-order Runge-Kutta method.

2.4 Computational Results

Consider the acoustic interface problem (2.1.1) with an incident wave

$$p_i(x,t) = p_0(x - c_1 t), \qquad u_i(x,t) = u_0(x - c_1 t) \tag{2.4.1a}$$

with the initial pulse

$$\mathbf{U}_0(x) = -f_0(t_0 - \frac{x}{c_1}) \begin{bmatrix} \rho_1 \\ \frac{1}{c_1} \end{bmatrix} = \begin{bmatrix} p_0 \\ u_0 \end{bmatrix}, \tag{2.4.1b}$$

where

$$f_0(\xi) = \begin{cases} \sin(w_c\xi) - \frac{21}{32}\sin(2w_c\xi) + \frac{63}{768}\sin(4w_c\xi) - \frac{1}{512}\sin(8w_c\xi), & \text{if } 0 < \xi < \frac{1}{f_c}, \\ 0, & \text{elsewhere.} \end{cases} \tag{2.4.1c}$$

When the incident wave hits the interface $x = \alpha$ it results in a reflected wave

$$p_r(x,t) = \frac{c_1\rho_1 - c_2\rho_2}{c_1\rho_1 + c_2\rho_2} p_0(x + c_1 t - 2(\alpha - \delta)), \qquad u_r(x,t) = \frac{c_2\rho_2 - c_1\rho_1}{c_1\rho_1 + c_2\rho_2} u_0(x + c_1 t - 2(\alpha - \delta)), \tag{2.4.1d}$$

with $\delta = c_1(t_0 - \frac{1}{2f_c})$, and a transmitted wave

$$p_t(x,t) = \frac{2c_2\rho_2}{c_1\rho_1 + c_2\rho_2} p_0(\frac{c_1}{c_2}(x - c_2 t - \alpha) + \alpha), \qquad u_t(x,t) = \frac{2c_1\rho_1}{c_1\rho_1 + c_2\rho_2} u_0(\frac{c_1}{c_2}(x - c_2 t - \alpha) + \alpha). \tag{2.4.1e}$$

Thus, the true solution of (2.1.1) can be written as

$$\mathbf{U}(x,t) = \begin{cases} \mathbf{U}_i(x,t) + \mathbf{U}_r(x,t), & \text{if } x < \alpha, \\ \mathbf{U}_t(x,t), & \text{if } x > \alpha, \end{cases} \tag{2.4.1f}$$

where $\mathbf{U}_i = [p_i, u_i]^T$, $\mathbf{U}_r = [p_r, u_r]^T$ and $\mathbf{U}_t = [p_t, u_t]^T$.

Example 2.4.1.

As a test problem we select the physical parameters $c_1 = 1m/s$, $\rho_1 = 2kg/m^3$, $c_2 = 2m/s$, $\rho_2 = 4kg/m^3$, $\alpha = 10^{-4}m$, $t_0 = 0s$, $w_c = 2\pi f_c$, $f_c = 0.5Hz$ and solve the acoustic interface problem (2.1.1) on the interval $[-5, 5]$ using uniform non fitted meshes having $N = 100, 120, 130, 140, 150$ elements and polynomial spaces of degrees $q = 1, 2, 3, 4$. We integrate in time using the classical fourth-order Runge-Kutta method from $t = 0$ to $t = 2$ with time steps $\Delta t = d\ h$, $d = 10^{-q}$ for IDGFE and IDPGFE methods and $h = 10/N$ is the mesh size. IDG method applied to the scaled problem uses $\Delta t = d\ h$, $d = 10^{-(q+1)}$ for $q = 1, 2, 3$ and $\Delta t = d\ h$, $d = 2 \cdot 10^{-(q+1)}$ for $q = 4$.

We present the L^2 errors and their orders of convergence at $t = 2$ in Tables 2.4.1, 2.4.2, 2.4.3 that suggest that the proposed three methods yield optimal convergence rates. We plot the true and numerical solutions for $N = 150$ and $q = 4$ at $t = 0, 2$ in Figure 2.4.1 to show that both solutions coincide.

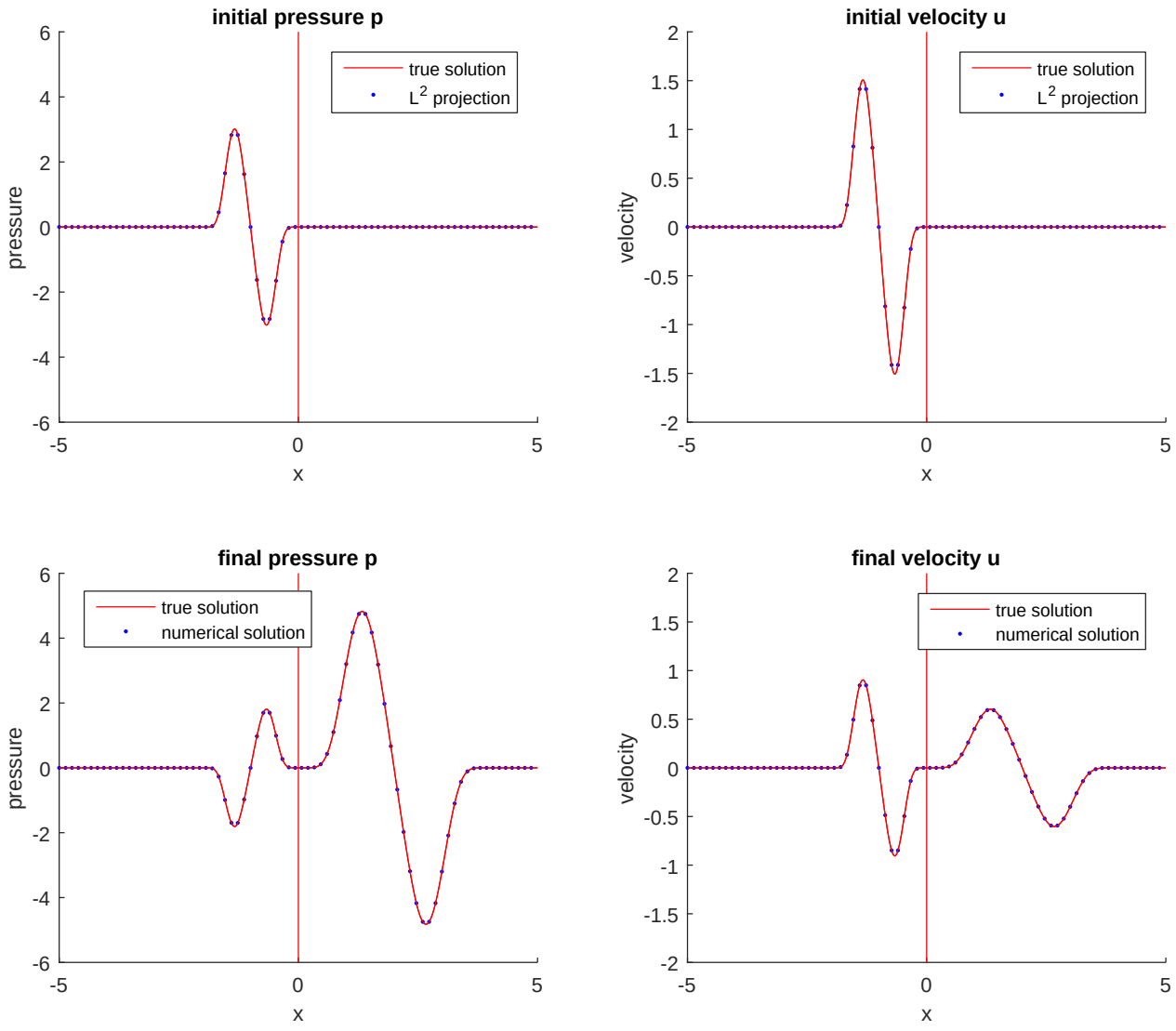

Figure 2.4.1: True and IDGFE pressures (left) and velocities (right) for Example 2.4.1 using $N = 150$ elements and $q = 4$ at $t = 0$ (top) and $t = 2$ (bottom).

$q=1$					$q=2$			
N	$\frac{\|p-p_h\|_{L^2}}{\|p\|_{L^2}}$	Order	$\frac{\|u-u_h\|_{L^2}}{\|u\|_{L^2}}$	Order	$\frac{\|p-p_h\|_{L^2}}{\|p\|_{L^2}}$	Order	$\frac{\|u-u_h\|_{L^2}}{\|u\|_{L^2}}$	Order
100	2.6743e-2	NA	2.9207e-2	NA	7.0329e-4	NA	1.1669e-3	NA
110	2.1103e-2	2.4849	2.3162e-2	2.4331	4.7916e-4	4.0261	8.3352e-4	3.5301
120	1.6907e-2	2.5482	1.8634e-2	2.4999	3.3702e-4	4.0443	6.1460e-4	3.5016
130	1.3735e-2	2.5957	1.5200e-2	2.5448	2.4414e-4	4.0276	4.6598e-4	3.4586
140	1.1302e-2	2.6311	1.2563e-2	2.5712	1.8174e-4	3.9835	3.6196e-4	3.4087
150	9.4087e-3	2.6571	1.0512e-2	2.5830	1.3866e-4	3.9207	2.8710e-4	3.3581
$q=3$					$q=4$			
N	$\frac{\|p-p_h\|_{L^2}}{\|p\|_{L^2}}$	Order	$\frac{\|u-u_h\|_{L^2}}{\|u\|_{L^2}}$	Order	$\frac{\|p-p_h\|_{L^2}}{\|p\|_{L^2}}$	Order	$\frac{\|u-u_h\|_{L^2}}{\|u\|_{L^2}}$	Order
100	2.5968e-5	NA	5.6914e-5	NA	4.4102e-5	NA	4.4295e-5	NA
110	4.0096e-4	-28.71	4.0138e-4	-20.49	5.7277e-7	45.57	1.4661e-6	35.76
120	1.0286e-5	42.098	2.5217e-5	31.805	3.6126e-7	5.2969	9.3950e-7	5.1148
130	7.0391e-6	4.7393	1.7874e-5	4.3001	2.3848e-7	5.1885	6.2588e-7	5.0746
140	5.0186e-6	4.5655	1.3064e-5	4.2298	1.6308e-7	5.1284	4.3041e-7	5.0524
150	3.6965e-6	4.4316	9.7916e-6	4.1792	1.1475e-7	5.0949	3.0400e-7	5.0398

Table 2.4.1: L^2 errors and orders of convergence for Example 2.4.1 with IDGFE method at $t = 2$.

Example 2.4.2.

Let us consider the acoustic interface problem where medium 1 is water and medium 2 is air with $c_1 = 1450m/s$, $\rho_1 = 1000kg/m^3$, $c_2 = 340m/s, \rho_2 = 1.3kg/m^3$, $\omega_c = 2\pi f_c$ and $f_c = 50Hz$.

We solve this problem on $[40, 140]$ using uniform meshes having $N = 105, 121, 208, 224, 240$ elements (having one interface element) for degrees $q = 1, 2, 3, 4$ and integrate from $t = 0.051s$ to $t = 0.091s$ using classical fourth-order Runge-Kutta method with time step sizes $\Delta t = d\,h$, $d = 10^{-5}$ for $q = 1$, $d = 10^{-(q+3)}$ for $q = 2, 3, 4$ and $h = 100/N$. The IDGFE solution for $q = 1$ exhibits large dispersion errors in Table 2.4.4 and thus optimal convergence rates are not observed in this case. Numerical solution is slightly shifted to the left compared to the true solution in Figure 2.4.5. As predicted in [9] high-degree approximations greatly reduce the dispersion errors and yields optimal $O(h^{q+1})$ convergence rates as shown for $q = 2, 3, 4$ in Table 2.4.4 and Figures 2.4.6, 2.4.7.

In Figures 2.4.2, 2.4.3, 2.4.4, the top two graphs show convergence rate for uniform mesh having $N = 100, 110, \cdots, 300$. The bottom two graphs show convergence rate for adjusted number of meshes. Blue line shows the original convergence rate in the top two graphs. Green line shows convergence rate for uniform meshes having $N = 105, 121, 208, 224, 240$ where $\hat{\alpha} \in (-0.8, -0.75)$ and red line shows convergence rate for uniform meshes having

$q=1$					$q=2$			
N	$\frac{\|p-p_h\|_{L^2}}{\|p\|_{L^2}}$	Order	$\frac{\|u-u_h\|_{L^2}}{\|u\|_{L^2}}$	Order	$\frac{\|p-p_h\|_{L^2}}{\|p\|_{L^2}}$	Order	$\frac{\|u-u_h\|_{L^2}}{\|u\|_{L^2}}$	Order
100	3.6094e-2	NA	4.6632e-2	NA	7.9294e-4	NA	1.5553e-3	NA
110	2.8672e-2	2.4152	3.7741e-2	2.2195	6.5112e-4	2.0675	1.1831e-3	2.8693
120	2.3089e-2	2.4893	3.0963e-2	2.2750	3.6693e-4	6.5913	8.3751e-4	3.9706
130	1.8826e-2	2.5498	2.5720e-2	2.3178	2.5943e-4	4.3314	6.4092e-4	3.3424
140	1.5528e-2	2.5992	2.1610e-2	2.3493	1.8775e-4	4.3633	5.0181e-4	3.3016
150	1.2942e-42	2.6396	1.8349e-2	2.3713	1.3887e-4	4.3714	4.0071e-4	3.2610
$q=3$					$q=4$			
N	$\frac{\|p-p_h\|_{L^2}}{\|p\|_{L^2}}$	Order	$\frac{\|u-u_h\|_{L^2}}{\|u\|_{L^2}}$	Order	$\frac{\|p-p_h\|_{L^2}}{\|p\|_{L^2}}$	Order	$\frac{\|u-u_h\|_{L^2}}{\|u\|_{L^2}}$	Order
100	5.0825e-5	NA	8.9168e-5	NA	7.3335e-7	NA	4.3557e-6	NA
110	1.4840e-5	12.916	5.1809e-5	5.6967	4.0216e-7	6.3034	2.7036e-6	5.0038
120	9.1154e-6	5.6011	3.6071e-5	4.1615	2.4056e-7	5.9057	1.7521e-6	4.9850
130	5.9309e-6	5.3695	2.5974e-5	4.1028	1.5331e-7	5.6284	1.1763e-6	4.9784
140	4.0543e-6	5.1329	1.9218e-5	4.0647	1.0236e-7	5.4518	8.1342e-7	4.9771
150	2.8886e-6	4.9138	1.4544e-5	4.0396	7.0793e-8	5.3440	5.7698e-7	4.9778

Table 2.4.2: L^2 errors and orders of convergence for Example 2.4.1 with IDG method applied to the scaled problem at $t = 2$.

$q=1$					$q=2$			
N	$\frac{\|p-p_h\|_{L^2}}{\|p\|_{L^2}}$	Order	$\frac{\|u-u_h\|_{L^2}}{\|u\|_{L^2}}$	Order	$\frac{\|p-p_h\|_{L^2}}{\|p\|_{L^2}}$	Order	$\frac{\|u-u_h\|_{L^2}}{\|u\|_{L^2}}$	Order
100	2.6999e-2	NA	3.5060e-2	NA	6.8302e-4	NA	1.0694e-3	NA
110	2.1326e-2	2.4747	2.7963e-2	2.3730	4.6140e-4	4.1156	7.5138e-4	3.7030
120	1.7096e-2	2.5408	2.2609e-2	2.4426	3.2141e-4	4.1554	5.4538e-4	3.6826
130	1.3893e-2	2.5917	1.8514e-2	2.4967	2.3039e-4	4.1593	4.0753e-4	3.6403
140	1.1432e-2	2.6310	1.5340e-2	2.5376	1.6961e-4	4.1327	3.1248e-4	3.5835
150	9.5145e-3	2.6614	1.2850e-2	2.5677	1.2797e-4	4.0828	2.4510e-4	3.5202
$q=3$					$q=4$			
N	$\frac{\|p-p_h\|_{L^2}}{\|p\|_{L^2}}$	Order	$\frac{\|u-u_h\|_{L^2}}{\|u\|_{L^2}}$	Order	$\frac{\|p-p_h\|_{L^2}}{\|p\|_{L^2}}$	Order	$\frac{\|u-u_h\|_{L^2}}{\|u\|_{L^2}}$	Order
100	2.4432e-5	NA	5.0183e-5	NA	4.4094e-5	NA	4.4142e-5	NA
110	4.0097e-4	-29.35	4.0200e-4	-21.83	5.4938e-7	46.011	1.3908e-6	36.276
120	9.5312e-6	42.975	2.2399e-5	33.185	3.4669e-7	5.2907	8.9421e-7	5.0767
130	6.4966e-6	4.7886	1.5960e-5	4.2345	2.2907e-7	5.1776	5.9721e-7	5.0431
140	4.6225e-6	4.5926	1.1725e-5	4.1603	1.5679e-7	5.1155	4.1151e-7	5.0256
150	3.4026e-6	4.4409	8.8304e-6	4.1100	1.1043e-7	5.0812	2.9113e-7	5.0162

Table 2.4.3: L^2 errors and orders of convergence for Example 2.4.1 with IDPGFE method at $t = 2$.

$N = 127, 143, 159, 175, 262, 278, 294$ where $\hat{\alpha} \in (0, 0.05)$. Meshes are designed by selecting the number for elements such that the corresponding physical interface element (x_l, x_{l+1}) is mapped into $(-1, 1)$ and physical interface $\alpha \in (x_l, x_{l+1})$ is mapped into reference interface $\hat{\alpha} \in (-1, 1)$. We plot the L^2 errors versus the number of elements in log-log scale in Figures 2.4.2, 2.4.3, 2.4.4.

We obtain that the error oscillates as it decreases with uniform mesh refinement. This is due to the fact that the error depends on the position of α within the interface elements. On specially designed meshes we observe that the error decreases smoothly when $\hat{\alpha}$ does not change much.

The true and numerical pressure and velocity coincide as shown in Figure 2.4.6. In this problem the transmitted IDGFE pressure is much smaller than the incident and reflected pressures and is plotted separately in Figure 2.4.7 which coincides with the true pressure.

$q = 1$					$q = 2$			
N	$\frac{\|p-p_h\|_{L^2}}{\|p\|_{L^2}}$	Order	$\frac{\|u-u_h\|_{L^2}}{\|u\|_{L^2}}$	Order	$\frac{\|p-p_h\|_{L^2}}{\|p\|_{L^2}}$	Order	$\frac{\|u-u_h\|_{L^2}}{\|u\|_{L^2}}$	Order
105	7.1916e-2	NA	3.5870e-1	NA	6.8117e-3	NA	1.8842e-1	NA
121	6.4568e-2	0.7599	3.0130e-1	1.2297	4.3000e-3	3.2434	1.3195e-1	2.5120
208	3.0646e-2	1.3755	1.3419e-1	1.4930	6.9107e-4	3.3745	3.3138e-2	2.5505
224	3.0534e-2	0.0494	1.2109e-1	1.3862	5.5910e-4	2.8596	2.6941e-2	2.7939
240	3.0463e-2	0.0338	1.1041e-1	1.3388	4.5885e-4	2.8640	2.2105e-2	2.8673
$q = 3$					$q = 4$			
N	$\frac{\|p-p_h\|_{L^2}}{\|p\|_{L^2}}$	Order	$\frac{\|u-u_h\|_{L^2}}{\|u\|_{L^2}}$	Order	$\frac{\|p-p_h\|_{L^2}}{\|p\|_{L^2}}$	Order	$\frac{\|u-u_h\|_{L^2}}{\|u\|_{L^2}}$	Order
105	6.3989e-4	NA	1.5431e-2	NA	1.0388e-4	NA	1.0735e-3	NA
121	3.9177e-4	3.4593	8.1492e-3	4.5014	5.4430e-5	4.5567	5.0048e-4	5.3802
208	5.2776e-5	3.7003	1.4417e-3	3.1972	4.5425e-6	4.5841	2.5220e-5	5.5154
224	3.9786e-5	3.8126	9.3264e-4	5.8776	3.1243e-6	5.0501	1.1362e-5	1.0760
240	3.0393e-5	3.9035	6.0543e-4	6.2628	2.1905e-6	5.1467	5.9673e-6	9.3337

Table 2.4.4: L^2 errors and orders of convergence for Example 2.4.2 using IDGFE method at $t = 0.091$.

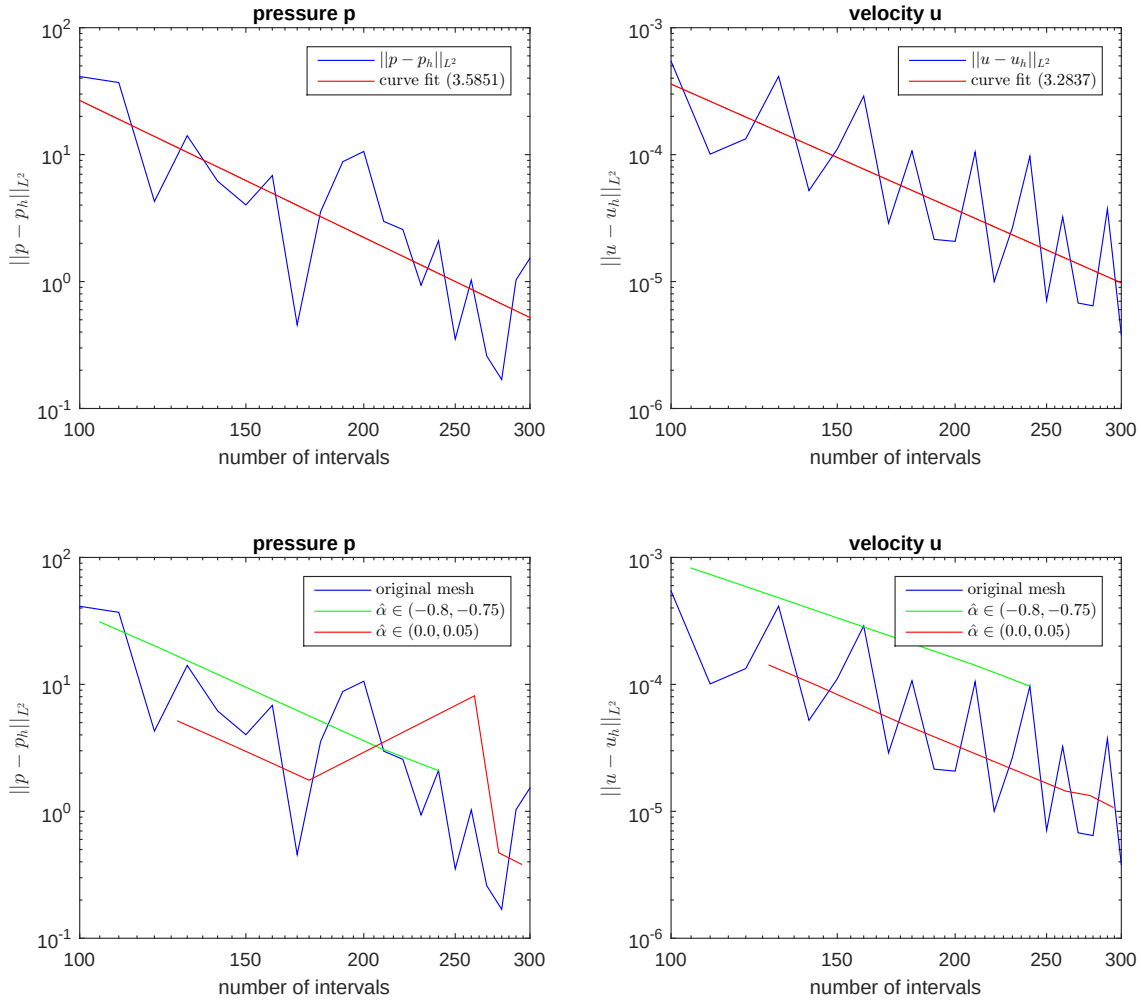

Figure 2.4.2: L^2 errors versus number of elements for Example 2.4.2 with $q = 2$ at $t = 0.091$ as log-log scale.

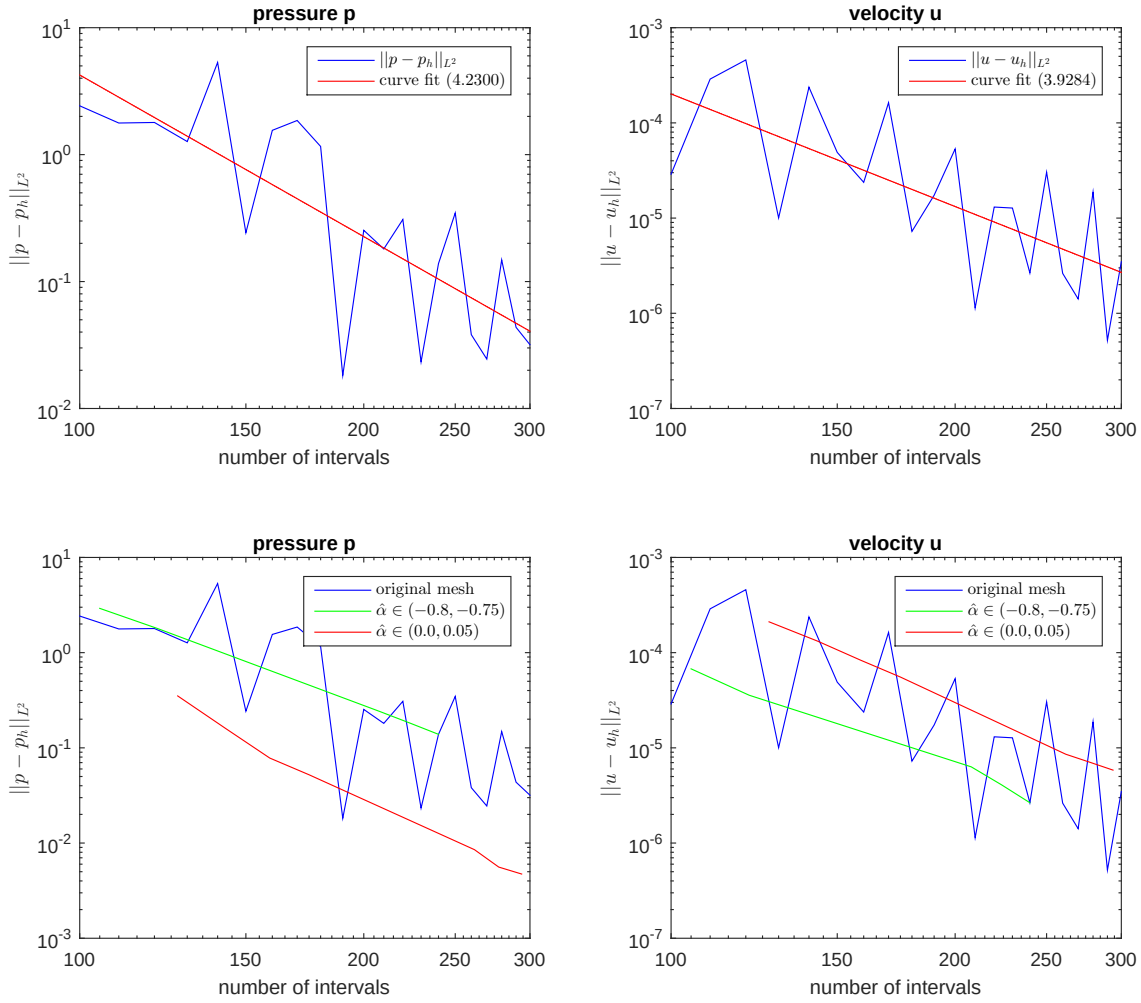

Figure 2.4.3: L^2 errors versus number of elements for Example 2.4.2 with $q = 3$ at $t = 0.091$ as log-log scale.

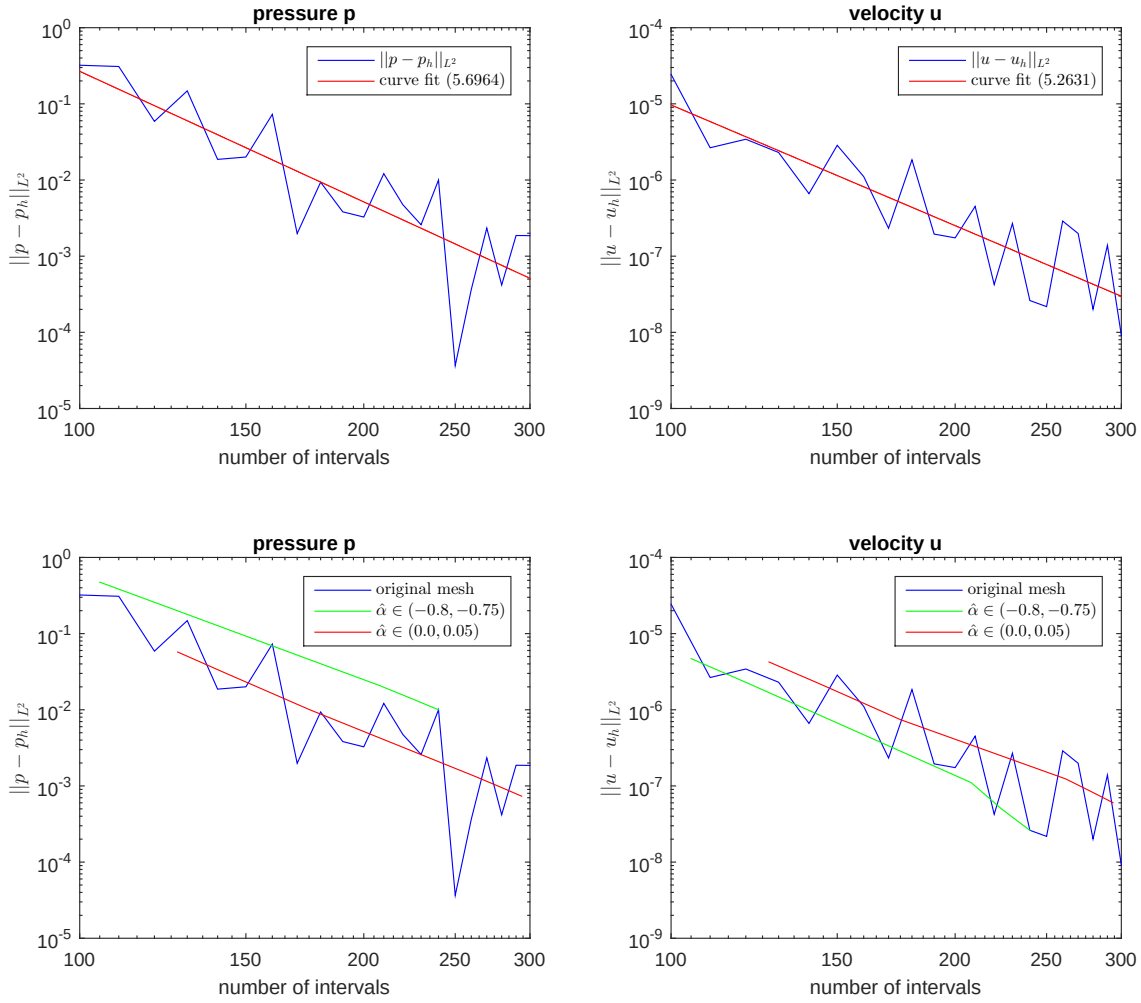

Figure 2.4.4: L^2 errors versus number of elements for Example 2.4.2 with $q = 4$ at $t = 0.091$ as log-log scale.

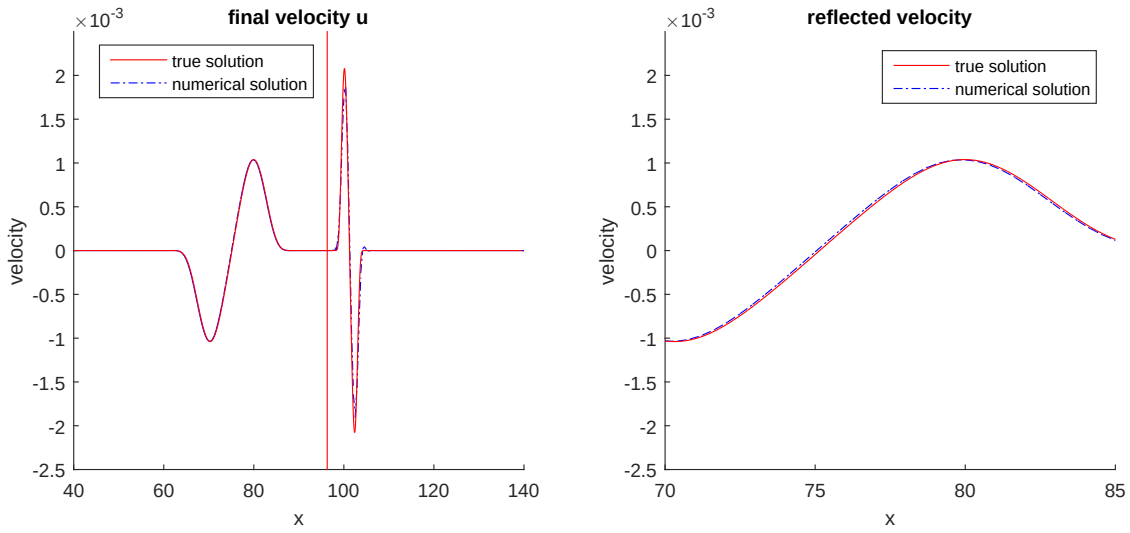

Figure 2.4.5: True and IDGFE velocities for Example 2.4.2 with $N = 240$ and $q = 1$ at $t = 0.091$.

Example 2.4.3.

In order to study the long term dispersive and dissipative properties of standard immersed DG method we solve the acoustic interface problem on $[a, b] = [-5, 5]$ with $\alpha = 10^{-4}m$, $c_1 = 1m/s$, $\rho_1 = 2kg/m^3$, $c_2 = 2m/s$ and $\rho_1 = 4kg/m^3$ subjected to periodic boundary conditions (2.3.28). The solution is periodic with period

$$T = \frac{\alpha - a}{c_1} + \frac{b - \alpha}{c_2} = 7.50005s. \tag{2.4.2}$$

We solve this problem for $0 \leq t \leq 15T$ and $0 \leq t \leq 50T$ using the uniform time step sizes $\Delta t = \frac{T}{1000}, \frac{T}{2000}, \frac{T}{4000}, \frac{T}{8000}$, respectively, for linear, quadratic, cubic and quartic IFE spaces.

On a uniform mesh having 100 elements, we plot the solution at $t = 0, 15T, 50T$ in Figures 2.4.8, 2.4.9, 2.4.10 and 2.4.11.

High dispersive and dissipative errors are shown in Figure 2.4.8 for linear IFE spaces and they decrease with higher order IFE spaces as shown in Figures 2.4.9, 2.4.10, 2.4.11.

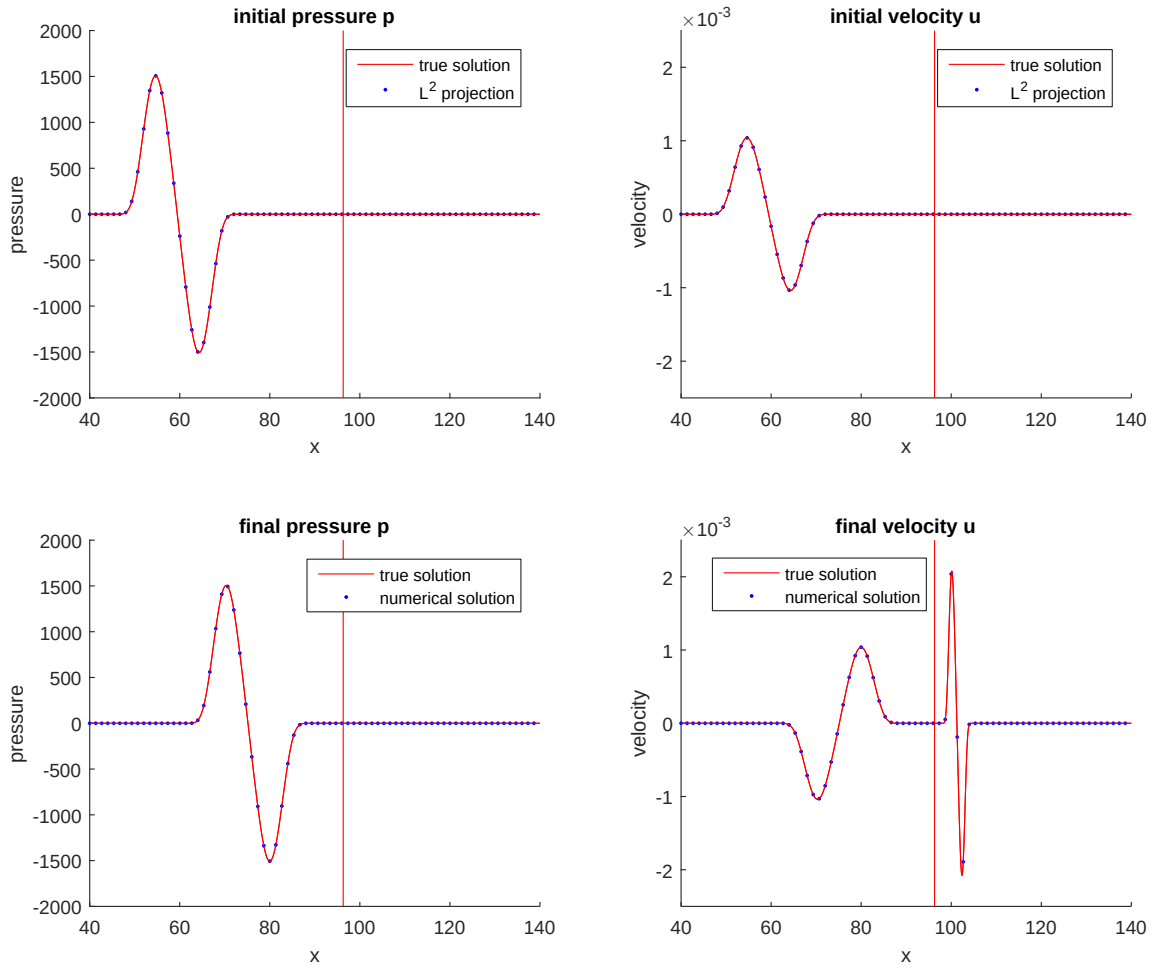

Figure 2.4.6: True and IDGFE pressures (left) and velocities (right) for Example 2.4.2 with $N = 300$ and $q = 4$ at $t = 0.051$ (top) and $t = 0.091$ (bottom).

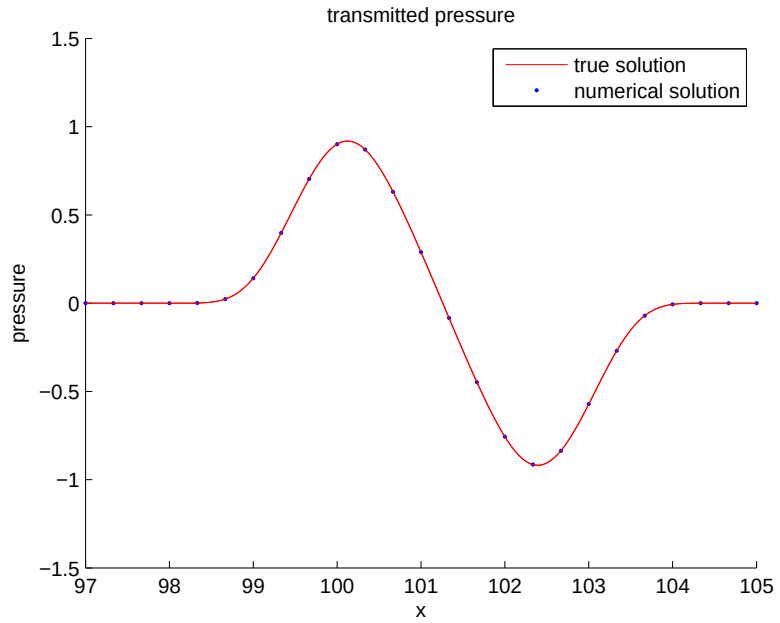

Figure 2.4.7: True and IDGFE transmitted pressure for Example 2.4.2 with $N = 300$, $q = 4$ at $t = 0.091$.

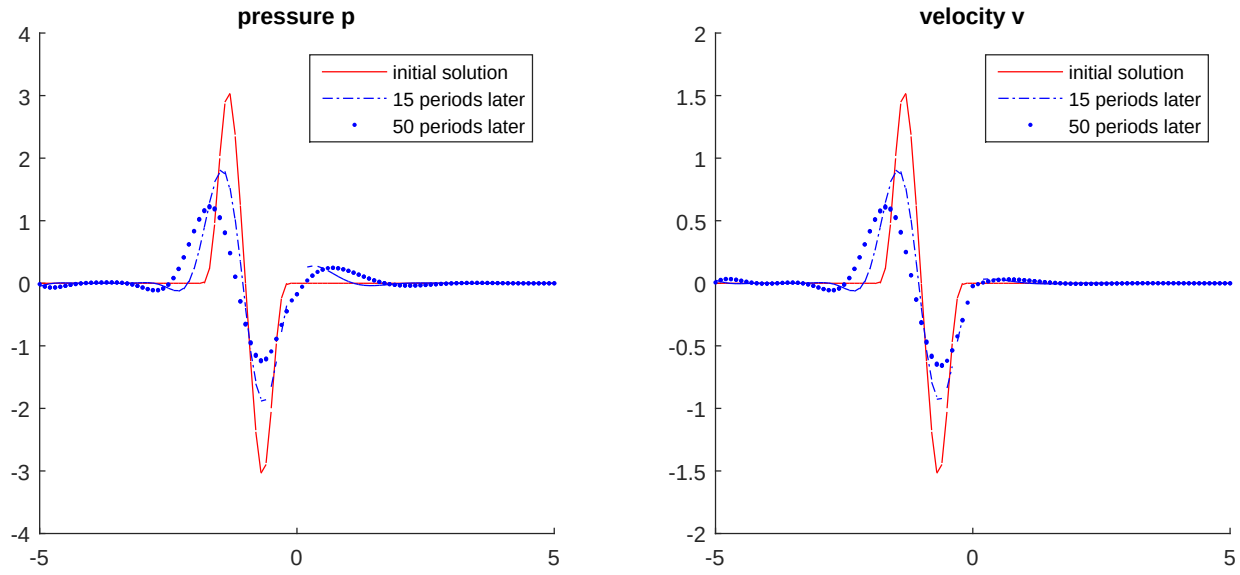

Figure 2.4.8: IDGFE solutions after 15 and 50 periods with linear IFE spaces.

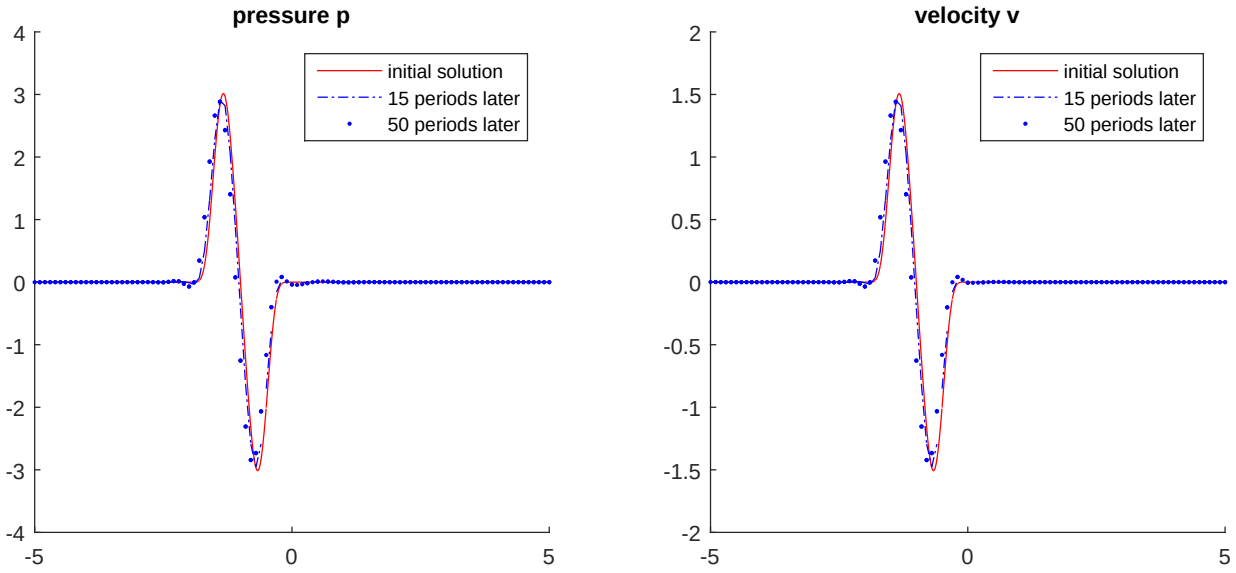

Figure 2.4.9: IDGFE solutions after 15 and 50 periods with quadratic IFE spaces.

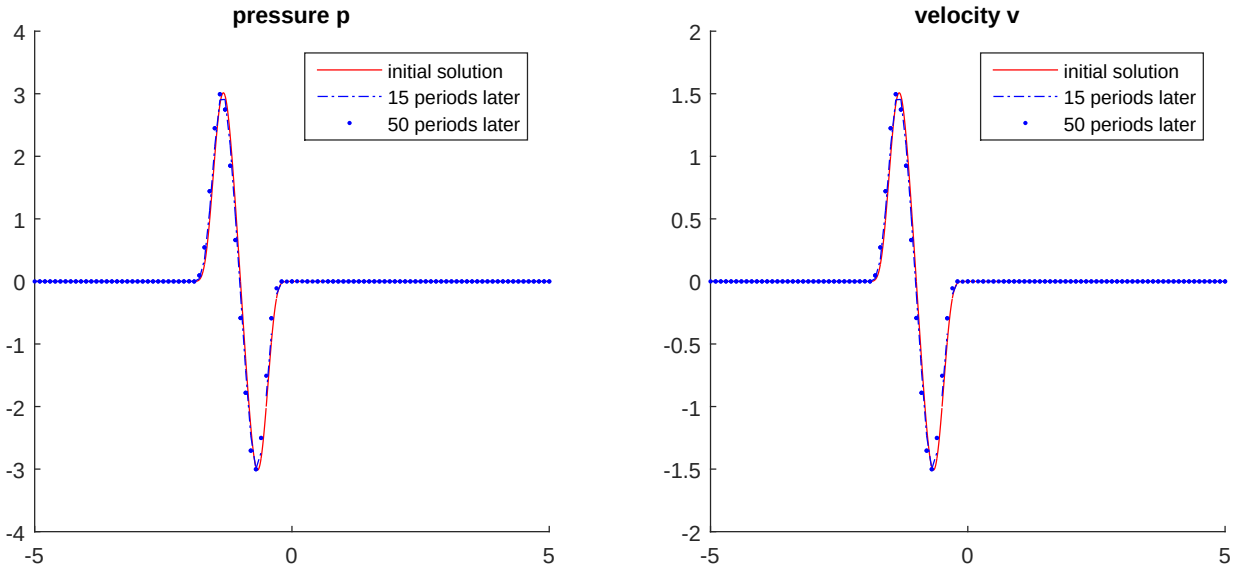

Figure 2.4.10: IDGFE solutions after 15 and 50 periods with cubic IFE spaces.

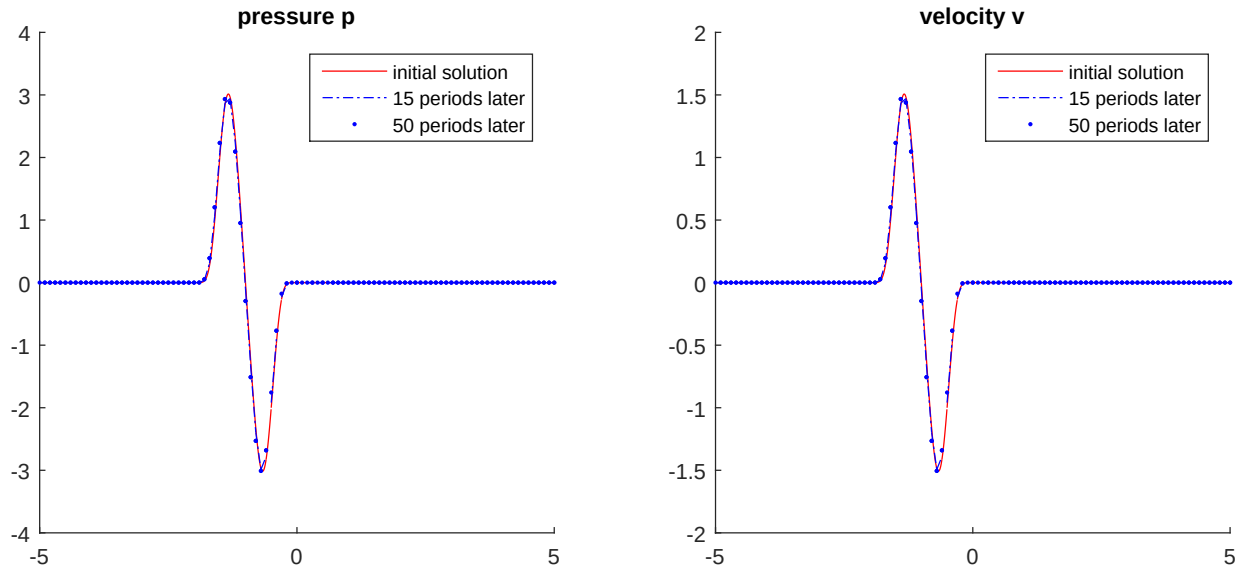

Figure 2.4.11: IDGFE solutions after 15 and 50 periods with quartic IFE spaces.

2.5 Stability for 1D Immersed DG Methods

We note that we do not have a proof for the stability of IDGFE method but numerical computations suggest its stability. We have a proof for the IDG method applied to the scaled problem and IDPGFE method. Since the proof for the IDG method applied to the scaled problem and IDPGFE method are similar, we only give the proof for IDPGFE method.

2.5.1 Stability Analysis

We have the numerical flux which is defined

$$\mathbf{F}(\mathbf{U}^+,\mathbf{U}^-)=\frac{1}{2}\mathbf{A}(\mathbf{U}^++\mathbf{U}^-)-\frac{1}{2}\left((1-\beta)|\mathbf{A}|+\frac{C}{h}\mathbf{I}\right)(\mathbf{U}^+-\mathbf{U}^-), \tag{2.5.1}$$

where $\mathbf{U}^+=\mathbf{U}(x_j^+)$ and $\mathbf{U}^-=\mathbf{U}(x_j^-)$ at mesh point $x=x_j$. $\mathbf{A}$ is the matrix in (2.1.1b), $\mathbf{I}$ is the identity matrix, C is a non negative constant, h is the mesh size and $\beta=1,0.5,0$ yield centered, partially upwind flux and fully upwind fluxes, respectively.

Theorem 2.5.1. *Let the interval I be split into $I_1=(a,\alpha)$ and $I_2=(\alpha,b)$. Let $\mathbf{U}$ be the solution of the acoustic problem (2.1.1a) satisfying the periodic boundary conditions (2.3.28) and jump condition (2.1.1h). Then the following holds.*

$$\epsilon(t)=\epsilon(t_0)\ \textit{for all}\ t\geq t_0, \tag{2.5.2a}$$

where

$$\epsilon(t) = \int_I \mathbf{U}^T(x,t)\mathbf{S}\mathbf{U}(x,t)dx = \sum_{i=1}^{2} \int_{I_i} \mathbf{U}_i^T(x,t)\mathbf{S}_i\mathbf{U}_i(x,t)dx, \tag{2.5.2b}$$

where $\mathbf{S}_i$ *is defined in (2.3.9a).*

Proof. Multiplying (2.1.1a) by $\mathbf{S}_i\mathbf{U}_i$ and integrate over I_i for $i = 1, 2$, we get the new formulation

$$\begin{aligned}&\int_a^\alpha \mathbf{U}_1^T\mathbf{S}_1\frac{\partial \mathbf{U}_1}{\partial t}dx + \int_\alpha^b \mathbf{U}_2^T\mathbf{S}_2\frac{\partial \mathbf{U}_2}{\partial t}dx + \int_a^\alpha \mathbf{U}_1^T\tilde{\mathbf{A}}\frac{\partial \mathbf{U}_1}{\partial x}dx \\ &+ \int_\alpha^b \mathbf{U}_2^T\tilde{\mathbf{A}}\frac{\partial \mathbf{U}_2}{\partial x}dx = 0,\end{aligned} \tag{2.5.3}$$

where

$$\tilde{\mathbf{A}} = \mathbf{S}\mathbf{A} = \begin{pmatrix} 0 & 1 \\ 1 & 0 \end{pmatrix}. \tag{2.5.4}$$

We can rewrite the equation as

$$\begin{aligned}&\frac{1}{2}\frac{\partial}{\partial t}\int_a^\alpha \mathbf{U}_1^T\mathbf{S}_1\mathbf{U}_1dx + \frac{1}{2}\frac{\partial}{\partial t}\int_\alpha^b \mathbf{U}_2^T\mathbf{S}_2\mathbf{U}_2dx + \frac{1}{2}\int_a^\alpha \frac{\partial}{\partial x}\mathbf{U}_1^T\tilde{\mathbf{A}}\mathbf{U}_1dx \\ &+\frac{1}{2}\int_\alpha^b \frac{\partial}{\partial x}\mathbf{U}_2^T\tilde{\mathbf{A}}\mathbf{U}_2dx = 0.\end{aligned} \tag{2.5.5}$$

By integration, we get

$$\begin{aligned}&\frac{1}{2}\frac{\partial}{\partial t}\int_a^\alpha \mathbf{U}_1^T\mathbf{S}_1\mathbf{U}_1dx + \frac{1}{2}\frac{\partial}{\partial t}\int_\alpha^b \mathbf{U}_2^T\mathbf{S}_2\mathbf{U}_2dx + \frac{1}{2}\mathbf{U}_1^T\tilde{\mathbf{A}}\mathbf{U}_1|_a^\alpha \\ &+\frac{1}{2}\mathbf{U}_2^T\tilde{\mathbf{A}}\mathbf{U}_2|_\alpha^b = 0.\end{aligned} \tag{2.5.6}$$

Since $\mathbf{U}$ is continuous at $x = \alpha$ and periodic on $[a, b]$, the second and third terms cancel out. Thus we obtain

$$\frac{1}{2}\frac{\partial}{\partial t}\int_a^\alpha \mathbf{U}_1^T\mathbf{S}_1\mathbf{U}_1dx + \frac{1}{2}\frac{\partial}{\partial t}\int_\alpha^b \mathbf{U}_2^T\mathbf{S}_2\mathbf{U}_2dx = 0, \tag{2.5.7}$$

which implies

$$\frac{\partial}{\partial t}\epsilon(t) = 0. \tag{2.5.8}$$

Integrating over time $[t_0, t]$ completes the proof. □

Theorem 2.5.2. *Let the interval I be split into N subintervals $a = x_0 < x_1 < \cdots < x_l < \alpha < x_{l+1} < \cdots < x_{N-1} < x_N = b$. Let $\mathbf{U}_h$ be the IDPGFE solution of the acoustic problem (2.1.1a) satisfying the periodic boundary conditions (2.3.28) and jump condition (2.1.1h). Then the following is true*

$$\epsilon_h(t) \leq \epsilon_h(t_0) \text{ for all } t \geq t_0, \tag{2.5.9a}$$

where

$$\begin{aligned}
\epsilon_h(t) &= \int_I \mathbf{U}_h^T(x,t)\mathbf{S}\mathbf{U}_h(x,t)dx \\
&= \sum_{j=0}^{l-1}\int_{x_j}^{x_{j+1}} \mathbf{U}_{1,h}^T(x,t)\mathbf{S}_1\mathbf{U}_{1,h}(x,t)dx + \int_{x_l}^{\alpha} \mathbf{U}_{1,h}^T(x,t)\mathbf{S}_1\mathbf{U}_{1,h}(x,t)dx \\
&+ \int_{\alpha}^{x_{l+1}} \mathbf{U}_{2,h}^T(x,t)\mathbf{S}_2\mathbf{U}_{2,h}(x,t)dx + \sum_{j=l+1}^{N-1}\int_{x_j}^{x_{j+1}} \mathbf{U}_{2,h}^T(x,t)\mathbf{S}_2\mathbf{U}_{2,h}(x,t)dx,
\end{aligned} \tag{2.5.9b}$$

where $\mathbf{S}_i$ is defined in (2.3.9a).

Proof. Summing over all elements using (2.3.19), (2.3.23) and (2.3.24), the IDPGFE formulation consists of finding $\mathbf{U}_h$ such that

$$\begin{aligned}
&\sum_{j=0}^{l-1}\int_{x_j}^{x_{j+1}} \mathbf{V}_{1,h}^T\mathbf{S}_1\frac{\partial \mathbf{U}_{1,h}}{\partial t}dx + \int_{x_l}^{\alpha} \mathbf{V}_{1,h}^T\mathbf{S}_1\frac{\partial \mathbf{U}_{1,h}}{\partial t}dx + \int_{\alpha}^{x_{l+1}} \mathbf{V}_{2,h}^T\mathbf{S}_2\frac{\partial \mathbf{U}_{2,h}}{\partial t}dx \\
&+ \sum_{j=l+1}^{N-1}\int_{x_j}^{x_{j+1}} \mathbf{V}_{2,h}^T\mathbf{S}_2\frac{\partial \mathbf{U}_{2,h}}{\partial t}dx + \sum_{j=0}^{l-1}\mathbf{V}_{1,h}^T\tilde{\mathbf{A}}\mathbf{U}_{1,h}\,|_{x=x_j}^{x=x_{j+1}} + \mathbf{V}_{1,h}^T\tilde{\mathbf{A}}\mathbf{U}_{1,h}\,|_{x=x_l}^{x=\alpha} \\
&+ \mathbf{V}_{2,h}^T\tilde{\mathbf{A}}\mathbf{U}_{2,h}\,|_{x=\alpha}^{x=x_{l+1}} + \sum_{j=l+1}^{N-1}\mathbf{V}_{2,h}^T\tilde{\mathbf{A}}\mathbf{U}_{2,h}\,|_{x=x_j}^{x=x_{j+1}} - \sum_{j=0}^{l-1}\int_{x_j}^{x_{j+1}} \frac{\partial \mathbf{V}_{1,h}^T}{\partial x}\tilde{\mathbf{A}}\mathbf{U}_{1,h}dx \\
&- \int_{x_l}^{\alpha} \frac{\partial \mathbf{V}_{1,h}^T}{\partial x}\tilde{\mathbf{A}}\mathbf{U}_{1,h}dx - \int_{\alpha}^{x_{l+1}} \frac{\partial \mathbf{V}_{2,h}^T}{\partial x}\tilde{\mathbf{A}}\mathbf{U}_{2,h}dx - \sum_{j=l+1}^{N-1}\int_{x_j}^{x_{j+1}} \frac{\partial \mathbf{V}_{2,h}^T}{\partial x}\tilde{\mathbf{A}}\mathbf{U}_{2,h}dx = 0,
\end{aligned} \tag{2.5.10}$$

where $\tilde{\mathbf{A}}$ is defined in (2.5.4).

By the periodicity on $[a,b]$ and the continuity of $\mathbf{V}_h$, $\mathbf{U}_h$ at $x = \alpha$, we obtain

$$\begin{aligned}
\mathbf{V}_{1,h}^T\tilde{\mathbf{A}}\mathbf{U}_{1,h}\,|_{x=\alpha} - \mathbf{V}_{2,h}^T\tilde{\mathbf{A}}\mathbf{U}_{2,h}\,|_{x=\alpha} &= 0, \\
\mathbf{V}_{1,h}^T\tilde{\mathbf{A}}\mathbf{U}_{1,h}\,|_{x=x_0} - \mathbf{V}_{2,h}^T\tilde{\mathbf{A}}\mathbf{U}_{2,h}\,|_{x=x_N} &= 0.
\end{aligned} \tag{2.5.11}$$

Applying (2.5.11) and the numerical flux (2.5.1) at $x = x_j$, x_{j+1}

$$\begin{aligned}
\tilde{\mathbf{A}}\mathbf{U}_h &= \mathbf{S}\mathbf{A}\mathbf{U}_h = \mathbf{S}\mathbf{F}(\mathbf{U}_h^+, \mathbf{U}_h^-) \\
&= \mathbf{S}\frac{1}{2}(\mathbf{A} - (1-\beta)|\mathbf{A}| - \frac{C}{h}\mathbf{I})\mathbf{U}_h^+ + \mathbf{S}\frac{1}{2}(\mathbf{A} + (1-\beta)|\mathbf{A}| + \frac{C}{h}\mathbf{I})\mathbf{U}_h^- \\
&= \frac{1}{2}(\tilde{\mathbf{A}} - (1-\beta)\mathbf{S}|\mathbf{A}| - \frac{C}{h}\mathbf{S})\mathbf{U}_h^+ + \frac{1}{2}(\tilde{\mathbf{A}} + (1-\beta)\mathbf{S}|\mathbf{A}| + \frac{C}{h}\mathbf{S})\mathbf{U}_h^-,
\end{aligned} \tag{2.5.12}$$

the 5, 6, 7, 8-th flux terms in (2.5.10) are

$$
\begin{aligned}
&+\left(\mathbf{V}_{1,h}^{-}{}^{T}\frac{1}{2}(\tilde{\mathbf{A}}-(1-\beta)\mathbf{S}_1|\mathbf{A}_1|-\frac{C}{h}\mathbf{S}_1)\mathbf{U}_{1,h}^{+}+\mathbf{V}_{1,h}^{-}{}^{T}\frac{1}{2}(\tilde{\mathbf{A}}+(1-\beta)\mathbf{S}_1|\mathbf{A}_1|+\frac{C}{h}\mathbf{S}_1)\mathbf{U}_{1,h}^{-}\right)|_{x=x_1}\\
&+\sum_{j=1}^{l-1}\left(\mathbf{V}_{1,h}^{-}{}^{T}\frac{1}{2}(\tilde{\mathbf{A}}-(1-\beta)\mathbf{S}_1|\mathbf{A}_1|-\frac{C}{h}\mathbf{S}_1)\mathbf{U}_{1,h}^{+}+\mathbf{V}_{1,h}^{-}{}^{T}\frac{1}{2}(\tilde{\mathbf{A}}+(1-\beta)\mathbf{S}_1|\mathbf{A}_1|+\frac{C}{h}\mathbf{S}_1)\mathbf{U}_{1,h}^{-}\right)|_{x=x_{j+1}}\\
&-\sum_{j=1}^{l-1}\left(\mathbf{V}_{1,h}^{+}{}^{T}\frac{1}{2}(\tilde{\mathbf{A}}-(1-\beta)\mathbf{S}_1|\mathbf{A}_1|-\frac{C}{h}\mathbf{S}_1)\mathbf{U}_{1,h}^{+}+\mathbf{V}_{1,h}^{+}{}^{T}\frac{1}{2}(\tilde{\mathbf{A}}+(1-\beta)\mathbf{S}_1|\mathbf{A}_1|+\frac{C}{h}\mathbf{S}_1)\mathbf{U}_{1,h}^{-}\right)|_{x=x_j}\\
&-\left(\mathbf{V}_{1,h}^{+}{}^{T}\frac{1}{2}(\tilde{\mathbf{A}}-(1-\beta)\mathbf{S}_1|\mathbf{A}_1|-\frac{C}{h}\mathbf{S}_1)\mathbf{U}_{1,h}^{+}+\mathbf{V}_{1,h}^{+}{}^{T}\frac{1}{2}(\tilde{\mathbf{A}}+(1-\beta)\mathbf{S}_1|\mathbf{A}_1|+\frac{C}{h}\mathbf{S}_1)\mathbf{U}_{1,h}^{-}\right)|_{x=x_l} \quad (2.5.13)\\
&+\left(\mathbf{V}_{2,h}^{-}{}^{T}\frac{1}{2}(\tilde{\mathbf{A}}-(1-\beta)\mathbf{S}_2|\mathbf{A}_2|-\frac{C}{h}\mathbf{S}_2)\mathbf{U}_{2,h}^{+}+\mathbf{V}_{2,h}^{-}{}^{T}\frac{1}{2}(\tilde{\mathbf{A}}+(1-\beta)\mathbf{S}_2|\mathbf{A}_2|+\frac{C}{h}\mathbf{S}_2)\mathbf{U}_{2,h}^{-}\right)|_{x=x_{l+1}}\\
&+\sum_{j=l+1}^{N-2}\left(\mathbf{V}_{2,h}^{-}{}^{T}\frac{1}{2}(\tilde{\mathbf{A}}-(1-\beta)\mathbf{S}_2|\mathbf{A}_2|-\frac{C}{h}\mathbf{S}_2)\mathbf{U}_{2,h}^{+}+\mathbf{V}_{2,h}^{-}{}^{T}\frac{1}{2}(\tilde{\mathbf{A}}+(1-\beta)\mathbf{S}_2|\mathbf{A}_2|+\frac{C}{h}\mathbf{S}_2)\mathbf{U}_{2,h}^{-}\right)|_{x=x_{j+1}}\\
&-\sum_{j=l+1}^{N-2}\left(\mathbf{V}_{2,h}^{+}{}^{T}\frac{1}{2}(\tilde{\mathbf{A}}-(1-\beta)\mathbf{S}_2|\mathbf{A}_2|-\frac{C}{h}\mathbf{S}_2)\mathbf{U}_{2,h}^{+}+\mathbf{V}_{2,h}^{+}{}^{T}\frac{1}{2}(\tilde{\mathbf{A}}+(1-\beta)\mathbf{S}_2|\mathbf{A}_2|+\frac{C}{h}\mathbf{S}_2)\mathbf{U}_{2,h}^{-}\right)|_{x=x_j}\\
&-\left(\mathbf{V}_{2,h}^{+}{}^{T}\frac{1}{2}(\tilde{\mathbf{A}}-(1-\beta)\mathbf{S}_2|\mathbf{A}_2|-\frac{C}{h}\mathbf{S}_2)\mathbf{U}_{2,h}^{+}+\mathbf{V}_{2,h}^{+}{}^{T}\frac{1}{2}(\tilde{\mathbf{A}}+(1-\beta)\mathbf{S}_2|\mathbf{A}_2|+\frac{C}{h}\mathbf{S}_2)\mathbf{U}_{2,h}^{-}\right)|_{x=x_{N-1}}.
\end{aligned}
$$

Shifting the index j from $j=1,\cdots,l-1$ to $j=2,\cdots,l$ for the second term, from $j=l+1,\cdots,N-2$ to $j=l+2,\cdots,N-1$ for the 6-th term, the flux terms are

$$
\begin{aligned}
&+\sum_{j=1}^{l}\left(\mathbf{V}_{1,h}^{-}{}^{T}\frac{1}{2}(\tilde{\mathbf{A}}-(1-\beta)\mathbf{S}_1|\mathbf{A}_1|-\frac{C}{h}\mathbf{S}_1)\mathbf{U}_{1,h}^{+}+\mathbf{V}_{1,h}^{-}{}^{T}\frac{1}{2}(\tilde{\mathbf{A}}+(1-\beta)\mathbf{S}_1|\mathbf{A}_1|+\frac{C}{h}\mathbf{S}_1)\mathbf{U}_{1,h}^{-}\right)|_{x=x_j}\\
&-\sum_{j=1}^{l}\left(\mathbf{V}_{1,h}^{+}{}^{T}\frac{1}{2}(\tilde{\mathbf{A}}-(1-\beta)\mathbf{S}_1|\mathbf{A}_1|-\frac{C}{h}\mathbf{S}_1)\mathbf{U}_{1,h}^{+}+\mathbf{V}_{1,h}^{+}{}^{T}\frac{1}{2}(\tilde{\mathbf{A}}+(1-\beta)\mathbf{S}_1|\mathbf{A}_1|+\frac{C}{h}\mathbf{S}_1)\mathbf{U}_{1,h}^{-}\right)|_{x=x_j}\\
&+\sum_{j=l+1}^{N-1}\left(\mathbf{V}_{2,h}^{-}{}^{T}\frac{1}{2}(\tilde{\mathbf{A}}-(1-\beta)\mathbf{S}_2|\mathbf{A}_2|-\frac{C}{h}\mathbf{S}_2)\mathbf{U}_{2,h}^{+}+\mathbf{V}_{2,h}^{-}{}^{T}\frac{1}{2}(\tilde{\mathbf{A}}+(1-\beta)\mathbf{S}_2|\mathbf{A}_2|+\frac{C}{h}\mathbf{S}_2)\mathbf{U}_{2,h}^{-}\right)|_{x=x_j}\\
&-\sum_{j=l+1}^{N-1}\left(\mathbf{V}_{2,h}^{+}{}^{T}\frac{1}{2}(\tilde{\mathbf{A}}-(1-\beta)\mathbf{S}_2|\mathbf{A}_2|-\frac{C}{h}\mathbf{S}_2)\mathbf{U}_{2,h}^{+}+\mathbf{V}_{2,h}^{+}{}^{T}\frac{1}{2}(\tilde{\mathbf{A}}+(1-\beta)\mathbf{S}_2|\mathbf{A}_2|+\frac{C}{h}\mathbf{S}_2)\mathbf{U}_{2,h}^{-}\right)|_{x=x_j}.
\end{aligned}
\quad (2.5.14)
$$

Setting $\mathbf{V}_{i,h}=\mathbf{U}_{i,h}$ for $i=1,2$, (2.5.10) is

$$
\begin{aligned}
&\sum_{j=0}^{l-1}\int_{x_j}^{x_{j+1}}\mathbf{U}_{1,h}^{T}\mathbf{S}_1\frac{\partial\mathbf{U}_{1,h}}{\partial t}dx+\int_{x_l}^{\alpha}\mathbf{U}_{1,h}^{T}\mathbf{S}_1\frac{\partial\mathbf{U}_{1,h}}{\partial t}dx+\int_{\alpha}^{x_{l+1}}\mathbf{U}_{2,h}^{T}\mathbf{S}_2\frac{\partial\mathbf{U}_{2,h}}{\partial t}dx\\
&+\sum_{j=l+1}^{N-1}\int_{x_j}^{x_{j+1}}\mathbf{U}_{2,h}^{T}\mathbf{S}_2\frac{\partial\mathbf{U}_{2,h}}{\partial t}dx
\end{aligned}
$$

$$
\begin{aligned}
&+\sum_{j=1}^{l}\left(\mathbf{U}_{1,h}^{-}{}^{T}\frac{1}{2}(\tilde{\mathbf{A}}-(1-\beta)\mathbf{S}_1|\mathbf{A}_1|-\frac{C}{h}\mathbf{S}_1)\mathbf{U}_{1,h}^{+}+\mathbf{U}_{1,h}^{-}{}^{T}\frac{1}{2}(\tilde{\mathbf{A}}+(1-\beta)\mathbf{S}_1|\mathbf{A}_1|+\frac{C}{h}\mathbf{S}_1)\mathbf{U}_{1,h}^{-}\right)|_{x=x_j}\\
&-\sum_{j=1}^{l}\left(\mathbf{U}_{1,h}^{+}{}^{T}\frac{1}{2}(\tilde{\mathbf{A}}-(1-\beta)\mathbf{S}_1|\mathbf{A}_1|-\frac{C}{h}\mathbf{S}_1)\mathbf{U}_{1,h}^{+}+\mathbf{U}_{1,h}^{+}{}^{T}\frac{1}{2}(\tilde{\mathbf{A}}+(1-\beta)\mathbf{S}_1|\mathbf{A}_1|+\frac{C}{h}\mathbf{S}_1)\mathbf{U}_{1,h}^{-}\right)|_{x=x_j}\\
&+\sum_{j=l+1}^{N-1}\left(\mathbf{U}_{2,h}^{-}{}^{T}\frac{1}{2}(\tilde{\mathbf{A}}-(1-\beta)\mathbf{S}_2|\mathbf{A}_2|-\frac{C}{h}\mathbf{S}_2)\mathbf{U}_{2,h}^{+}+\mathbf{U}_{2,h}^{-}{}^{T}\frac{1}{2}(\tilde{\mathbf{A}}+(1-\beta)\mathbf{S}_2|\mathbf{A}_2|+\frac{C}{h}\mathbf{S}_2)\mathbf{U}_{2,h}^{-}\right)|_{x=x_j}\\
&-\sum_{j=l+1}^{N-1}\left(\mathbf{U}_{2,h}^{+}{}^{T}\frac{1}{2}(\tilde{\mathbf{A}}-(1-\beta)\mathbf{S}_2|\mathbf{A}_2|-\frac{C}{h}\mathbf{S}_2)\mathbf{U}_{2,h}^{+}+\mathbf{U}_{2,h}^{+}{}^{T}\frac{1}{2}(\tilde{\mathbf{A}}+(1-\beta)\mathbf{S}_2|\mathbf{A}_2|+\frac{C}{h}\mathbf{S}_2)\mathbf{U}_{2,h}^{-}\right)|_{x=x_j}\\
&-\sum_{j=0}^{l-1}\int_{x_j}^{x_{j+1}}\frac{\partial\mathbf{U}_{1,h}^{T}}{\partial x}\tilde{\mathbf{A}}\mathbf{U}_{1,h}dx-\int_{x_l}^{\alpha}\frac{\partial\mathbf{U}_{1,h}^{T}}{\partial x}\tilde{\mathbf{A}}\mathbf{U}_{1,h}dx-\int_{\alpha}^{x_{l+1}}\frac{\partial\mathbf{U}_{2,h}^{T}}{\partial x}\tilde{\mathbf{A}}\mathbf{U}_{2,h}dx\\
&-\sum_{j=l+1}^{N-1}\int_{x_j}^{x_{j+1}}\frac{\partial\mathbf{U}_{2,h}^{T}}{\partial x}\tilde{\mathbf{A}}\mathbf{U}_{2,h}dx=0. \qquad (2.5.15)
\end{aligned}
$$

Using $\frac{\partial\mathbf{U}_h^T}{\partial x}\tilde{\mathbf{A}}\mathbf{U}_h=\frac{1}{2}\frac{\partial}{\partial x}(\mathbf{U}_h^T\tilde{\mathbf{A}}\mathbf{U}_h)$ due to the symmetry of $\tilde{\mathbf{A}}$, the terms of the last two lines are

$$
\begin{aligned}
&-\sum_{j=0}^{l-1}\frac{1}{2}\int_{x_j}^{x_{j+1}}\frac{\partial}{\partial x}(\mathbf{U}_{1,h}^{T}\tilde{\mathbf{A}}\mathbf{U}_{1,h})dx-\frac{1}{2}\int_{x_l}^{\alpha}\frac{\partial}{\partial x}(\mathbf{U}_{1,h}^{T}\tilde{\mathbf{A}}\mathbf{U}_{1,h})dx-\frac{1}{2}\int_{\alpha}^{x_{l+1}}\frac{\partial}{\partial x}(\mathbf{U}_{2,h}^{T}\tilde{\mathbf{A}}\mathbf{U}_{2,h})dx\\
&-\sum_{j=l+1}^{N-1}\frac{1}{2}\int_{x_j}^{x_{j+1}}\frac{\partial}{\partial x}(\mathbf{U}_{2,h}^{T}\tilde{\mathbf{A}}\mathbf{U}_{2,h})dx. \qquad (2.5.16)
\end{aligned}
$$

By integration and the continuity at $x=\alpha$, we obtain

$$
\begin{aligned}
&-\sum_{j=0}^{l-1}\frac{1}{2}\mathbf{U}_{1,h}^{-}{}^{T}\tilde{\mathbf{A}}\mathbf{U}_{1,h}^{-}|_{x=x_{j+1}}+\sum_{j=0}^{l-1}\frac{1}{2}\mathbf{U}_{1,h}^{+}{}^{T}\tilde{\mathbf{A}}\mathbf{U}_{1,h}^{+}|_{x=x_j}+\frac{1}{2}\mathbf{U}_{1,h}^{+}{}^{T}\tilde{\mathbf{A}}\mathbf{U}_{1,h}^{+}|_{x=x_l} \qquad (2.5.17)\\
&-\frac{1}{2}\mathbf{U}_{2,h}^{-}{}^{T}\tilde{\mathbf{A}}\mathbf{U}_{2,h}^{-}|_{x=x_{l+1}}-\sum_{j=l+1}^{N-1}\frac{1}{2}\mathbf{U}_{2,h}^{-}{}^{T}\tilde{\mathbf{A}}\mathbf{U}_{2,h}^{-}|_{x=x_{j+1}}+\sum_{j=l+1}^{N-1}\frac{1}{2}\mathbf{U}_{2,h}^{+}{}^{T}\tilde{\mathbf{A}}\mathbf{U}_{2,h}^{+}|_{x=x_j}.
\end{aligned}
$$

Again applying periodicity on $[a,b]$ and shifting the index, we obtain

$$
\begin{aligned}
&-\sum_{j=1}^{l}\frac{1}{2}\mathbf{U}_{1,h}^{-}{}^{T}\tilde{\mathbf{A}}\mathbf{U}_{1,h}^{-}|_{x=x_j}+\sum_{j=1}^{l}\frac{1}{2}\mathbf{U}_{1,h}^{+}{}^{T}\tilde{\mathbf{A}}\mathbf{U}_{1,h}^{+}|_{x=x_j}-\sum_{j=l+1}^{N-1}\frac{1}{2}\mathbf{U}_{2,h}^{-}{}^{T}\tilde{\mathbf{A}}\mathbf{U}_{2,h}^{-}|_{x=x_j}\\
&+\sum_{j=l+1}^{N-1}\frac{1}{2}\mathbf{U}_{2,h}^{+}{}^{T}\tilde{\mathbf{A}}\mathbf{U}_{2,h}^{+}|_{x=x_j}. \qquad (2.5.18)
\end{aligned}
$$

Thus (2.5.15) becomes

$$\sum_{j=0}^{l-1}\int_{x_j}^{x_{j+1}} \mathbf{U}_{1,h}^T\mathbf{S}_1\frac{\partial \mathbf{U}_{1,h}}{\partial t}dx+\int_{x_l}^{\alpha} \mathbf{U}_{1,h}^T\mathbf{S}_1\frac{\partial \mathbf{U}_{1,h}}{\partial t}dx+\int_{\alpha}^{x_{l+1}} \mathbf{U}_{2,h}^T\mathbf{S}_2\frac{\partial \mathbf{U}_{2,h}}{\partial t}dx$$
$$+\sum_{j=l+1}^{N-1}\int_{x_j}^{x_{j+1}} \mathbf{U}_{2,h}^T\mathbf{S}_2\frac{\partial \mathbf{U}_{2,h}}{\partial t}dx$$
$$+\sum_{j=1}^{l}\left(\mathbf{U}_{1,h}^{-}{}^T\frac{1}{2}(\tilde{\mathbf{A}}-(1-\beta)\mathbf{S}_1|\mathbf{A}_1|-\frac{C}{h}\mathbf{S}_1)\mathbf{U}_{1,h}^{+}+\mathbf{U}_{1,h}^{-}{}^T\frac{1}{2}(\tilde{\mathbf{A}}+(1-\beta)\mathbf{S}_1|\mathbf{A}_1|+\frac{C}{h}\mathbf{S}_1)\mathbf{U}_{1,h}^{-}\right)|_{x=x_j}$$
$$-\sum_{j=1}^{l}\left(\mathbf{U}_{1,h}^{+}{}^T\frac{1}{2}(\tilde{\mathbf{A}}-(1-\beta)\mathbf{S}_1|\mathbf{A}_1|-\frac{C}{h}\mathbf{S}_1)\mathbf{U}_{1,h}^{+}+\mathbf{U}_{1,h}^{+}{}^T\frac{1}{2}(\tilde{\mathbf{A}}+(1-\beta)\mathbf{S}_1|\mathbf{A}_1|+\frac{C}{h}\mathbf{S}_1)\mathbf{U}_{1,h}^{-}\right)|_{x=x_j}$$
$$+\sum_{j=l+1}^{N-1}\left(\mathbf{U}_{2,h}^{-}{}^T\frac{1}{2}(\tilde{\mathbf{A}}-(1-\beta)\mathbf{S}_2|\mathbf{A}_2|-\frac{C}{h}\mathbf{S}_2)\mathbf{U}_{2,h}^{+}+\mathbf{U}_{2,h}^{-}{}^T\frac{1}{2}(\tilde{\mathbf{A}}+(1-\beta)\mathbf{S}_2|\mathbf{A}_2|+\frac{C}{h}\mathbf{S}_2)\mathbf{U}_{2,h}^{-}\right)|_{x=x_j}$$
$$-\sum_{j=l+1}^{N-1}\left(\mathbf{U}_{2,h}^{+}{}^T\frac{1}{2}(\tilde{\mathbf{A}}-(1-\beta)\mathbf{S}_2|\mathbf{A}_2|-\frac{C}{h}\mathbf{S}_2)\mathbf{U}_{2,h}^{+}+\mathbf{U}_{2,h}^{+}{}^T\frac{1}{2}(\tilde{\mathbf{A}}+(1-\beta)\mathbf{S}_2|\mathbf{A}_2|+\frac{C}{h}\mathbf{S}_2)\mathbf{U}_{2,h}^{-}\right)|_{x=x_j}$$
$$-\sum_{j=1}^{l}\frac{1}{2}\mathbf{U}_{1,h}^{-}{}^T\tilde{\mathbf{A}}\mathbf{U}_{1,h}^{-}|_{x=x_j}+\sum_{j=1}^{l}\frac{1}{2}\mathbf{U}_{1,h}^{+}{}^T\tilde{\mathbf{A}}\mathbf{U}_{1,h}^{+}|_{x=x_j}-\sum_{j=l+1}^{N-1}\frac{1}{2}\mathbf{U}_{2,h}^{-}{}^T\tilde{\mathbf{A}}\mathbf{U}_{2,h}^{-}|_{x=x_j}$$
$$+\sum_{j=l+1}^{N-1}\frac{1}{2}\mathbf{U}_{2,h}^{+}{}^T\tilde{\mathbf{A}}\mathbf{U}_{2,h}^{+}|_{x=x_j}=0. \tag{2.5.19}$$

All the terms $\mathbf{U}_{i,h}^{-}{}^T\tilde{\mathbf{A}}\mathbf{U}_{i,h}^{-}|_{x=x_j}$, $\mathbf{U}_{i,h}^{-}{}^T\tilde{\mathbf{A}}\mathbf{U}_{i,h}^{+}|_{x=x_j}$, $\mathbf{U}_{i,h}^{+}{}^T\tilde{\mathbf{A}}\mathbf{U}_{i,h}^{-}|_{x=x_j}$ $\mathbf{U}_{i,h}^{+}{}^T\tilde{\mathbf{A}}\mathbf{U}_{i,h}^{+}|_{x=x_j}$ cancel each other to obtain

$$\sum_{j=0}^{l-1}\int_{x_j}^{x_{j+1}} \mathbf{U}_{1,h}^T\mathbf{S}_1\frac{\partial \mathbf{U}_{1,h}}{\partial t}dx+\int_{x_l}^{\alpha} \mathbf{U}_{1,h}^T\mathbf{S}_1\frac{\partial \mathbf{U}_{1,h}}{\partial t}dx+\int_{\alpha}^{x_{l+1}} \mathbf{U}_{2,h}^T\mathbf{S}_2\frac{\partial \mathbf{U}_{2,h}}{\partial t}dx$$
$$+\sum_{j=l+1}^{N-1}\int_{x_j}^{x_{j+1}} \mathbf{U}_{2,h}^T\mathbf{S}_2\frac{\partial \mathbf{U}_{2,h}}{\partial t}dx \tag{2.5.20}$$
$$+\sum_{j=1}^{l}\left(-\mathbf{U}_{1,h}^{-}{}^T\frac{1}{2}((1-\beta)\mathbf{S}_1|\mathbf{A}_1|+\frac{C}{h}\mathbf{S}_1)\mathbf{U}_{1,h}^{+}+\mathbf{U}_{1,h}^{-}{}^T\frac{1}{2}((1-\beta)\mathbf{S}_1|\mathbf{A}_1|+\frac{C}{h}\mathbf{S}_1)\mathbf{U}_{1,h}^{-}\right)|_{x=x_j}$$
$$+\sum_{j=1}^{l}\left(\mathbf{U}_{1,h}^{+}{}^T\frac{1}{2}((1-\beta)\mathbf{S}_1|\mathbf{A}_1|+\frac{C}{h}\mathbf{S}_1)\mathbf{U}_{1,h}^{+}-\mathbf{U}_{1,h}^{+}{}^T\frac{1}{2}((1-\beta)\mathbf{S}_1|\mathbf{A}_1|+\frac{C}{h}\mathbf{S}_1)\mathbf{U}_{1,h}^{-}\right)|_{x=x_j}$$
$$+\sum_{j=l+1}^{N-1}\left(-\mathbf{U}_{2,h}^{-}{}^T\frac{1}{2}((1-\beta)\mathbf{S}_2|\mathbf{A}_2|+\frac{C}{h}\mathbf{S}_2)\mathbf{U}_{2,h}^{+}+\mathbf{U}_{2,h}^{-}{}^T\frac{1}{2}((1-\beta)\mathbf{S}_2|\mathbf{A}_2|+\frac{C}{h}\mathbf{S}_2)\mathbf{U}_{2,h}^{-}\right)|_{x=x_j}$$
$$+\sum_{j=l+1}^{N-1}\left(\mathbf{U}_{2,h}^{+}{}^T\frac{1}{2}((1-\beta)\mathbf{S}_2|\mathbf{A}_2|+\frac{C}{h}\mathbf{S}_2)\mathbf{U}_{2,h}^{+}-\mathbf{U}_{2,h}^{+}{}^T\frac{1}{2}((1-\beta)\mathbf{S}_2|\mathbf{A}_2|+\frac{C}{h}\mathbf{S}_2)\mathbf{U}_{2,h}^{-}\right)|_{x=x_j}=0.$$

Factoring the last four terms yields

$$\sum_{j=0}^{l-1}\int_{x_j}^{x_{j+1}}\mathbf{U}_{1,h}^T\mathbf{S}_1\frac{\partial\mathbf{U}_{1,h}}{\partial t}dx+\int_{x_l}^{\alpha}\mathbf{U}_{1,h}^T\mathbf{S}_1\frac{\partial\mathbf{U}_{1,h}}{\partial t}dx+\int_{\alpha}^{x_{l+1}}\mathbf{U}_{2,h}^T\mathbf{S}_2\frac{\partial\mathbf{U}_{2,h}}{\partial t}dx$$
$$+\sum_{j=l+1}^{N-1}\int_{x_j}^{x_{j+1}}\mathbf{U}_{2,h}^T\mathbf{S}_2\frac{\partial\mathbf{U}_{2,h}}{\partial t}dx$$
$$+\sum_{j=1}^{l}\left((\mathbf{U}_{1,h}^+-\mathbf{U}_{1,h}^-)^T\frac{1}{2}((1-\beta)\mathbf{S}_1|\mathbf{A}_1|+\frac{C}{h}\mathbf{S}_1)(\mathbf{U}_{1,h}^+-\mathbf{U}_{1,h}^-)\right)|_{x=x_j} \tag{2.5.21}$$
$$+\sum_{j=l+1}^{N-1}\left((\mathbf{U}_{2,h}^+-\mathbf{U}_{2,h}^-)^T\frac{1}{2}((1-\beta)\mathbf{S}_2|\mathbf{A}_2|+\frac{C}{h}\mathbf{S}_2)(\mathbf{U}_{2,h}^+-\mathbf{U}_{2,h}^-)\right)|_{x=x_j}=0.$$

Using the notation $[\mathbf{U}_i]_j=(\mathbf{U}_{i,h}^+-\mathbf{U}_{i,h}^-)\,|_{x=x_j}$ for $i=1,2$, we write

$$\sum_{j=0}^{l-1}\int_{x_j}^{x_{j+1}}\mathbf{U}_{1,h}^T\mathbf{S}_1\frac{\partial\mathbf{U}_{1,h}}{\partial t}dx+\int_{x_l}^{\alpha}\mathbf{U}_{1,h}^T\mathbf{S}_1\frac{\partial\mathbf{U}_{1,h}}{\partial t}dx+\int_{\alpha}^{x_{l+1}}\mathbf{U}_{2,h}^T\mathbf{S}_2\frac{\partial\mathbf{U}_{2,h}}{\partial t}dx$$
$$+\sum_{j=l+1}^{N-1}\int_{x_j}^{x_{j+1}}\mathbf{U}_{2,h}^T\mathbf{S}_2\frac{\partial\mathbf{U}_{2,h}}{\partial t}dx+\sum_{j=1}^{l}\left([\mathbf{U}_{1,h}]_j^T\frac{1}{2}((1-\beta)\mathbf{S}_1|\mathbf{A}_1|+\frac{C}{h}\mathbf{S}_1)[\mathbf{U}_{1,h}]_j\right)$$
$$+\sum_{j=l+1}^{N-1}\left([\mathbf{U}_{2,h}]_j^T\frac{1}{2}((1-\beta)\mathbf{S}_2|\mathbf{A}_2|+\frac{C}{h}\mathbf{S}_2)[\mathbf{U}_{2,h}]_j\right)=0. \tag{2.5.22}$$

Since C is nonnegative, h is the mesh size, $0\le\beta\le1$, $\mathbf{S}_i$ and $\mathbf{S}_i|\mathbf{A}_i|$ for $i=1,2$ are positive symmetric definite, we have

$$[\mathbf{U}_{i,h}]_j^T\frac{1}{2}((1-\beta)\mathbf{S}_i|\mathbf{A}_i|+\frac{C}{h}\mathbf{S}_i)[\mathbf{U}_{i,h}]_j\ge0,\quad\text{for } i=1,2. \tag{2.5.23}$$

Thus we get

$$\sum_{j=0}^{l-1}\frac{1}{2}\frac{\partial}{\partial t}\int_{x_j}^{x_{j+1}}\mathbf{U}_{1,h}^T\mathbf{S}_1\mathbf{U}_{1,h}dx+\frac{1}{2}\frac{\partial}{\partial t}\int_{x_l}^{\alpha}\mathbf{U}_{1,h}^T\mathbf{S}_1\mathbf{U}_{1,h}dx+\frac{1}{2}\frac{\partial}{\partial t}\int_{\alpha}^{x_{l+1}}\mathbf{U}_{2,h}^T\mathbf{S}_2\mathbf{U}_{2,h}dx$$
$$+\sum_{j=l+1}^{N-1}\frac{1}{2}\frac{\partial}{\partial t}\int_{x_j}^{x_{j+1}}\mathbf{U}_{2,h}^T\mathbf{S}_2\mathbf{U}_{2,h}dx\le0. \tag{2.5.24}$$

This implies

$$\frac{\partial}{\partial t}\epsilon_h(t)\le0. \tag{2.5.25}$$

Integrating over time $[t_0, t]$ completes the proof. $\square$

We note that if $\beta = 1$ and $C = 0$, then

$$\frac{\partial}{\partial t}\epsilon_h(t) = 0. \tag{2.5.26}$$

2.5.2 A Computational Stability Study

We perform a computational stability study for the three methods applied to the acoustic problem (2.1.1) on the interval $[40, 140]$ with periodic boundary conditions (2.3.28) using a uniform mesh having 50 elements and plot the eigenvalues of $\mathbf{A}_{h,q}^{G}$, $\mathbf{A}_{h,q}^{GS}$ and $\mathbf{A}_{h,q}^{PG}$ in (2.3.8), (2.3.18) and (2.3.29), respectively. In order to investigate the advantages and disadvantages of each method, we present eigenvalues with various parameters, interface positions and fluxes. Spectrum distributions are presented for three centered ($\beta = 1$), partially upwind ($\beta = 0.5$) and fully upwind flux ($\beta = 0$), respectively, with the maximum real part of eigenvalues. The penalty term is zero unless indicated otherwise.

In order to show the effect of varying c and ρ, and the effect of linear IFE and standard linear Lagrange spaces for homogeneous media, we consider two media, the first one with $c_1 = 1m/s$ and $\rho_1 = 1kg/m^3$ and refer to it by med1 and the second one with $c_2 = 1.5m/s$ and $\rho_2 = 2kg/m^3$ and refer to it by med2. For instance, the interface problem where med1 occupies I_1 and med2 occupies I_2 will be referred to as med1/med2. The interface point is $96.3m$ and linear IFE spaces and standard Lagrange spaces are used. We present the eigenvalues of the matrices $\mathbf{A}_{h,q}^{G}$, $\mathbf{A}_{h,q}^{GS}$ and $\mathbf{A}_{h,q}^{PG}$ in Figures 2.5.1, 2.5.2, 2.5.3, 2.5.4 and 2.5.5.

For homogeneous problem med1/med1, linear IFE and standard Lagrange spaces yield circular spectrum in Figures 2.5.1, 2.5.2. In Figure 2.5.3 we present the spectrum for med2/med2 problem and in Figure 2.5.4 we present the spectrum for med1/med2 interface problem where the small circle corresponds to med1 and large circle corresponds to med2. We plot spectrum for med1/med1, med2/med2 and med1/med2 in Figure 2.5.5.

We repeat the previous experiments for the water/water, air/air and water/air acoustic problems and plot the spectra in Figures 2.5.6, 2.5.7, 2.5.8, 2.5.9 and 2.5.10. We observe similar behavior above. We observe that IDG method applied to the scaled problem is very inefficient especially for water/air problem since the eigenvalues of $\mathbf{A}_{h,q}^{GS}$ are very large ($-3\ 10^9$ for $\beta = 0.5$, $-7\ 10^9$ for $\beta = 0$) as shown in Figure 2.5.9.

Figure 2.5.11 shows the eigenvalues for the acoustic problem water/air with interface $\alpha = 96m$, a fitted mesh. There is no interface element since $\alpha = 96m$ is a mesh point which implies that the three methods with three fluxes are stable. The spectra shown in Figure 2.5.11 are different from those of Figure 2.5.9 especially for $\mathbf{A}_{h,q}^{G}$. We observe additional two eigenvalues of $\mathbf{A}_{h,q}^{G}$ with $\beta = 0$ in Figure 2.5.9 by comparing with Figure 2.5.11.

In order to show the effect of the penalty term, we consider two media, the first one with

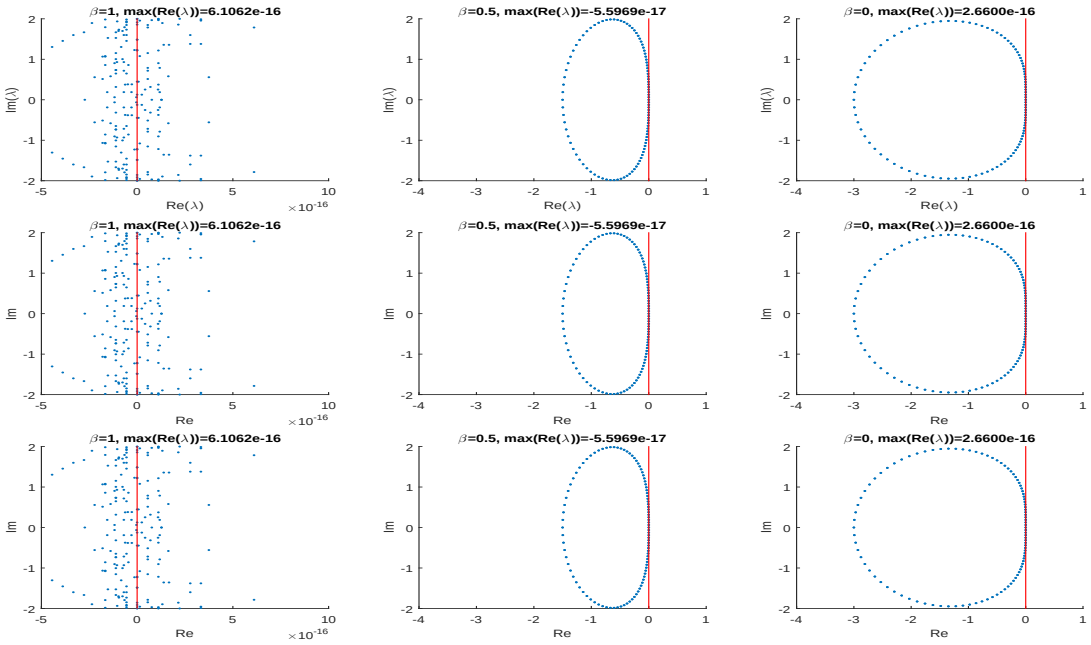

Figure 2.5.1: Eigenvalues of $\mathbf{A}_{h,q}^{G}$ (top), $\mathbf{A}_{h,q}^{GS}$ (middle), $\mathbf{A}_{h,q}^{PG}$ (bottom) with $\beta = 1$ (left), $\beta = 0.5$ (center), $\beta = 0$ (right) for linear IFE spaces for med1/med1 problem.

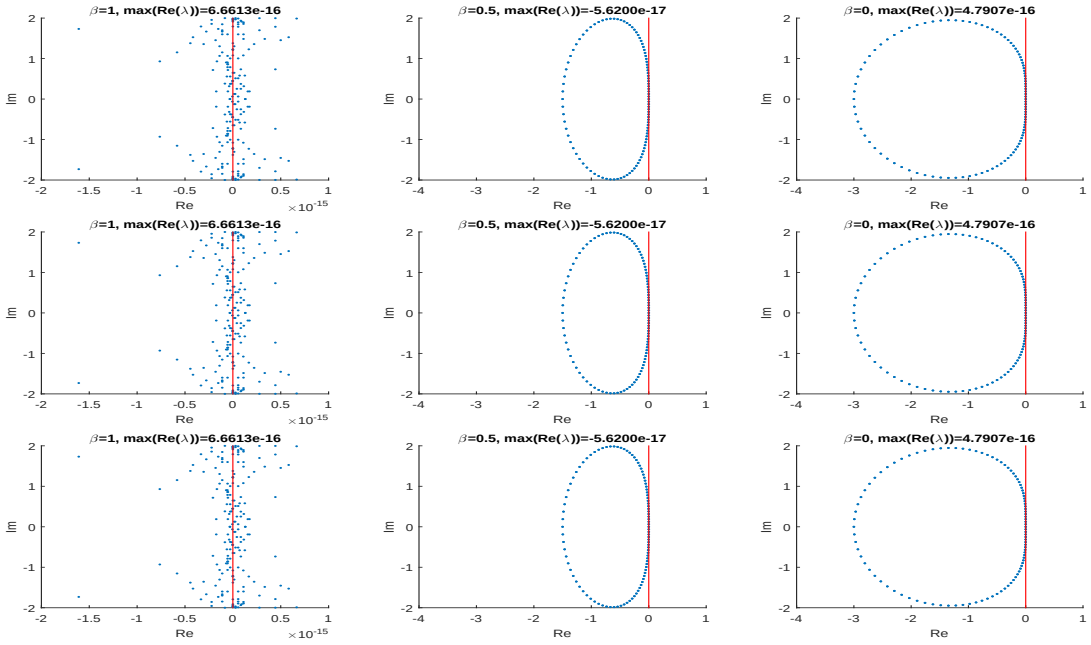

Figure 2.5.2: Eigenvalues of $\mathbf{A}_{h,q}^{G}$ (top), $\mathbf{A}_{h,q}^{GS}$ (middle), $\mathbf{A}_{h,q}^{PG}$ (bottom) with $\beta = 1$ (left), $\beta = 0.5$ (center), $\beta = 0$ (right) for standard linear Lagrange spaces for med1/med1 problem.

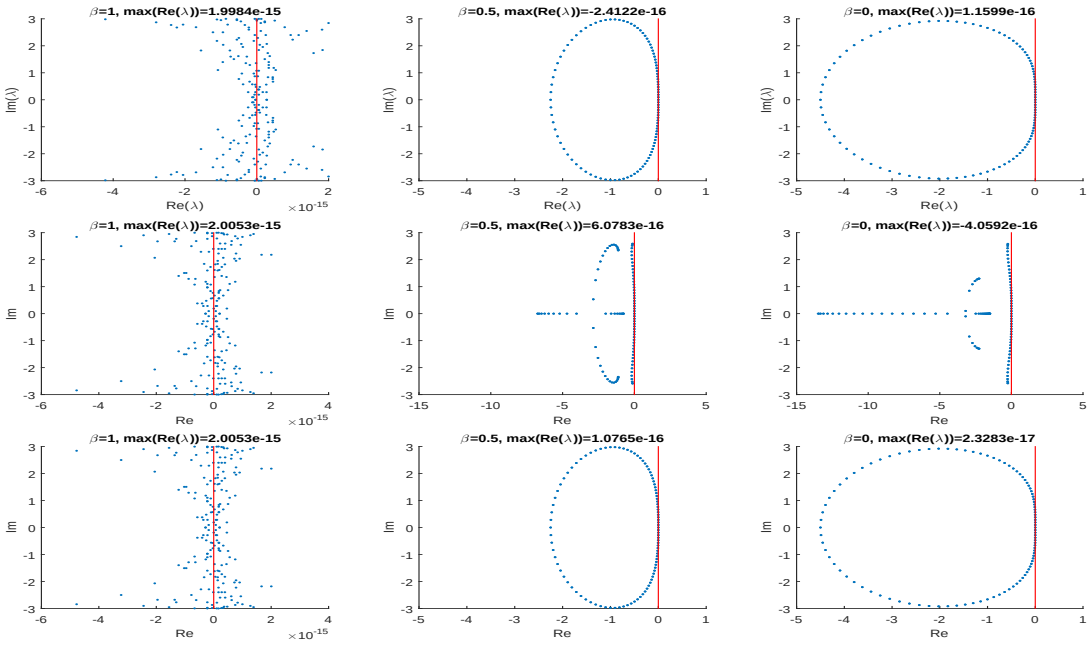

Figure 2.5.3: Eigenvalues of $\mathbf{A}_{h,q}^{G}$ (top), $\mathbf{A}_{h,q}^{GS}$ (middle), $\mathbf{A}_{h,q}^{PG}$ (bottom) with $\beta = 1$ (left), $\beta = 0.5$ (center), $\beta = 0$ (right) for med2/med2 problem.

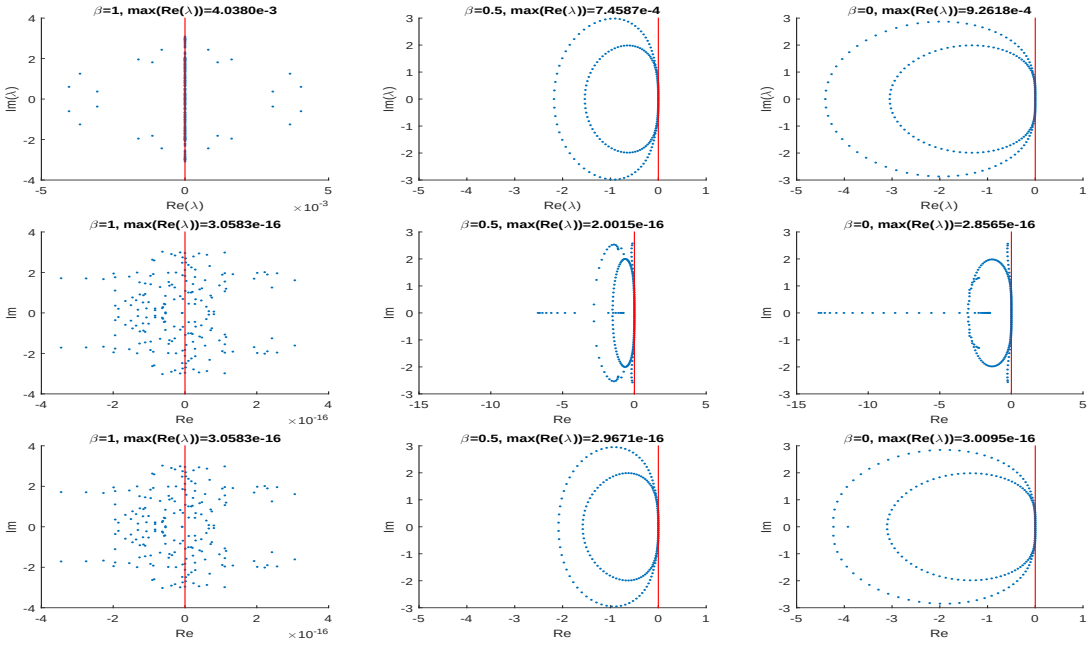

Figure 2.5.4: Eigenvalues of $\mathbf{A}_{h,q}^{G}$ (top), $\mathbf{A}_{h,q}^{GS}$ (middle), $\mathbf{A}_{h,q}^{PG}$ (bottom) with $\beta = 1$ (left), $\beta = 0.5$ (center), $\beta = 0$ (right) for med1/med2 problem.

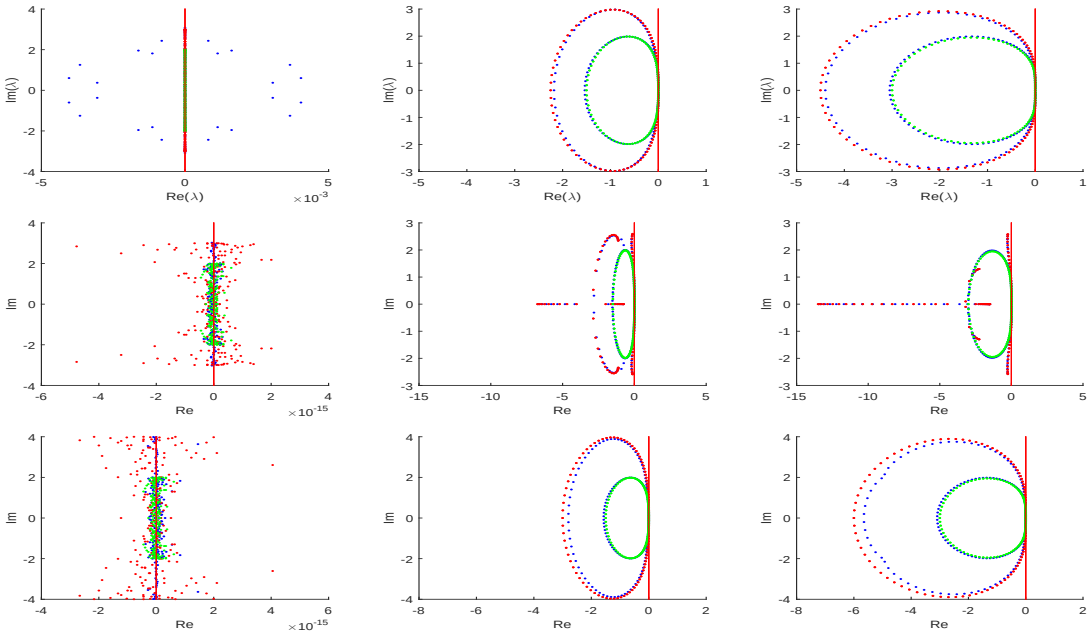

Figure 2.5.5: Eigenvalues of $\mathbf{A}_{h,q}^{G}$ (top), $\mathbf{A}_{h,q}^{GS}$ (middle), $\mathbf{A}_{h,q}^{PG}$ (bottom) with $\beta = 1$ (left), $\beta = 0.5$ (center), $\beta = 0$ (right), med1/med1 (green), med2/med2 (red), med1/med2 (blue) problems.

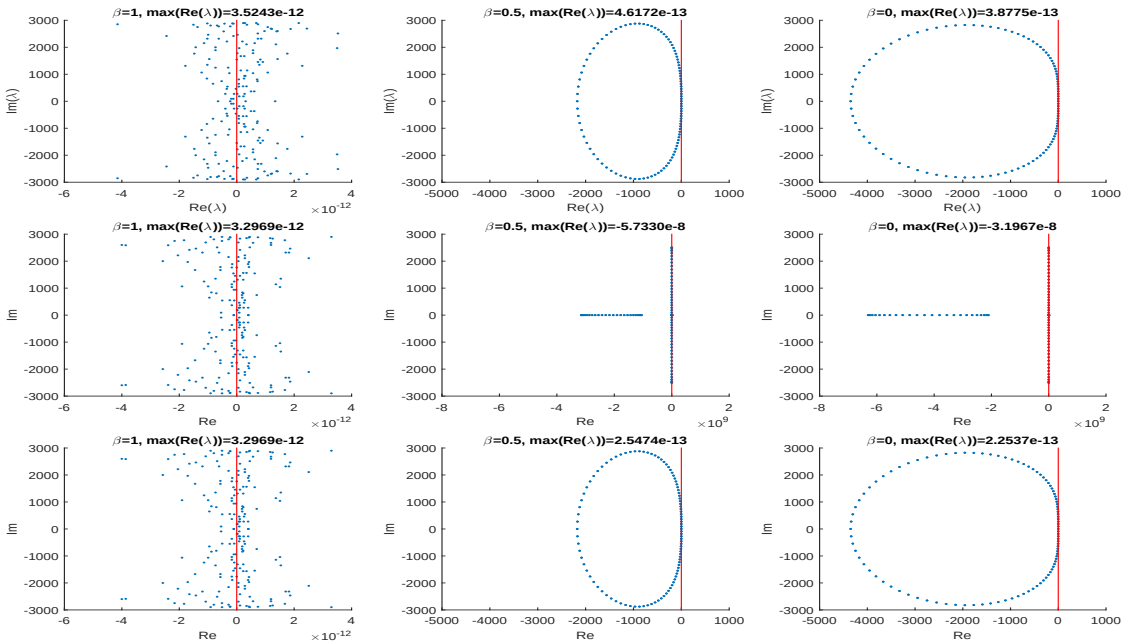

Figure 2.5.6: Eigenvalues of $\mathbf{A}_{h,q}^{G}$ (top), $\mathbf{A}_{h,q}^{GS}$ (middle), $\mathbf{A}_{h,q}^{PG}$ (bottom) with $\beta = 1$ (left), $\beta = 0.5$ (center), $\beta = 0$ (right) for linear IFE spaces for water/water problem.

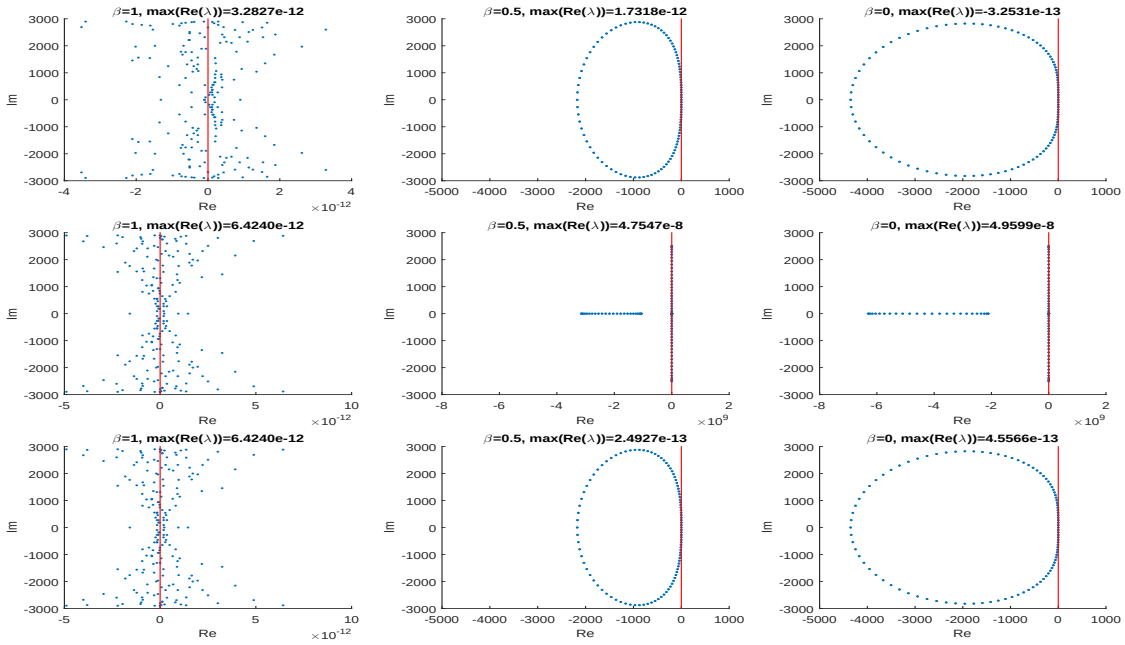

Figure 2.5.7: Eigenvalues of $\mathbf{A}_{h,q}^{G}$ (top), $\mathbf{A}_{h,q}^{GS}$ (middle), $\mathbf{A}_{h,q}^{PG}$ (bottom) with $\beta = 1$ (left), $\beta = 0.5$ (center), $\beta = 0$ (right) for standard linear Lagrange spaces for water/water problem.

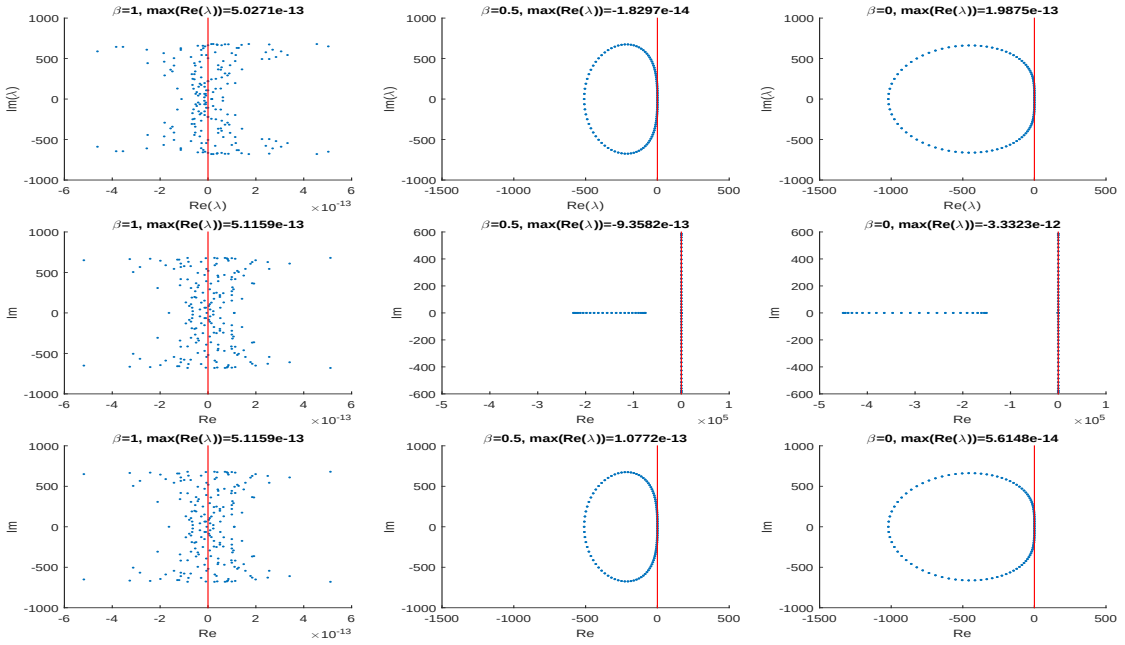

Figure 2.5.8: Eigenvalues of $\mathbf{A}_{h,q}^{G}$ (top), $\mathbf{A}_{h,q}^{GS}$ (middle), $\mathbf{A}_{h,q}^{PG}$ (bottom) with $\beta = 1$ (left), $\beta = 0.5$ (center), $\beta = 0$ (right) for air/air problem.

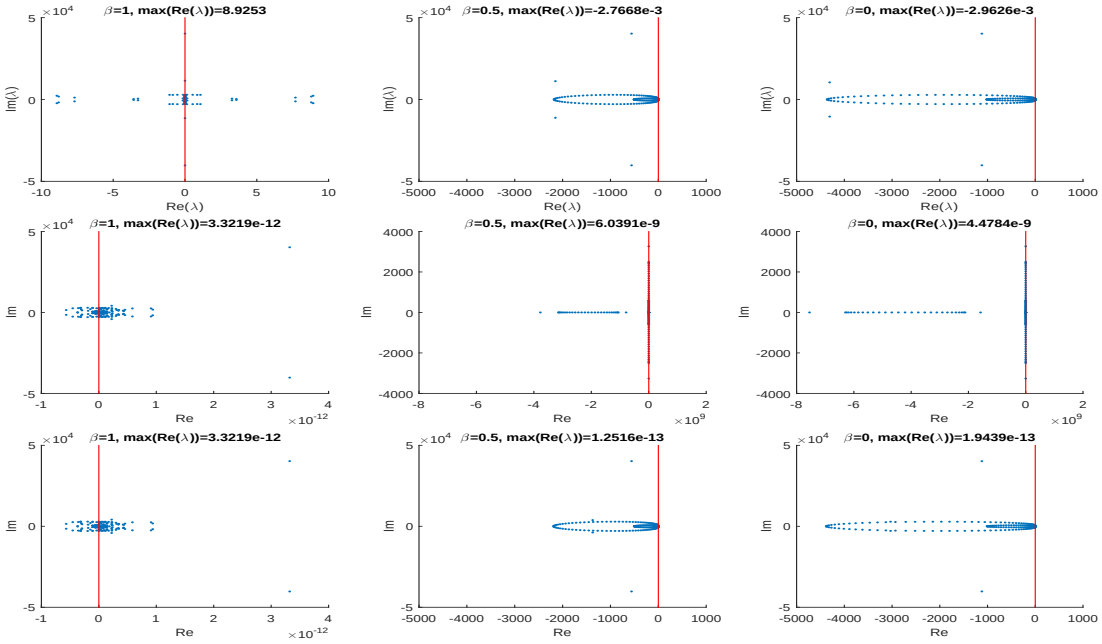

Figure 2.5.9: Eigenvalues of $\mathbf{A}_{h,q}^{G}$ (top), $\mathbf{A}_{h,q}^{GS}$ (middle), $\mathbf{A}_{h,q}^{PG}$ (bottom) with $\beta = 1$ (left), $\beta = 0.5$ (center), $\beta = 0$ (right) for water/air problem.

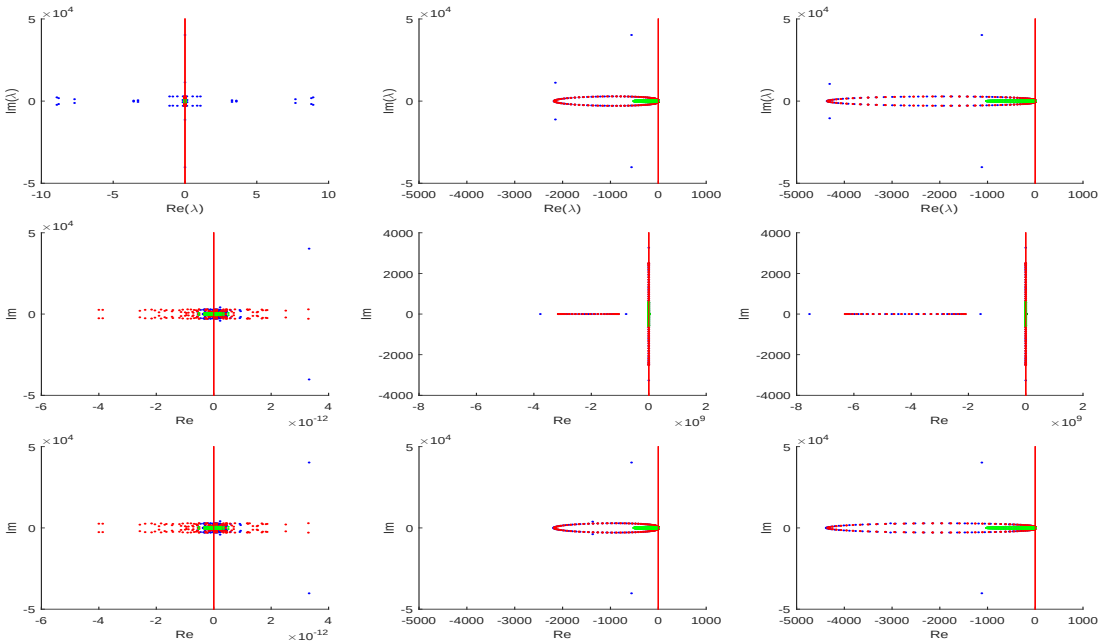

Figure 2.5.10: Eigenvalues of $\mathbf{A}_{h,q}^{G}$ (top), $\mathbf{A}_{h,q}^{GS}$ (middle), $\mathbf{A}_{h,q}^{PG}$ (bottom) with $\beta = 1$ (left), $\beta = 0.5$ (center), $\beta = 0$ (right), water/water (red), air/air (green), water/air (blue) for problems.

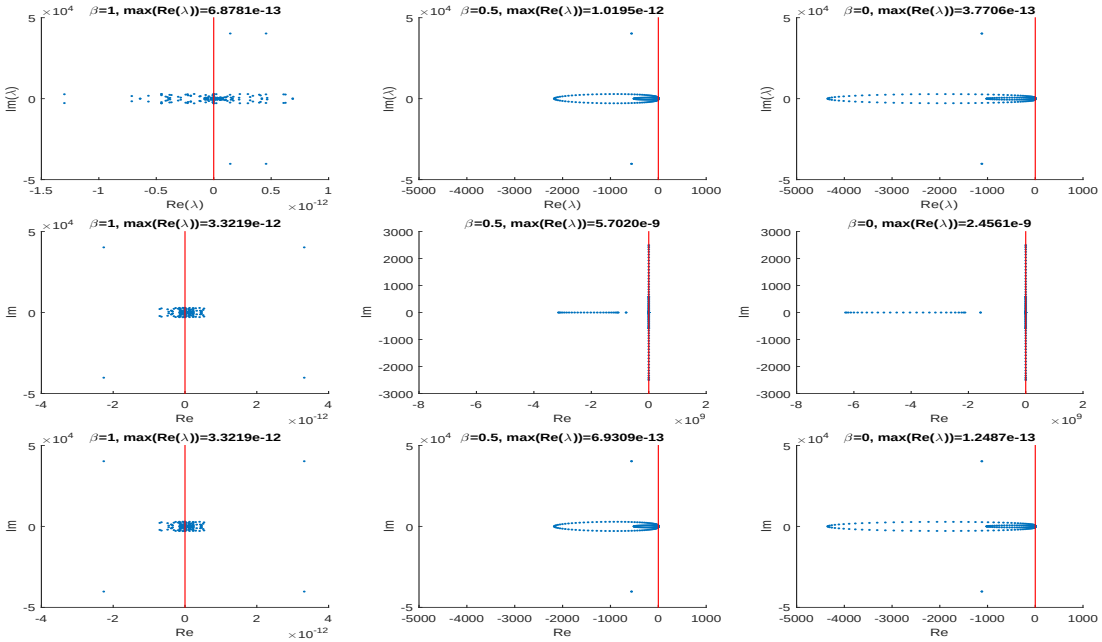

Figure 2.5.11: Eigenvalues of $\mathbf{A}_{h,q}^{G}$ (top), $\mathbf{A}_{h,q}^{GS}$ (middle), $\mathbf{A}_{h,q}^{PG}$ (bottom) with $\beta = 1$ (left), $\beta = 0.5$ (center), $\beta = 0$ (right) for water/air problem on a fitted mesh.

$c_1 = 1m/s$, $\rho_1 = 2kg/m^3$ and refer to it by med3 and the second one with $c_2 = 1.5m/s$, $\rho_2 = 4.5kg/m^3$ and refer to it by med4 with $\alpha = 96.3m$. We use linear IFE spaces and show the spectra in Figures 2.5.12, 2.5.13, 2.5.14 and 2.5.15 for $C = 0$, 1, 10, 100. We see that the spectra is moved to the left with increasing C which means more dissipation.

We consider the acoustic problem med3/med4 for various interface points α. We plot the eigenvalues of $\mathbf{A}_{h,q}^{G}$, $\mathbf{A}_{h,q}^{GS}$ and $\mathbf{A}_{h,q}^{PG}$ in Figures 2.5.16, 2.5.17, 2.5.18 and 2.5.19 for $\alpha = 96.3$, 96.8, 97.3 and $97.8m$. The interface points $\alpha = 96.3$, 96.8, 97.3, 97.8 on the physical element (x_l, x_{l+1}) are mapped to $\hat{\alpha} = -0.7, -0.2, 0.3, 0.8$ onto the reference element $(-1, 1)$. So, the interface point α moves within one interface element and the number of elements of med3 and med4 remain the same. We observe a small changes in the eigenvalues.

Figures 2.5.20, 2.5.21, 2.5.22 and 2.5.23 for the interface $\alpha = 56.3$, 76.3, 96.3 and $116.3m$ suggest that as the interface point α moves on the domain, the number of eigenvalues on the circle changes. We see that the spectrum of $\mathbf{A}_{h,q}^{G}$, $\mathbf{A}_{h,q}^{GS}$ and $\mathbf{A}_{h,q}^{PG}$ is moved from large circle to small circle with increasing α since the number of elements of medium 1 increases and the number of elements of medium 2 decreases which implies that the small circle is a set of eigenvalues for med3 and the large circle is a set of eigenvalues for med4.

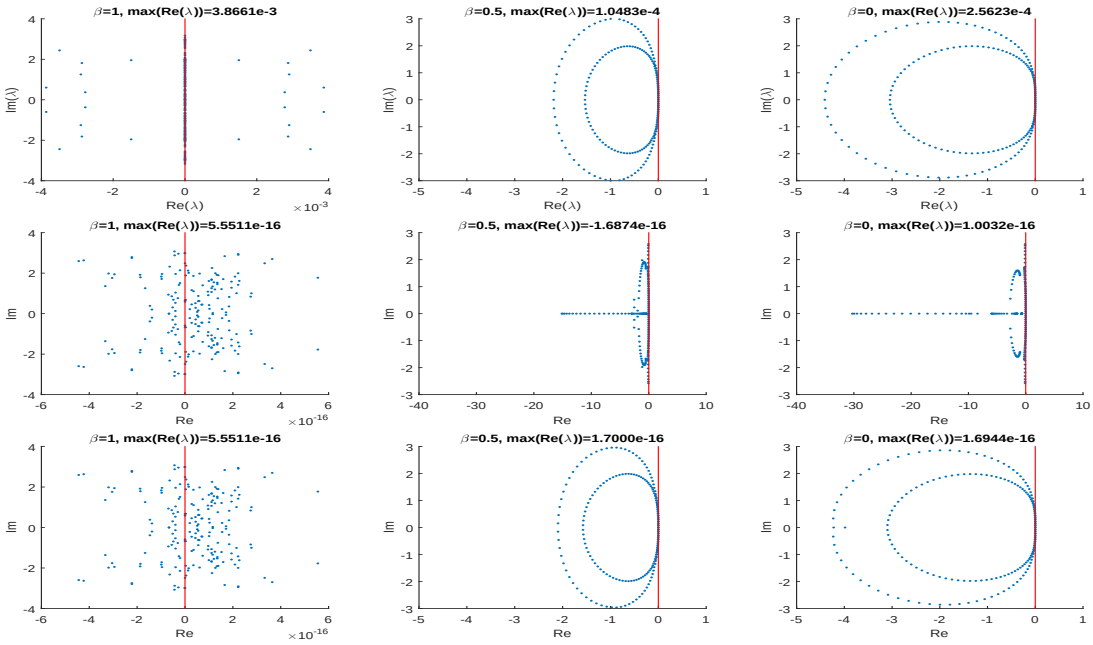

Figure 2.5.12: Eigenvalues of $\mathbf{A}_{h,q}^{G}$ (top), $\mathbf{A}_{h,q}^{GS}$ (middle), $\mathbf{A}_{h,q}^{PG}$ (bottom) with $\beta = 1$ (left), $\beta = 0.5$ (center), $\beta = 0$ (right) and $C = 0$ for med3/med4 problem.

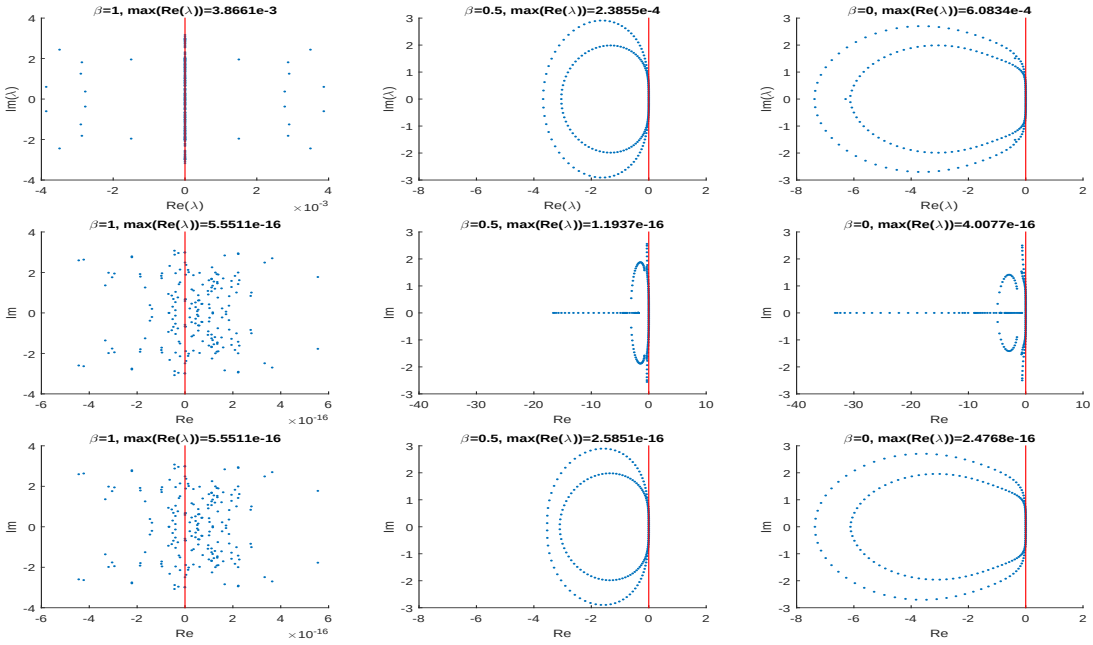

Figure 2.5.13: Eigenvalues of $\mathbf{A}_{h,q}^{G}$ (top), $\mathbf{A}_{h,q}^{GS}$ (middle), $\mathbf{A}_{h,q}^{PG}$ (bottom) with $\beta = 1$ (left), $\beta = 0.5$ (center), $\beta = 0$ (right) and $C = 1$ for med3/med4 problem.

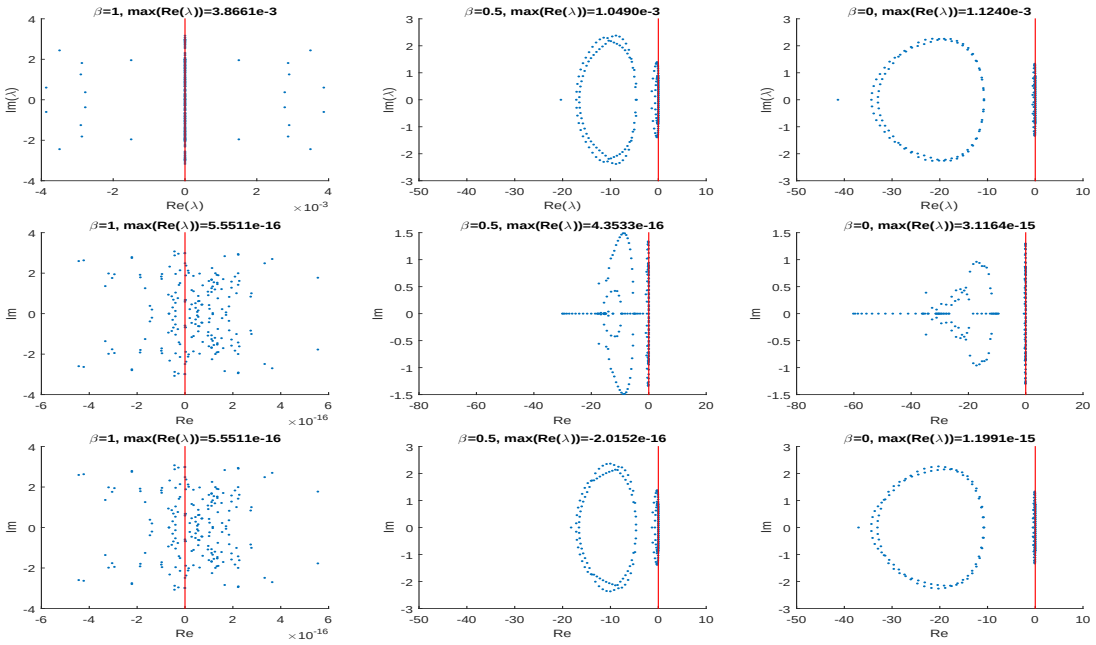

Figure 2.5.14: Eigenvalues of $\mathbf{A}_{h,q}^{G}$ (top), $\mathbf{A}_{h,q}^{GS}$ (middle), $\mathbf{A}_{h,q}^{PG}$ (bottom) with $\beta = 1$ (left), $\beta = 0.5$ (center), $\beta = 0$ (right) and $C = 10$ for med3/med4 problem.

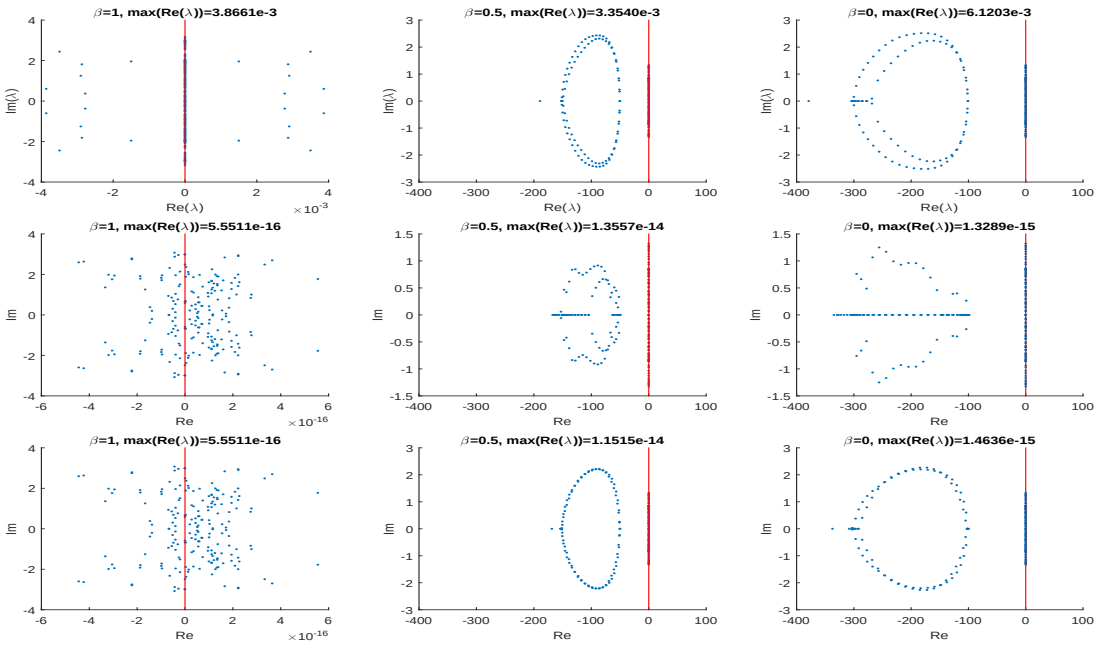

Figure 2.5.15: Eigenvalues of $\mathbf{A}_{h,q}^{G}$ (top), $\mathbf{A}_{h,q}^{GS}$ (middle), $\mathbf{A}_{h,q}^{PG}$ (bottom) with $\beta = 1$ (left), $\beta = 0.5$ (center), $\beta = 0$ (right) and $C = 100$ for med3/med4 problem.

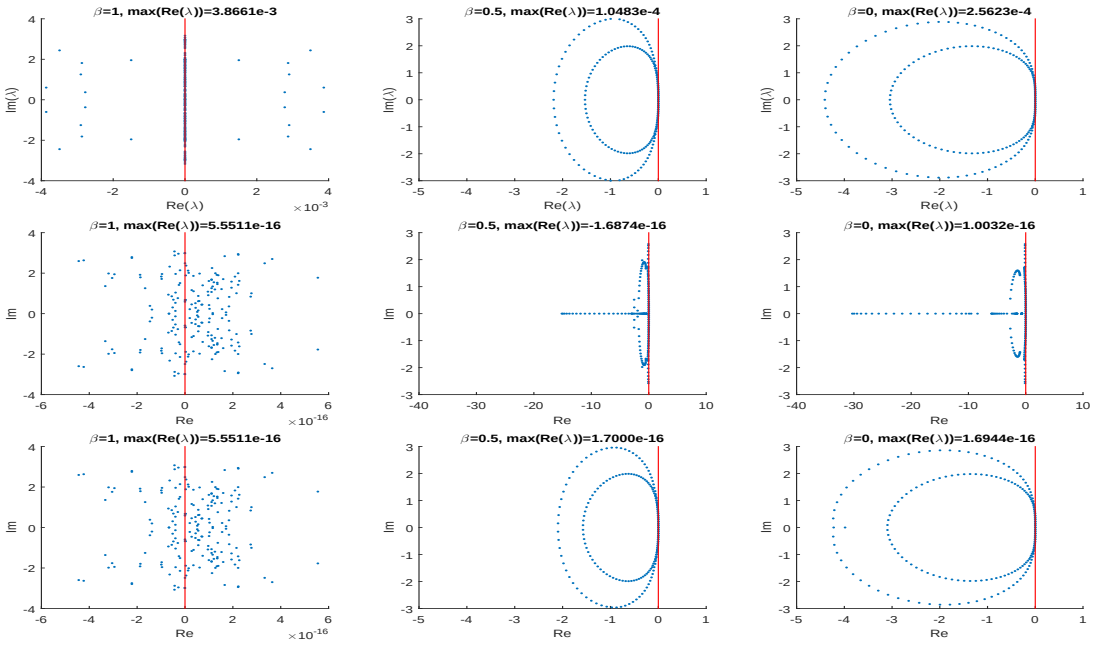

Figure 2.5.16: Eigenvalues of $\mathbf{A}_{h,q}^{G}$ (top), $\mathbf{A}_{h,q}^{GS}$ (middle), $\mathbf{A}_{h,q}^{PG}$ (bottom) with $\beta = 1$ (left), $\beta = 0.5$ (center), $\beta = 0$ (right) and $\alpha = 96.3m$ for med3/med4 problem.

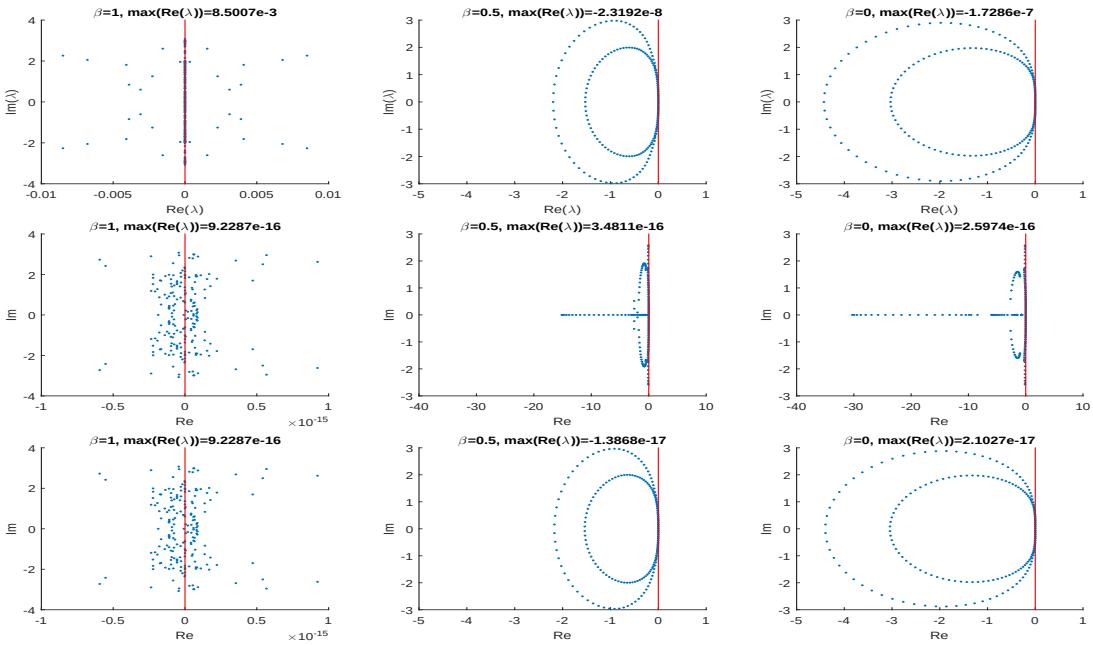

Figure 2.5.17: Eigenvalues of $\mathbf{A}_{h,q}^{G}$ (top), $\mathbf{A}_{h,q}^{GS}$ (middle), $\mathbf{A}_{h,q}^{PG}$ (bottom) with $\beta = 1$ (left), $\beta = 0.5$ (center), $\beta = 0$ (right) and $\alpha = 96.8m$ for med3/med4 problem.

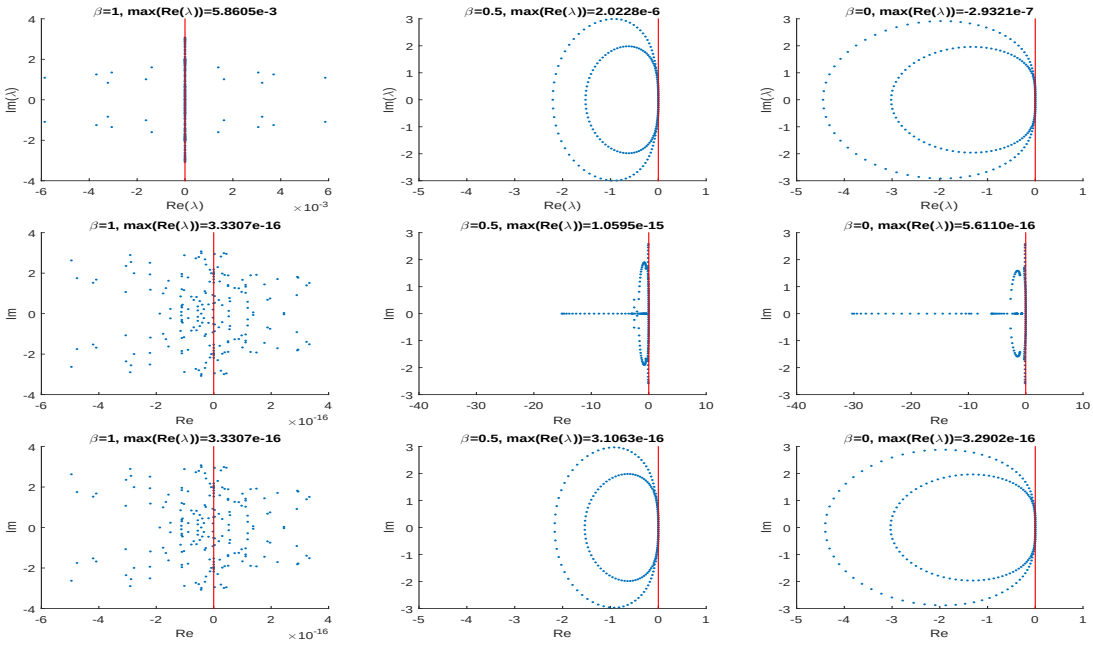

Figure 2.5.18: Eigenvalues of $\mathbf{A}_{h,q}^{G}$ (top), $\mathbf{A}_{h,q}^{GS}$ (middle), $\mathbf{A}_{h,q}^{PG}$ (bottom) with $\beta = 1$ (left), $\beta = 0.5$ (center), $\beta = 0$ (right) and $\alpha = 97.3m$ for med3/med4 problem.

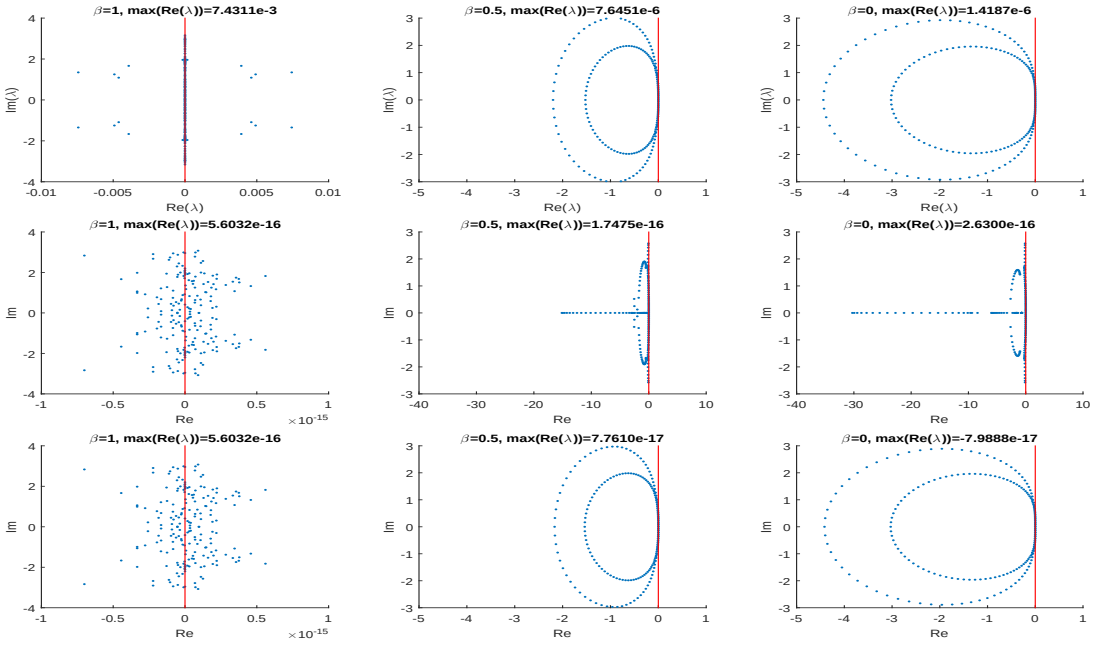

Figure 2.5.19: Eigenvalues of $\mathbf{A}_{h,q}^{G}$ (top), $\mathbf{A}_{h,q}^{GS}$ (middle), $\mathbf{A}_{h,q}^{PG}$ (bottom) with $\beta = 1$ (left), $\beta = 0.5$ (center), $\beta = 0$ (right) and $\alpha = 97.8m$ for med3/med4 problem.

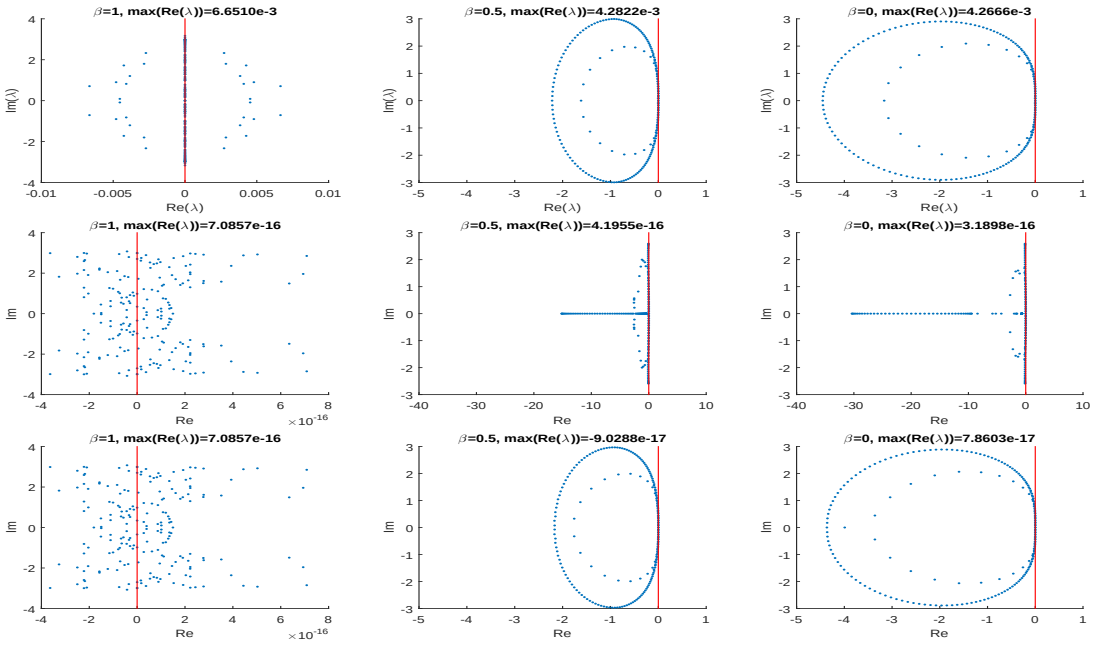

Figure 2.5.20: Eigenvalues of $\mathbf{A}_{h,q}^{G}$ (top), $\mathbf{A}_{h,q}^{GS}$ (middle), $\mathbf{A}_{h,q}^{PG}$ (bottom) with $\beta = 1$ (left), $\beta = 0.5$ (center), $\beta = 0$ (right) and $\alpha = 56.3m$ for med3/med4 problem.

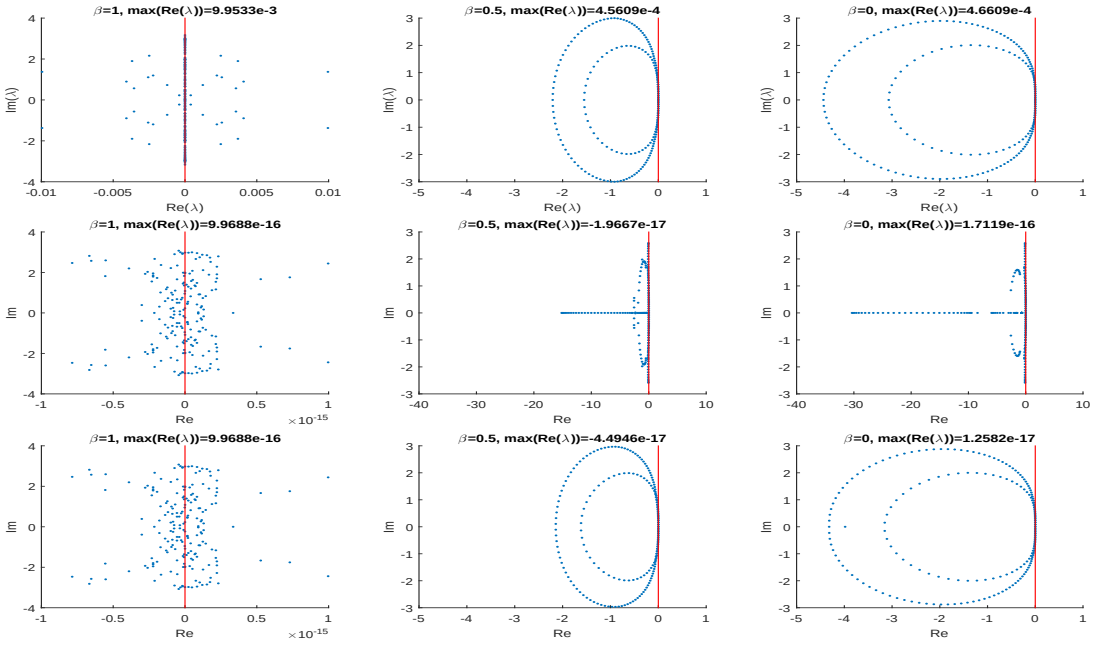

Figure 2.5.21: Eigenvalues of $\mathbf{A}_{h,q}^{G}$ (top), $\mathbf{A}_{h,q}^{GS}$ (middle), $\mathbf{A}_{h,q}^{PG}$ (bottom) with $\beta = 1$ (left), $\beta = 0.5$ (center), $\beta = 0$ (right) and $\alpha = 76.3m$ for med3/med4 problem.

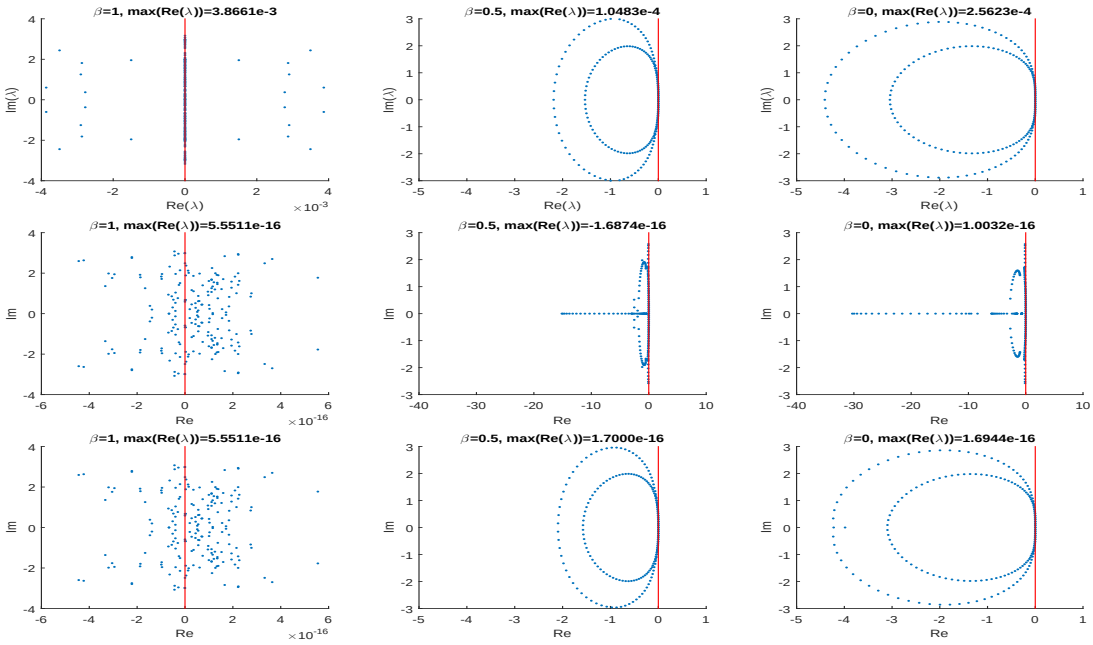

Figure 2.5.22: Eigenvalues of $\mathbf{A}_{h,q}^{G}$ (top), $\mathbf{A}_{h,q}^{GS}$ (middle), $\mathbf{A}_{h,q}^{PG}$ (bottom) with $\beta = 1$ (left), $\beta = 0.5$ (center), $\beta = 0$ (right) and $\alpha = 96.3m$ for med3/med4 problem.

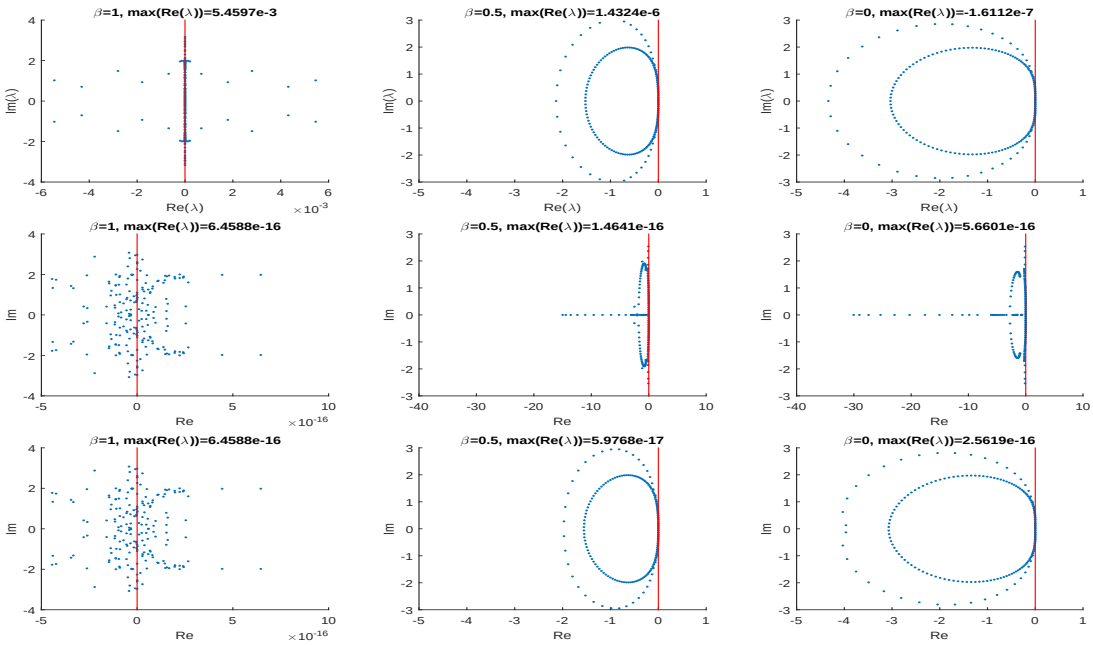

Figure 2.5.23: Eigenvalues of $\mathbf{A}_{h,q}^{G}$ (top), $\mathbf{A}_{h,q}^{GS}$ (middle), $\mathbf{A}_{h,q}^{PG}$ (bottom) with $\beta = 1$ (left), $\beta = 0.5$ (center), $\beta = 0$ (right) and $\alpha = 116.3m$ for med3/med4 problem.

Chapter 3

IFE Spaces for the Two Dimensional Acoustic Problem

In this chapter, we present immersed finite element spaces for two dimensional problems. We first state the two dimensional interface problem.

3.1 Problem Statement

Let p and $\mathbf{v} = [u, v]^T$, respectively, be the pressure and velocity vector defined on a two dimensional domain Ω consisting of two subdomains Ω_1 and Ω_2 separated by an interface Γ such that $\Omega = \Omega_1 \cup \Omega_2 \cup \Gamma$ and $\tilde{\Omega} = \Omega_1 \cup \Omega_2$ and with $\partial\Omega$ denoting the boundary of Ω as illustrated in Figure 3.1.1. We assume that p and $\mathbf{v}$ satisfy the acoustic problem

$$\begin{cases} \frac{\partial p}{\partial t} + \rho c^2 \nabla \cdot \mathbf{v} &= 0 \\ \frac{\partial \mathbf{v}}{\partial t} + \frac{1}{\rho}\nabla p &= 0 \end{cases}, \quad (x, y) \in \tilde{\Omega}, \quad t > 0, \tag{3.1.1a}$$

where the density ρ and the speed of sound c are piecewise constant functions such that $c|_{\Omega_i} = c_i$ and $\rho|_{\Omega_i} = \rho_i$, $i = 1, 2$ as illustrated in Figure 3.1.1.

Letting $\boldsymbol{\nu}$ denote the unit normal vector on the interface Γ, the pressure and velocity satisfy the interface conditions

$$[p]_\Gamma = 0, \tag{3.1.1b}$$

$$[\mathbf{v} \cdot \boldsymbol{\nu}]_\Gamma = 0, \tag{3.1.1c}$$

where $[w] = w_1 - w_2$ denotes the jump across the interface. This system has a unique solution given initial and appropriate boundary conditions.

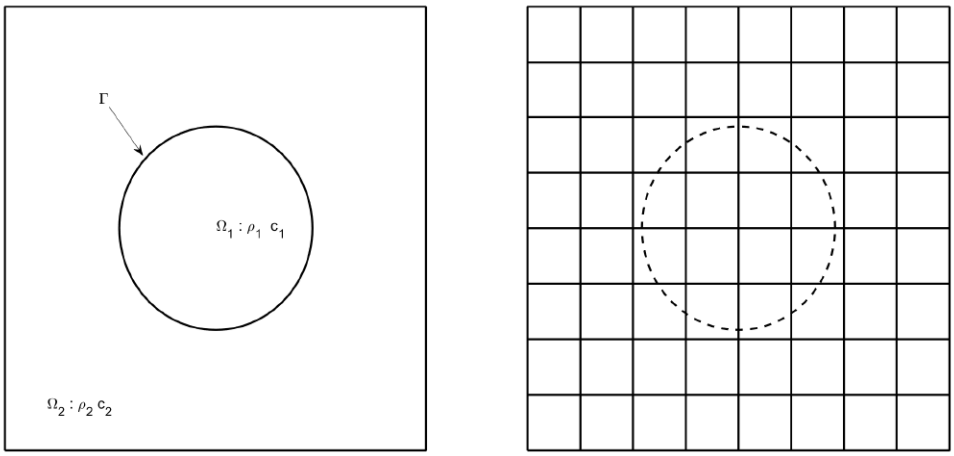

Figure 3.1.1: A domain containing two fluids separated by an interface Γ (left) and a non fitting mesh (right).

Next, we write the acoustic problem as a first-order symmetrizable linear hyperbolic system of partial differential equations for $\mathbf{U} = [p, u, v]^T$ having the form

$$\frac{\partial \mathbf{U}}{\partial t} + \mathbf{A}\frac{\partial \mathbf{U}}{\partial x} + \mathbf{B}\frac{\partial \mathbf{U}}{\partial y} = 0,\ (x, y)\ \in\ \tilde{\Omega},\ t > t_0, \tag{3.1.2a}$$

where

$$\mathbf{A}|_{\Omega_i} = \mathbf{A}_i = \begin{pmatrix} 0 & \rho_i c_i^2 & 0 \\ \frac{1}{\rho_i} & 0 & 0 \\ 0 & 0 & 0 \end{pmatrix},\ \mathbf{B}|_{\Omega_i} = \mathbf{B}_i = \begin{pmatrix} 0 & 0 & \rho_i c_i^2 \\ 0 & 0 & 0 \\ \frac{1}{\rho_i} & 0 & 0 \end{pmatrix},\ i = 1, 2. \tag{3.1.2b}$$

In order to define boundary conditions and numerical fluxes we recall that the matrices $\mathbf{A}_i,\ i = 1, 2$, can be split as $\mathbf{A}_i = \mathbf{A}_i^+ + \mathbf{A}_i^-$ where $\mathbf{A}_i^+$ and $\mathbf{A}_i^-$, respectively, have non negative and non positive eigenvalues. A similar splitting can be obtained for $\mathbf{B}_i = \mathbf{B}_i^+ + \mathbf{B}_i^-,\ i = 1, 2$. In order to construct such splitting we note that every $n \times n$ symmetrizable matrix can be factored as $\mathbf{A}_i = \mathbf{P}\mathbf{\Lambda}\mathbf{P}^{-1}$, $\mathbf{\Lambda} = diag(\lambda_1, \lambda_2, \cdots, \lambda_n)$ where λ_i are the real eigenvalues of $\mathbf{A}_i$. Let $|\mathbf{\Lambda}| = diag(|\lambda_1|, |\lambda_2|, \cdots, |\lambda_n|)$ and define $\mathbf{\Lambda}^{\pm} = \frac{\mathbf{\Lambda} \pm |\mathbf{\Lambda}|}{2}$ and $\mathbf{A}_i^{\pm} = \mathbf{P}\Lambda^{\pm}\mathbf{P}^{-1}$. The matrices $\mathbf{B}_i$ can be split in the same manner.

If, for instance, the system (3.1.2a) of partial differential equations is subjected to the interface conditions and the inflow boundary conditions

$$(\mathbf{A}n_x + \mathbf{B}n_y)^- \mathbf{U}|_{\partial\Omega} = g, \tag{3.1.2c}$$

where $\boldsymbol{n} = (n_x, n_y)^T$ is the unit outward normal vector on $\partial\Omega$, and the initial condition

$$\mathbf{U}(x, y, 0) = \mathbf{U}_0(x, y), \text{ in } \Omega, \tag{3.1.2d}$$

it has a unique solution.

In order to apply the discontinuous Galerkin method to the acoustic problem (3.1.2) we partition the domain Ω into N^2 rectangular elements and use standard polynomials on non interface elements containing one fluid and specially designed piecewise polynomial IFE shape functions on interface elements containing more than one fluid. We start by showing how to construct interface polynomial spaces and shape functions.

3.2 IFE Spaces

Elements containing one fluid are equipped with standard polynomial basis functions while elements containing two fluids separated by an interface will be equipped with piecewise polynomial functions: one piece on each fluid which are connected together by jump conditions across the interface. Applying the physical interface condition (3.1.1b) and (3.1.1c) leads to continuous immersed shape functions for the pressure while only the normal component of immersed shape functions for the velocity is continuous on linear interfaces. To obtain a reduced number of high-degree immersed shape functions we need additional interface conditions referred to as "extended jump conditions" which are derived from the acoustic problem by assuming smooth initial and boundary conditions.

More precisely, the extended jump conditions are obtained by differentiating the first equation in (3.1.1a) with respect to t and using the second equation in (3.1.1a) to replace $\partial\mathbf{v}/\partial t$ in the right hand side to show that the true pressure satisfies the following second order wave equation. Similarly, the velocity also satisfies the second-order equation. Thus, we have

$$\frac{\partial^2 p}{\partial t^2} = c^2 \Delta p, \qquad \frac{\partial^2 \mathbf{v}}{\partial t^2} = c^2 \nabla(\nabla \cdot \mathbf{v}). \tag{3.2.1}$$

Taking the curl of the second equation in (3.1.1a) and assuming that $\nabla \times \mathbf{v}(x, y, 0) = 0$ we show that the velocity satisfies $\nabla \times \mathbf{v} = 0$ at all times. Moreover, applying the identity $\nabla(\nabla \cdot \mathbf{v}) = \nabla \times \nabla \times \mathbf{v} + \Delta\mathbf{v}$, one can show that $\mathbf{v}$ also satisfies the second-order wave equation $\frac{\partial^2 \mathbf{v}}{\partial t^2} = c^2 \Delta \mathbf{v}$.

From (3.2.1) one can easily show that on $\tilde{\Omega}$ and $t > 0$ we have

$$\frac{\partial^{2m} p}{\partial t^{2m}} = c^{2m} \Delta^m p, \quad \frac{\partial^{2m} \mathbf{v}}{\partial t^{2m}} = c^{2m} (\nabla\nabla\cdot)^m \mathbf{v}, \ m = 1, 2, \cdots . \tag{3.2.2}$$

By differentiating (3.2.2) with respect to t and applying the acoustic equations (3.1.1a) we obtain on $\tilde{\Omega}$ and $t > 0$

$$\begin{array}{lll} \frac{\partial^{2m+1} p}{\partial t^{2m+1}} & = c^{2m} \Delta^m \frac{\partial p}{\partial t} & = -c^{2m} \Delta^m (\rho c^2 \nabla \cdot \mathbf{v}), \\ \frac{\partial^{2m+1} \mathbf{v}}{\partial t^{2m+1}} & = c^{2m} (\nabla\nabla\cdot)^m \frac{\partial \mathbf{v}}{\partial t} & = -\frac{c^{2m}}{\rho} \nabla(\Delta^m p), \end{array} \qquad m = 1, 2, \cdots . \tag{3.2.3}$$

The physical interface conditions (3.1.1b) and (3.1.1c) yield $[\frac{\partial^l p}{\partial t^l}]_\Gamma = 0$ and $[(\frac{\partial^l \mathbf{v}}{\partial t^l}) \cdot \boldsymbol{\nu}]_\Gamma = 0$, for all $l \geq 0$. Thus, we infer that from $\nabla \times \mathbf{v} = 0$, (3.2.2) and (3.2.3) for $m \geq 0$, the pressure satisfies

$$[c^{2m} \Delta^m p]_\Gamma = 0, \tag{3.2.4a}$$

$$[\frac{c^{2m}}{\rho} (\nabla(\Delta^m p)) \cdot \boldsymbol{\nu}]_\Gamma = 0, \tag{3.2.4b}$$

and the velocity satisfies

$$[c^{2m} (\nabla\nabla\cdot)^m \mathbf{v}) \cdot \boldsymbol{\nu}]_\Gamma = 0, \tag{3.2.5a}$$

$$[\rho c^{2m+2} \Delta^m (\nabla \cdot \mathbf{v})]_\Gamma = 0, \tag{3.2.5b}$$

$$[\frac{\partial^m (\nabla \times \mathbf{v})}{\partial x^l \partial y^{m-l}}]_\Gamma = 0, \ l = 0, 1, \cdots, m. \tag{3.2.5c}$$

Applying the relation $(\nabla\nabla\cdot)^m \mathbf{v} = \nabla \Delta^{m-1} (\nabla \cdot \mathbf{v})$ for $m \geq 1$, the jump condition (3.2.5a) for $m \geq 1$ may be written as $[c^{2m} (\nabla (\nabla \cdot \Delta^{m-1} \mathbf{v})) \cdot \boldsymbol{\nu}]_\Gamma = 0$.

For instance, for the bilinear IFE shape functions we use the interface conditions (3.2.4) and (3.2.5) for $m = 0$ to write

$$\begin{cases} [p]_\Gamma = 0, \\ [\frac{1}{\rho} (\nabla p \cdot \boldsymbol{\nu})]_\Gamma = 0, \end{cases} \tag{3.2.6}$$

for the pressure and

$$\begin{cases} [\mathbf{v} \cdot \boldsymbol{\nu}]_\Gamma = 0, \\ [\rho c^2 (\nabla \cdot \mathbf{v})]_\Gamma = 0, \\ [\frac{\partial u}{\partial y} - \frac{\partial v}{\partial x}]_\Gamma = 0, \end{cases} \tag{3.2.7}$$

for the velocity.

The biquadratic IFE functions for the pressure must satisfy (3.2.6) and

$$[c^2 \Delta p]_\Gamma = 0, \tag{3.2.8}$$

while the biquadratic velocity must satisfy (3.2.7) and

$$\begin{cases} [\mathbf{c}^2 (\nabla\nabla \cdot \mathbf{v}) \cdot \boldsymbol{\nu}]_\Gamma = 0, \\ [\frac{\partial^2 u}{\partial x \partial y} - \frac{\partial^2 v}{\partial x^2}]_\Gamma = 0, \\ [\frac{\partial^2 u}{\partial y^2} - \frac{\partial^2 v}{\partial y \partial x}]_\Gamma = 0. \end{cases} \tag{3.2.9}$$

Higher-degree Q_k IFE spaces for the pressure can be constructed such that: *(i)* if k is even, the pressure must satisfy (3.2.4a) for $m = 0, 1, \cdots, \frac{k}{2}$ and (3.2.4b) for $m = 0, 1, \cdots, \frac{k}{2} - 1$, *(ii)* if k is odd, the pressure must satisfy (3.2.4) for $m = 0, 1, \cdots, \lfloor \frac{k}{2} \rfloor$. Similarly, higher-degree Q_k IFE spaces for the velocity can be constructed such that: *(i)* if k is even, the velocity must satisfy (3.2.5a) for $m = 0, 1, \cdots, \frac{k}{2}$, (3.2.5b) for $m = 0, 1, \cdots, \frac{k}{2} - 1$, and (3.2.5c) for $m = 0, 1, \cdots, k - 1$, *(ii)* if k is odd, the velocity must satisfy (3.2.5a), (3.2.5b) for $m = 0, 1, \cdots, \lfloor \frac{k}{2} \rfloor$ and (3.2.5c) for $m = 0, 1, \cdots, k - 1$.

3.2.1 Construction of Lagrange IFE Spaces

Let Q_k be the space of polynomial of degree at most $k = 1, 2, \cdots$ with respect to each variable in two dimensions. We now turn to the construction of IFE basis functions and spaces. First we consider piecewise Q_k immersed finite element shape functions on an interface element and assume that the pressure is a piecewise polynomial in Q_k while $\mathbf{v}$ is a piecewise polynomial in $(Q_k)^2$. We further require each of the piecewise Q_k polynomial pressure and velocity to satisfy the interface jump conditions (3.1.1b) and (3.1.1c).

To be more precise let us partition the domain into a uniform rectangular mesh with non interface elements containing only one fluid and interface elements which are cut by the interface and contain two fluids. Each interface rectangular element $T = \square A_1A_2A_3A_4$ with vertices $A_i = (x_i, y_i)^T,\ i = 1, 2, 3, 4$ is such that the interface Γ intersects two edges at $D = (x_D, y_D)^T$ and $E = (x_E, y_E)^T$ called interface points. The interface $\widetilde{DE} = \Gamma \cap T$ is approximated by the line segment $\overline{DE}$ (for bilinear approximation) to separate T into two polygonal domains T_1 and T_2 such that T_i contains vertices of T that are in $\Omega_i,\ i = 1, 2$. For higher-order approximations use $\widetilde{DE}$ to split T into T_1 and T_2. Topologically, we consider reference interface elements of type I with two adjacent edges cut by the interface, type II interface element with two opposite edges cut by the interface, type III element where the interface passes through one vertex and cut an opposite edge and type IV where the interface passes through two opposite vertices. For an illustration see Figure 3.2.1.

Let $\mathcal{T}_h$, $\mathcal{T}_h^S$ and $\mathcal{T}_h^I$, respectively, denote the set all elements in the mesh, the set of all non interface and the set of all interface elements.

constructed on the reference element $\hat{T} = \square\hat{A}_1\hat{A}_2\hat{A}_3\hat{A}_4$ with vertices $\hat{A}_1 = (0, 0)^T,\ \hat{A}_2 = (1, 0)^T$, $\hat{A}_3 = (0, 1)^T,\ \hat{A}_4 = (1, 1)^T$. Let $X = (x, y)^T$ and $\hat{X} = (\hat{x}, \hat{y})^T$ and let

$$\hat{X} = G(X) = MX + B, \tag{3.2.10}$$

be the standard affine mapping from an arbitrary element T to the reference element $\hat{T}$ such that $\hat{A}_i = G(A_i),\ i = 1, 2, 3, 4$. We further note that each interface element T is mapped into a reference element of the same type where $\hat{E} = G(E)$ and $\hat{D} = G(D)$ and $\overline{\hat{D}\hat{E}} = G(\overline{DE})$. Furthermore, the interface points are $\hat{E} = G(E)$ and $\hat{D} = G(D)$. Each interface element is mapped into one of the four reference elements shown in Figure 3.2.1 where we omitted the $\hat{}$. From now on we work on reference elements but omit the $\hat{}$ unless needed for clarity. Now we are ready to describe an algorithm for constructing IFE bilinear shape functions $p^{(i)},\ i = 1, 2, 3, 4$ of Lagrange type for the pressure. We define the IFE spaces on an arbitrary interface element $T = T_1 \cup T_2$ as

$$\mathcal{R}_p^1(T) = \{U \mid U|_{T_l} \in Q_1,\ l = 1, 2,\ [U]_{\overline{DE}} = 0,\ [\frac{1}{\rho}\nabla U \cdot \boldsymbol{\nu}]_{\overline{DE}} = 0, [\frac{\partial^2 U}{\partial x \partial y}]_{\overline{DE}} = 0\}, \tag{3.2.11}$$

equipped with a Lagrange type IFE basis $p^{(i)},\ i = 1, 2, 3, 4$.

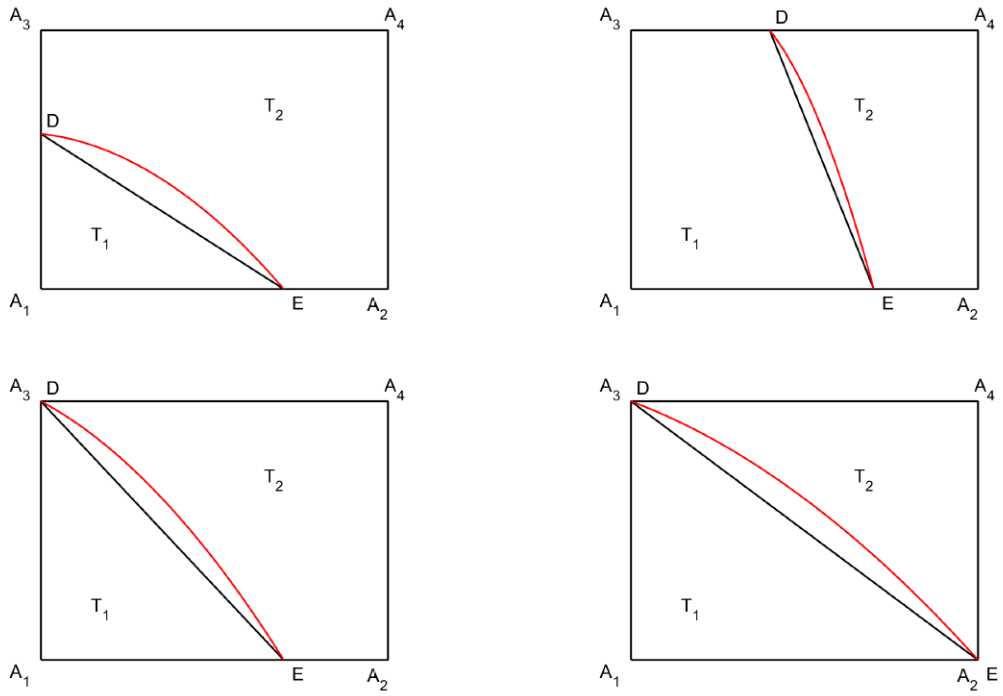

Figure 3.2.1: Reference interface elements of type I, II, III, IV (upper left) to (lower right).

If $L_i,\ i = 1, 2, 3, 4$ are the standard Lagrange bilinear shape functions such that $L_i(A_j) = \delta_{ij}$ on the reference element. We use the standard shape functions to construct the Lagrange bilinear IFE basis functions $p^{(i)}$ satisfying $p^{(i)}(A_j) = \delta_{ij}$ by

$$p^{(i)} = L_i + \phi^{(0),i}, \qquad i = 1, 2, 3, 4, \tag{3.2.12a}$$

where, on the reference element of type I,

$$\phi^{(0),i} = \begin{cases} c_2 L_2 + c_3 L_3 + c_4 L_4, & \text{on } T_1, \\ c_1 L_1, & \text{on } T_2. \end{cases} \tag{3.2.12b}$$

On the reference element of type II, we have

$$\phi^{(0),i} = \begin{cases} c_2 L_2 + c_4 L_4, & \text{on } T_1, \\ c_1 L_1 + c_3 L_3, & \text{on } T, \end{cases} \tag{3.2.12c}$$

on the reference element of type III,

$$\phi^{(0),i} = \begin{cases} c_2 L_2 + c_4 L_4, & \text{on } T_1, \\ c_1 L_1, & \text{on } T_2. \end{cases} \tag{3.2.12d}$$

On reference element of type IV

$$\phi^{(0),i} = \begin{cases} c_4 L_4, & \text{on } T_1, \\ c_1 L_1, & \text{on } T_2. \end{cases} \tag{3.2.12e}$$

For instance, the coefficients c_1, c_2, c_3, c_4 for defining $p^{(i)}$ on interface element of type I and II are determined by imposing the following four interface jump and consistency conditions:

$$p_1^{(i)}(D) - p_2^{(i)}(D) = 0, \tag{3.2.13a}$$

$$p_1^{(i)}(E) - p_2^{(i)}(E) = 0, \tag{3.2.13b}$$

$$\frac{1}{\rho_1}\frac{\partial p_1^{(i)}}{\partial \boldsymbol{\nu}}(\frac{D+E}{2}) - \frac{1}{\rho_2}\frac{\partial p_2^{(i)}}{\partial \boldsymbol{\nu}}(\frac{D+E}{2}) = 0, \tag{3.2.13c}$$

$$\frac{\partial^2 p_1^{(i)}}{\partial x \partial y}(E) - \frac{\partial^2 p_2^{(i)}}{\partial x \partial y}(E) = 0. \tag{3.2.13d}$$

The resulting 4×4 square linear systems yield a unique set of IFE shape functions with the following properties [1, 2]: *(i)* If $\rho_1 = \rho_2$ the IFE shape functions become the standard bilinear Lagrange shape functions, *(ii)* they yield finite element interpolants and solutions with optimal convergence rates under quasi-uniform mesh refinement and *(iii)* they form a partition of unity.

Next, we define the bilinear IFE spaces for the velocity as

$$\mathcal{R}_{\mathbf{v}}^1(T) = \{V \mid V|_{T_i} \in (Q_1)^2,\ [V \cdot \boldsymbol{\nu}]_{\overline{DE}} = 0,\ [\rho c^2 \nabla \cdot V]_{\overline{DE}} = 0, [\nabla \times V]_{\overline{DE}} = 0, [\frac{\partial^2 V}{\partial x \partial y}]_{\overline{DE}} = 0\}. \tag{3.2.14}$$

We now construct bilinear immersed shape functions for the velocity $\mathbf{v} = (u, v)^T$ by writing the standard bilinear Lagrange shape functions for $(Q_1)^2$ as

$$\mathbf{L}^{(i),l} = L_i \mathbf{e}_l, \quad i = 1, 2, 3, 4,\ l = 1, 2, \tag{3.2.15}$$

where $\mathbf{e}_l,\ l = 1, 2$ are the canonical vectors in $\mathbb{R}^2$.

On the reference interface element $T = T_1 \cup T_2$ of type I shown in Figure 3.2.1 we write Lagrange IFE shape functions $\mathbf{v}^{(i),l}, i = 1, 2, 3, 4,\ l = 1, 2$ satisfying $\mathbf{v}^{(i),l}(A_j) = \delta_{ij}\mathbf{e}_l$ as

$$\mathbf{v}^{(i),m} = \mathbf{L}^{(i),m} + \boldsymbol{\psi}^{(0),i}, \quad i = 1, 2, 3, 4, \quad m = 1, 2, \tag{3.2.16a}$$

where

$$\boldsymbol{\psi}^{(0),i} = \begin{cases} \sum_{l=1}^{2}\sum_{j=2}^{4} c^{(j),l}\mathbf{L}^{(j),l}, & \text{on } T_1, \\ c^{(1),1}\mathbf{L}^{(1),1} + c^{(1),2}\mathbf{L}^{(1),2}, & \text{on } T_2. \end{cases} \tag{3.2.16b}$$

On the reference interface element of type II

$$\boldsymbol{\psi}^{(0),i} = \begin{cases} \sum_{l=1}^{2} \left(c^{(2),l} \mathbf{L}^{(2),l} + c^{(4),l} \mathbf{L}^{(4),l} \right), & \text{on } T_1, \\ \sum_{l=1}^{2} \left(c^{(1),l} \mathbf{L}^{(1),l} + c^{(3),l} \mathbf{L}^{(3),l} \right), & \text{on } T_2. \end{cases} \tag{3.2.16c}$$

On the reference interface element of type III

$$\boldsymbol{\psi}^{(0),i} = \begin{cases} \sum_{l=1}^{2} \left(c^{(2),l} \mathbf{L}^{(2),l} + c^{(4),l} \mathbf{L}^{(4),l} \right), & \text{on } T_1, \\ \sum_{l=1}^{2} \left(c^{(1),l} \mathbf{L}^{(1),l} \right), & \text{on } T_2. \end{cases} \tag{3.2.16d}$$

On the reference interface element of type IV

$$\boldsymbol{\psi}^{(0),i} = \begin{cases} \sum_{l=1}^{2} \left(c^{(4),l} \mathbf{L}^{(4),l} \right), & \text{on } T_1, \\ \sum_{l=1}^{2} \left(c^{(1),l} \mathbf{L}^{(1),l} \right), & \text{on } T_2. \end{cases} \tag{3.2.16e}$$

We determine the coefficients of $\mathbf{v}^{(i),m}$ on an interface element of type I and II by imposing the interface and consistency conditions

$$\begin{aligned} \mathbf{v}_1^{(i),m} \cdot \boldsymbol{\nu}(D) - \mathbf{v}_2^{(i),m} \cdot \boldsymbol{\nu}(D) &= 0, && \text{(3.2.17a)} \\ \mathbf{v}_1^{(i),m} \cdot \boldsymbol{\nu}(E) - \mathbf{v}_2^{(i),m} \cdot \boldsymbol{\nu}(E) &= 0, && \text{(3.2.17b)} \\ \rho_1 c_1^2 \nabla \cdot \mathbf{v}_1^{(i),m}(\frac{D+E}{2}) - \rho_2 c_2^2 \nabla \cdot \mathbf{v}_2^{(i),m}(\frac{D+E}{2}) &= 0, && \text{(3.2.17c)} \\ \left(\frac{\partial u_1^{(i),m}}{\partial y} - \frac{\partial v_1^{(i),m}}{\partial x} \right)(\frac{D+E}{2}) - \left(\frac{\partial u_2^{(i),m}}{\partial y} - \frac{\partial v_2^{(i),m}}{\partial x} \right)(\frac{D+E}{2}) &= 0, && \text{(3.2.17d)} \\ \frac{\partial^2 \mathbf{v}_1^{(i),m}}{\partial x \partial y}(D) - \frac{\partial^2 \mathbf{v}_2^{(i),m}}{\partial x \partial y}(D) &= 0. && \text{(3.2.17e)} \end{aligned}$$

For instance, on the interface element of type I and II, the interface conditions (3.2.17) for each shape function $\mathbf{v}^{(i),m}$, lead to a rectangular system of 6 linear equations and 8 coefficients $\mathbf{c} = [c^{(1),1}, c^{(2),1}, c^{(3),1}, c^{(4),1}, c^{(1),2}, c^{(2),2}, c^{(3),2}, c^{(4),2}]^T$ written as $\mathbf{Mc} = \mathbf{b}$. In the following theorem we prove that the matrix $\mathbf{M}$ is full row rank for bilinear IFE spaces.

Theorem 3.2.1. *The IFE bilinear shape functions for the velocity on reference interface elements defined by (3.2.16) and (3.2.17) lead to a linear system* $\mathbf{Mc} = \mathbf{b}$ *with a full row rank matrix.*

proof. On the reference interface element $[0,1]^2$ of type I such that $E=(a,0)$ and $D=(0,b)$, $0<a,b<1$, the matrix $\mathbf{M}$ with $r=\frac{\rho_1 c_1^2}{\rho_2 c_2^2}$ is given as

$$\mathbf{M}=\begin{bmatrix} b(b-1) & 0 & b^2 & 0 & a(b-1) & 0 & ab & 0 \\ b(a-1) & ab & 0 & 0 & a(a-1) & a^2 & 0 & 0 \\ 1-\frac{b}{2} & -r(\frac{b}{2}-1) & -\frac{br}{2} & \frac{br}{2} & 1-\frac{a}{2} & -\frac{ar}{2} & -r(\frac{a}{2}-1) & \frac{ar}{2} \\ 1-\frac{a}{2} & -\frac{a}{2} & 1-\frac{a}{2} & \frac{a}{2} & \frac{b}{2}-1 & \frac{b}{2}-1 & \frac{b}{2} & -\frac{b}{2} \\ -1 & -1 & -1 & 1 & 0 & 0 & 0 & 0 \\ 0 & 0 & 0 & 0 & -1 & -1 & -1 & 1 \end{bmatrix}, \tag{3.2.18}$$

with $det(\mathbf{M}(:,[2,3,4,6,7,8]) = -abr(a^2+b^2) < 0$ for $a>0,\ b>0$ which shows that $\mathbf{M}$ is full rank.

On the reference interface element of type II such that $E=(a,0)$ and $D=(b,1)$, $0<a,b<1$, the matrix $\mathbf{M}$ is given by

$$\mathbf{M}=\begin{bmatrix} 0 & 0 & b-1 & b & 0 & 0 & (a-b)(b-1) & b(a-b) \\ a-1 & a & 0 & 0 & (a-b)(a-1) & a(a-b) & 0 & 0 \\ \frac{1}{2} & \frac{r}{2} & \frac{1}{2} & \frac{r}{2} & 1-\frac{a+b}{2} & -\frac{r}{2}(a+b) & \frac{a+b}{2}-1 & \frac{r}{2}(a+b) \\ 1-\frac{a+b}{2} & -\frac{a+b}{2} & \frac{a+b}{2}-1 & \frac{a+b}{2} & -\frac{1}{2} & -\frac{1}{2} & -\frac{1}{2} & -\frac{1}{2} \\ -1 & -1 & 1 & 1 & 0 & 0 & 0 & 0 \\ 0 & 0 & 0 & 0 & -1 & -1 & 1 & 1 \end{bmatrix}, \tag{3.2.19}$$

with $det(\mathbf{M}(:,[1,2,3,5,6,7]) = (1-b)(ar+(b-a)^2+1-a) > 0$ which establishes that $\mathbf{M}$ is full rank.

On a reference interface element of type III with $E=(a,0)$, $0<a<1$, and $D=(0,1)$ the matrix $\mathbf{M}$ is given by

$$\mathbf{M}=\begin{bmatrix} a-1 & a & 0 & a(a-1) & a^2 & 0 \\ 1/2 & r/2 & r/2 & 1-a/2 & -(ar)/2 & (ar)/2 \\ 1-a/2 & -a/2 & a/2 & -1/2 & -1/2 & -1/2 \\ -1 & -1 & 1 & 0 & 0 & 0 \\ 0 & 0 & 0 & -1 & -1 & 1 \end{bmatrix}, \tag{3.2.20}$$

with $det(\mathbf{M}(:,[1,2,3,4,6])) = (r(a-2)(a+1)+a(a-3))/2 < 0$ which proves that $\mathbf{M}$ is full rank.

Finally, we consider the reference interface element of type IV with $E=(1,0)$ and $D=(0,1)$ where the matrix $\mathbf{M}$ is given by

$$\mathbf{M}=\begin{bmatrix} 1/2 & r/2 & 1/2 & r/2 \\ 1/2 & 1/2 & -1/2 & -1/2 \\ -1 & 1 & 0 & 0 \\ 0 & 0 & -1 & 1 \end{bmatrix}, \tag{3.2.21}$$

with $det(\mathbf{M}) = 1 + r > 0$ which proves that $\mathbf{M}$ is full rank. $\square$

Since on interface elements of type I,II,III and IV the $m \times n$ matrix $\mathbf{M}$ is full row rank, the SVD decomposition $\mathbf{M} = \mathbf{U}\mathbf{S}\mathbf{V}^T$, where $\mathbf{S}$ contains the singular values $\sigma_i \neq 0,\ i = 1, 2, \cdots, m$, leads to $\mathbf{M}\mathbf{M}^T = \mathbf{U}\ \mathbf{S}\ \mathbf{S}^T\ \mathbf{U}^T = \mathbf{U}\mathbf{\Sigma}\mathbf{U}^T$, where $\mathbf{\Sigma} = diag(\sigma_1^2, \cdots, \sigma_m^2)$ which, in turn, shows that $\mathbf{M}\mathbf{M}^T$ is invertible. Finally, the pseudo-right-inverse of $\mathbf{M}$ is $\mathbf{M}^T(\mathbf{M}\mathbf{M}^T)^{-1}$ and the minimum-norm particular solution of $\mathbf{M}\mathbf{c} = \mathbf{b}$ is $\mathbf{c}^{(0)} = \mathbf{M}^T(\mathbf{M}\mathbf{M}^T)^{-1}\mathbf{b}$. Furthermore, if $\mathbf{c}^{(j)},\ j = 1, 2$ denote a basis of the null space of $\mathbf{M}$, the set of all solutions of $\mathbf{M}\mathbf{c} = \mathbf{b}$ is $\mathbf{c}^{(0)} + span\{\mathbf{c}^{(1)}, \mathbf{c}^{(2)}\}$.

We construct the IFE shape functions for the velocity on element of type I and II by following the steps:

1. Find a basis $\mathbf{c}^{(1)}, \mathbf{c}^{(2)}$ of the null space of $\mathbf{M}$
2. Compute the minimum-norm particular solution $\mathbf{c}^{(0)}$ of $\mathbf{M}\mathbf{c} = \mathbf{b}$ for each of the eight IFE shape functions
3. Replace the coefficients in (3.2.16) by the minimum-norm solutions $\mathbf{c}^{(0)}$ for each vertex to obtain eight IFE shape functions

$$\mathbf{v}^{(i),m}, \quad i = 1, 2, 3, 4,\ m = 1, 2, \tag{3.2.22}$$

4. Substitute the coefficients $\mathbf{c}^{(1)}$ and $\mathbf{c}^{(2)}$ in (3.2.16b), (3.2.16c), (3.2.16d) or (3.2.16e) depending on the type of element to obtain two additional "bubble" IFE functions $\mathbf{w}^{(1)}$ and $\mathbf{w}^{(2)}$ such that $\mathbf{w}^{(i)}(A_j) = 0, \quad j = 1, 2, 3, 4,\ i = 1, 2.$

Thus, the IFE bilinear spaces for the velocity is

$$\mathcal{R}_{\mathbf{v}}^1(T) = span\{\mathbf{v}^{(i),m},\ i = 1, 2, 3, 4,\ m = 1, 2,\ \mathbf{w}^{(1)}, \mathbf{w}^{(2)}\}. \tag{3.2.23}$$

We note that one may also construct IFE functions for the velocity that satisfy the continuity of the normal derivative only which leads to higher dimensional IFE spaces. Another possibility is to include, in addition to the continuity of the normal derivative, the smoothness of the curl of the velocity and/or jump in the term for divergence jump. We note that the IFE functions for the pressure are continuous while the IFE functions for the velocity are discontinuous across linear interface which is consistent with the true solutions.

In order to construct higher-degree Q_k IFE shape functions for the pressure we order the Q_k vertices A_{ij} as $Z_1,\ Z_2, \cdots, Z_{(k+1)^2}$ and consider the associated standard Lagrange Q_k shape functions $L_1,\ L_2, \cdots, L_{(k+1)^2}$, where $L_i(Z_j) = \delta_{ij}$. Without loss of generality, we consider an interface element $T = T_1 \cup T_2$ such that no vertex of T is on Γ, and let $\mathcal{I}_l$ denote the set of indices j, $1 \leq j \leq (k+1)^2$, such that $Z_j \in T_l$, for $l = 1, 2$. In this general case, if the curved interface $\widetilde{DE}$ is parameterized by $t \to X(t) = (x_1(t), x_2(t)),\ t = [0, 1]$ where $X(0) = D$ and

$X(1) = E$, we define $k+1$ interface points $X_s = X(\xi_s),\ s = 0, 1, 2, \cdots, k$ and ξ_s are the roots of Legendre polynomial of degree $k+1$ shifted to [0,1].

High-degree Q_k IFE shape functions of Lagrange type for the pressure such that $p^{(i)}(Z_j) = \delta_{ij},\quad i, j = 1, 2, \cdots, (k+1)^2$, can be obtained as

$$p^{(i)} = L_i + \phi^{(0),i},\quad i = 1, 2, \cdots, (k+1)^2, \tag{3.2.24}$$

where

$$\phi^{(0),i} = \begin{cases} \sum\limits_{j\in\mathcal{I}_2} c_j L_j, & \text{on } T_1, \\ \sum\limits_{j\in\mathcal{I}_1} c_j L_j, & \text{on } T_2. \end{cases} \tag{3.2.25}$$

We determine the coefficients $c_1, c_2, \cdots, c_{(k+1)^2}$ for each IFE shape function $p^{(i)}$ by imposing the following interface conditions

$$c_1^{2m}\left(\Delta^m p_1^{(i)}\right)(X_s) - c_2^{2m}\left(\Delta^m p_2^{(i)}\right)(X_s) = 0,$$
$$s = 0, 1, \cdots, k-2m,\ m = 0, 1, \cdots, \lfloor\frac{k}{2}\rfloor, \tag{3.2.26a}$$

$$\frac{c_1^{2m}}{\rho_1}\left(\nabla(\Delta^m p_1^{(i)})\right)\cdot\boldsymbol{\nu}(X_s) - \frac{c_2^{2m}}{\rho_2}\left(\nabla(\Delta^m p_2^{(i)})\right)\cdot\boldsymbol{\nu}(X_s) = 0,$$
$$s = 0, 1, \cdots, k-2m-1,\ m = 0, 1, \cdots, \lfloor\frac{k-1}{2}\rfloor, \tag{3.2.26b}$$

and consistency conditions

$$\frac{\partial^m p_1^{(i)}}{\partial x^{m-j}\partial y^j} - \frac{\partial^m p_2^{(i)}}{\partial x^{m-j}\partial y^j} = 0,\ k+1 \le m \le 2k,\ m-k \le j \le k. \tag{3.2.26c}$$

The above equations yield a $(k+1)^2 \times (k+1)^2$ system of linear algebraic equations for each IFE shape function. The system has a unique solution provided the interface is linear or the mesh is fine enough for curved interfaces. Moreover, the resulting IFE shape functions are consistent with the standard Q_k shape functions and the IFE spaces for the pressure is

$$\mathcal{R}_p^k(T) = \{U \mid U|_{T_l} \in Q_k,\ l = 1, 2,\ U\ satisfies\ (3.2.26)\}. \tag{3.2.27}$$

Higher-degree piecewise Q_k IFE functions for the velocity are defined by

$$\mathbf{v}^{(i),l} = \mathbf{L}^{(i),l} + \boldsymbol{\psi}^{(0),i},\qquad i = 1, 2, \cdots, (k+1)^2,\ l = 1, 2, \tag{3.2.28a}$$

where

$$\boldsymbol{\psi}^{(0),i} = \begin{cases} \sum\limits_{l=1}^{2}\sum\limits_{j\in\mathcal{I}_2} c^{(j),l}\mathbf{L}^{(j),l}, & \text{on } T_1, \\ \sum\limits_{l=1}^{2}\sum\limits_{j\in\mathcal{I}_1} c^{(j),l}\mathbf{L}^{(j),l}, & \text{on } T_2. \end{cases} \tag{3.2.28b}$$

The coefficients in $\mathbf{v}^{(i),l}$ are determined by the following interface and consistency conditions

$$
\begin{aligned}
[c^{2m}(\nabla\nabla\cdot)^m\mathbf{v})\cdot\boldsymbol{\nu}](X_s) &= 0, s=0,1,\cdots,k-2m,\ m=0,1,\cdots,\lfloor\frac{k}{2}\rfloor, && \text{(3.2.29a)}\\
[\rho c^{2m+2}\Delta^m(\nabla\cdot\mathbf{v})](X_s) &= 0, s=0,1,\cdots,k-2m-1,\ m=0,1,\cdots,\lfloor\frac{k-1}{2}\rfloor, && \text{(3.2.29b)}\\
[\frac{\partial^m(\nabla\times\mathbf{v})}{\partial x^l\partial y^{m-l}}](X_0) &= 0,\ l=0,1,\cdots,m, m=0,1,\cdots,k-1, && \text{(3.2.29c)}\\
[\frac{\partial^m\mathbf{v}}{\partial x^{m-j}\partial y^j}](X_0) &= 0,\ m=k+1,k+2,\cdots,2k,\\
&\quad j=m-k,m-k+1,\cdots,k. && \text{(3.2.29d)}
\end{aligned}
$$

Thus, on an interface element of type I we obtain a system of linear system $\mathbf{Mc}=\mathbf{b}$ for the coefficients $\mathbf{c}=[c^{(1),1},c^{(1),2},c^{(2),1},c^{(2),2},\cdots,c^{((k+1)^2),1},c^{((k+1)^2),2}]^T$, $\mathbf{c}\in\mathbb{R}^{2(k+1)^2}$ satisfying $(k+1)(2k+1)$ equations given in (3.2.29). Assuming $\mathbf{M}$ is full row rank the nullity of $\mathbf{M}$ is $k+1$. We compute the $2(k+1)^2$ Lagrange shape functions using the minimum-norm solution of each $\mathbf{Mc}=\mathbf{b}$ in (3.2.29) for each IFE. Then, we compute a basis of the null space of $\mathbf{M}$ as $\{\mathbf{c}^{(1)},\mathbf{c}^{(2)},\cdots,\mathbf{c}^{(k+1)}\}$ and substitute each $\mathbf{c}^{(i)}$ in (3.2.28b) to obtain the associated IFE functions $\mathbf{w}^{(i)},\ i=1,2,\cdots,(k+1)$ such that $\mathbf{w}^{(i)}(Z_j)=0,\ i=1,2,\cdots,k+1,\ j=1,2,\cdots(k+1)^2$. Hence, the IFE spaces for the velocity is

$$
\mathcal{R}^k_{\mathbf{v}}(T)=span\{\mathbf{v}^{(i),m},\ i=1,2,\cdots,(k+1)^2,\ m=1,2,\ \mathbf{w}^{(1)},\mathbf{w}^{(2)},\cdots,\mathbf{w}^{(k+1)}\}. \quad \text{(3.2.30)}
$$

Corollary 3.2.1. *Bilinear IFE shape functions for velocity $\mathbf{v}^{(i),l}$, $i=1,2,3,4$, $l=1,2$ of the form (3.2.16) and extra basis $\mathbf{w}^{(1)}$, $\mathbf{w}^{(2)}$ satisfying jump, extended, curl-free and consistency conditions (3.2.17) on the reference element $(0,1)^2$ exist on $\mathcal{R}^1_{\mathbf{v}}$ defined in (3.2.14).*

Proof. (3.2.16) and (3.2.17) lead to a rectangular system $\mathbf{Mc}=\mathbf{b}$ with a full row rank by Theorem 3.2.1. Also, the minimum-norm particular solution $\mathbf{c}=[c^{(1),1},c^{(2),1},c^{(3),1},c^{(4),1},c^{(1),2},c^{(2),2},c^{(3),2},c^{(4),2}]^T$ in (3.2.16) exists for all type of elements in Figure 3.2.1 by the below argument of Theorem 3.2.1. Thus $\mathbf{v}^{(i),l}$, $i=1,2,3,4$, $l=1,2$ and $\mathbf{w}^{(1)}$, $\mathbf{w}^{(2)}$ exist on $\mathcal{R}^1_{\mathbf{v}}$. □

By a direct computation we can see that the IFE shape functions for the pressure:

- Form a partition of unity.
- Reduce to the standard shape functions if $\rho_1=\rho_2$ and $c_1=c_2$.
- Reduce to the standard shape functions if the interface leaves the element.

Similarly, we can see that the IFE shape functions for the velocity form a partition of unity provided a proper scaling is applied to the bubble functions $\mathbf{w}^{(1)},\mathbf{w}^{(2)},\cdots,\mathbf{w}^{(k+1)}$.

3.2.2 Alternative Way to Construct Lagrange IFE Shape Functions

We also construct the bilinear shape function for the pressure $p^{(i)}$, $i = 1, 2, 3, 4$ by writing

$$p^{(i)} = \begin{cases} p_1^{(i)} & = a_1 + a_2 x + a_3 y + a_4 xy, \quad \text{on } T_1, \\ p_2^{(i)} & = b_1 + b_2 x + b_3 y + b_4 xy, \quad \text{on } T_2, \end{cases} \tag{3.2.31}$$

and enforcing the Lagrange condition $p_k^{(i)}(A_j) = \delta_{ij}$, $i, j = 1, 2, 3, 4$ and the jump conditions (3.2.13). Similarly the shape function $\mathbf{v}^{(i),l}$, $i = 1, 2, 3, 4$, $l = 1, 2$, $\mathbf{w}^{(1)}, \mathbf{w}^{(2)}$ are obtained by writing

$$\mathbf{v}^{(i),l} = \begin{cases} \mathbf{v}_1^{(i),l} = \begin{pmatrix} u_1^{(i),l} \\ v_1^{(i),l} \end{pmatrix} = \begin{pmatrix} c_1 + c_2 x + c_3 y + c_4 xy \\ d_1 + d_2 x + d_3 y + d_4 xy \end{pmatrix}, & \text{on } T_1, \\ \mathbf{v}_2^{(i),l} = \begin{pmatrix} u_2^{(i),l} \\ v_2^{(i),l} \end{pmatrix} = \begin{pmatrix} e_1 + e_2 x + e_3 y + e_4 xy \\ f_1 + f_2 x + f_3 y + f_4 xy \end{pmatrix}, & \text{on } T_2, \end{cases} \tag{3.2.32}$$

and enforcing the Lagrange conditions $\mathbf{v}_k^{(i),1}(A_j) = [\delta_{ij}, 0]^T$, $\mathbf{v}_k^{(i),2}(A_j) = [0, \delta_{i,j}]^T$ for $i = 1, 2, 3, 4$, $k = 1, 2$ and (3.2.17) where $k = 1$ if A_j is on the region T_1 and $k = 2$ if A_j is on the region T_2. Thus an 8×8 linear system is used to find 8 coefficients a_j, b_j, $j = 1, 2, 3, 4$ in (3.2.31). Similarly a 16×14 linear system is used to find 16 coefficients c_j, d_j, e_j, f_j, $j = 1, 2, 3, 4$ in (3.2.32) with 14 conditions for the velocity. Since the number of conditions is less than the number of unknowns, two extra basis $\mathbf{w}^{(1)}, \mathbf{w}^{(2)}$ are added from the null space of 16×14 matrix.

In the same way, we construct the biquadratic shape function on an interface elements cut by a line interface, we apply Lagrange conditions $p_k^{(i)}(A_j) = \delta_{ij}$, $i, j = 1, 2, \cdots, 9$ to the pressure

$$p^{(i)} = \begin{cases} p_1^{(i)} & = a_1 + a_2 x + a_3 y + a_4 xy + a_5 x^2 + a_6 y^2 + a_7 x^2 y + a_8 xy^2 + a_9 x^2 y^2, \quad \text{on } T_1, \\ p_2^{(i)} & = b_1 + b_2 x + b_3 y + b_4 xy + b_5 x^2 + b_6 y^2 + b_7 x^2 y + b_8 xy^2 + b_9 x^2 y^2, \quad \text{on } T_2, \end{cases} \tag{3.2.33}$$

together with interface jump conditions

$$\begin{aligned} & p_1^{(i)}(D) - p_2^{(i)}(D) = 0, p_1^{(i)}(\frac{D+E}{2}) - p_2^{(i)}(\frac{D+E}{2}) = 0, \\ & p_1^{(i)}(E) - p_2^{(i)}(E) = 0, \end{aligned} \tag{3.2.34a}$$

extended conditions

$$\begin{aligned} & \frac{1}{\rho_1}\frac{\partial p_1^{(i)}}{\partial \boldsymbol{\nu}}(D) - \frac{1}{\rho_2}\frac{\partial p_2^{(i)}}{\partial \boldsymbol{\nu}}(D) = 0, \frac{1}{\rho_1}\frac{\partial p_1^{(i)}}{\partial \boldsymbol{\nu}}(E) - \frac{1}{\rho_2}\frac{\partial p_2^{(i)}}{\partial \boldsymbol{\nu}}(E) = 0, \\ & c_1^2 \Delta p_1^{(i)}(\frac{D+E}{2}) - c_2^2 \Delta p_2^{(i)}(\frac{D+E}{2}) = 0, \end{aligned} \tag{3.2.34b}$$

and consistency conditions

$$\frac{\partial^3 p_1^{(i)}}{\partial^2 x \partial y}(D) - \frac{\partial^3 p_2^{(i)}}{\partial^2 x \partial y}(D) = 0, \frac{\partial^3 p_1^{(i)}}{\partial x \partial^2 y}(D) - \frac{\partial^3 p_2^{(i)}}{\partial x \partial^2 y}(D) = 0,$$
$$\frac{\partial^4 p_1^{(i)}}{\partial^2 x \partial^2 y}(D) - \frac{\partial^4 p_2^{(i)}}{\partial^2 x \partial^2 y}(D) = 0. \tag{3.2.34c}$$

For the velocity, we apply $\mathbf{v}_k^{(i),1}(A_j) = [\delta_{ij}, 0]^T$, $\mathbf{v}_k^{(i),2}(A_j) = [0, \delta_{i,j}]^T$ for $i = 1, 2, \cdots, 9$, to

$$\mathbf{v}^{(i),l} = \begin{cases} \mathbf{v}_1^{(i),l} = \begin{pmatrix} u_1^{(i),l} \\ v_1^{(i),l} \end{pmatrix} \\ = \begin{pmatrix} c_1 + c_2 x + c_3 y + c_4 xy + c_5 x^2 + c_6 y^2 + c_7 x^2 y + c_8 x y^2 + c_9 x^2 y^2 \\ d_1 + d_2 x + d_3 y + d_4 xy + d_5 x^2 + d_6 y^2 + d_7 x^2 y + d_8 x y^2 + d_9 x^2 y^2 \end{pmatrix}, & \text{on } T_1, \\ \mathbf{v}_2^{(i),l} = \begin{pmatrix} u_2^{(i),l} \\ v_2^{(i),l} \end{pmatrix} \\ = \begin{pmatrix} e_1 + e_2 x + e_3 y + e_4 xy + e_5 x^2 + e_6 y^2 + e_7 x^2 y + e_8 x y^2 + e_9 x^2 y^2 \\ f_1 + f_2 x + f_3 y + f_4 xy + f_5 x^2 + f_6 y^2 + f_7 x^2 y + f_8 x y^2 + f_9 x^2 y^2 \end{pmatrix}, & \text{on } T_2. \end{cases} \tag{3.2.35}$$

We further apply the interface jump conditions

$$\mathbf{v}_1 \cdot \boldsymbol{\nu}(D) - \mathbf{v}_2 \cdot \boldsymbol{\nu}(D) = 0, \mathbf{v}_1 \cdot \boldsymbol{\nu}(\frac{D+E}{2}) - \mathbf{v}_2 \cdot \boldsymbol{\nu}(\frac{D+E}{2}) = 0,$$
$$\mathbf{v}_1 \cdot \boldsymbol{\nu}(E) - \mathbf{v}_2 \cdot \boldsymbol{\nu}(E) = 0, \tag{3.2.36a}$$

extended conditions

$$\rho_1 c_1^2 \nabla \cdot \mathbf{v}_1(D) - \rho_2 c_2^2 \nabla \cdot \mathbf{v}_2(D) = 0, \rho_1 c_1^2 \nabla \cdot \mathbf{v}_1(E) - \rho_2 c_2^2 \nabla \cdot \mathbf{v}_2(E) = 0,$$
$$c_1^2 (\nabla \nabla \cdot \mathbf{v}_1) \cdot \vec{v})(\frac{D+E}{2}) - c_2^2 (\nabla \nabla \cdot \mathbf{v}_2) \cdot \vec{v})(\frac{D+E}{2}) = 0, \tag{3.2.36b}$$

curl-free conditions

$$\left(\frac{\partial u_1}{\partial y} - \frac{\partial v_1}{\partial x}\right)(\frac{D+E}{2}) - \left(\frac{\partial u_2}{\partial y} - \frac{\partial v_2}{\partial x}\right)(\frac{D+E}{2}) = 0,$$
$$\left(\frac{\partial^2 u_1}{\partial y \partial x} - \frac{\partial^2 v_1}{\partial^2 x}\right)(\frac{D+E}{2}) - \left(\frac{\partial^2 u_2}{\partial y \partial x} - \frac{\partial^2 v_2}{\partial^2 x}\right)(\frac{D+E}{2}) = 0,$$
$$\left(\frac{\partial^2 u_1}{\partial^2 y} - \frac{\partial^2 v_1}{\partial x \partial y}\right)(\frac{D+E}{2}) - \left(\frac{\partial^2 u_2}{\partial^2 y} - \frac{\partial^2 v_2}{\partial x \partial y}\right)(\frac{D+E}{2}) = 0, \tag{3.2.36c}$$

and consistency conditions

$$\begin{aligned}
&\frac{\partial^3 u_1}{\partial^2 x \partial y}(D) - \frac{\partial^3 u_2}{\partial^2 x \partial y}(D) = 0, \frac{\partial^3 u_1}{\partial x \partial^2 y}(D) - \frac{\partial^3 u_2}{\partial x \partial^2 y}(D) = 0,\\
&\frac{\partial^4 u_1}{\partial^2 x \partial^2 y}(D) - \frac{\partial^4 u_2}{\partial^2 x \partial^2 y}(D) = 0,\\
&\frac{\partial^3 v_1}{\partial^2 x \partial y}(D) - \frac{\partial^3 v_2}{\partial^2 x \partial y}(D) = 0, \frac{\partial^3 v_1}{\partial x \partial^2 y}(D) - \frac{\partial^3 v_2}{\partial x \partial^2 y}(D) = 0,\\
&\frac{\partial^4 v_1}{\partial^2 x \partial^2 y}(D) - \frac{\partial^4 v_2}{\partial^2 x \partial^2 y}(D) = 0.
\end{aligned} \tag{3.2.36d}$$

In this case, an 18×18 linear system is solved to find 18 coefficients a_j, b_j, $j = 1, 2, \cdots, 9$ in (3.2.33) and a 36×33 linear system is solved to find 36 coefficients c_j, d_j, e_j, f_j, $j = 1, 2, \cdots, 9$ in (3.2.35) with 33 conditions for the biquadratic shape function for the velocity. Since the number of conditions is less than the number of unknowns, three extra basis $\mathbf{w}^{(1)}, \mathbf{w}^{(2)}, \mathbf{w}^{(3)}$ are added from the null space of 36×33 matrix.

To construct the biquadratic shape function on an interface element cut by a curved interface, we consider the parametric equation of the curved interface $X(t)$, $-1 \le t \le 1$ satisfying $X(-1) = D$ and $X(1) = E$ and use $X_0 = X(-\sqrt{\frac{3}{5}})$, $X_1 = X(0)$ and $X_2 = X(\sqrt{\frac{3}{5}})$ instead of D, $\frac{D+E}{2}$ and E.

3.2.3 Construction of Non Lagrange IFE Spaces

Non Lagrange IFE shape functions for $\mathcal{R}^k_{\mathbf{v}}(T)$ can be constructed by writing

$$\mathbf{v} = \begin{cases} \mathbf{v}_1 = \sum_{n=0}^{k} \sum_{l=0}^{k} a_j^{n,l} x^n y^l, \text{ on } T_1, \\ \mathbf{v}_2 = \sum_{n=0}^{k} \sum_{l=0}^{k} b_j^{n,l} x^n y^l, \text{ on } T_2, \end{cases} \tag{3.2.37}$$

and applying the jump conditions (3.2.29) to $\mathbf{v}$ to obtain a rectangular linear system $\mathbf{Mc} = \mathbf{b}$ where $\mathbf{c} \in \mathbb{R}^{4(k+1)^2}$ is the vector for all coefficients of $\mathbf{v}$. Here $\mathbf{M}$ is a full row rank rectangular matrix and its nullity is $N = 4(k+1)^2 - (k+1)(2k+1)$. We first compute a basis $\mathbf{c}^{(i)}$, $i = 1, 2, \cdots, N$ of the null space of $\mathbf{M}$ and substitute each $\mathbf{c}^{(i)}$ in (3.2.37) to obtain the associated IFE basis function $\mathbf{v}^{(i)}$.

Before we prove that the resulting matrix is full row rank for bilinear IFE spaces we define the spaces $\mathbf{Q}_1 = Q_1 \times Q_1$, $\mathbf{X}_1 = \mathbf{Q}_1 \times \mathbf{Q}_1$ and the functionals $\mathcal{L}_i : \mathbf{X}_1 \to \mathbb{R}$ such that for

$\mathbf{q} = (\mathbf{v}_1, \mathbf{v}_2) \in \mathbf{X}_1$, $\mathbf{v}_j = [u_j, v_j]^T$, we have

$$\mathcal{L}_1(\mathbf{q}) = \mathbf{v}_1 \cdot \boldsymbol{\nu}(D) - \mathbf{v}_2 \cdot \boldsymbol{\nu}(D), \tag{3.2.38a}$$

$$\mathcal{L}_2(\mathbf{q}) = \mathbf{v}_1 \cdot \boldsymbol{\nu}(E) - \mathbf{v}_2 \cdot \boldsymbol{\nu}(E), \tag{3.2.38b}$$

$$\mathcal{L}_3(\mathbf{q}) = \rho_1 c_1^2 \nabla \cdot \mathbf{v}_1(\frac{D+E}{2}) - \rho_2 c_2^2 \nabla \cdot \mathbf{v}_2(\frac{D+E}{2}), \tag{3.2.38c}$$

$$\mathcal{L}_4(\mathbf{q}) = \left(\frac{\partial u_1}{\partial y} - \frac{\partial v_1}{\partial x}\right)(\frac{D+E}{2}) - \left(\frac{\partial u_2}{\partial y} - \frac{\partial v_2}{\partial x}\right)(\frac{D+E}{2}), \tag{3.2.38d}$$

$$\mathcal{L}_5(\mathbf{q}) = \frac{\partial^2 u_1}{\partial x \partial y} - \frac{\partial^2 u_2}{\partial x \partial y}, \tag{3.2.38e}$$

$$\mathcal{L}_6(\mathbf{q}) = \frac{\partial^2 v_1}{\partial x \partial y} - \frac{\partial^2 v_2}{\partial x \partial y}. \tag{3.2.38f}$$

Lemma 3.2.1. *The functionals (3.2.38) are linearly independent on* $\mathbf{X}_1$ *on all types of interface elements.*

Proof. Assume that

$$\hat{L}(\mathbf{q}) = \sum_{i=1}^{6} C_i \mathcal{L}_i(\mathbf{q}) = 0, \quad \text{for all } \mathbf{q} \in \mathbf{X}_1, \tag{3.2.39}$$

and show that $C_i = 0,\ i = 1, 2, \cdots, 6$ by applying $\hat{L}$ to $\mathbf{q} = [\mathbf{v}_1, \mathbf{v}_2]$ with $\mathbf{v}_2 = [0, 0]^T$.
First, selecting

$$\mathbf{v}_1 = [a_1 x + b_1 y, b_1 x - a_1 y]^T, \tag{3.2.40}$$

one can easily check that $\mathcal{L}_i(\mathbf{q}) = 0,\ i = 3, 4, 5, 6$ for all values of a_1 and b_1.
Next, we select a_1 and b_1 such $\mathcal{L}_1(\mathbf{q}) = 1$ and $\mathcal{L}_2(\mathbf{q}) = 0$ which leads to the equations

$$\mathbf{v}_1 \cdot \boldsymbol{\nu}(D) = 1, \tag{3.2.41}$$

$$\mathbf{v}_1 \cdot \boldsymbol{\nu}(E) = 0. \tag{3.2.42}$$

If $D = (x_D, y_D)^T$ and $E = (x_E, y_E)^T$ we obtain the following linear system

$$\begin{bmatrix} x_D\nu_1 - y_D\nu_2 & y_D\nu_1 + x_D\nu_2 \\ x_E\nu_1 - y_E\nu_2 & y_E\nu_1 + x_E\nu_2 \end{bmatrix} \begin{bmatrix} a_1 \\ b_1 \end{bmatrix} = \begin{bmatrix} 1 \\ 0 \end{bmatrix}, \tag{3.2.43}$$

with determinant $x_D y_E - x_E y_D = \overrightarrow{A_1 D} \cdot \overrightarrow{A_1 E}^{\perp}$ where A_1 is the lower left vertex of an reference interface element shown in Figure 3.2.1. Thus, the matrix is singular if and only if A_1, D and E are colinear which is not allowed for all types of interface elements. Therefore, we can solve for a_1 and b_1 to find non zero $\mathbf{q}^1$ and $\mathbf{q}^2$ such that $\mathcal{L}_i(\mathbf{q}^j) = \delta_{ij},\ i, j = 1, 2$ which shows that $C_1 = 0$ and $C_2 = 0$.
Next we select $\mathbf{v}_1 = [x + y, x + y]^T$ to show that $C_3 = 0$ and $\mathbf{v}_1 = [x - y, x - y]^T$ to show that $C_4 = 0$. Finally, using $\mathbf{v}_1 = [xy, 0]^T$ and $\mathbf{v}_1 = [0, xy]^T$, respectively, we establish that $C_5 = C_6 = 0$ which concludes the proof. □

Now we are ready to define a global immersed discontinuous finite element space as

$$\mathcal{U}_h^k = \{\mathbf{U}_h \mid \mathbf{U}_h|_T \ (Q_k)^3,\ T \in \mathcal{T}_h^S,\ \mathbf{U}_h|_T \in \mathcal{R}_p^k(T) \times \mathcal{R}_{\mathbf{v}}^k(T),\ T \in \mathcal{T}_h^I\}, \tag{3.2.44}$$

where all functions $\mathbf{U}_h$ are fully discontinuous across element boundaries. Furthermore, the IFE shape functions are discontinuous across physical interfaces yielding a discontinuous $\mathbf{U}_h$ across the interface.

We also use the local spaces

$$\mathcal{U}_h^k(T) = \begin{cases} (Q_k)^3, & \text{for } T \in \mathcal{T}_h^S, \\ \mathcal{R}_p^k(T) \times \mathcal{R}_{\mathbf{v}}^k(T), & \text{for } T \in \mathcal{T}_h^I. \end{cases} \tag{3.2.45}$$

3.3 Examples of IFE Shape Functions

We compute bilinear immersed shape functions using (3.2.13) and (3.2.17) for pressure and velocity. The biquadratic immersed shape functions are constructed from (3.2.34) and (3.2.36), respectively, for pressure and velocity. We compute shape functions on $(0,1)^2$ for type I with $D = (0, 0.6)$ and $E = (0.7, 0)$, and type II with $D = (0.4, 1)$ and $(0.7, 0)$ using the parameters $c_1 = 1$, $\rho_1 = 1$, $c_2 = 20$, $\rho_2 = 15$. We plot Lagrange type shape functions for pressure in Figures 3.3.1 and 3.3.6. Lagrange and Non Lagrange type shape functions for velocity are shown in Figures 3.3.2, 3.3.3, 3.3.4, 3.3.5, 3.3.7, 3.3.8, 3.3.9 and 3.3.10. We observe that the shape functions for the velocity are discontinuous across the interface.

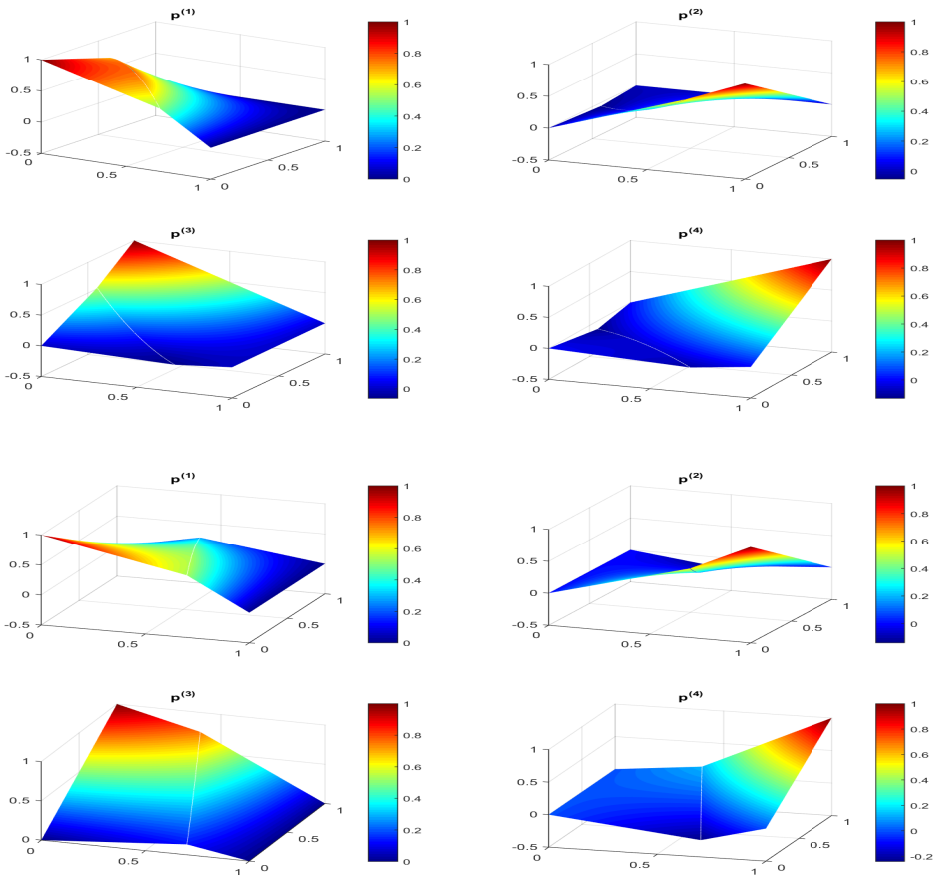

Figure 3.3.1: Lagrange bilinear IFE shape functions for the pressure on element of type I (top) and II (bottom).

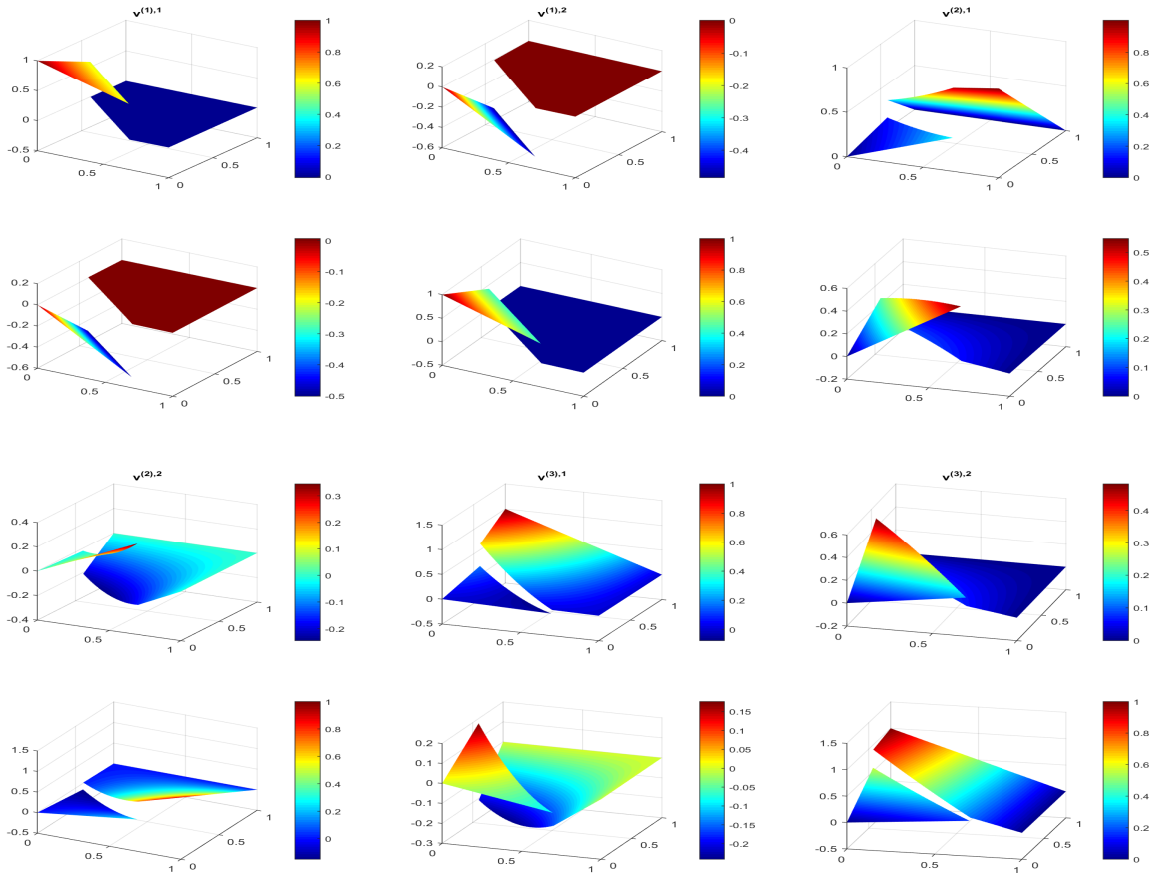

Figure 3.3.2: Lagrange bilinear IFE shape functions $\mathbf{v}^{(i),l}$, $i = 1, 2, 3$, $l = 1, 2$ for the velocity on element of type I.

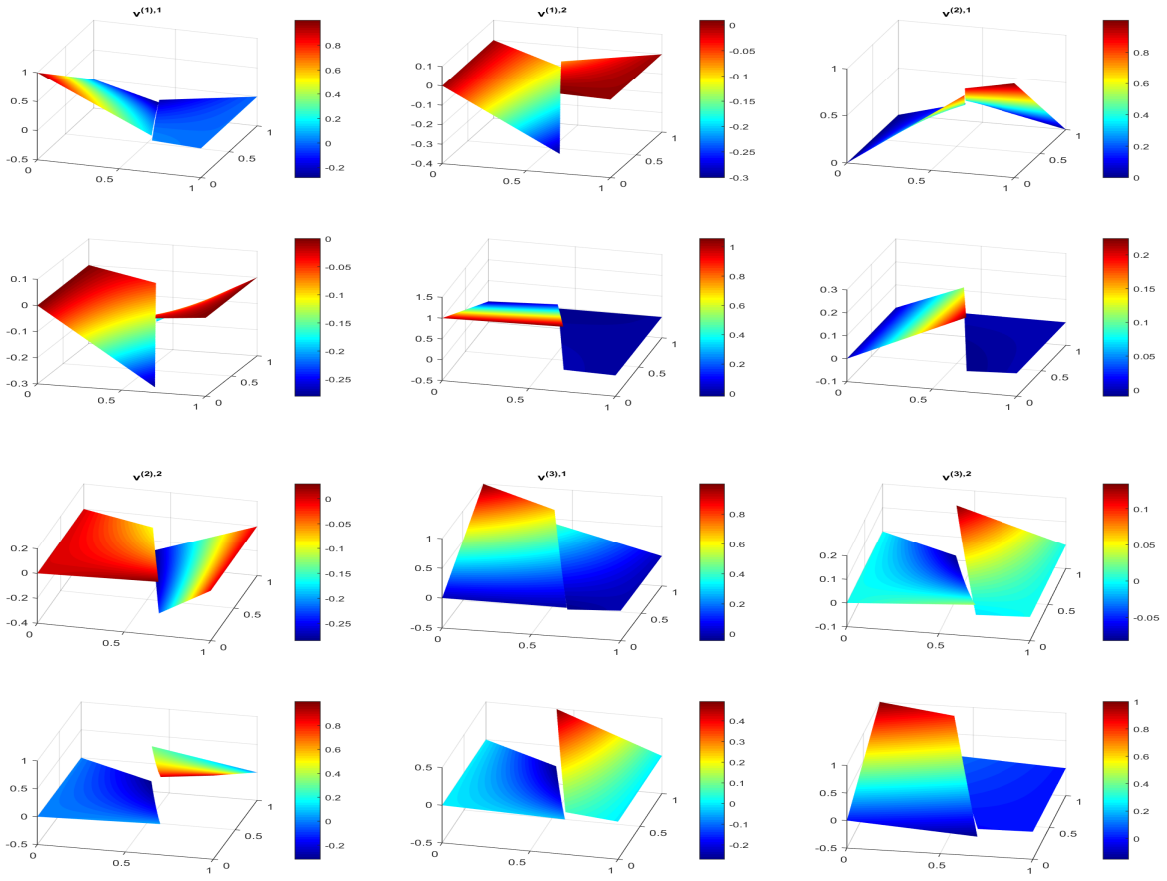

Figure 3.3.3: Lagrange bilinear IFE shape functions $\mathbf{v}^{(i),l}$, $i = 1, 2, 3$, $l = 1, 2$ for the velocity on element of type II.

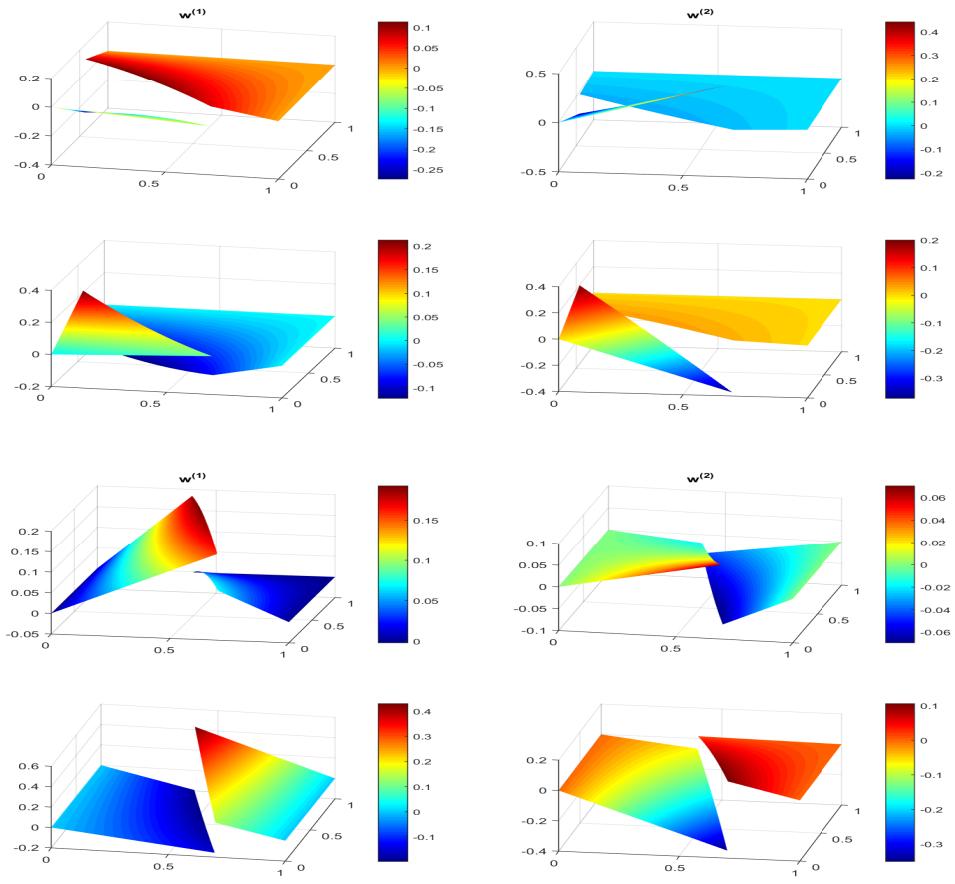

Figure 3.3.4: Lagrange bilinear IFE shape functions $\mathbf{w}^{(i)}$, $i = 1, 2$ for the velocity on element of type I (top) and II (bottom).

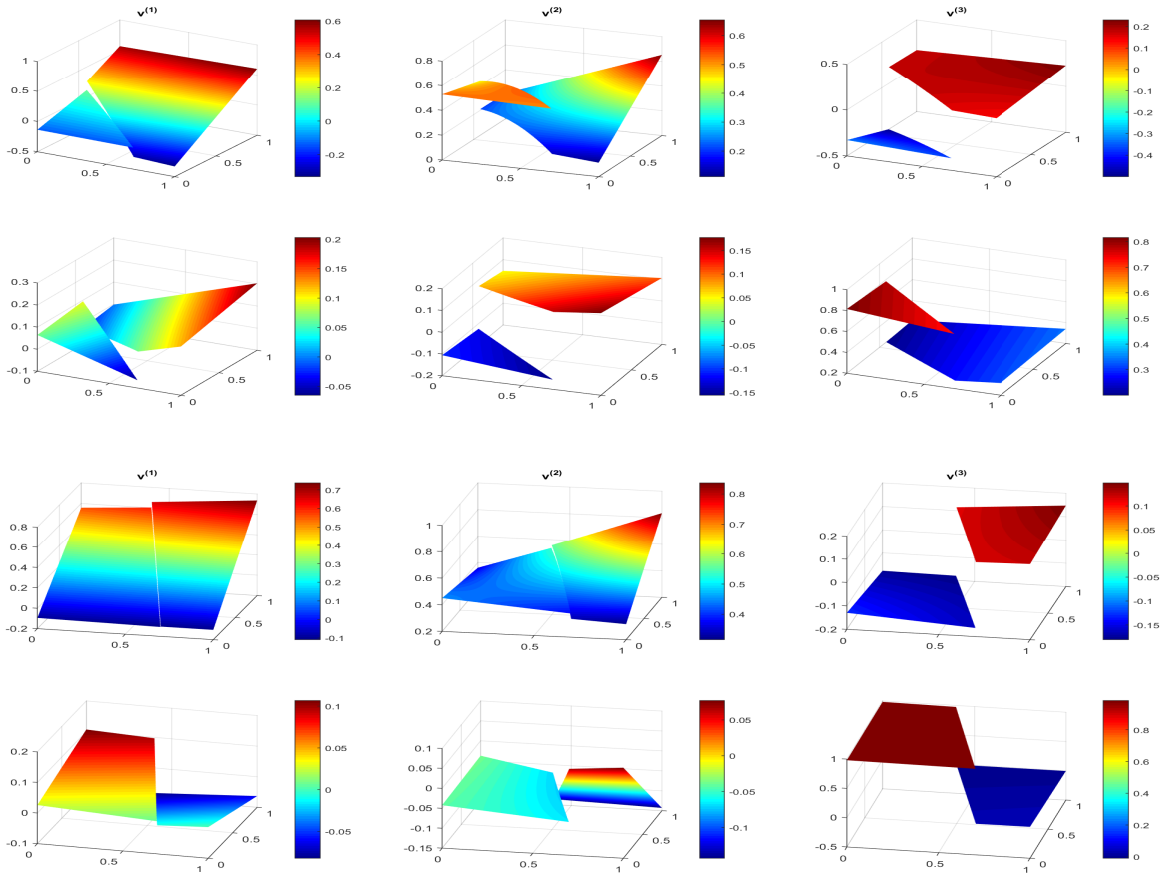

Figure 3.3.5: Non Lagrange bilinear IFE shape functions $\mathbf{v}^{(i)}$, $i = 1, 2, 3$ for the velocity on element of type I (top) and II (bottom).

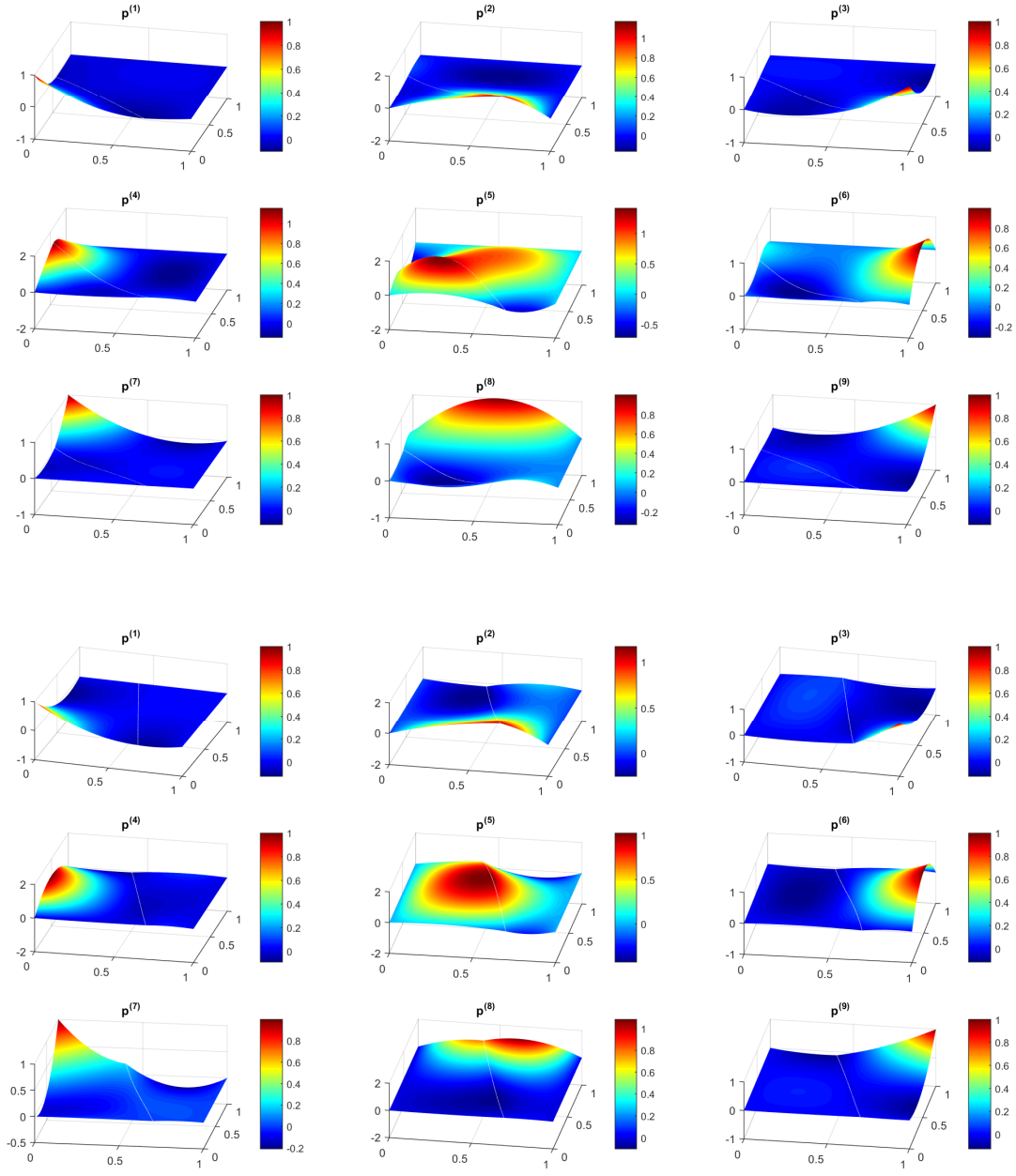

Figure 3.3.6: Lagrange biquadratic IFE shape functions for the pressure on element of type I (top) and II (bottom).

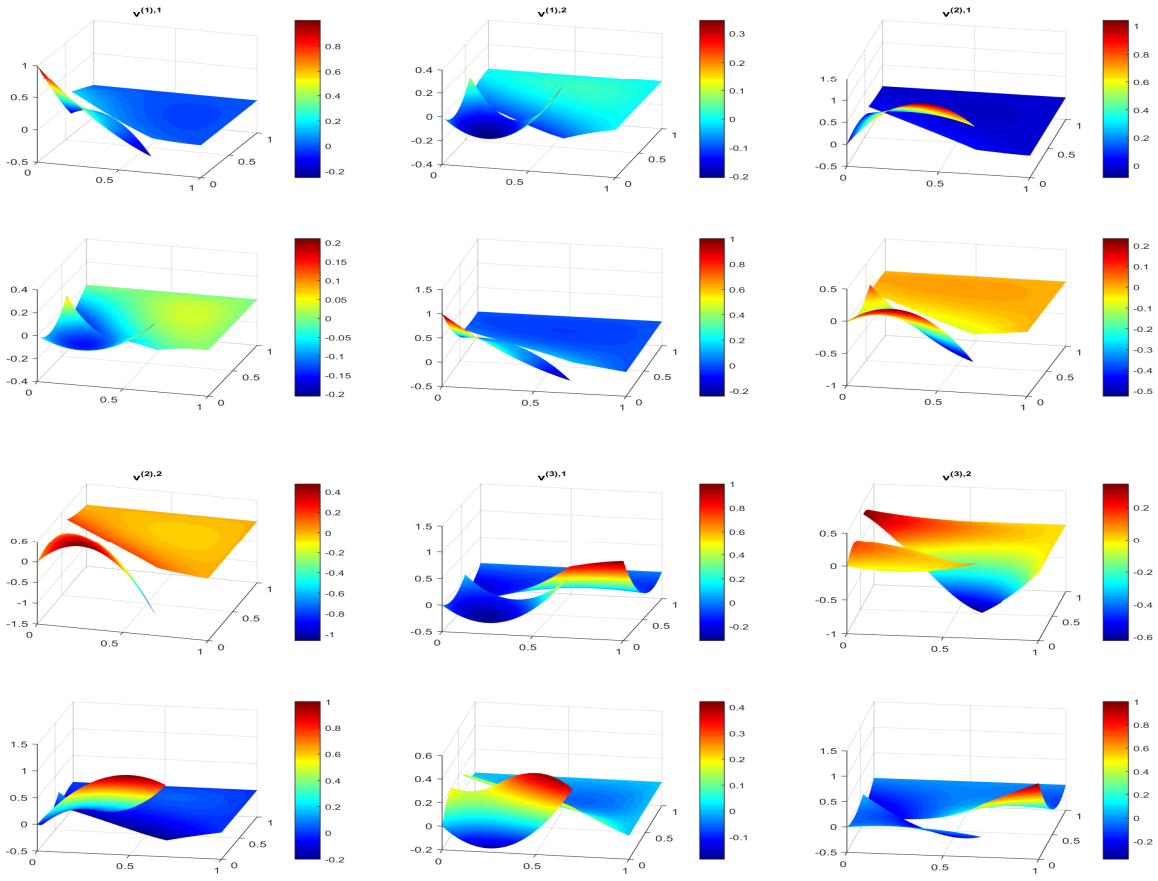

Figure 3.3.7: Lagrange biquadratic IFE shape functions $\mathbf{v}^{(i),l}$, $i = 1, 2, 3$, $l = 1, 2$ for the velocity on element of type I.

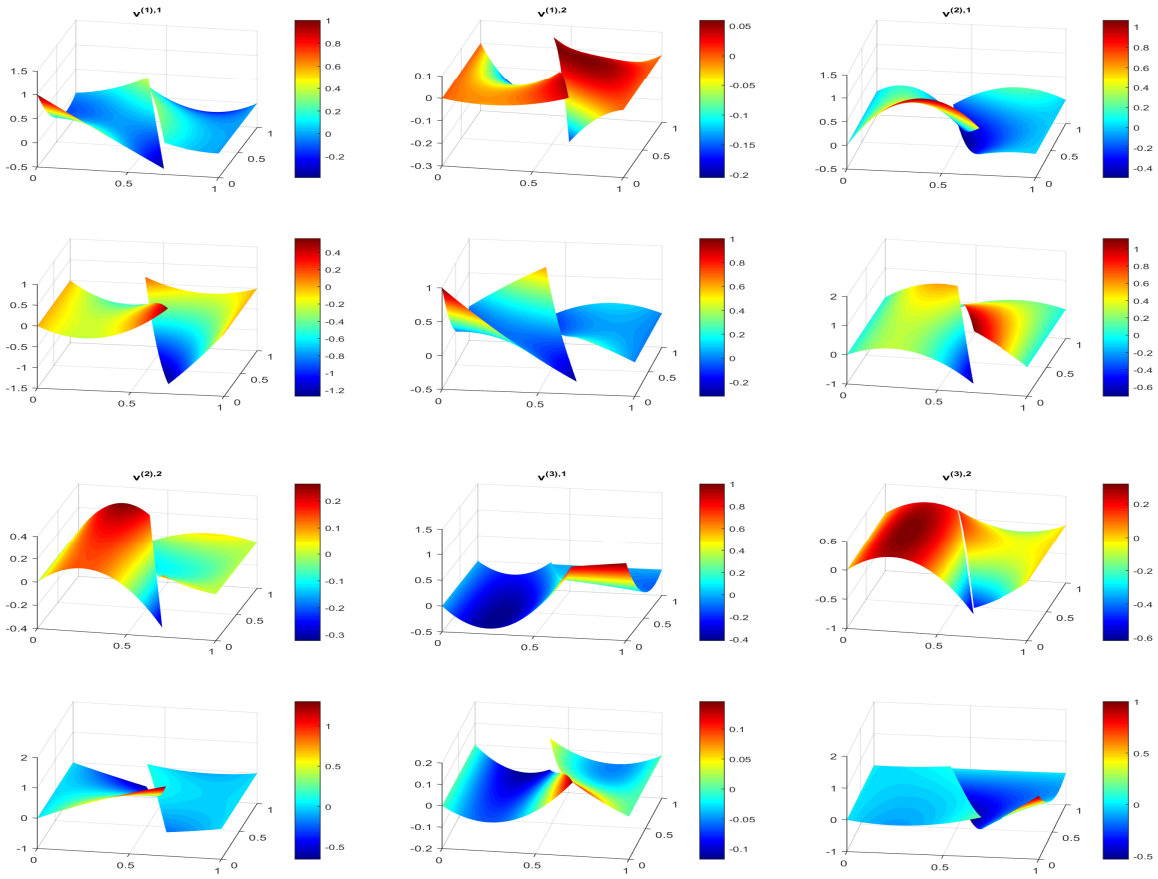

Figure 3.3.8: Lagrange biquadratic IFE shape functions $\mathbf{v}^{(i),l}$, $i = 1, 2, 3$, $l = 1, 2$ for the velocity on element of type II.

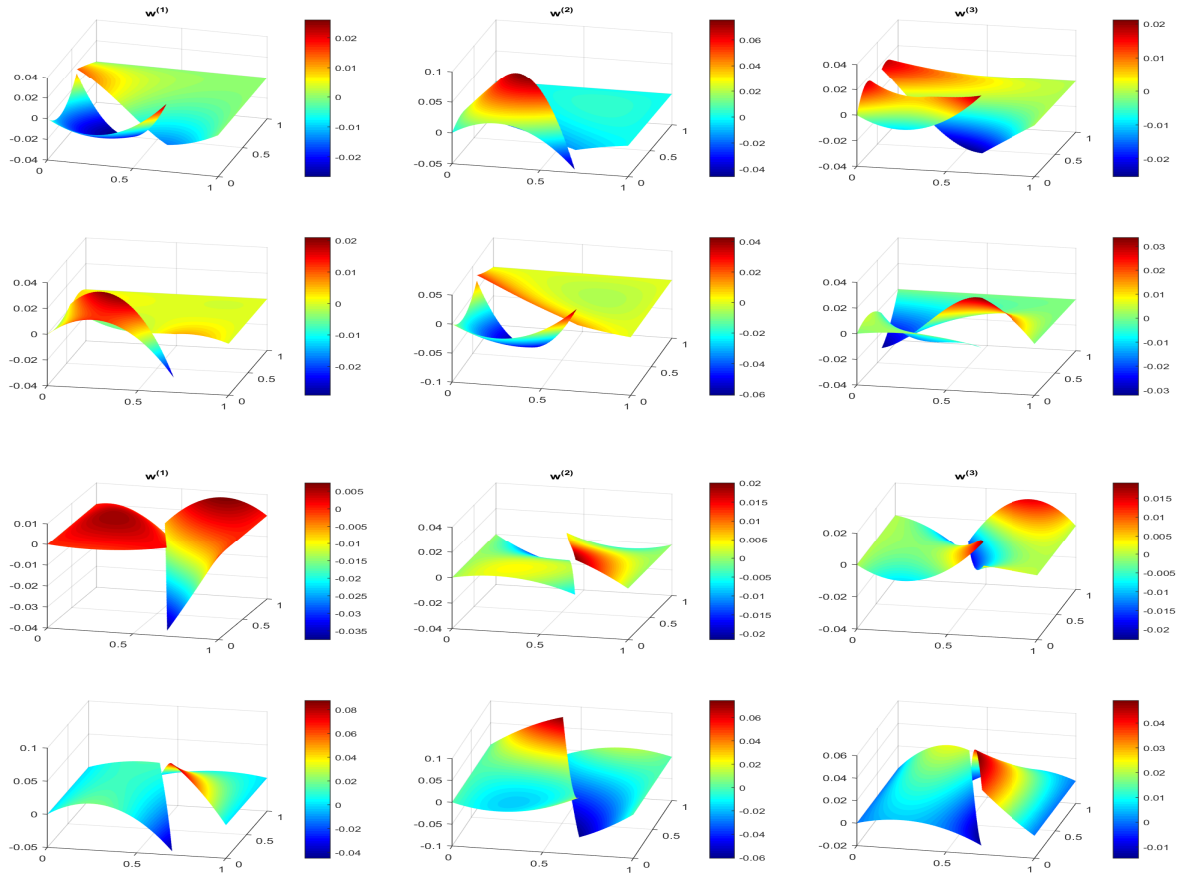

Figure 3.3.9: Lagrange biquadratic IFE shape functions $\mathbf{w}^{(i)}$, $i = 1, 2, 3$ for the velocity on element of type I (top) and II (bottom).

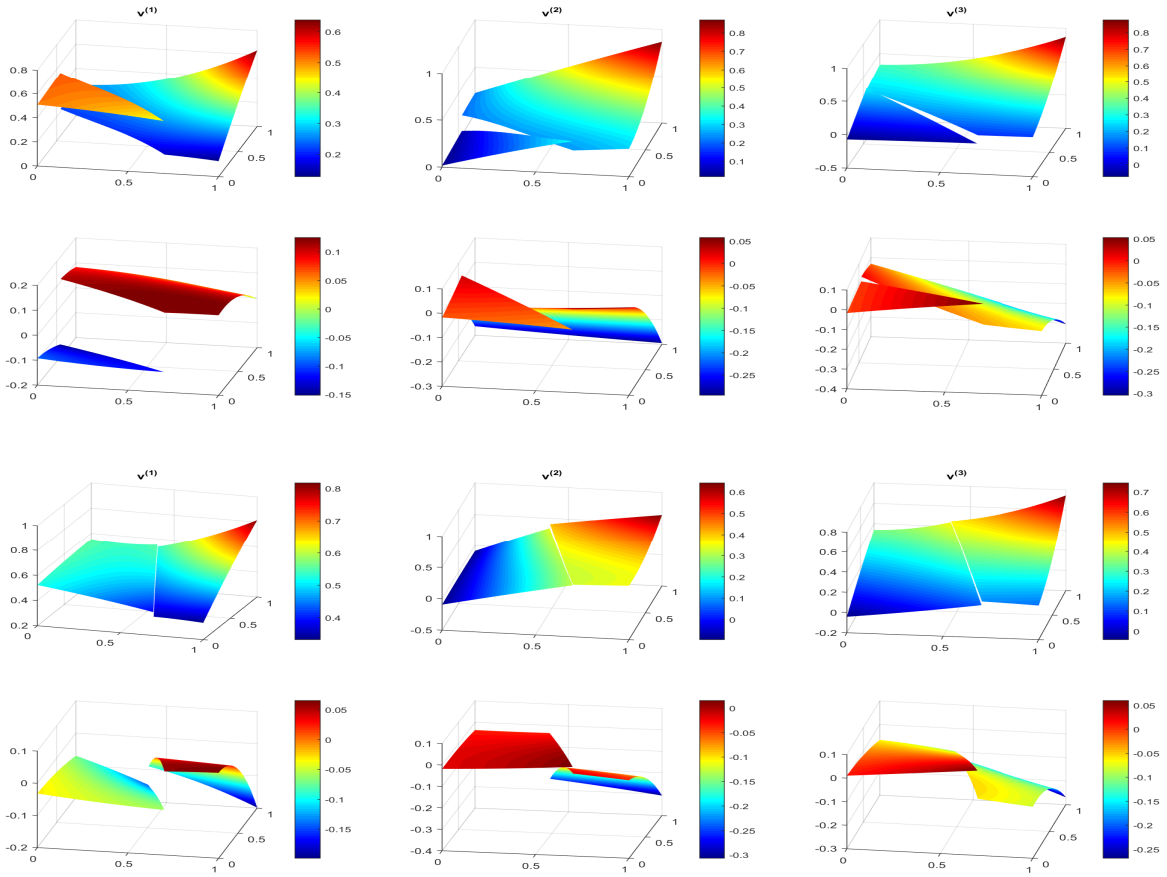

Figure 3.3.10: Non Lagrange biquadratic IFE shape functions $\mathbf{v}^{(i)}$, $i = 1, 2, 3$ for the velocity on element of type I (top) and II (bottom).

3.4 Approximation Capability of the IFE Spaces

Since we constructed IFE spaces, we define the pressure and velocity, the space of piecewise Q_k polynomial functions defined on the mesh such that the pressure $p(x,y,t)|_T$ is approximated by

$$p_h^{(T)} = \begin{cases} \sum_{i=1}^{(k+1)^2} c^{(i)}(t) L_i(x,y), & \text{for } T \in \mathcal{T}_h^S, \\ \sum_{i=1}^{(k+1)^2} c^{(i)}(t) p^{(i)}(x,y), & \text{for } T \in \mathcal{T}_h^I, \end{cases} \tag{3.4.1a}$$

while the velocity $\mathbf{v}(x,y,t)|_T$ is approximated by

$$\mathbf{v}_h^{(T)} = \begin{cases} \sum_{l=1}^{2} \sum_{i=1}^{(k+1)^2} c^{(i),l}(t) \mathbf{L}^{(i),l}(x,y), & \text{for } T \in \mathcal{T}_h^S, \\ \sum_{l=1}^{2} \sum_{i=1}^{(k+1)^2} c^{(i),l}(t) \mathbf{v}^{(i),l}(x,y) + \sum_{i=1}^{(k+1)} d^{(i)}(t) \mathbf{w}^{(i)}(x,y), & \text{for } T \in \mathcal{T}_h^I. \end{cases} \tag{3.4.1b}$$

Thus, $\mathbf{U}$ is approximated as

$$\mathbf{U}|_T = [p|_T, (\mathbf{v}|_T)^T]^T \approx \mathbf{U}_h|_T = [p_h^{(T)}, (\mathbf{v}_h^{(T)})^T]^T. \tag{3.4.1c}$$

Now in order to measure the approximation capability of the IFE spaces, we define the true solution of the two dimensional acoustic interface problem (3.1.2), we follow [68, 69]. First, we consider the initial condition

$$\mathbf{U}_0(x,y) = \mathcal{A}_i \psi(\mathbf{k}_i \cdot \mathbf{x} - \omega_c t_0) \mathbf{Z}_i, \tag{3.4.2}$$

where $\mathbf{x} = (x,y)^T$,

$$\psi(\xi) = \sin(\xi) e^{-4\xi^2}, \tag{3.4.3}$$

$\mathbf{Z}_i = [1, \frac{\alpha}{\rho_1 c_1}, \frac{\beta}{\rho_1 c_1}]^T$ and $\mathbf{k}_i = \frac{\omega_c}{c_1}(\alpha,\beta)^T$ with $\alpha^2 + \beta^2 = 1$. Finally, w_c is the wave frequency and $\mathcal{A}_i = 1$ is the amplitude of incident wave. The incident wave starts in Ω_1 and moves with speed c_1 in the direction of the vector $(\alpha,\beta)^T$ until it hits the linear interface to generate a reflected and a transmitted waves as illustrated in Figure 3.4.1. Thus, the true solution can be written as

$$\mathbf{U}(x,y,t) = \begin{cases} \mathbf{U}_i(x,y,t) + \mathbf{U}_r(x,y,t), & \text{if } (x,y) \in \Omega_1, \\ \mathbf{U}_t(x,y,t), & \text{if } (x,y) \in \Omega_2, \end{cases} \tag{3.4.4a}$$

where

$$\mathbf{U}_i = \mathcal{A}_i \psi(\mathbf{k}_i \cdot \mathbf{x} - \omega_c(t+t_0)) \mathbf{Z}_i, \quad \text{(incident wave)} \tag{3.4.4b}$$

$$\mathbf{U}_r = \mathcal{A}_r \psi(\mathbf{k}_r \cdot \mathbf{x} - \omega_c(t+t_0)) \mathbf{Z}_r, \quad \text{(reflected wave)} \tag{3.4.4c}$$

$$\mathbf{U}_t = \mathcal{A}_t \psi(\mathbf{k}_t \cdot \mathbf{x} - \omega_c(t+t_0)) \mathbf{Z}_t, \quad \text{(transmitted wave)} \tag{3.4.4d}$$

with $\mathbf{Z}_r = [1, \frac{\alpha_r}{\rho_1 c_1}, \frac{\beta_r}{\rho_1 c_1}]^T$ and $\mathbf{Z}_t = [1, \frac{\alpha_t}{\rho_2 c_2}, \frac{\beta_t}{\rho_2 c_2}]^T$, $\mathcal{A}_i = 1$, $\mathcal{A}_r, \mathcal{A}_t$, respectively, are the amplitudes of incident, reflected and transmitted waves. The direction vectors $\mathbf{k}_r = (\alpha_r, \beta_r)^T$, $\mathbf{k}_t = (\alpha_t, \beta_t)^T$ are given by

$$\mathbf{k}_r = \frac{\omega_c}{c_1}(-\alpha\cos^2\theta + 2\beta\cos\theta\sin\theta + \alpha\sin^2\theta, \beta\cos^2\theta + 2\alpha\cos\theta\sin\theta - \beta\sin^2\theta)^T,$$

$$\mathbf{k}_t = \frac{\omega_c}{c_2}\left(\sqrt{1-\left(\frac{c_2}{c_1}\right)^2(\alpha\sin\theta+\beta\cos\theta)^2}\ \cos\theta + \frac{c_2}{c_1}(\alpha\sin\theta+\beta\cos\theta)\sin\theta,\right.$$

$$\left.-\sqrt{1-\left(\frac{c_2}{c_1}\right)^2(\alpha\sin\theta+\beta\cos\theta)^2}\sin\theta + \frac{c_2}{c_1}(\alpha\sin\theta+\beta\cos\theta)\cos\theta\right)^T.$$

The amplitudes are given by

$$\mathcal{A}_r = \frac{\rho_2 c_2\cos\theta_1 - \rho_1 c_1\cos\theta_2}{\rho_2 c_2\cos\theta_1 + \rho_1 c_1\cos\theta_2}\mathcal{A}_i, \qquad \mathcal{A}_t = \frac{2\rho_2 c_2\cos\theta_1}{\rho_2 c_2\cos\theta_1+\rho_1 c_1\cos\theta_2}\mathcal{A}_i, \tag{3.4.4e}$$

where the angles θ, θ_1 and θ_2 are shown in Figure 3.4.1.

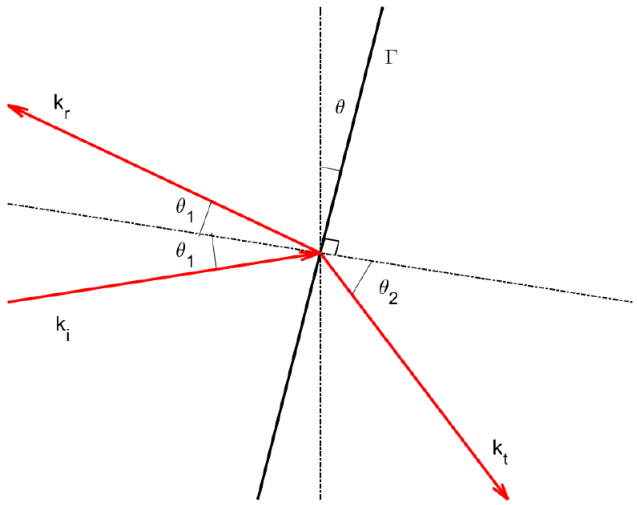

Figure 3.4.1: Sketch of the incident, reflected and transmitted directions for an oblique linear interface.

We show the approximation capability of the IFE spaces by showing the L^2 projection errors and orders of convergence on uniform Cartesian meshes having $N = 100^2, 150^2, 200^2, 250^2, 300^2, 350^2, 400^2$ and present the results in Tables 3.4.1 and 3.4.2 which suggest optimal convergence rates.

Example 3.4.1.

Let us consider the acoustic interface problem (3.1.2) on the domain $\Omega = (0, 20)^2$ divided by the linear interface $\Gamma = \{(x, y) \mid y = -5x + 70.05555\}$ into $\Omega_1 = \{(x, y) \in \Omega \mid y < -5x + 70.05555\}$ and $\Omega_2 = \{(x, y) \in \Omega \mid y > -5x + 70.05555\}$. We assume that for the medium occupying Ω_1, $c_1 = 1m/s$, $\rho_1 = 1kg/m^3$ and for the medium occupying Ω_2, $c_2 = 2m/s$, $\rho_2 = 1.5kg/m^3$. Moreover, the problem is subjected to the initial condition (3.4.2) with $t_0 = 13.6649$, $\omega_c = 1$, $(\alpha, \beta) = (2, 1)/\sqrt{5}$.

Bilinear						
N	$\frac{\|p-p_h\|_{L^2}}{\|p\|_{L^2}}$	Order	$\frac{\|u-u_h\|_{L^2}}{\|u\|_{L^2}}$	Order	$\frac{\|v-v_h\|_{L^2}}{\|v\|_{L^2}}$	Order
100^2	9.7237e-3	NA	1.8370e-2	NA	1.2727e-2	NA
150^2	4.3503e-3	1.9837	8.2303e-3	1.9802	5.7116e-3	1.9761
200^2	2.4527e-3	1.9920	4.6424e-3	1.9904	3.2254e-3	1.9864
250^2	1.5713e-3	1.9953	2.9749e-3	1.9943	2.0685e-3	1.9908
300^2	1.0918e-3	1.9969	2.0673e-3	1.9963	1.4382e-3	1.9931
350^2	8.0243e-4	1.9978	1.5194e-3	1.9974	1.0575e-3	1.9946
400^2	6.1448e-4	1.9985	1.1636e-3	1.9980	8.1015e-4	1.9957
Biquadratic						
N	$\frac{\|p-p_h\|_{L^2}}{\|p\|_{L^2}}$	Order	$\frac{\|u-u_h\|_{L^2}}{\|u\|_{L^2}}$	Order	$\frac{\|v-v_h\|_{L^2}}{\|v\|_{L^2}}$	Order
100^2	7.5444e-4	NA	1.4945e-3	NA	9.8789e-4	NA
150^2	2.2584e-4	2.9748	4.4994e-4	2.9606	2.9586e-4	2.9736
200^2	9.5608e-5	2.9879	1.9118e-4	2.9751	1.2533e-4	2.9857
250^2	4.9029e-5	2.9929	9.8280e-5	2.9820	6.4305e-5	2.9905
300^2	2.8397e-5	2.9954	5.7020e-5	2.9861	3.7260e-5	2.9931
350^2	1.7891e-5	2.9968	3.5967e-5	2.9892	2.3482e-5	2.9951
400^2	1.1992e-5	2.9963	2.4203e-5	2.9665	1.5761e-5	2.9860

Table 3.4.1: L^2 relative errors and orders of convergence for the bilinear and biquadratic IFE spaces at $t = 5$ for Example 3.4.1.

Example 3.4.2.

Let us consider the acoustic interface problem (3.1.2) consists of the water/air on the domain $\Omega = (0, 200)^2$ divided by the linear interface $\Gamma = \{(x, y) \mid y = -5x + 700.05555\}$ into $\Omega_1 = \{(x, y) \in \Omega \mid y < -5x + 700.05555\}$ and $\Omega_2 = \{(x, y) \in \Omega \mid y > -5x + 700.05555\}$. The physical parameters for water/air are $c_1 = 1450m/s$, $\rho_1 = 1000kg/m^3$, $c_2 = 340m/s$, $\rho_2 = 1.3kg/m^3$. The problem is subjected to the initial condition (3.4.2) with $t_0 = 0.1244$, $\omega_c = 100$, $(\alpha, \beta) = (2, 1)/\sqrt{5}$.

Bilinear						
N	$\frac{\|p-p_h\|_{L^2}}{\|p\|_{L^2}}$	Order	$\frac{\|u-u_h\|_{L^2}}{\|u\|_{L^2}}$	Order	$\frac{\|v-v_h\|_{L^2}}{\|v\|_{L^2}}$	Order
100^2	9.7724e-3	NA	9.4544e-2	NA	8.1467e-2	NA
150^2	4.3594e-3	1.9909	4.5645e-2	1.7959	3.9229e-2	1.8023
200^2	2.4553e-3	1.9956	2.6484e-2	1.8922	2.2739e-2	1.8957
250^2	1.5723e-3	1.9975	1.7215e-2	1.9304	1.4773e-2	1.9327
300^2	1.0922e-3	1.9983	1.2062e-2	1.9509	1.0348e-2	1.9527
350^2	8.0256e-4	1.9988	8.9127e-3	1.9631	7.6442e-3	1.9645
400^2	6.1453e-4	1.9992	6.8503e-3	1.9709	5.8744e-3	1.9721
Biquadratic						
N	$\frac{\|p-p_h\|_{L^2}}{\|p\|_{L^2}}$	Order	$\frac{\|u-u_h\|_{L^2}}{\|u\|_{L^2}}$	Order	$\frac{\|v-v_h\|_{L^2}}{\|v\|_{L^2}}$	Order
100^2	5.8930e-4	NA	2.2813e-2	NA	1.9729e-2	NA
150^2	1.7305e-4	3.0221	7.5375e-3	2.7313	6.4920e-3	2.7414
200^2	7.2612e-5	3.0187	3.3250e-3	2.8449	2.8588e-3	2.8510
250^2	3.7047e-5	3.0158	1.7408e-3	2.9001	1.4953e-3	2.9044
300^2	2.1386e-5	3.0135	1.0208e-3	2.9275	8.7628e-4	2.9309
350^2	1.3443e-5	3.0118	6.4839e-4	2.9441	5.5637e-4	2.9468
400^2	8.9934e-6	3.0105	4.3699e-4	2.9549	3.7486e-4	2.9572

Table 3.4.2: L^2 relative errors and orders of convergence for the bilinear and biquadratic IFE spaces at $t = 0.02$ for Example 3.4.2.

3.5 Other Conditions for IFE Shape Functions

IFE shape functions for pressure are generated by using interface and consistency conditions. Additional curl-free condition is added to generate IFE shape functions for velocity but not necessary. Thus, there are the other combinations of conditions to generate IFE shape functions.

We note that the number of curl-free conditions is $\frac{k(k+1)}{2}$ and if the curl-free conditions are omitted we obtain $\frac{k(k+1)}{2}$ extra IFE shape functions for the velocity. Here we construct bilinear and biquadratic IFE spaces using the parameters of Example 3.4.1 without curl-free conditions. We compute the L^2 projection of the exact solution onto the IFE spaces on 100^2, 150^2, 200^2, 250^2, 300^2, 350^2, 400^2 elements. We show in Table 3.5.1 and plot the errors in Figure 3.5.1. These spaces have optimal approximation capabilities and match those of curl-free spaces. We finally note that curl-free IFE spaces may be more efficient since they lead to smaller IFE spaces.

Bilinear						
N	$\frac{\|p-p_h\|_{L^2}}{\|p\|_{L^2}}$	Order	$\frac{\|u-u_h\|_{L^2}}{\|u\|_{L^2}}$	Order	$\frac{\|v-v_h\|_{L^2}}{\|v\|_{L^2}}$	Order
100^2	9.7237e-3	NA	1.8371e-2	NA	1.2687e-2	NA
150^2	4.3503e-3	1.9837	8.2303e-3	1.9803	5.6996e-3	1.9735
200^2	2.4527e-3	1.9920	4.6423e-3	1.9904	3.2204e-3	1.9845
250^2	1.5713e-3	1.9953	2.9749e-3	1.9943	2.0659e-3	1.9895
300^2	1.0918e-3	1.9969	2.0673e-3	1.9963	1.4367e-3	1.9920
350^2	8.0243e-4	1.9978	1.5195e-3	1.9973	1.0566e-3	1.9936
400^2	6.1448e-4	1.9985	1.1636e-3	1.9982	8.0952e-4	1.9948
Biquadratic						
N	$\frac{\|p-p_h\|_{L^2}}{\|p\|_{L^2}}$	Order	$\frac{\|u-u_h\|_{L^2}}{\|u\|_{L^2}}$	Order	$\frac{\|v-v_h\|_{L^2}}{\|v\|_{L^2}}$	Order
100^2	7.5444e-4	NA	1.4945e-3	NA	9.8937e-4	NA
150^2	2.2584e-4	2.9748	4.4992e-4	2.9608	2.9630e-4	2.9736
200^2	9.5608e-5	2.9879	1.9118e-4	2.9750	1.2548e-4	2.9868
250^2	4.9029e-5	2.9929	9.8277e-5	2.9820	6.4358e-5	2.9920
300^2	2.8397e-5	2.9954	5.7017e-5	2.9861	3.7279e-5	2.9949
350^2	1.7891e-5	2.9968	3.5967e-5	2.9890	2.3490e-5	2.9960
400^2	1.1992e-5	2.9963	2.4206e-5	2.9655	1.5766e-5	2.9860

Table 3.5.1: L^2 relative errors and orders of convergence for the bilinear and biquadratic IFE spaces at $t = 5$ for Example 3.4.1 without curl-free condition.

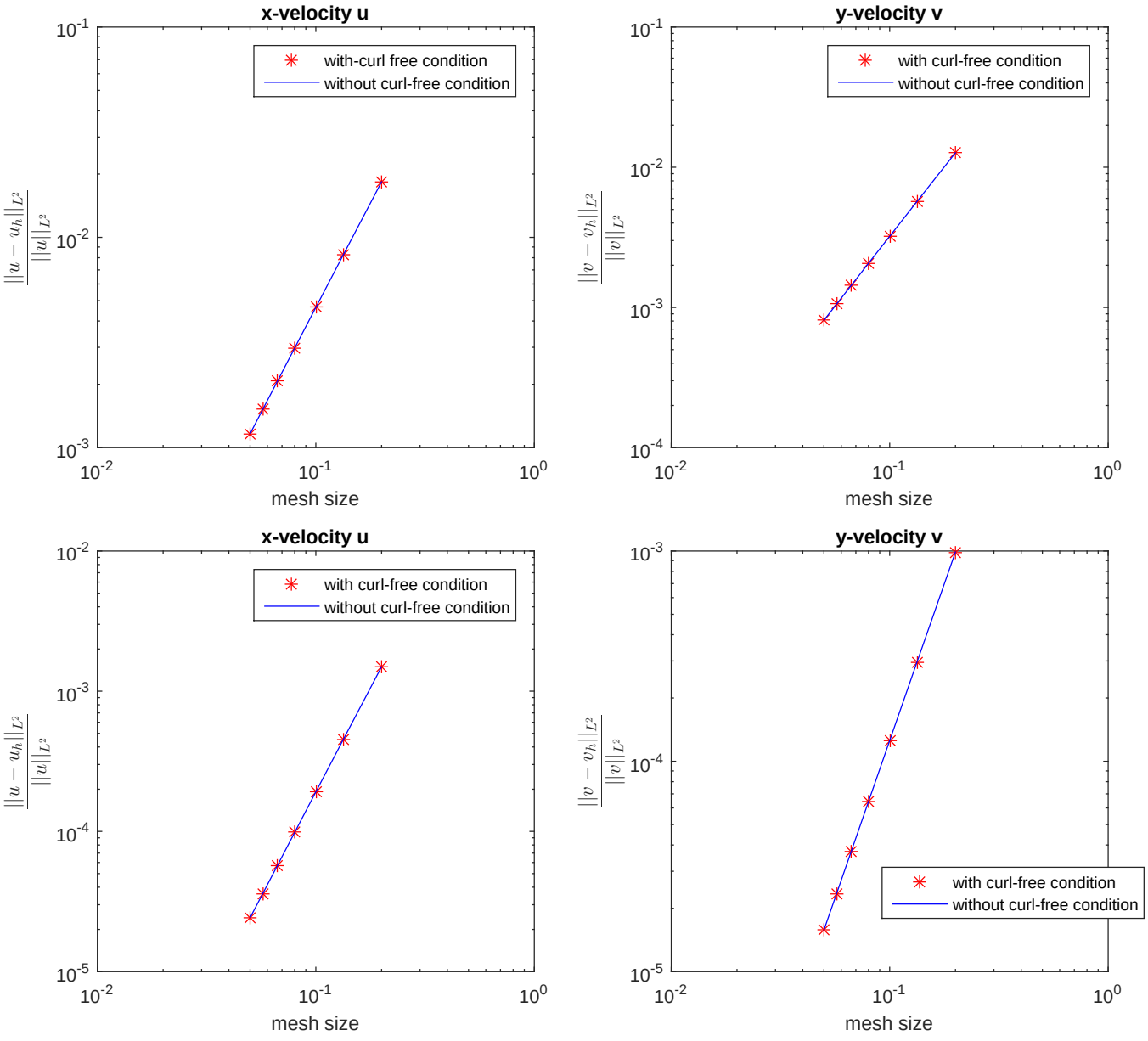

Figure 3.5.1: L^2 relative errors for velocity using bilinear (top) and biquadratic (bottom) IFE spaces with curl-free conditions ($*$) and without (solid) for Example 3.4.1.

Chapter 4

Immersed Discontinuous Galerkin Formulations for the Two Dimensional Acoustic Problem

4.1 Spatial Discretization

We consider three discontinuous finite element formulations, a discontinuous Gakerkin method, a discontinuous Galerkin method applied to the scaled problem and Petrov-Galerkin method. At the end of this section we discuss integration schemes to compute integrals on interface elements.

We partition the domain Ω into N^2 square elements and use standard Lagrange shape functions on non interface elements and IFE shape functions on interface elements. We construct an immersed discontinuous Galerkin finite element method to solve the system (3.1.2a).

4.1.1 Standard Discontinuous Galerkin Formulation

The weak DG formulation on a non interface element shown in Figure 4.1.1 is obtained by multiplying (3.1.2a) by a test vector function $\mathbf{V}$, integrating over the element and applying the divergence theorem to obtain

$$\int_T \mathbf{V}^T \frac{\partial \mathbf{U}}{\partial t} dxdy + \int_{\Gamma_2^+} \mathbf{V}^T \mathbf{A}\mathbf{U} dy - \int_{\Gamma_2^-} \mathbf{V}^T \mathbf{A}\mathbf{U} dy \tag{4.1.1}$$
$$+ \int_{\Gamma_1^+} \mathbf{V}^T \mathbf{B}\mathbf{U} dx - \int_{\Gamma_1^-} \mathbf{V}^T \mathbf{B}\mathbf{U} dx - \int_T \frac{\partial \mathbf{V}^T}{\partial x} \mathbf{A}\mathbf{U} dxdy - \int_T \frac{\partial \mathbf{V}^T}{\partial y} \mathbf{B}\mathbf{U} dxdy = 0.$$

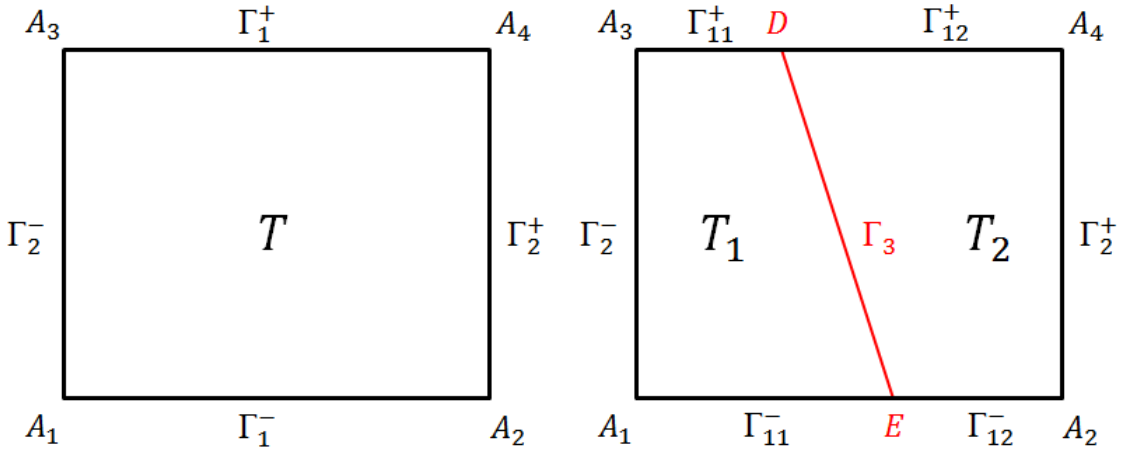

Figure 4.1.1: Non interface and interface elements.

We obtain the discrete weak DG formulation by: *(i)* replacing $\mathbf{U}$ by $\mathbf{U}_h \in \mathcal{U}_h^k$ given in (3.4.1), *(ii)* testing against $\mathbf{V}_h \in (Q_k)^3$ and *(iii)* defining the numerical flux $(\widehat{\mathbf{BU}_h})|_{\Gamma_1^\pm}$ for a discontinuous $\mathbf{U}_h$ across $\Gamma_1^\pm$ by

$$\widehat{\mathbf{BU}_h}|_{\Gamma_1^+} = \mathbf{B}^+\mathbf{U}_h^+ + \mathbf{B}^-\mathbf{U}_h^-, \ \widehat{\mathbf{BU}_h}|_{\Gamma_1^-} = \mathbf{B}^+\mathbf{U}_h^- + \mathbf{B}^-\mathbf{U}_h^+. \tag{4.1.2a}$$

Similarly on $\Gamma_2^\pm$ we use

$$\widehat{\mathbf{AU}_h}|_{\Gamma_2^+} = \mathbf{A}^+\mathbf{U}_h^+ + \mathbf{A}^-\mathbf{U}_h^-, \ \widehat{\mathbf{AU}_h}|_{\Gamma_2^-} = \mathbf{A}^+\mathbf{U}_h^- + \mathbf{A}^-\mathbf{U}_h^+, \tag{4.1.2b}$$

where $\mathbf{U}_h^\pm(\mathbf{x}) = \lim_{\epsilon\to 0^\pm} \mathbf{U}_h(\mathbf{x} - \epsilon\boldsymbol{n})$. Here $\boldsymbol{n} = (n_x, n_y)^T$ is the outward unit normal vector at a point $\mathbf{x}$ on the boundary of T.

The immersed discontinuous Galerkin solution $\mathbf{U}_h$ satisfies

$$\begin{aligned}
&\int_T \mathbf{V}_h^T \frac{\partial \mathbf{U}_h}{\partial t} dxdy + \int_{\Gamma_2^+} \mathbf{V}_h^{+T} \mathbf{A}^+ \mathbf{U}_h^+ dy + \int_{\Gamma_2^+} \mathbf{V}_h^{+T} \mathbf{A}^- \mathbf{U}_h^- dy - \int_{\Gamma_2^-} \mathbf{V}_h^{+T} \mathbf{A}^+ \mathbf{U}_h^- dy \\
&- \int_{\Gamma_2^-} \mathbf{V}_h^{+T} \mathbf{A}^- \mathbf{U}_h^+ dy + \int_{\Gamma_1^+} \mathbf{V}_h^{+T} \mathbf{B}^+ \mathbf{U}_h^+ dx + \int_{\Gamma_1^+} \mathbf{V}_h^{+T} \mathbf{B}^- \mathbf{U}_h^- dx - \int_{\Gamma_1^-} \mathbf{V}_h^{+T} \mathbf{B}^+ \mathbf{U}_h^- dx \\
&- \int_{\Gamma_1^-} \mathbf{V}_h^{+T} \mathbf{B}^- \mathbf{U}_h^+ dx - \int_T \frac{\partial \mathbf{V}_h^T}{\partial x} \mathbf{A} \mathbf{U}_h dxdy - \int_T \frac{\partial \mathbf{V}_h^T}{\partial y} \mathbf{B} \mathbf{U}_h dxdy = 0, \ \forall \ \mathbf{V}_h \in (Q_k)^3.
\end{aligned} \tag{4.1.3}$$

Next, let us consider an interface element of type II cut by the interface Γ into T_1 and T_2 and $T = T_1 \cup T_2$ as illustrated in Figure 4.1.1. Here $\Gamma_3 = \overline{DE}$ for bilinear IFE spaces and $\Gamma_3 = \widetilde{DE}$ for $k >$ 1-degree IFE spaces.

Let us multiply (3.1.2a) by a test function $\mathbf{V}$, integrate over T_1 and apply the divergence theorem to obtain the weak formulation

$$\int_{T_1} \mathbf{V}_1^T \frac{\partial \mathbf{U}_1}{\partial t} dxdy + \int_{\Gamma_3} \mathbf{V}_1^T (n_{1x}\mathbf{A}_1 + n_{1y}\mathbf{B}_1)\mathbf{U}_1 ds - \int_{\Gamma_2^-} \mathbf{V}_1^T \mathbf{A}_1 \mathbf{U}_1 dy + \int_{\Gamma_{11}^+} \mathbf{V}_1^T \mathbf{B}_1 \mathbf{U}_1 dx$$
$$- \int_{\Gamma_{11}^-} \mathbf{V}_1^T \mathbf{B}_1 \mathbf{U}_1 dx - \int_{T_1} \frac{\partial \mathbf{V}_1^T}{\partial x} \mathbf{A}_1 \mathbf{U}_1 dxdy - \int_{T_1} \frac{\partial \mathbf{V}_1^T}{\partial y} \mathbf{B}_1 \mathbf{U}_1 dxdy = 0. \tag{4.1.4}$$

Similarly on T_2 we write

$$\int_{T_2} \mathbf{V}_2^T \frac{\partial \mathbf{U}_2}{\partial t} dxdy + \int_{\Gamma_2^+} \mathbf{V}_2^T \mathbf{A}_2 \mathbf{U}_2 dy + \int_{\Gamma_3} \mathbf{V}_2^T (n_{2x}\mathbf{A}_2 + n_{2y}\mathbf{B}_2)\mathbf{U}_2 ds + \int_{\Gamma_{12}^+} \mathbf{V}_2^T \mathbf{B}_2 \mathbf{U}_2 dx$$
$$- \int_{\Gamma_{12}^-} \mathbf{V}_2^T \mathbf{B}_2 \mathbf{U}_2 dx - \int_{T_2} \frac{\partial \mathbf{V}_2^T}{\partial x} \mathbf{A}_2 \mathbf{U}_2 dxdy - \int_{T_2} \frac{\partial \mathbf{V}_2^T}{\partial y} \mathbf{B}_2 \mathbf{U}_2 dxdy = 0. \tag{4.1.5}$$

Adding (4.1.4) and (4.1.5), replacing $\mathbf{U}$ by $\mathbf{U}_h \in \mathcal{U}_h^k$ and $\mathbf{V}$ by $\mathbf{V}_h \in \mathcal{U}_h^k(T)$ and applying numerical flux (4.1.2) to the terms on the boundary of T, $\mathbf{U}_h$ satisfies:

$$\int_{T_1} \mathbf{V}_{1,h}^T \frac{\partial \mathbf{U}_{1,h}}{\partial t} dxdy + \int_{T_2} \mathbf{V}_{2,h}^T \frac{\partial \mathbf{U}_{2,h}}{\partial t} dxdy + \int_{\Gamma_3} \mathbf{V}_{1,h}^T (n_{1x}\mathbf{A}_1 + n_{1y}\mathbf{B}_1)\mathbf{U}_{1,h} ds$$
$$+ \int_{\Gamma_3} \mathbf{V}_{2,h}^T (n_{2x}\mathbf{A}_2 + n_{2y}\mathbf{B}_2)\mathbf{U}_{2,h} ds + \int_{\Gamma_2^+} {\mathbf{V}_{2,h}^+}^T \mathbf{A}_2^+ \mathbf{U}_{2,h}^+ dy + \int_{\Gamma_2^+} {\mathbf{V}_{2,h}^+}^T \mathbf{A}_2^- \mathbf{U}_{2,h}^- dy$$
$$- \int_{\Gamma_2^-} {\mathbf{V}_{1,h}^+}^T \mathbf{A}_1^+ \mathbf{U}_{1,h}^- dy - \int_{\Gamma_2^-} {\mathbf{V}_{1,h}^+}^T \mathbf{A}_1^- \mathbf{U}_{1,h}^+ dy + \int_{\Gamma_{11}^+} {\mathbf{V}_{1,h}^+}^T \mathbf{B}_1^+ \mathbf{U}_{1,h}^+ dx + \int_{\Gamma_{12}^+} {\mathbf{V}_{2,h}^+}^T \mathbf{B}_2^+ \mathbf{U}_{2,h}^+ dx$$
$$+ \int_{\Gamma_{11}^+} {\mathbf{V}_{1,h}^+}^T \mathbf{B}_1^- \mathbf{U}_{1,h}^- dx + \int_{\Gamma_{12}^+} {\mathbf{V}_{2,h}^+}^T \mathbf{B}_2^- \mathbf{U}_{2,h}^- dx - \int_{\Gamma_{11}^-} {\mathbf{V}_{1,h}^+}^T \mathbf{B}_1^+ \mathbf{U}_{1,h}^- dx - \int_{\Gamma_{12}^-} {\mathbf{V}_{2,h}^+}^T \mathbf{B}_2^+ \mathbf{U}_{2,h}^- dx$$
$$- \int_{\Gamma_{11}^-} {\mathbf{V}_{1,h}^+}^T \mathbf{B}_1^- \mathbf{U}_{1,h}^+ dx - \int_{\Gamma_{12}^-} {\mathbf{V}_{2,h}^+}^T \mathbf{B}_2^- \mathbf{U}_{2,h}^+ dx - \int_{T_1} \frac{\partial \mathbf{V}_{1,h}^T}{\partial x} \mathbf{A}_1 \mathbf{U}_{1,h} dxdy$$
$$- \int_{T_2} \frac{\partial \mathbf{V}_{2,h}^T}{\partial x} \mathbf{A}_2 \mathbf{U}_{2,h} dxdy - \int_{T_1} \frac{\partial \mathbf{V}_{1,h}^T}{\partial y} \mathbf{B}_1 \mathbf{U}_{1,h} dxdy - \int_{T_2} \frac{\partial \mathbf{V}_{2,h}^T}{\partial y} \mathbf{B}_2 \mathbf{U}_{2,h} dxdy = 0, \tag{4.1.6}$$

where $\boldsymbol{\nu}_1 = (n_{1x}, n_{1y})^T$ and $\boldsymbol{\nu}_2 = (n_{2x}, n_{2y})^T$, respectively, are the outer unit normal vectors on the interface Γ_3 for T_1 and T_2.

Combining the previous equation on the interface elements and the DG formulation on non interface elements we obtain the following system of ordinary differential equations

$$\frac{d\mathbf{C}}{dt} = \mathbf{A}_{h,q}^G \mathbf{C}, \tag{4.1.7}$$

where $\mathbf{C}$ is a global solution vector and $\mathbf{A}_{h,q}^G$ is a global matrix.

4.1.2 Galerkin Formulation for Scaled Problem

Since the previous Galerkin formulation is not stable for two dimensional problems with high contrast media, we will propose a stable formulation. First we scale the problem by multiplying the acoustic wave equation (3.1.2a) by

$$\mathbf{S}_i = \mathbf{S}|_{I_i} = \begin{pmatrix} \frac{1}{\rho_i c_i^2} & 0 & 0 \\ 0 & \rho_i & 0 \\ 0 & 0 & \rho_i \end{pmatrix}, \text{ for } i = 1, 2 \tag{4.1.8}$$

to obtain

$$\mathbf{S}\frac{\partial \mathbf{U}}{\partial t} + \tilde{\mathbf{A}}\frac{\partial \mathbf{U}}{\partial x} + \tilde{\mathbf{B}}\frac{\partial \mathbf{U}}{\partial y} = 0, \tag{4.1.9}$$

where

$$\tilde{\mathbf{A}} = \mathbf{SA} = \begin{pmatrix} 0 & 1 & 0 \\ 1 & 0 & 0 \\ 0 & 0 & 0 \end{pmatrix}, \ \tilde{\mathbf{B}} = \mathbf{SB} = \begin{pmatrix} 0 & 0 & 1 \\ 0 & 0 & 0 \\ 1 & 0 & 0 \end{pmatrix}. \tag{4.1.10}$$

We use the standard DG weak formulation on a non interface element by multiplying (4.1.9) by a test vector function $\mathbf{V}$ and integrating over the element, we get

$$\int_T \mathbf{V}^T \mathbf{S}\frac{\partial \mathbf{U}}{\partial t} dxdy + \int_T \mathbf{V}^T \tilde{\mathbf{A}}\frac{\partial \mathbf{U}}{\partial x} dx + \int_T \mathbf{V}^T \tilde{\mathbf{B}}\frac{\partial \mathbf{U}}{\partial y} dy = 0. \tag{4.1.11}$$

Integrating over the element and applying the divergence theorem to obtain

$$\begin{aligned} &\int_T \mathbf{V}^T \mathbf{S}\frac{\partial \mathbf{U}}{\partial t} dxdy + \int_{\Gamma_2^+} \mathbf{V}^T \tilde{\mathbf{A}}\mathbf{U} dy - \int_{\Gamma_2^-} \mathbf{V}^T \tilde{\mathbf{A}}\mathbf{U} dy + \int_{\Gamma_1^+} \mathbf{V}^T \tilde{\mathbf{B}}\mathbf{U} dx - \int_{\Gamma_1^-} \mathbf{V}^T \tilde{\mathbf{B}}\mathbf{U} dx \\ &- \int_T \frac{\partial \mathbf{V}^T}{\partial x}\tilde{\mathbf{A}}\mathbf{U} dxdy - \int_T \frac{\partial \mathbf{V}^T}{\partial y}\tilde{\mathbf{B}}\mathbf{U} dxdy = 0. \end{aligned} \tag{4.1.12}$$

We obtain the discrete weak DG formulation applied to the scaled problem by: *(i)* replacing $\mathbf{U}$ by $\mathbf{U}_h \in \mathcal{U}_h^k$ given in (3.4.1) , *(ii)* testing against $\mathbf{V}_h \in (Q_k)^3$ and *(iii)* defining the numerical flux $\widehat{(\tilde{\mathbf{B}}\mathbf{U}_h)}|_{\Gamma_1^\pm}$ for a discontinuous $\mathbf{U}_h$ across $\Gamma_1^\pm$ by

$$\widehat{\tilde{\mathbf{B}}\mathbf{U}_h}|_{\Gamma_1^+} = \tilde{\mathbf{B}}^+\mathbf{U}_h^+ + \tilde{\mathbf{B}}^-\mathbf{U}_h^- = (\mathbf{SB})^+\mathbf{U}_h^+ + (\mathbf{SB})^-\mathbf{U}_h^-, \tag{4.1.13a}$$

$$\widehat{\tilde{\mathbf{B}}\mathbf{U}_h}|_{\Gamma_1^-} = \tilde{\mathbf{B}}^+\mathbf{U}_h^- + \tilde{\mathbf{B}}^-\mathbf{U}_h^+ = (\mathbf{SB})^+\mathbf{U}_h^- + (\mathbf{SB})^-\mathbf{U}_h^+. \tag{4.1.13b}$$

Similarly on $\Gamma_2^\pm$ we use

$$\widehat{\tilde{\mathbf{A}}\mathbf{U}_h}|_{\Gamma_2^+} = \tilde{\mathbf{A}}^+\mathbf{U}_h^+ + \tilde{\mathbf{A}}^-\mathbf{U}_h^- = (\mathbf{SA})^+\mathbf{U}_h^+ + (\mathbf{SA})^-\mathbf{U}_h^-, \tag{4.1.13c}$$

$$\widehat{\tilde{\mathbf{A}}\mathbf{U}_h}|_{\Gamma_2^-} = \tilde{\mathbf{A}}^+\mathbf{U}_h^- + \tilde{\mathbf{A}}^-\mathbf{U}_h^+ = (\mathbf{SA})^+\mathbf{U}_h^- + (\mathbf{SA})^-\mathbf{U}_h^+, \tag{4.1.13d}$$

where $\mathbf{U}_h^{\pm}(\mathbf{x}) = \lim_{\epsilon\to 0^{\pm}} \mathbf{U}_h(\mathbf{x} - \epsilon \boldsymbol{n})$ and $\boldsymbol{n} = (n_x, n_y)^T$ is the outward unit normal vector at a point $\mathbf{x}$ on the boundary of T.

The immersed discontinuous Galerkin solution $\mathbf{U}_h$ satisfies

$$\begin{aligned}
&\int_T \mathbf{V}_h^T \mathbf{S} \frac{\partial \mathbf{U}_h}{\partial t} dxdy + \int_{\Gamma_2^+} \mathbf{V}_h^{+T} \tilde{\mathbf{A}}^+ \mathbf{U}_h^+ dy + \int_{\Gamma_2^+} \mathbf{V}_h^{+T} \tilde{\mathbf{A}}^- \mathbf{U}_h^- dy - \int_{\Gamma_2^-} \mathbf{V}_h^{+T} \tilde{\mathbf{A}}^+ \mathbf{U}_h^- dy \\
&- \int_{\Gamma_2^-} \mathbf{V}_h^{+T} \tilde{\mathbf{A}}^- \mathbf{U}_h^+ dy + \int_{\Gamma_1^+} \mathbf{V}_h^{+T} \tilde{\mathbf{B}}^+ \mathbf{U}_h^+ dx + \int_{\Gamma_1^+} \mathbf{V}_h^{+T} \tilde{\mathbf{B}}^- \mathbf{U}_h^- dx - \int_{\Gamma_1^-} \mathbf{V}_h^{+T} \tilde{\mathbf{B}}^+ \mathbf{U}_h^- dx \\
&- \int_{\Gamma_1^-} \mathbf{V}_h^{+T} \tilde{\mathbf{B}}^- \mathbf{U}_h^+ dx - \int_T \frac{\partial \mathbf{V}_h^T}{\partial x} \tilde{\mathbf{A}} \mathbf{U}_h dxdy - \int_T \frac{\partial \mathbf{V}_h^T}{\partial y} \tilde{\mathbf{B}} \mathbf{U}_h dxdy = 0, \ \forall\ \mathbf{V}_h \in (Q_k)^3.
\end{aligned} \tag{4.1.14}$$

Next, we consider an interface element of type II cut by the interface Γ into T_1 and T_2 and $T = T_1 \cup T_2$ as illustrated in Figure 4.1.1 and $\Gamma_3 = \overline{DE}$ for bilinear IFE spaces and $\Gamma_3 = \widetilde{DE}$ for $k >$ 1-degree IFE spaces.

Let us multiply (4.1.9) by a test function $\mathbf{V}$, integrate over T_1 and apply the divergence theorem to obtain the weak formulation

$$\begin{aligned}
&\int_{T_1} \mathbf{V}_1^T \mathbf{S}_1 \frac{\partial \mathbf{U}_1}{\partial t} dxdy + \int_{\Gamma_3} \mathbf{V}_1^T (n_{1x} \tilde{\mathbf{A}} + n_{1y} \tilde{\mathbf{B}}) \mathbf{U}_1 ds - \int_{\Gamma_2^-} \mathbf{V}_1^T \tilde{\mathbf{A}} \mathbf{U}_1 dy + \int_{\Gamma_{11}^+} \mathbf{V}_1^T \tilde{\mathbf{B}} \mathbf{U}_1 dx \\
&- \int_{\Gamma_{11}^-} \mathbf{V}_1^T \tilde{\mathbf{B}} \mathbf{U}_1 dx - \int_{T_1} \frac{\partial \mathbf{V}_1^T}{\partial x} \tilde{\mathbf{A}} \mathbf{U}_1 dxdy - \int_{T_1} \frac{\partial \mathbf{V}_1^T}{\partial y} \tilde{\mathbf{B}} \mathbf{U}_1 dxdy = 0.
\end{aligned} \tag{4.1.15}$$

Similarly on T_2 on write

$$\begin{aligned}
&\int_{T_2} \mathbf{V}_2^T \mathbf{S}_1 \frac{\partial \mathbf{U}_2}{\partial t} dxdy + \int_{\Gamma_2^+} \mathbf{V}_2^T \tilde{\mathbf{A}} \mathbf{U}_2 dy + \int_{\Gamma_3} \mathbf{V}_2^T (n_{2x} \tilde{\mathbf{A}} + n_{2y} \tilde{\mathbf{B}}) \mathbf{U}_2 ds + \int_{\Gamma_{12}^+} \mathbf{V}_2^T \tilde{\mathbf{B}} \mathbf{U}_2 dx \\
&- \int_{\Gamma_{12}^-} \mathbf{V}_2^T \tilde{\mathbf{B}} \mathbf{U}_2 dx - \int_{T_2} \frac{\partial \mathbf{V}_2^T}{\partial x} \tilde{\mathbf{A}} \mathbf{U}_2 dxdy - \int_{T_2} \frac{\partial \mathbf{V}_2^T}{\partial y} \tilde{\mathbf{B}} \mathbf{U}_2 dxdy = 0.
\end{aligned} \tag{4.1.16}$$

Adding (4.1.15) and (4.1.16), replacing $\mathbf{U}$ by $\mathbf{U}_h \in \mathcal{U}_h^k$ and $\mathbf{V}$ by $\mathbf{V}_h \in \mathcal{U}_h^k(T)$ and applying numerical flux (4.1.13) for the terms on the boundary of T_1, T_2, $\mathbf{U}_h$ satisfies:

$$\begin{aligned}
&\int_{T_1} \mathbf{V}_{1,h}^T \mathbf{S}_1 \frac{\partial \mathbf{U}_{1,h}}{\partial t} dxdy + \int_{T_2} \mathbf{V}_{2,h}^T \mathbf{S}_2 \frac{\partial \mathbf{U}_{2,h}}{\partial t} dxdy + \int_{\Gamma_3} \mathbf{V}_{1,h}^T (n_{1x} \tilde{\mathbf{A}} + n_{1y} \tilde{\mathbf{B}}) \mathbf{U}_{1,h} ds \\
&+ \int_{\Gamma_3} \mathbf{V}_{2,h}^T (n_{2x} \tilde{\mathbf{A}} + n_{2y} \tilde{\mathbf{B}}) \mathbf{U}_{2,h} ds + \int_{\Gamma_2^+} \mathbf{V}_{2,h}^{+\ T} \tilde{\mathbf{A}}^+ \mathbf{U}_{2,h}^+ dy + \int_{\Gamma_2^+} \mathbf{V}_{2,h}^{+\ T} \tilde{\mathbf{A}}^- \mathbf{U}_{2,h}^- dy \\
&- \int_{\Gamma_2^-} \mathbf{V}_{1,h}^{+\ T} \tilde{\mathbf{A}}^+ \mathbf{U}_{1,h}^- dy - \int_{\Gamma_2^-} \mathbf{V}_{1,h}^{+\ T} \tilde{\mathbf{A}}^- \mathbf{U}_{1,h}^+ dy + \int_{\Gamma_{11}^+} \mathbf{V}_{1,h}^{+\ T} \tilde{\mathbf{B}}^+ \mathbf{U}_{1,h}^+ dx + \int_{\Gamma_{12}^+} \mathbf{V}_{2,h}^{+\ T} \tilde{\mathbf{B}}^+ \mathbf{U}_{2,h}^+ dx
\end{aligned}$$

$$+\int_{\Gamma_{11}^+}{\mathbf{V}_{1,h}^+}^T\tilde{\mathbf{B}}^-\mathbf{U}_{1,h}^-dx+\int_{\Gamma_{12}^+}{\mathbf{V}_{2,h}^+}^T\tilde{\mathbf{B}}^-\mathbf{U}_{2,h}^-dx-\int_{\Gamma_{11}^-}{\mathbf{V}_{1,h}^+}^T\tilde{\mathbf{B}}^+\mathbf{U}_{1,h}^-dx-\int_{\Gamma_{12}^-}{\mathbf{V}_{2,h}^+}^T\tilde{\mathbf{B}}^+\mathbf{U}_{2,h}^-dx$$
$$-\int_{\Gamma_{11}^-}{\mathbf{V}_{1,h}^+}^T\tilde{\mathbf{B}}^-\mathbf{U}_{1,h}^+dx-\int_{\Gamma_{12}^-}{\mathbf{V}_{2,h}^+}^T\tilde{\mathbf{B}}^-\mathbf{U}_{2,h}^+dx-\int_{T_1}\frac{\partial\mathbf{V}_{1,h}^T}{\partial x}\tilde{\mathbf{A}}\mathbf{U}_{1,h}dxdy$$
$$-\int_{T_2}\frac{\partial\mathbf{V}_{2,h}^T}{\partial x}\tilde{\mathbf{A}}\mathbf{U}_{2,h}dxdy-\int_{T_1}\frac{\partial\mathbf{V}_{1,h}^T}{\partial y}\tilde{\mathbf{B}}\mathbf{U}_{1,h}dxdy-\int_{T_2}\frac{\partial\mathbf{V}_{2,h}^T}{\partial y}\tilde{\mathbf{B}}\mathbf{U}_{2,h}dxdy=0, \tag{4.1.17}$$

where $\boldsymbol{\nu}_1=(n_{1x},n_{1y})^T$ and $\boldsymbol{\nu}_2=(n_{2x},n_{2y})^T$, respectively, are the outer unit normal vectors on the interface Γ_3 for T_1 and T_2.

Let us note that the term

$$\int_{\Gamma_3}\mathbf{V}_{1,h}^T(n_{1x}\tilde{\mathbf{A}}+n_{1y}\tilde{\mathbf{B}})\mathbf{U}_{1,h}ds+\int_{\Gamma_3}\mathbf{V}_{2,h}^T(n_{2x}\tilde{\mathbf{A}}+n_{2y}\tilde{\mathbf{B}})\mathbf{U}_{2,h}ds \tag{4.1.18}$$

in (4.1.17) is zero for bilinear IFE spaces and higher-degree IFE spaces with linear interfaces. However, it is non zero for the curved interface with $k>1$-degree IFE spaces because we take only finite points on the curved interface to construct IFE spaces but the integration is along the curve Γ_3 which is may lead to instabilities. Adding the penalty term

$$-\frac{1}{2}\int_{\Gamma_3}\mathbf{V}_{1,h}^T(n_{1x}\tilde{\mathbf{A}}+n_{1y}\tilde{\mathbf{B}})\mathbf{U}_{1,h}ds-\frac{1}{2}\int_{\Gamma_3}\mathbf{V}_{2,h}^T(n_{2x}\tilde{\mathbf{A}}+n_{2y}\tilde{\mathbf{B}})\mathbf{U}_{2,h}ds, \tag{4.1.19}$$

we obtain stable formulation

$$\int_{T_1}\mathbf{V}_{1,h}^T\mathbf{S}_1\frac{\partial\mathbf{U}_{1,h}}{\partial t}dxdy+\int_{T_2}\mathbf{V}_{2,h}^T\mathbf{S}_2\frac{\partial\mathbf{U}_{2,h}}{\partial t}dxdy+\frac{1}{2}\int_{\Gamma_3}\mathbf{V}_{1,h}^T(n_{1x}\tilde{\mathbf{A}}+n_{1y}\tilde{\mathbf{B}})\mathbf{U}_{1,h}ds$$
$$+\frac{1}{2}\int_{\Gamma_3}\mathbf{V}_{2,h}^T(n_{2x}\tilde{\mathbf{A}}+n_{2y}\tilde{\mathbf{B}})\mathbf{U}_{2,h}ds+\int_{\Gamma_2^+}{\mathbf{V}_{2,h}^+}^T\tilde{\mathbf{A}}^+\mathbf{U}_{2,h}^+dy+\int_{\Gamma_2^+}{\mathbf{V}_{2,h}^+}^T\tilde{\mathbf{A}}^-\mathbf{U}_{2,h}^-dy$$
$$-\int_{\Gamma_2^-}{\mathbf{V}_{1,h}^+}^T\tilde{\mathbf{A}}^+\mathbf{U}_{1,h}^-dy-\int_{\Gamma_2^-}{\mathbf{V}_{1,h}^+}^T\tilde{\mathbf{A}}^-\mathbf{U}_{1,h}^+dy+\int_{\Gamma_{11}^+}{\mathbf{V}_{1,h}^+}^T\tilde{\mathbf{B}}^+\mathbf{U}_{1,h}^+dx+\int_{\Gamma_{12}^+}{\mathbf{V}_{2,h}^+}^T\tilde{\mathbf{B}}^+\mathbf{U}_{2,h}^+dx$$
$$+\int_{\Gamma_{11}^+}{\mathbf{V}_{1,h}^+}^T\tilde{\mathbf{B}}^-\mathbf{U}_{1,h}^-dx+\int_{\Gamma_{12}^+}{\mathbf{V}_{2,h}^+}^T\tilde{\mathbf{B}}^-\mathbf{U}_{2,h}^-dx-\int_{\Gamma_{11}^-}{\mathbf{V}_{1,h}^+}^T\tilde{\mathbf{B}}^+\mathbf{U}_{1,h}^-dx-\int_{\Gamma_{12}^-}{\mathbf{V}_{2,h}^+}^T\tilde{\mathbf{B}}^+\mathbf{U}_{2,h}^-dx$$
$$-\int_{\Gamma_{11}^-}{\mathbf{V}_{1,h}^+}^T\tilde{\mathbf{B}}^-\mathbf{U}_{1,h}^+dx-\int_{\Gamma_{12}^-}{\mathbf{V}_{2,h}^+}^T\tilde{\mathbf{B}}^-\mathbf{U}_{2,h}^+dx-\int_{T_1}\frac{\partial\mathbf{V}_{1,h}^T}{\partial x}\tilde{\mathbf{A}}\mathbf{U}_{1,h}dxdy$$
$$-\int_{T_2}\frac{\partial\mathbf{V}_{2,h}^T}{\partial x}\tilde{\mathbf{A}}\mathbf{U}_{2,h}dxdy-\int_{T_1}\frac{\partial\mathbf{V}_{1,h}^T}{\partial y}\tilde{\mathbf{B}}\mathbf{U}_{1,h}dxdy-\int_{T_2}\frac{\partial\mathbf{V}_{2,h}^T}{\partial y}\tilde{\mathbf{B}}\mathbf{U}_{2,h}dxdy=0. \tag{4.1.20}$$

Stability of this information will be proved in Theorem 5.1.3.

Combining the previous equation on the interface elements and the DG formulation on non interface elements for scaled problem, we obtain the following system of ordinary differential equations

$$\frac{d\mathbf{C}}{dt}=\mathbf{A}_{h,q}^{GS}\mathbf{C}, \tag{4.1.21}$$

where $\mathbf{C}$ is a global solution vector and $A_{h,q}^{GS}$ is a global matrix.

4.1.3 Discontinuous Petrov-Galerkin Formulation

Since immersed discontinuous Galerkin formulation applied to the scaled problem has a small stability region compared to the standard immersed discontinuous Galerkin formulation for homogeneous problem, we propose a stable and more efficient formulation.

In order to obtain this formulation on a non interface element, we multiply (3.1.2a) by a test function $\mathbf{SV}$, integrate over the element and apply the divergence theorem

$$\int_T \mathbf{V}^T\mathbf{S}\frac{\partial \mathbf{U}}{\partial t}dxdy + \int_{\Gamma_2^+} \mathbf{V}^T\mathbf{SAU}dy - \int_{\Gamma_2^-} \mathbf{V}^T\mathbf{SAU}dy + \int_{\Gamma_1^+} \mathbf{V}^T\mathbf{SBU}dx - \int_{\Gamma_1^-} \mathbf{V}^T\mathbf{SBU}dx$$
$$- \int_T \frac{\partial \mathbf{V}^T}{\partial x}\tilde{\mathbf{A}}\mathbf{U}dxdy - \int_T \frac{\partial \mathbf{V}^T}{\partial y}\tilde{\mathbf{B}}\mathbf{U}dxdy = 0, \tag{4.1.22}$$

where $\tilde{\mathbf{A}}$ and $\tilde{\mathbf{B}}$ are defined in (4.1.10).

We obtain the discrete weak DPG formulation by: *(i)* replacing $\mathbf{U}$ by $\mathbf{U}_h \in \mathcal{U}_h^k$ given in (3.4.1), *(ii)* testing against $\mathbf{V}_h \in (Q_k)^3$ and *(iii)* defining the numerical flux $(\widehat{\mathbf{BU}_h})|_{\Gamma_1^\pm}$ for a discontinuous $\mathbf{U}_h$ across $\Gamma_1^\pm$ by

$$\widehat{\mathbf{BU}_h}|_{\Gamma_1^+} = \mathbf{B}^+\mathbf{U}_h^+ + \mathbf{B}^-\mathbf{U}_h^-,\ \widehat{\mathbf{BU}_h}|_{\Gamma_1^-} = \mathbf{B}^+\mathbf{U}_h^- + \mathbf{B}^-\mathbf{U}_h^+. \tag{4.1.23a}$$

Similarly on $\Gamma_2^\pm$ we use

$$\widehat{\mathbf{AU}_h}|_{\Gamma_2^+} = \mathbf{A}^+\mathbf{U}_h^+ + \mathbf{A}^-\mathbf{U}_h^-,\ \widehat{\mathbf{AU}_h}|_{\Gamma_2^-} = \mathbf{A}^+\mathbf{U}_h^- + \mathbf{A}^-\mathbf{U}_h^+, \tag{4.1.23b}$$

where $\mathbf{U}_h^\pm(\mathbf{x}) = \lim_{\epsilon\to 0^\pm} \mathbf{U}_h(\mathbf{x} - \epsilon\boldsymbol{n})$. Here $\boldsymbol{n} = (n_x, n_y)^T$ is the outward unit normal vector at a point $\mathbf{x}$ on the boundary of T.

Applying the numerical flux, the Petrov-Galerkin formulation consists of finding $\mathbf{U}_h$ such that

$$\int_T \mathbf{V}_h^T\mathbf{S}\frac{\partial \mathbf{U}_h}{\partial t}dxdy + \int_{\Gamma_2^+} \mathbf{V}_h^{+T}\mathbf{SA}^+\mathbf{U}_h^+dy + \int_{\Gamma_2^+} \mathbf{V}_h^{+T}\mathbf{SA}^-\mathbf{U}_h^-dy - \int_{\Gamma_2^-} \mathbf{V}_h^{+T}\mathbf{SA}^+\mathbf{U}_h^-dy$$
$$- \int_{\Gamma_2^-} \mathbf{V}_h^{+T}\mathbf{SA}^-\mathbf{U}_h^+dy + \int_{\Gamma_1^+} \mathbf{V}_h^{+T}\mathbf{SB}^+\mathbf{U}_h^+dx + \int_{\Gamma_1^+} \mathbf{V}_h^{+T}\mathbf{SB}^-\mathbf{U}_h^-dx - \int_{\Gamma_1^-} \mathbf{V}_h^{+T}\mathbf{SB}^+\mathbf{U}_h^-dx$$
$$- \int_{\Gamma_1^-} \mathbf{V}_h^{+T}\mathbf{SB}^-\mathbf{U}_h^+dx - \int_T \frac{\partial \mathbf{V}_h^T}{\partial x}\tilde{\mathbf{A}}\mathbf{U}_h dxdy - \int_T \frac{\partial \mathbf{V}_h^T}{\partial y}\tilde{\mathbf{B}}\mathbf{U}_h dxdy = 0,\ \forall\ \mathbf{V}_h \in (Q_k)^3. \tag{4.1.24}$$

Here, let us consider an interface element of type II cut by the interface Γ into T_1 and T_2 and $T = T_1 \cup T_2$ as illustrated in Figure 4.1.1 where $\Gamma_3 = \overline{DE}$ for bilinear IFE spaces and $\Gamma_3 = \widetilde{DE}$ for $k >$ 1-degree IFE spaces.

Multiplying a test function (3.1.2a) by $\mathbf{SV}$, integrating over T_1 and applying the divergence theorem, we obtain

$$\int_{T_1} \mathbf{V}_1^T \mathbf{S}_1 \frac{\partial \mathbf{U}_1}{\partial t} dxdy + \int_{\Gamma_3} \mathbf{V}_1^T (n_{1x}\tilde{\mathbf{A}} + n_{1y}\tilde{\mathbf{B}})\mathbf{U}_1 ds - \int_{\Gamma_2^-} \mathbf{V}_1^T \mathbf{S}_1 \mathbf{A}_1 \mathbf{U}_1 dy + \int_{\Gamma_{11}^+} \mathbf{V}_1^T \mathbf{S}_1 \mathbf{B}_1 \mathbf{U}_1 dx$$
$$- \int_{\Gamma_{11}^-} \mathbf{V}_1^T \mathbf{S}_1 \mathbf{B}_1 \mathbf{U}_1 dx - \int_{T_1} \frac{\partial \mathbf{V}_1^T}{\partial x} \tilde{\mathbf{A}} \mathbf{U}_1 dxdy - \int_{T_1} \frac{\partial \mathbf{V}_1^T}{\partial y} \tilde{\mathbf{B}} \mathbf{U}_1 dxdy = 0. \tag{4.1.25}$$

Similarly on T_2 we get

$$\int_{T_2} \mathbf{V}_2^T \mathbf{S}_2 \frac{\partial \mathbf{U}_2}{\partial t} dxdy + \int_{\Gamma_2^+} \mathbf{V}_2^T \mathbf{S}_2 \mathbf{A}_2 \mathbf{U}_2 dy + \int_{\Gamma_3} \mathbf{V}_2^T (n_{2x}\tilde{\mathbf{A}} + n_{2y}\tilde{\mathbf{B}})\mathbf{U}_2 ds + \int_{\Gamma_{12}^+} \mathbf{V}_2^T \mathbf{S}_2 \mathbf{B}_2 \mathbf{U}_2 dx$$
$$- \int_{\Gamma_{12}^-} \mathbf{V}_2^T \mathbf{S}_2 \mathbf{B}_2 \mathbf{U}_2 dx - \int_{T_2} \frac{\partial \mathbf{V}_2^T}{\partial x} \tilde{\mathbf{A}} \mathbf{U}_2 dxdy - \int_{T_2} \frac{\partial \mathbf{V}_2^T}{\partial y} \tilde{\mathbf{B}} \mathbf{U}_2 dxdy = 0. \tag{4.1.26}$$

Combining (4.1.25) and (4.1.26), replacing $\mathbf{U}$ by $\mathbf{U}_h \in \mathcal{U}_h^k$ and $\mathbf{V}$ by $\mathbf{V}_h \in \mathcal{U}_h^k(T)$ and applying numerical flux (4.1.23) for the terms on the boundary of T_1, T_2, DPG formulation is to find $\mathbf{U}_h$ satisfying

$$\int_{T_1} \mathbf{V}_{1,h}^T \mathbf{S}_1 \frac{\partial \mathbf{U}_{1,h}}{\partial t} dxdy + \int_{T_2} \mathbf{V}_{2,h}^T \mathbf{S}_2 \frac{\partial \mathbf{U}_{2,h}}{\partial t} dxdy + \int_{\Gamma_3} \mathbf{V}_{1,h}^T (n_{1x}\tilde{\mathbf{A}} + n_{1y}\tilde{\mathbf{B}})\mathbf{U}_{1,h} ds$$
$$+ \int_{\Gamma_3} \mathbf{V}_{2,h}^T (n_{2x}\tilde{\mathbf{A}} + n_{2y}\tilde{\mathbf{B}})\mathbf{U}_{2,h} ds + \int_{\Gamma_2^+} {\mathbf{V}_{2,h}^+}^T \mathbf{S}_2 \mathbf{A}_2^+ \mathbf{U}_{2,h}^+ dy + \int_{\Gamma_2^+} {\mathbf{V}_{2,h}^+}^T \mathbf{S}_2 \mathbf{A}_2^- \mathbf{U}_{2,h}^- dy$$
$$- \int_{\Gamma_2^-} {\mathbf{V}_{1,h}^+}^T \mathbf{S}_1 \mathbf{A}_1^+ \mathbf{U}_{1,h}^- dy - \int_{\Gamma_2^-} {\mathbf{V}_{1,h}^+}^T \mathbf{S}_1 \mathbf{A}_1^- \mathbf{U}_{1,h}^+ dy + \int_{\Gamma_{11}^+} {\mathbf{V}_{1,h}^+}^T \mathbf{S}_1 \mathbf{B}_1^+ \mathbf{U}_{1,h}^+ dx$$
$$+ \int_{\Gamma_{12}^+} {\mathbf{V}_{2,h}^+}^T \mathbf{S}_2 \mathbf{B}_2^+ \mathbf{U}_{2,h}^+ dx + \int_{\Gamma_{11}^+} {\mathbf{V}_{1,h}^+}^T \mathbf{S}_1 \mathbf{B}_1^- \mathbf{U}_{1,h}^- dx + \int_{\Gamma_{12}^+} {\mathbf{V}_{2,h}^+}^T \mathbf{S}_2 \mathbf{B}_2^- \mathbf{U}_{2,h}^- dx$$
$$- \int_{\Gamma_{11}^-} {\mathbf{V}_{1,h}^+}^T \mathbf{S}_1 \mathbf{B}_1^+ \mathbf{U}_{1,h}^- dx - \int_{\Gamma_{12}^-} {\mathbf{V}_{2,h}^+}^T \mathbf{S}_2 \mathbf{B}_2^+ \mathbf{U}_{2,h}^- dx - \int_{\Gamma_{11}^-} {\mathbf{V}_{1,h}^+}^T \mathbf{S}_1 \mathbf{B}_1^- \mathbf{U}_{1,h}^+ dx$$
$$- \int_{\Gamma_{12}^-} {\mathbf{V}_{2,h}^+}^T \mathbf{S}_2 \mathbf{B}_2^- \mathbf{U}_{2,h}^+ dx - \int_{T_1} \frac{\partial \mathbf{V}_{1,h}^T}{\partial x} \tilde{\mathbf{A}} \mathbf{U}_{1,h} dxdy - \int_{T_2} \frac{\partial \mathbf{V}_{2,h}^T}{\partial x} \tilde{\mathbf{A}} \mathbf{U}_{2,h} dxdy$$
$$- \int_{T_1} \frac{\partial \mathbf{V}_{1,h}^T}{\partial y} \tilde{\mathbf{B}} \mathbf{U}_{1,h} dxdy - \int_{T_2} \frac{\partial \mathbf{V}_{2,h}^T}{\partial y} \tilde{\mathbf{B}} \mathbf{U}_{2,h} dxdy = 0, \tag{4.1.27}$$

where $\boldsymbol{\nu}_1 = (n_{1x}, n_{1y})^T$ and $\boldsymbol{\nu}_2 = (n_{2x}, n_{2y})^T$, respectively, are the outer unit normal vectors on the interface Γ_3 for T_1 and T_2.

The term

$$\int_{\Gamma_3} \mathbf{V}_{1,h}^T(n_{1x}\tilde{\mathbf{A}} + n_{1y}\tilde{\mathbf{B}})\mathbf{U}_{1,h}ds + \int_{\Gamma_3} \mathbf{V}_{2,h}^T(n_{2x}\tilde{\mathbf{A}} + n_{2y}\tilde{\mathbf{B}})\mathbf{U}_{2,h}ds \tag{4.1.28}$$

in (4.1.27) is non zero for the curved interface with $k > 1$-degree IFE spaces because we use only finite points on the curved interface to construct IFE spaces. We add the penalty term

$$-\frac{1}{2}\int_{\Gamma_3} \mathbf{V}_{1,h}^T(n_{1x}\tilde{\mathbf{A}} + n_{1y}\tilde{\mathbf{B}})\mathbf{U}_{1,h}ds - \frac{1}{2}\int_{\Gamma_3} \mathbf{V}_{2,h}^T(n_{2x}\tilde{\mathbf{A}} + n_{2y}\tilde{\mathbf{B}})\mathbf{U}_{2,h}ds, \tag{4.1.29}$$

in order to obtain the stable formulation

$$\begin{aligned}
&\int_{T_1} \mathbf{V}_{1,h}^T\mathbf{S}_1\frac{\partial \mathbf{U}_{1,h}}{\partial t}dxdy + \int_{T_2} \mathbf{V}_{2,h}^T\mathbf{S}_2\frac{\partial \mathbf{U}_{2,h}}{\partial t}dxdy + \frac{1}{2}\int_{\Gamma_3} \mathbf{V}_{1,h}^T(n_{1x}\tilde{\mathbf{A}} + n_{1y}\tilde{\mathbf{B}})\mathbf{U}_{1,h}ds \\
&+\frac{1}{2}\int_{\Gamma_3} \mathbf{V}_{2,h}^T(n_{2x}\tilde{\mathbf{A}} + n_{2y}\tilde{\mathbf{B}})\mathbf{U}_{2,h}ds + \int_{\Gamma_2^+} {\mathbf{V}_{2,h}^+}^T\mathbf{S}_2\mathbf{A}_2^+\mathbf{U}_{2,h}^+dy + \int_{\Gamma_2^+} {\mathbf{V}_{2,h}^+}^T\mathbf{S}_2\mathbf{A}_2^-\mathbf{U}_{2,h}^-dy \\
&- \int_{\Gamma_2^-} {\mathbf{V}_{1,h}^+}^T\mathbf{S}_1\mathbf{A}_1^+\mathbf{U}_{1,h}^-dy - \int_{\Gamma_2^-} {\mathbf{V}_{1,h}^+}^T\mathbf{S}_1\mathbf{A}_1^-\mathbf{U}_{1,h}^+dy + \int_{\Gamma_{11}^+} {\mathbf{V}_{1,h}^+}^T\mathbf{S}_1\mathbf{B}_1^+\mathbf{U}_{1,h}^+dx \\
&+ \int_{\Gamma_{12}^+} {\mathbf{V}_{2,h}^+}^T\mathbf{S}_2\mathbf{B}_2^+\mathbf{U}_{2,h}^+dx + \int_{\Gamma_{11}^+} {\mathbf{V}_{1,h}^+}^T\mathbf{S}_1\mathbf{B}_1^-\mathbf{U}_{1,h}^-dx + \int_{\Gamma_{12}^+} {\mathbf{V}_{2,h}^+}^T\mathbf{S}_2\mathbf{B}_2^-\mathbf{U}_{2,h}^-dx \\
&- \int_{\Gamma_{11}^-} {\mathbf{V}_{1,h}^+}^T\mathbf{S}_1\mathbf{B}_1^+\mathbf{U}_{1,h}^-dx - \int_{\Gamma_{12}^-} {\mathbf{V}_{2,h}^+}^T\mathbf{S}_2\mathbf{B}_2^+\mathbf{U}_{2,h}^-dx - \int_{\Gamma_{11}^-} {\mathbf{V}_{1,h}^+}^T\mathbf{S}_1\mathbf{B}_1^-\mathbf{U}_{1,h}^+dx \\
&- \int_{\Gamma_{12}^-} {\mathbf{V}_{2,h}^+}^T\mathbf{S}_2\mathbf{B}_2^-\mathbf{U}_{2,h}^+dx - \int_{T_1} \frac{\partial \mathbf{V}_{1,h}^T}{\partial x}\tilde{\mathbf{A}}\mathbf{U}_{1,h}dxdy - \int_{T_2} \frac{\partial \mathbf{V}_{2,h}^T}{\partial x}\tilde{\mathbf{A}}\mathbf{U}_{2,h}dxdy \\
&- \int_{T_1} \frac{\partial \mathbf{V}_{1,h}^T}{\partial y}\tilde{\mathbf{B}}\mathbf{U}_{1,h}dxdy - \int_{T_2} \frac{\partial \mathbf{V}_{2,h}^T}{\partial y}\tilde{\mathbf{B}}\mathbf{U}_{2,h}dxdy = 0.
\end{aligned} \tag{4.1.30}$$

Summing (4.1.24) over all non interface elements and (4.1.30) over all interface elements, the immersed DPG formulation can be written in the compact semi discrete form

$$\sum_{j=1}^{N}\int_{T_j} \mathbf{U}_h\mathbf{S}\mathbf{U}_{h,t} + \mathcal{A}(\mathbf{V}_h, \mathbf{U}_h) = 0, \tag{4.1.31}$$

where T_j is j-th elements and N is the number of elements. Stability of IDPGFE solution and skew symmetry of $\mathcal{A}(\mathbf{V}_h, \mathbf{U}_h)$ in a compact form will be proved in Theorems 5.1.2 and 5.1.3.

Combining the previous equation (4.1.30) on interface elements and DPG formulation (4.1.24) on non interface elements, we obtain the following system of ordinary differential equations

$$\frac{d\mathbf{C}}{dt} = \mathbf{A}_{h,q}^{PG}\mathbf{C}, \tag{4.1.32}$$

where $\mathbf{C}$ is a global solution vector and $\mathbf{A}_{h,q}^{PG}$ is a global matrix.

The weak formulation may be derived in a similar manner on an element of type I where a vertical and a horizontal edges are cut by the interface.

Here we note that the only difference between IDG formulation applied to the scaled problem and IDPGFE formulation lies in the definition of the numerical flux. The IDG formulation applied to the scaled problem uses

$$\widehat{\tilde{\mathbf{B}}\mathbf{U}_h}|_{\Gamma_1^+} = \tilde{\mathbf{B}}^+\mathbf{U}_h^+ + \tilde{\mathbf{B}}^-\mathbf{U}_h^- = (\mathbf{SB})^+\mathbf{U}_h^+ + (\mathbf{SB})^-\mathbf{U}_h^-, \tag{4.1.33a}$$

$$\widehat{\tilde{\mathbf{B}}\mathbf{U}_h}|_{\Gamma_1^-} = \tilde{\mathbf{B}}^+\mathbf{U}_h^- + \tilde{\mathbf{B}}^-\mathbf{U}_h^+ = (\mathbf{SB})^+\mathbf{U}_h^- + (\mathbf{SB})^-\mathbf{U}_h^+, \tag{4.1.33b}$$

$$\widehat{\tilde{\mathbf{A}}\mathbf{U}_h}|_{\Gamma_2^+} = \tilde{\mathbf{A}}^+\mathbf{U}_h^+ + \tilde{\mathbf{A}}^-\mathbf{U}_h^- = (\mathbf{SA})^+\mathbf{U}_h^+ + (\mathbf{SA})^-\mathbf{U}_h^-, \tag{4.1.33c}$$

$$\widehat{\tilde{\mathbf{A}}\mathbf{U}_h}|_{\Gamma_2^-} = \tilde{\mathbf{A}}^+\mathbf{U}_h^- + \tilde{\mathbf{A}}^-\mathbf{U}_h^+ = (\mathbf{SA})^+\mathbf{U}_h^- + (\mathbf{SA})^-\mathbf{U}_h^+, \tag{4.1.33d}$$

whereas IDPGFE method uses

$$\widehat{\tilde{\mathbf{B}}\mathbf{U}_h}|_{\Gamma_1^+} = \mathbf{S}\widehat{\mathbf{B}\mathbf{U}_h}|_{\Gamma_1^+} = \mathbf{S}\mathbf{B}^+\mathbf{U}_h^+ + \mathbf{S}\mathbf{B}^-\mathbf{U}_h^-, \tag{4.1.34a}$$

$$\widehat{\tilde{\mathbf{B}}\mathbf{U}_h}|_{\Gamma_1^-} = \mathbf{S}\widehat{\mathbf{B}\mathbf{U}_h}|_{\Gamma_1^-} = \mathbf{S}\mathbf{B}^+\mathbf{U}_h^- + \mathbf{S}\mathbf{B}^-\mathbf{U}_h^+, \tag{4.1.34b}$$

$$\widehat{\tilde{\mathbf{A}}\mathbf{U}_h}|_{\Gamma_2^+} = \mathbf{S}\widehat{\mathbf{A}\mathbf{U}_h}|_{\Gamma_2^+} = \mathbf{S}\mathbf{A}^+\mathbf{U}_h^+ + \mathbf{S}\mathbf{A}^-\mathbf{U}_h^-, \tag{4.1.34c}$$

$$\widehat{\tilde{\mathbf{A}}\mathbf{U}_h}|_{\Gamma_2^-} = \mathbf{S}\widehat{\mathbf{A}\mathbf{U}_h}|_{\Gamma_2^-} = \mathbf{S}\mathbf{A}^+\mathbf{U}_h^- + \mathbf{S}\mathbf{A}^-\mathbf{U}_h^+, \tag{4.1.34d}$$

with the matrices

$$(\mathbf{SA})^+ = \begin{pmatrix} \frac{1}{2} & \frac{1}{2} & 0 \\ \frac{1}{2} & \frac{1}{2} & 0 \\ 0 & 0 & 0 \end{pmatrix}, \ (\mathbf{SA})^- = \begin{pmatrix} -\frac{1}{2} & \frac{1}{2} & 0 \\ \frac{1}{2} & -\frac{1}{2} & 0 \\ 0 & 0 & 0 \end{pmatrix}, \tag{4.1.35a}$$

$$(\mathbf{SB})^+ = \begin{pmatrix} \frac{1}{2} & 0 & \frac{1}{2} \\ 0 & 0 & 0 \\ \frac{1}{2} & 0 & \frac{1}{2} \end{pmatrix}, \ (\mathbf{SB})^- = \begin{pmatrix} -\frac{1}{2} & \frac{1}{2} & 0 \\ 0 & 0 & 0 \\ \frac{1}{2} & -\frac{1}{2} & 0 \end{pmatrix}, \tag{4.1.35b}$$

$$\mathbf{SA}^+ = \begin{pmatrix} \frac{1}{2\rho c} & \frac{1}{2} & 0 \\ \frac{1}{2} & \frac{\rho c}{2} & 0 \\ 0 & 0 & 0 \end{pmatrix}, \ \mathbf{SA}^- = \begin{pmatrix} -\frac{1}{2\rho c} & \frac{1}{2} & 0 \\ \frac{1}{2} & -\frac{\rho c}{2} & 0 \\ 0 & 0 & 0 \end{pmatrix}, \tag{4.1.35c}$$

$$\mathbf{SB}^+ = \begin{pmatrix} \frac{1}{2\rho c} & 0 & \frac{1}{2} \\ 0 & 0 & 0 \\ \frac{1}{2} & 0 & \frac{\rho c}{2} \end{pmatrix}, \ \mathbf{SB}^- = \begin{pmatrix} -\frac{1}{2\rho c} & 0 & \frac{1}{2} \\ 0 & 0 & 0 \\ \frac{1}{2} & 0 & -\frac{\rho c}{2} \end{pmatrix}, \tag{4.1.35d}$$

where ρ and c are the density and sound speed.

We further note that a non interface element may have interface neighboring elements. Summing (4.1.24) over all non interface elements and (4.1.30) over all interface elements, enforcing inflow boundary conditions (3.1.2c) and periodic boundary conditions one can easily show that

$$\int_{\partial\Omega} (\mathbf{A}n_x + \mathbf{B}n_y)\mathbf{U}ds = 0, \tag{4.1.36}$$

where $\boldsymbol{n} = (n_x, n_y)^T$ is the unit outward normal vector on $\partial\Omega$, and projecting $\mathbf{U}_0(x, y)$ onto $\mathcal{U}_h^k$ using the L^2 inner product we obtain an initial value problem for the finite element coefficients. The resulting system of ordinary differential equations is integrated in time using the classical fourth-order Runge-Kutta method on a cluster of processors in parallel with a local time-stepping algorithm.

4.1.4 2D Integration on Interface Elements

In order to perform integration on the interface element, we split the interface element into triangles shown in Figure 4.1.2, use a quadrature on each triangle and add all contributions. Gaussian quadrature for triangle is applied on the reference triangle which T_r is mapped into

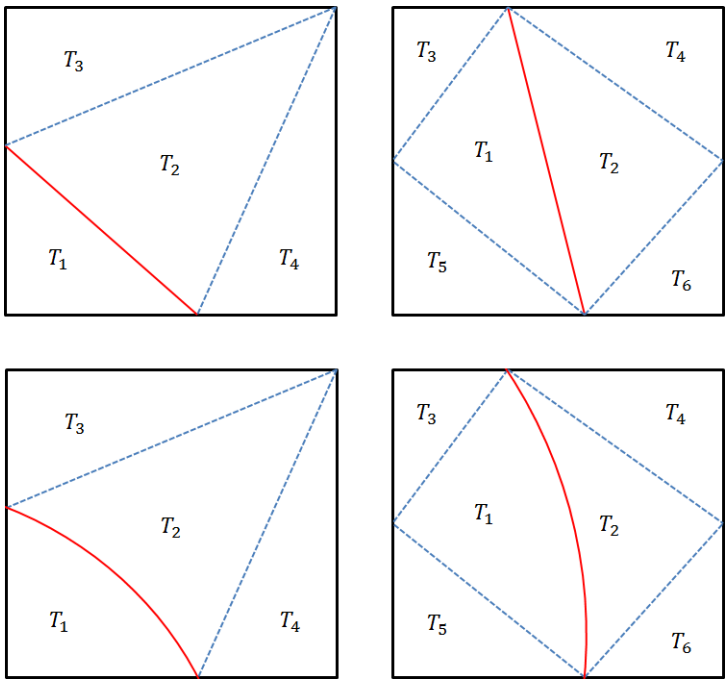

Figure 4.1.2: Integration on an interface element of type I (left) and II (right) for linear (top) and curved (bottom) interface.

physical triangle T_p as illustrated in Figure 4.1.3.

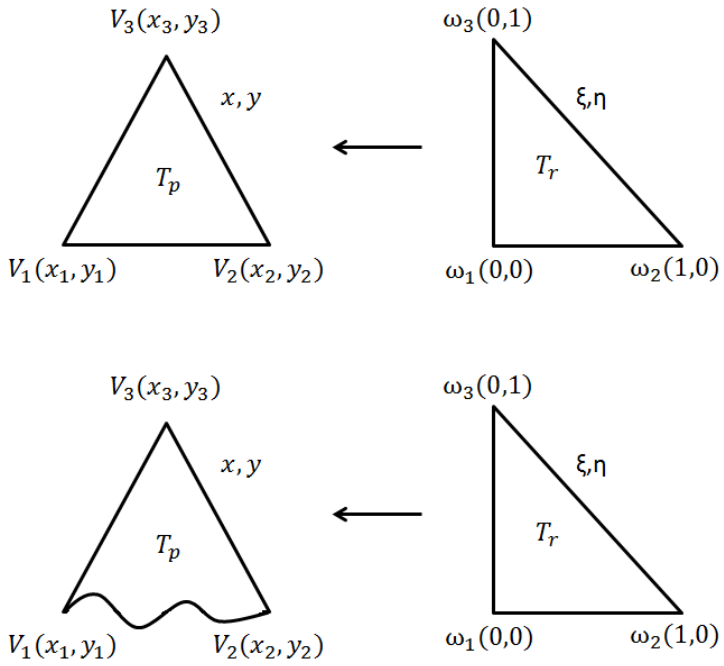

Figure 4.1.3: Transformation between physical and reference triangles for straight-edge (top) and curved-edge (bottom) triangles.

For straight-edge triangle $T_r = V_1V_2V_3$ we use the transformation: $T_r \to T_p$ given by

$$\omega = (1 - \xi - \eta)V_1 + \xi V_2 + \eta V_3, \tag{4.1.37}$$

while for curved-edge triangle T_p we use the transformation

$$\omega = \begin{cases} \frac{1-\xi-\eta}{1-\xi} Z(\xi) + \frac{\xi\eta}{1-\xi} V_2 + \eta V_3, & \text{if } \xi \neq 1, \\ V_2, & \text{if } \xi = 1, \end{cases} \tag{4.1.38}$$

where $Z(\xi)$ is a parametric equation for $0 \leq \xi \leq 1$ and $Z(0) = V_1$, $Z(1) = V_2$. By the change of variables, transforming from T_r to T_p is

$$\int_{T_p} f(x, y)dxdy = \int_{T_r} f(\xi, \eta)Jd\xi d\eta, \tag{4.1.39}$$

where jacobian factor $J = \left|\frac{\partial(x,y)}{\partial(\xi,\eta)}\right|$ is

$$J = |(x_2 - x_1)(y_3 - y_1) - (y_2 - y_1)(x_3 - x_1)| \tag{4.1.40}$$

for straight-edge triangles and

$$J = \left| \left(\frac{-\eta}{(1-\xi)^2} Z_1(\xi) + \frac{1-\xi-\eta}{1-\xi} \frac{\partial Z_1(\xi)}{\partial \xi} + \frac{\eta}{(1-\xi)^2} x_2 \right) \left(\frac{-1}{1-\xi} Z_2(\xi) + \frac{\xi}{1-\xi} y_2 + y_3 \right) \right.$$
$$\left. - \left(\frac{-\eta}{(1-\xi)^2} Z_2(\xi) + \frac{1-\xi-\eta}{1-\xi} \frac{\partial Z_2(\xi)}{\partial \xi} + \frac{\eta}{(1-\xi)^2} y_2 \right) \left(\frac{-1}{1-\xi} Z_1(\xi) + \frac{\xi}{1-\xi} x_2 + x_3 \right) \right| \tag{4.1.41}$$

for curved-edge triangles.

Thus, on the interface element T we have

$$\int_T f(x,y)dxdy = \sum_{j=1}^{N} \int_{T_j} f(x,y)dxdy, \tag{4.1.42}$$

where $N = 4$ for type I and $N = 6$ for type II as shown in Figure 4.1.2.

4.2 Temporal Discretization

In this section, we present a fourth-order Runge-Kutta time integration method with local time-stepping and parallel implementation using MPI.

4.2.1 Local Time Stepping

When implementing a local time-stepping algorithm one of the challenges one faces is how to advance the solution on elements lying near the interface of subregions with different time steps. Since the DG solution on a given element is coupled to the solution on its neighbors, one needs a special scheme to advance the solution in time. Our local time-stepping algorithm uses an interpolation scheme on the coarse elements to advance the solution on neighboring elements with small time steps. In order to illustrate the local time-stepping algorithm we consider one dimensional problems with two subregions $\tilde{\Omega}_1$, $\tilde{\Omega}_2$ with time step sizes Δt_1, $\Delta t_2 = (\lceil \frac{c_2}{c_1} \rceil)^{-1} \Delta t_1$, respectively. For instance, for $c_1 = 2m/s$, $c_2 = 5.1m/s$, we have $\Delta t_1 = 3\Delta t_2$ as illustrated in Figure 4.2.1. We also discuss the extension of our algorithm to two dimensional problems.

Time Integration Algorithm

The three immersed DG methods we have discussed earlier lead to a system of ordinary differential equation of the form

$$\begin{cases} \frac{d\mathbf{C}}{dt} = \mathcal{F}(t, \mathbf{C}), \\ \\ \mathbf{C}_0 = \mathbf{C}(t_0), \end{cases} \tag{4.2.1}$$

where

$$\mathbf{C} = \begin{pmatrix} \mathbf{c}^{(1)} \\ \mathbf{c}^{(2)} \\ \\ \vdots \\ \mathbf{c}^{(N)} \end{pmatrix} \tag{4.2.2}$$

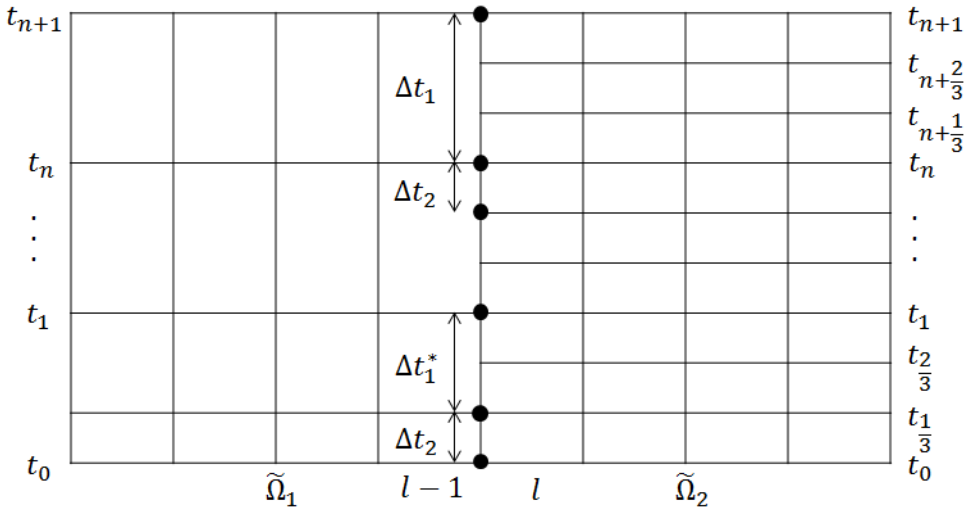

Figure 4.2.1: Sketch for local time-stepping algorithm.

is a global solution vector and $\mathbf{c}^{(l)}$ is a vector of the local finite element solution on an element l. The function $\mathcal{F}$ is

$$\mathcal{F}(t,\mathbf{C}) = \begin{pmatrix} f^{(1)}(t,\mathbf{c}^L,\mathbf{c}^{(1)},\mathbf{c}^{(2)}) \\ f^{(2)}(t,\mathbf{c}^{(1)},\mathbf{c}^{(2)},\mathbf{c}^{(3)}) \\ \vdots \\ f^{(N)}(t,\mathbf{c}^{(N-1)},\mathbf{c}^{(N)},\mathbf{c}^L) \end{pmatrix}, \tag{4.2.3}$$

where $f^{(l)}(t,\mathbf{c}^{(l-1)},\mathbf{c}^{(l)},\mathbf{c}^{(1+1)})$ is a function on an element l and $\mathbf{c}^L$, $\mathbf{c}^R$ are computed from inflow boundary condition.

First, we describe how to integrate from t_0 to t_1. Step 1 is the global time-stepping from t_0 to $t_{\frac{1}{3}}$ on all elements in $\Omega = \tilde{\Omega}_1 \cup \tilde{\Omega}_2$ using time step size Δt_2. In Step 2, we apply the local time-stepping from $t_{\frac{1}{3}}$ to t_1 on $\tilde{\Omega}_1$ using time step size $\Delta t_1^* = \frac{2}{3}\Delta t_1 = 2\Delta t_2$. In Step 3, we use the local time-stepping from $t_{\frac{1}{3}}$ to $t_{\frac{2}{3}}$ on $\tilde{\Omega}_2$ using time step size Δt_2. Similarly, in Step 4, we apply the local time-stepping from $t_{\frac{2}{3}}$ to t_1 using time step size Δt_2.

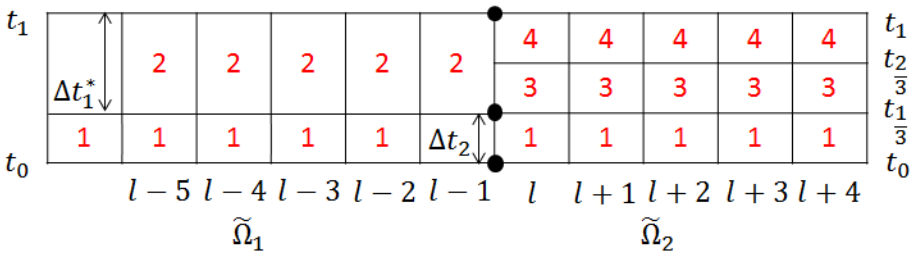

Figure 4.2.2: Local time-stepping algorithm at $t = t_0$.

Step 1:

- Integrate all the elements from $t = t_0$ to $t_{\frac{1}{3}}$ on $\Omega = \tilde{\Omega}_1 \cup \tilde{\Omega}_2$.

$$\begin{cases} \text{Stage 1: Compute } \mathbf{K}_1 = \mathcal{F}(t_0, \mathbf{C}_0). \\ \text{Stage 2: Compute } \mathbf{K}_2 = \mathcal{F}(t_0 + \frac{\Delta t_2}{2}, \mathbf{C}_0 + \frac{\Delta t_2}{2}\mathbf{K}_1). \\ \text{Stage 3: Compute } \mathbf{K}_3 = \mathcal{F}(t_0 + \frac{\Delta t_2}{2}, \mathbf{C}_0 + \frac{\Delta t_2}{2}\mathbf{K}_2). \\ \text{Stage 4: Compute } \mathbf{K}_4 = \mathcal{F}(t_0 + \Delta t_2, \mathbf{C}_0 + \Delta t_2 \mathbf{K}_3). \\ \text{Solution: } \mathbf{C}_{\frac{1}{3}} = \mathbf{C}_0 + \frac{\Delta t_2}{6}(\mathbf{K}_1 + 2\mathbf{K}_2 + 2\mathbf{K}_3 + \mathbf{K}_4). \end{cases}$$

We illustrate the time integration on one element. Time integration will be the same on other elements $1, \cdots, l-1$ in $\tilde{\Omega}_1$ and $l, \cdots, N$ in $\tilde{\Omega}_2$. Since we need neighboring elements at each stage, in order to obtain $\mathbf{K}_i^{(l-1)}$, we need $\mathbf{K}_{i-1}^{(l-2)}$, $\mathbf{K}_{i-1}^{(l-1)}$ and $\mathbf{K}_{i-1}^{(l)}$.

Step 2:

- Integrate element $l-1$ from $t = t_{\frac{1}{3}}$ to t_1 on $\tilde{\Omega}_1$.

$$\begin{cases} \text{Stage 1: Compute } \mathbf{K}_1^{(l-4)}, \mathbf{K}_1^{(l-3)}, \mathbf{K}_1^{(l-2)}, \mathbf{K}_1^{(l-1)}, \mathbf{K}_1^{(l)}, \mathbf{K}_1^{(l+1)}, \mathbf{K}_1^{(l+2)} \text{ at } t = t_{\frac{1}{3}}. \\ \text{Stage 2: Compute } \mathbf{K}_2^{(l-3)}, \mathbf{K}_2^{(l-2)}, \mathbf{K}_2^{(l-1)}, \mathbf{K}_2^{(l)}, \mathbf{K}_2^{(l+1)} \text{ at } t = t_{\frac{1}{3}} + \frac{\Delta t_1^*}{2}. \\ \text{Stage 3: Compute } \mathbf{K}_3^{(l-2)}, \mathbf{K}_3^{(l-1)}, \mathbf{K}_3^{(l)} \text{ at } t = t_{\frac{1}{3}} + \frac{\Delta t_1^*}{2}. \\ \text{Stage 4: Compute } \mathbf{K}_4^{(l-1)} \text{ at } t = t_{\frac{1}{3}} + \Delta t_1^*. \\ \text{Solution: } \mathbf{c}_1^{(l-1)} = \mathbf{c}_{\frac{1}{3}}^{(l-1)} + \frac{\Delta t_1^*}{6}(\mathbf{K}_1^{(l-1)} + 2\mathbf{K}_2^{(l-1)} + 2\mathbf{K}_3^{(l-1)} + \mathbf{K}_4^{(l-1)}). \end{cases}$$

Each $\mathbf{K}_i$, $i = 1, 2, 3, 4$ has the following form:
Stage 1:

$$\mathbf{K}_1^{(j)} = f^{(j)}(t_{\frac{1}{3}}, \mathbf{c}_{\frac{1}{3}}^{(j-1)}, \mathbf{c}_{\frac{1}{3}}^{(j)}, \mathbf{c}_{\frac{1}{3}}^{(l+1)}), \ j = l-4, \cdots, l+2.$$

Stage 2:

$$\mathbf{K}_2^{(j)} = f^{(j)}(t_{\frac{1}{3}} + \frac{\Delta t_1^*}{2}, \mathbf{c}_{\frac{1}{3}}^{(j-1)} + \frac{\Delta t_1^*}{2}\mathbf{K}_1^{(j-1)}, \mathbf{c}_{\frac{1}{3}}^{(j)} + \frac{\Delta t_1^*}{2}\mathbf{K}_1^{(j)}, \mathbf{c}_{\frac{1}{3}}^{(j+1)} + \frac{\Delta t_1^*}{2}\mathbf{K}_1^{(j+1)}), \quad j = l-3, \cdots, l+1.$$

Stage 3:

$$\mathbf{K}_3^{(j)} = f^{(j)}(t_{\frac{1}{3}} + \frac{\Delta t_1^*}{2}, \mathbf{c}_{\frac{1}{3}}^{(j-1)} + \frac{\Delta t_1^*}{2}\mathbf{K}_2^{(j-1)}, \mathbf{c}_{\frac{1}{3}}^{(j)} + \frac{\Delta t_1^*}{2}\mathbf{K}_2^{(j)}, \mathbf{c}_{\frac{1}{3}}^{(j+1)} + \frac{\Delta t_1^*}{2}\mathbf{K}_2^{(j+1)}), \quad j = l-2, l-1, l.$$

Stage 4:

$$\mathbf{K}_4^{(l-1)} = f^{(l-1)}(t_{\frac{1}{3}} + \Delta t_1^*, \mathbf{c}_{\frac{1}{3}}^{(l-2)} + \Delta t_1^* \mathbf{K}_3^{(l-2)}, \mathbf{c}_{\frac{1}{3}}^{(l-1)} + \Delta t_1^* \mathbf{K}_3^{(l-1)}, \mathbf{c}_{\frac{1}{3}}^{(l)} + \Delta t_1^* \mathbf{K}_3^{(l)}).$$

Step 3:

- Integrate element l from $t = t_{\frac{1}{3}}$ to $t_{\frac{2}{3}}$ on $\tilde{\Omega}_2$.

$$\begin{cases} \text{Stage 1: Compute } \mathbf{K}_1^{(l-3)}, \mathbf{K}_1^{(l-2)}, \mathbf{K}_1^{(l-1)}, \mathbf{K}_1^{(l)}, \mathbf{K}_1^{(l+1)}, \mathbf{K}_1^{(l+2)}, \mathbf{K}_1^{(l+3)} \text{ at } t = t_{\frac{1}{3}}. \\ \text{Stage 2: Compute } \mathbf{K}_2^{(l-2)}, \mathbf{K}_2^{(l-1)}, \mathbf{K}_2^{(l)}, \mathbf{K}_2^{(l+1)}, \mathbf{K}_2^{(l+2)} \text{ at } t = t_{\frac{1}{3}} + \frac{\Delta t_2}{2}. \\ \text{Stage 3: Compute } \mathbf{K}_3^{(l-1)}, \mathbf{K}_3^{(l)}, \mathbf{K}_3^{(l+1)} \text{ at } t = t_{\frac{1}{3}} + \frac{\Delta t_2}{2}. \\ \text{Stage 4: Compute } \mathbf{K}_4^{(l)} \text{ at } t = t_{\frac{1}{3}} + \Delta t_2. \\ \text{Solution: } \mathbf{c}_{\frac{2}{3}}^{(l)} = \mathbf{c}_{\frac{1}{3}}^{(l)} + \frac{\Delta t_2}{6}(\mathbf{K}_1^{(l)} + 2\mathbf{K}_2^{(l)} + 2\mathbf{K}_3^{(l)} + \mathbf{K}_4^{(l)}). \end{cases}$$

Each $\mathbf{K}_i$, $i = 1, 2, 3, 4$ has the following form:
Stage 1:

$$\mathbf{K}_1^{(j)} = f^{(j)}(t_{\frac{1}{3}}, \mathbf{c}_{\frac{1}{3}}^{(j-1)}, \mathbf{c}_{\frac{1}{3}}^{(j)}, \mathbf{c}_{\frac{1}{3}}^{(j+1)}),\ j = l-3, \cdots, l+3.$$

Stage 2:

$$\mathbf{K}_2^{(j)} = f^{(j)}(t_{\frac{1}{3}} + \frac{\Delta t_2}{2}, \mathbf{c}_{\frac{1}{3}}^{(j-1)} + \frac{\Delta t_2}{2}\mathbf{K}_1^{(j-1)}, \mathbf{c}_{\frac{1}{3}}^{(j)} + \frac{\Delta t_2}{2}\mathbf{K}_1^{(j)}, \mathbf{c}_{\frac{1}{3}}^{(j+1)} + \frac{\Delta t_2}{2}\mathbf{K}_1^{(j+1)}),$$
$$j = l-2, \cdots, l+2.$$

Stage 3:

$$\mathbf{K}_3^{(j)} = f^{(j)}(t_{\frac{1}{3}} + \frac{\Delta t_2}{2}, \mathbf{c}_{\frac{1}{3}}^{(j-1)} + \frac{\Delta t_2}{2}\mathbf{K}_2^{(j-1)}, \mathbf{c}_{\frac{1}{3}}^{(j)} + \frac{\Delta t_2}{2}\mathbf{K}_2^{(j)}, \mathbf{c}_{\frac{1}{3}}^{(j+1)} + \frac{\Delta t_2}{2}\mathbf{K}_2^{(j+1)}),$$
$$j = l-1, l, l+1.$$

Stage 4:

$$\mathbf{K}_4^{(l)} = f^{(l)}(t_{\frac{1}{3}} + \Delta t_2, \mathbf{c}_{\frac{1}{3}}^{(l-1)} + \Delta t_2\mathbf{K}_3^{(l-1)}, \mathbf{c}_{\frac{1}{3}}^{(l)} + \Delta t_2\mathbf{K}_3^{(l)}, \mathbf{c}_{\frac{1}{3}}^{(l+1)} + \Delta t_2\mathbf{K}_3^{(l+1)}).$$

Step 4:

- Integrate element l from $t = t_{\frac{2}{3}}$ to t_1 on $\tilde{\Omega}_2$.
  We need $\mathbf{c}_{\frac{2}{3}}^{(l-4)}, \mathbf{c}_{\frac{2}{3}}^{(l-3)}, \mathbf{c}_{\frac{2}{3}}^{(l-2)}, \mathbf{c}_{\frac{2}{3}}^{(l-1)}$. We will discuss how to get those values below.

$$\begin{cases} \text{Stage 1: Compute } \mathbf{K}_1^{(l-3)}, \mathbf{K}_1^{(l-2)}, \mathbf{K}_1^{(l-1)}, \mathbf{K}_1^{(l)}, \mathbf{K}_1^{(l+1)}, \mathbf{K}_1^{(l+2)}, \mathbf{K}_1^{(l+3)} \text{ at } t = t_{\frac{2}{3}}. \\ \text{Stage 2: Compute } \mathbf{K}_2^{(l-2)}, \mathbf{K}_2^{(l-1)}, \mathbf{K}_2^{(l)}, \mathbf{K}_2^{(l+1)}, \mathbf{K}_2^{(l+2)} \text{ at } t = t_{\frac{2}{3}} + \frac{\Delta t_2}{2}. \\ \text{Stage 3: Compute } \mathbf{K}_3^{(l-1)}, \mathbf{K}_3^{(l)}, \mathbf{K}_3^{(l+1)} \text{ at } t = t_{\frac{2}{3}} + \frac{\Delta t_2}{2}. \\ \text{Stage 4: Compute } \mathbf{K}_4^{(l)} \text{ at } t = t_{\frac{2}{3}} + \Delta t_2. \\ \text{Solution: } \mathbf{c}_1^{(l)} = \mathbf{c}_{\frac{2}{3}}^{(l)} + \frac{\Delta t_2}{6}(\mathbf{K}_1^{(l)} + 2\mathbf{K}_2^{(l)} + 2\mathbf{K}_3^{(l)} + \mathbf{K}_4^{(l)}). \end{cases}$$

Each $\mathbf{K}_i$, $i = 1, 2, 3, 4$ has the following form:
Stage 1:

$$\mathbf{K}_1^{(j)} = f^{(j)}(t_{\frac{2}{3}}, \mathbf{c}_{\frac{2}{3}}^{(j-1)}, \mathbf{c}_{\frac{2}{3}}^{(j)}, \mathbf{c}_{\frac{2}{3}}^{(j+1)}), \ j = l-3, \cdots, l+3.$$

Stage 2:

$$\mathbf{K}_2^{(j)} = f^{(j)}(t_{\frac{2}{3}} + \frac{\Delta t_2}{2}, \mathbf{c}_{\frac{2}{3}}^{(j-1)} + \frac{\Delta t_2}{2}\mathbf{K}_1^{(j-1)}, \mathbf{c}_{\frac{2}{3}}^{(j)} + \frac{\Delta t_2}{2}\mathbf{K}_1^{(j)}, \mathbf{c}_{\frac{2}{3}}^{(j+1)} + \frac{\Delta t_2}{2}\mathbf{K}_1^{(j+1)}),$$
$$j = l-2, \cdots, l+2.$$

Stage 3:

$$\mathbf{K}_3^{(j)} = f^{(j)}(t_{\frac{2}{3}} + \frac{\Delta t_2}{2}, \mathbf{c}_{\frac{2}{3}}^{(j-1)} + \frac{\Delta t_2}{2}\mathbf{K}_2^{(j-1)}, \mathbf{c}_{\frac{2}{3}}^{(j)} + \frac{\Delta t_2}{2}\mathbf{K}_2^{(j)}, \mathbf{c}_{\frac{2}{3}}^{(j+1)} + \frac{\Delta t_2}{2}\mathbf{K}_2^{(j+1)}),$$
$$j = l-1, l, l+1.$$

Stage 4:

$$\mathbf{K}_4^{(l)} = f^{(l)}(t_{\frac{2}{3}} + \Delta t_2, \mathbf{c}_{\frac{2}{3}}^{(l-1)} + \Delta t_2\mathbf{K}_3^{(l-1)}, \mathbf{c}_{\frac{2}{3}}^{(l)} + \Delta t_2\mathbf{K}_3^{(l)}, \mathbf{c}_{\frac{2}{3}}^{(l+1)} + \Delta t_2\mathbf{K}_3^{(l+1)}).$$

Next, we explain how to integrate from t_n to t_{n+1} for $n \geq 1$. In Step 1, we apply the local time-stepping from t_n to t_{n+1} on $\tilde{\Omega}_1$ using time step size Δt_1. Steps 2, 3 and 4 are the local time-stepping from t_n to $t_{n+\frac{1}{3}}$ and from $t_{n+\frac{1}{3}}$ to $t_{n+\frac{2}{3}}$ and from $t_{n+\frac{2}{3}}$ to t_{n+1}, respectively, using time step size Δt_2 on $\tilde{\Omega}_2$.

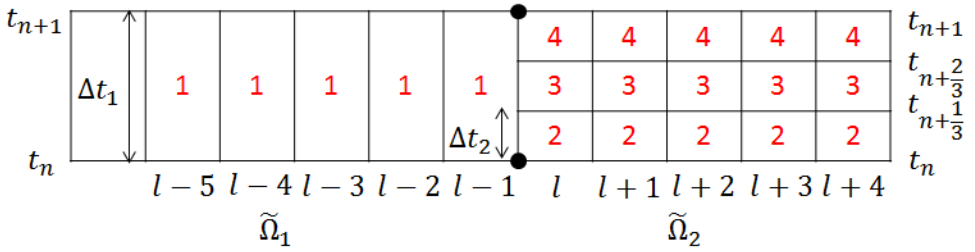

Figure 4.2.3: Local time-stepping algorithm at $t = t_n$, $n \geq 1$.

Step 1:

- Integrate element $l-1$ from $t = t_n$ to t_{n+1} on $\tilde{\Omega}_1$.

$$\begin{cases} \text{Stage 1: Compute } \mathbf{K}_1^{(l-4)}, \mathbf{K}_1^{(l-3)}, \mathbf{K}_1^{(l-2)}, \mathbf{K}_1^{(l-1)}, \mathbf{K}_1^{(l)}, \mathbf{K}_1^{(l+1)}, \mathbf{K}_1^{(l+2)} \text{ at } t = t_n. \\ \text{Stage 2: Compute } \mathbf{K}_2^{(l-3)}, \mathbf{K}_2^{(l-2)}, \mathbf{K}_2^{(l-1)}, \mathbf{K}_2^{(l)}, \mathbf{K}_2^{(l+1)} \text{ at } t = t_n + \frac{\Delta t_1}{2}. \\ \text{Stage 3: Compute } \mathbf{K}_3^{(l-2)}, \mathbf{K}_3^{(l-1)}, \mathbf{K}_3^{(l)} \text{ at } t = t_n + \frac{\Delta t_1}{2}. \\ \text{Stage 4: Compute } \mathbf{K}_4^{(l-1)} \text{ at } t = t_n + \Delta t_1. \\ \text{Solution: } \mathbf{c}_{n+1}^{(l-1)} = \mathbf{c}_n^{(l-1)} + \frac{\Delta t_1}{6}(\mathbf{K}_1^{(l-1)} + 2\mathbf{K}_2^{(l-1)} + 2\mathbf{K}_3^{(l-1)} + \mathbf{K}_4^{(l-1)}). \end{cases}$$

Each $\mathbf{K}_i$, $i = 1, 2, 3, 4$ has the following form:
Stage 1:

$$\mathbf{K}_1^{(j)} = f^{(j)}(t_n, \mathbf{c}_n^{(j-1)}, \mathbf{c}_n^{(j)}, \mathbf{c}_n^{(j+1)}),\ j = l-4, \cdots, l+2.$$

Stage 2:

$$\mathbf{K}_2^{(j)} = f^{(j)}(t_n + \frac{\Delta t_1}{2}, \mathbf{c}_n^{(j-1)} + \frac{\Delta t_1}{2}\mathbf{K}_1^{(j-1)}, \mathbf{c}_n^{(j)} + \frac{\Delta t_1}{2}\mathbf{K}_1^{(j)}, \mathbf{c}_n^{(j+1)} + \frac{\Delta t_1}{2}\mathbf{K}_1^{(j+1)}),$$
$$j = l-3, \cdots, l+1.$$

Stage 3:

$$\mathbf{K}_3^{(j)} = f^{(j)}(t_n + \frac{\Delta t_1}{2}, \mathbf{c}_n^{(j-1)} + \frac{\Delta t_1}{2}\mathbf{K}_2^{(j-1)}, \mathbf{c}_n^{(j)} + \frac{\Delta t_1}{2}\mathbf{K}_2^{(j)}, \mathbf{c}_n^{(j+1)} + \frac{\Delta t_1}{2}\mathbf{K}_2^{(j+1)}),$$
$$j = l-2, l-1, l.$$

Stage 4:

$$\mathbf{K}_4^{(l-1)} = f^{(l-1)}(t_n + \Delta t_1, \mathbf{c}_n^{(l-2)} + \Delta t_1\mathbf{K}_3^{(l-2)}, \mathbf{c}_n^{(l-1)} + \Delta t_1\mathbf{K}_3^{(l-1)}, \mathbf{c}_n^{(l)} + \Delta t_1\mathbf{K}_3^{(l)}).$$

Step 2:

- Integrate element l from $t = t_n$ to $t_{n+\frac{1}{3}}$ on $\tilde{\Omega}_2$.

$$\begin{cases} \text{Stage 1: Compute } \mathbf{K}_1^{(l-3)}, \mathbf{K}_1^{(l-2)}, \mathbf{K}_1^{(l-1)}, \mathbf{K}_1^{(l)}, \mathbf{K}_1^{(l+1)}, \mathbf{K}_1^{(l+2)}, \mathbf{K}_1^{(l+3)} \text{ at } t = t_n. \\ \text{Stage 2: Compute } \mathbf{K}_2^{(l-2)}, \mathbf{K}_2^{(l-1)}, \mathbf{K}_2^{(l)}, \mathbf{K}_2^{(l+1)}, \mathbf{K}_2^{(l+2)} \text{ at } t = t_n + \frac{\Delta t_2}{2}. \\ \text{Stage 3: Compute } \mathbf{K}_3^{(l-1)}, \mathbf{K}_3^{(l)}, \mathbf{K}_3^{(l+1)} \text{ at } t = t_n + \frac{\Delta t_2}{2}. \\ \text{Stage 4: Compute } \mathbf{K}_4^{(l)} \text{ at } t = t_n + \Delta t_2. \\ \text{Solution: } \mathbf{c}_{n+\frac{1}{3}}^{(l)} = \mathbf{c}_n^{(l)} + \frac{\Delta t_2}{6}(\mathbf{K}_1^{(l)} + 2\mathbf{K}_2^{(l)} + 2\mathbf{K}_3^{(l)} + \mathbf{K}_4^{(l)}). \end{cases}$$

Each $\mathbf{K}_i$, $i = 1, 2, 3, 4$ has the following form:
Stage 1:

$$\mathbf{K}_1^{(j)} = f^{(j)}(t_n, \mathbf{c}_n^{(j-1)}, \mathbf{c}_n^{(j)}, \mathbf{c}_n^{(j+1)}),\ j = l-3, \cdots, l+3.$$

Stage 2:

$$\mathbf{K}_2^{(j)} = f^{(j)}(t_n + \frac{\Delta t_2}{2}, \mathbf{c}_n^{(j-1)} + \frac{\Delta t_2}{2}\mathbf{K}_1^{(j-1)}, \mathbf{c}_n^{(j)} + \frac{\Delta t_2}{2}\mathbf{K}_1^{(j)}, \mathbf{c}_n^{(j+1)} + \frac{\Delta t_2}{2}\mathbf{K}_1^{(j+1)}),$$
$$j = l-2, \cdots, l+2.$$

Stage 3:

$$\mathbf{K}_3^{(j)} = f^{(j)}(t_n + \frac{\Delta t_2}{2}, \mathbf{c}_n^{(j-1)} + \frac{\Delta t_2}{2}\mathbf{K}_2^{(j-1)}, \mathbf{c}_n^{(j)} + \frac{\Delta t_2}{2}\mathbf{K}_2^{(j)}, \mathbf{c}_n^{(j+1)} + \frac{\Delta t_2}{2}\mathbf{K}_2^{(j+1)}),$$
$$j = l-1, l, l+1.$$

Stage 4:

$$\mathbf{K}_4^{(l)} = f^{(l)}(t_n + \Delta t_2, \mathbf{c}_n^{(l-1)} + \Delta t_2\mathbf{K}_3^{(l-1)}, \mathbf{c}_n^{(l)} + \Delta t_2\mathbf{K}_3^{(l)}, \mathbf{c}_n^{(l+1)} + \Delta t_2\mathbf{K}_3^{(l+1)}).$$

Step 3:

- Integrate element l from $t = t_{n+\frac{1}{3}}$ to $t = t_{n+\frac{2}{3}}$ on $\tilde{\Omega}_2$.
  We need $\mathbf{c}_{n+\frac{1}{3}}^{(l-4)}, \mathbf{c}_{n+\frac{1}{3}}^{(l-3)}, \mathbf{c}_{n+\frac{1}{3}}^{(l-2)}, \mathbf{c}_{n+\frac{1}{3}}^{(l-1)}$.

$$\begin{cases} \text{Stage 1: Compute } \mathbf{K}_1^{(l-3)}, \mathbf{K}_1^{(l-2)}, \mathbf{K}_1^{(l-1)}, \mathbf{K}_1^{(l)}, \mathbf{K}_1^{(l+1)}, \mathbf{K}_1^{(l+2)}, \mathbf{K}_1^{(l+3)} \text{ at } t = t_{n+\frac{1}{3}}. \\ \text{Stage 2: Compute } \mathbf{K}_2^{(l-2)}, \mathbf{K}_2^{(l-1)}, \mathbf{K}_2^{(l)}, \mathbf{K}_2^{(l+1)}, \mathbf{K}_2^{(l+2)} \text{ at } t = t_{n+\frac{1}{3}} + \frac{\Delta t_2}{2}. \\ \text{Stage 3: Compute } \mathbf{K}_3^{(l-1)}, \mathbf{K}_3^{(l)}, \mathbf{K}_3^{(l+1)} \text{ at } t = t_{n+\frac{1}{3}} + \frac{\Delta t_2}{2}. \\ \text{Stage 4: Compute } \mathbf{K}_4^{(l)} \text{ at } t = t_{n+\frac{1}{3}} + \Delta t_2. \\ \text{Solution: } \mathbf{c}_{n+\frac{2}{3}}^{(l)} = \mathbf{c}_{n+\frac{1}{3}}^{(l)} + \frac{\Delta t_2}{6}(\mathbf{K}_1^{(l)} + 2\mathbf{K}_2^{(l)} + 2\mathbf{K}_3^{(l)} + \mathbf{K}_4^{(l)}). \end{cases}$$

  Each $\mathbf{K}_i$, $i = 1, 2, 3, 4$ has the following form:
  Stage 1:

$$\mathbf{K}_1^{(j)} = f^{(j)}(t_{n+\frac{1}{3}}, \mathbf{c}_{n+\frac{1}{3}}^{(j-1)}, \mathbf{c}_{n+\frac{1}{3}}^{(j)}, \mathbf{c}_{n+\frac{1}{3}}^{(j+1)}), \ j = l-3, \cdots, l+3.$$

  Stage 2:

$$\mathbf{K}_2^{(j)} = f^{(j)}(t_{n+\frac{1}{3}} + \frac{\Delta t_2}{2}, \mathbf{c}_{n+\frac{1}{3}}^{(j-1)} + \frac{\Delta t_2}{2}\mathbf{K}_1^{(j-1)}, \mathbf{c}_{n+\frac{1}{3}}^{(j)} + \frac{\Delta t_2}{2}\mathbf{K}_1^{(j)}, \mathbf{c}_{n+\frac{1}{3}}^{(j+1)} + \frac{\Delta t_2}{2}\mathbf{K}_1^{(j+1)}), \quad j = l-2, \cdots, l+2.$$

  Stage 3:

$$\mathbf{K}_3^{(j)} = f^{(j)}(t_{n+\frac{1}{3}} + \frac{\Delta t_2}{2}, \mathbf{c}_{n+\frac{1}{3}}^{(j-1)} + \frac{\Delta t_2}{2}\mathbf{K}_2^{(j-1)}, \mathbf{c}_{n+\frac{1}{3}}^{(j)} + \frac{\Delta t_2}{2}\mathbf{K}_2^{(j)}, \mathbf{c}_{n+\frac{1}{3}}^{(j+1)} + \frac{\Delta t_2}{2}\mathbf{K}_2^{(j+1)}), \quad j = l-1, l, l+1.$$

  Stage 4:

$$\mathbf{K}_4^{(l)} = f^{(l)}(t_{n+\frac{1}{3}} + \Delta t_2, \mathbf{c}_{n+\frac{1}{3}}^{(l-1)} + \Delta t_2\mathbf{K}_3^{(l-1)}, \mathbf{c}_{n+\frac{1}{3}}^{(l)} + \Delta t_2\mathbf{K}_3^{(l)}, \mathbf{c}_{n+\frac{1}{3}}^{(l+1)} + \Delta t_2\mathbf{K}_3^{(l+1)}).$$

Step 4:

- Integrate element l from $t = t_{n+\frac{2}{3}}$ to t_{n+1} on $\tilde{\Omega}_2$.
  We need $\mathbf{c}_{n+\frac{2}{3}}^{(l-4)}, \mathbf{c}_{n+\frac{2}{3}}^{(l-3)}, \mathbf{c}_{n+\frac{2}{3}}^{(l-2)}, \mathbf{c}_{n+\frac{2}{3}}^{(l-1)}$.

$$\begin{cases} \text{Stage 1: Compute } \mathbf{K}_1^{(l-3)}, \mathbf{K}_1^{(l-2)}, \mathbf{K}_1^{(l-1)}, \mathbf{K}_1^{(l)}, \mathbf{K}_1^{(l+1)}, \mathbf{K}_1^{(l+2)}, \mathbf{K}_1^{(l+3)} \text{ at } t = t_{n+\frac{2}{3}}. \\ \text{Stage 2: Compute } \mathbf{K}_2^{(l-2)}, \mathbf{K}_2^{(l-1)}, \mathbf{K}_2^{(l)}, \mathbf{K}_2^{(l+1)}, \mathbf{K}_2^{(l+2)} \text{ at } t = t_{n+\frac{2}{3}} + \frac{\Delta t_2}{2}. \\ \text{Stage 3: Compute } \mathbf{K}_3^{(l-1)}, \mathbf{K}_3^{(l)}, \mathbf{K}_3^{(l+1)} \text{ at } t = t_{n+\frac{2}{3}} + \frac{\Delta t_2}{2}. \\ \text{Stage 4: Compute } \mathbf{K}_4^{(l)} \text{ at } t = t_{n+\frac{2}{3}} + \Delta t_2. \\ \text{Solution: } \mathbf{c}_{n+1}^{(l)} = \mathbf{c}_{n+\frac{2}{3}}^{(l)} + \frac{\Delta t_2}{6}(\mathbf{K}_1^{(l)} + 2\mathbf{K}_2^{(l)} + 2\mathbf{K}_3^{(l)} + \mathbf{K}_4^{(l)}). \end{cases}$$

Each $\mathbf{K}_i$, $i = 1, 2, 3, 4$ has the following form:
Stage 1:

$$\mathbf{K}_1^{(j)} = f^{(j)}(t_{n+\frac{2}{3}}, \mathbf{c}_{n+\frac{2}{3}}^{(j-1)}, \mathbf{c}_{n+\frac{2}{3}}^{(j)}, \mathbf{c}_{n+\frac{2}{3}}^{(j+1)}),\ j = l-3, \cdots, l+3.$$

Stage 2:

$$\mathbf{K}_2^{(j)} = f^{(j)}(t_{n+\frac{2}{3}} + \frac{\Delta t_2}{2}, \mathbf{c}_{n+\frac{2}{3}}^{(j-1)} + \frac{\Delta t_2}{2}\mathbf{K}_1^{(j-1)}, \mathbf{c}_{n+\frac{2}{3}}^{(j)} + \frac{\Delta t_2}{2}\mathbf{K}_1^{(j)}, \mathbf{c}_{n+\frac{2}{3}}^{(j+1)} + \frac{\Delta t_2}{2}\mathbf{K}_1^{(j+1)}),$$
$$j = l-2, \cdots, l+2.$$

Stage 3:

$$\mathbf{K}_3^{(j)} = f^{(j)}(t_{n+\frac{2}{3}} + \frac{\Delta t_2}{2}, \mathbf{c}_{n+\frac{2}{3}}^{(j-1)} + \frac{\Delta t_2}{2}\mathbf{K}_2^{(j-1)}, \mathbf{c}_{n+\frac{2}{3}}^{(j)} + \frac{\Delta t_2}{2}\mathbf{K}_2^{(j)}, \mathbf{c}_{n+\frac{2}{3}}^{(j+1)} + \frac{\Delta t_2}{2}\mathbf{K}_2^{(j+1)}),$$
$$j = l-1, l, l+1.$$

Stage 4:

$$\mathbf{K}_4^{(l)} = f^{(l)}(t_{n+\frac{2}{3}} + \Delta t_2, \mathbf{c}_{n+\frac{2}{3}}^{(l-1)} + \Delta t_2\mathbf{K}_3^{(l-1)}, \mathbf{c}_{n+\frac{2}{3}}^{(l)} + \Delta t_2\mathbf{K}_3^{(l)}, \mathbf{c}_{n+\frac{2}{3}}^{(l+1)} + \Delta t_2\mathbf{K}_3^{(l+1)}).$$

Interpolation

In Step 3 in Figure 4.2.3, in order to integrate the element l from $t_{n+\frac{1}{3}}$ to $t_{n+\frac{2}{3}}$ on $\tilde{\Omega}_2$, one needs $\mathbf{c}_{n+\frac{1}{3}}^{(l-4)}$, $\mathbf{c}_{n+\frac{1}{3}}^{(l-3)}$, $\mathbf{c}_{n+\frac{1}{3}}^{(l-2)}$ and $\mathbf{c}_{n+\frac{1}{3}}^{(l-1)}$ which are computed using interpolation as described below:

We note that vectors $\mathbf{y}^{(k)}(t)$ and $\mathbf{c}^{(k)}$ are computed componentwise.

$$\begin{cases} \textit{For } k = l-4 : l-1, \\ \quad 1.\ \textit{Find } \mathbf{y}^{(k)}(t) \textit{ such that} \\ \qquad \begin{cases} \mathbf{y}^{(k)}(t_{n+1}) & = \mathbf{c}_{n+1}^{(k)}, \\ \mathbf{y}^{(k)}(t_n) & = \mathbf{c}_n^{(k)}, \\ \frac{d\mathbf{y}^{(k)}(t_n)}{dt} & = f^{(k)}(t_n, \mathbf{c}_n^{(k-1)}, \mathbf{c}_n^{(k)}, \mathbf{c}_n^{(k+1)}), \\ \mathbf{y}^{(k)}(t_{n-\frac{1}{3}}) & = \mathbf{c}_{n-\frac{1}{3}}^{(k)} \ (\textit{which is available from the previous step}), \end{cases} \\ \quad 2.\ \mathbf{c}_{n+\frac{1}{3}}^{(k)} = \mathbf{y}^{(k)}(t_{n+\frac{1}{3}}). \end{cases} \tag{4.2.4}$$

Two Dimensional Implementation

This local time-stepping algorithm has been extended to two dimensional problems. For instance, let $\tilde{\Omega}_1$, $\tilde{\Omega}_2$, respectively, denote the regions exterior and interior with the circle with time step sizes Δt_1 and Δt_2 such that $\Delta t_1 > \Delta t_2$ shown in Figure 4.2.4 (left). In order to integrate an interface element with time step size Δt_2 one needs information from neighboring elements. The elements in $\tilde{\Omega}_1$ needed to integrate interface elements are shown in yellow 4.2.4 (left). Similarly, the case $\Delta t_1 < \Delta t_2$ is shown in Figure 4.2.4 (right).

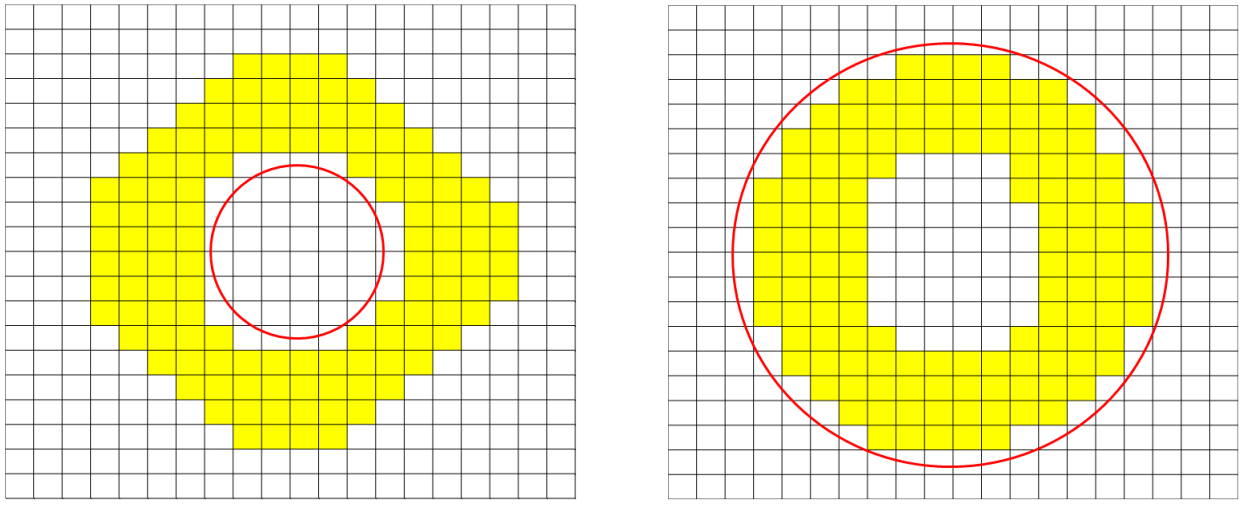

Figure 4.2.4: Interpolation region for the problem of $\Delta t_1 > \Delta t_2$ (left) and $\Delta t_1 < \Delta t_2$ (right).

Efficiency

Let the number of elements in $\tilde{\Omega}_1$, $\tilde{\Omega}_2$ be N_1, N_2, respectively, and Δt_1, Δt_2 be time step sizes for $\tilde{\Omega}_1$, $\tilde{\Omega}_2$. Let us assume $2c_1 \leq c_2$ with $M = \lceil \frac{c_2}{c_1} \rceil$ to obtain $\Delta t_1 = M \Delta t_2$. Let T denote the computational cost for integration from t_n to t_{n+1} measured by the number of space-time cells and given by $T = N_1 + MN_2$ for local time-stepping and $T = MN_1 + MN_2$ for global time-stepping. We define the ratio of the computational costs for local time-stepping versus global time-stepping as

$$R = \frac{N_1 + MN_2}{MN_1 + MN_2} = \frac{\frac{1}{M}N_1 + N_2}{N_1 + N_2} = \frac{\frac{1}{M}\frac{N_1}{N_2} + 1}{\frac{N_1}{N_2} + 1} < 1. \tag{4.2.5}$$

R is small for large M ($\frac{c_2}{c_1} >> 1$) or large $\frac{N_1}{N_2}$ (the number of elements in $\tilde{\Omega}_2$ is much smaller than that in $\tilde{\Omega}_1$) which implies that the local time-stepping is more efficient. Figure 4.2.5 shows the relation between R, M and $\frac{N_1}{N_2}$.

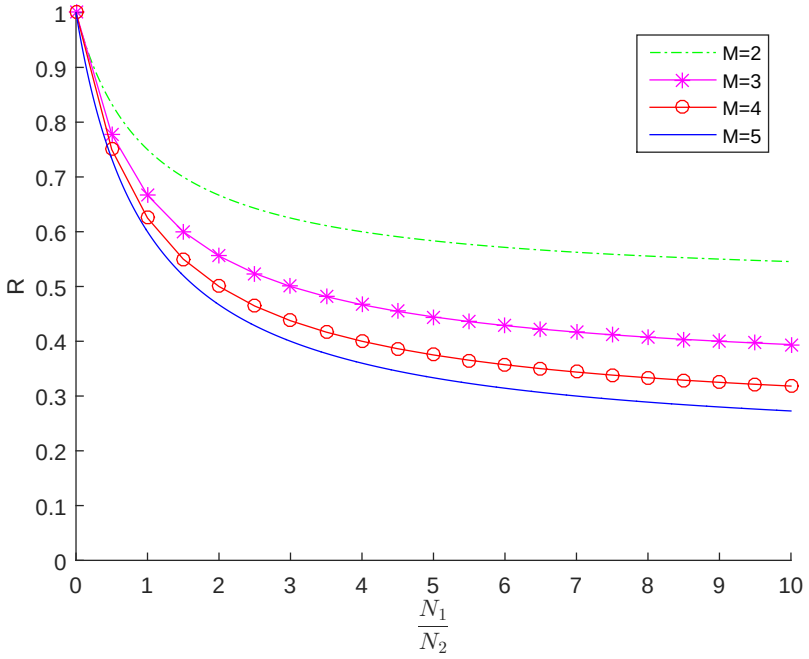

Figure 4.2.5: Ratio of computational costs for local time-stepping and global time-stepping versus $\frac{N_1}{N_2}$.

4.2.2 Parallel Computing

In order to save computational time, the code is written in C programming language with MPI (message passing interface). The domain is split into several regions and each region is assigned to a process to perform time integration. Since discontinuous Galerkin methods use neighboring elements, there is a need for communication between processes. Thus additional buffer zones are needed to store values obtained from neighboring processes as illustrated in Figure 4.2.6. For this reason, the speed-up does not increase linearly with increasing number of processes.

We consider a system of ordinary differential equation of immersed DG methods of the form

$$\begin{cases} \frac{d\mathbf{C}}{dt} = \mathcal{F}(t, \mathbf{C}), \\ \\ \mathbf{C}_0 = \mathbf{C}(t_0), \end{cases} \tag{4.2.6}$$

where $\mathbf{C}$ is a global solution vector. We split the initial solution $\mathbf{C}_0$ into $\mathbf{C}_0^{(0)}, \cdots, \mathbf{C}_0^{(M)}$ for M processes. Boundary values $\mathbf{B^b}$, $\mathbf{B^t}$ are updated after each call to $\mathcal{F}^{(j)}$ when applying the

fourth-order Runge-Kutta method:

$$\begin{cases} \mathbf{K}_1^{(j)} = \mathcal{F}^{(j)}(t_i, \mathbf{C}_i^{(j)}) \\ \text{Propagate } \mathbf{K}_1^{(j)} \text{ to neighboring processes} \\ \mathbf{K}_2^{(j)} = \mathcal{F}^{(j)}(t_i + \frac{\Delta t}{2}, \mathbf{C}_i^{(j)} + \frac{\Delta t}{2}\mathbf{K}_1^{(j)}) \\ \text{Propagate } \mathbf{K}_2^{(j)} \text{ to neighboring processes} \\ \mathbf{K}_3^{(j)} = \mathcal{F}^{(j)}(t_i + \frac{\Delta t}{2}, \mathbf{C}_i^{(j)} + \frac{\Delta t}{2}\mathbf{K}_2^{(j)}) \\ \text{Propagate } \mathbf{K}_3^{(j)} \text{ to neighboring processes} \\ \mathbf{K}_4^{(j)} = \mathcal{F}^{(j)}(t_i + \Delta t, \mathbf{C}_i^{(j)} + \Delta t\mathbf{K}_3^{(j)}) \\ \text{Propagate } \mathbf{K}_4^{(j)} \text{ to neighboring processes} \end{cases} \tag{4.2.7}$$

where Δt is a time step size, $\mathbf{C}_i = \mathbf{C}(t_i)$ and $\mathcal{F}^{(j)}$ is a function of (4.2.6) on process j.

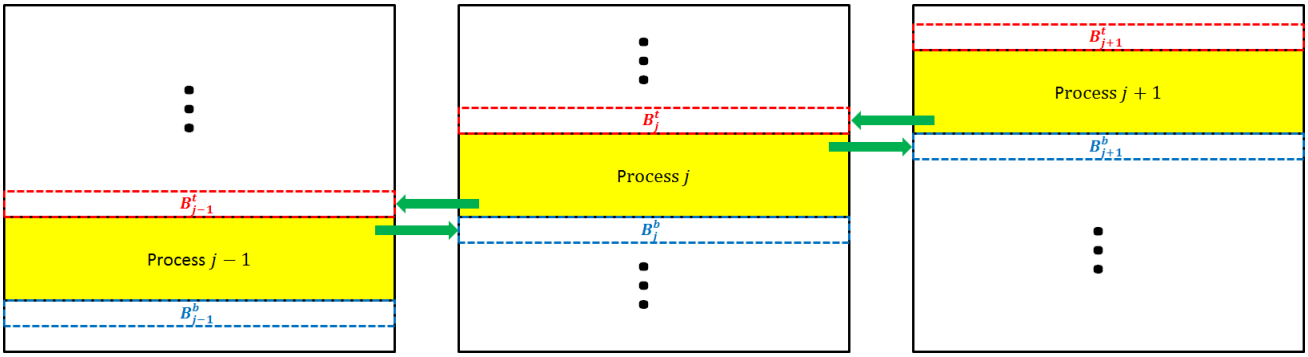

Figure 4.2.6: Diagram for exchanging boundary values between processes.

In order to obtain the final solution $\mathbf{C}_N = \mathbf{C}(t_N)$, we merge $\mathbf{C}_N^{(0)}, \cdots, \mathbf{C}_N^{(M)}$ from all the processes at $t = t_N$. The main steps in our parallel algorithm are given as:

$$
\begin{cases}
\text{1. } L^2 \textit{ projection at the initial time } t = t_0 \textit{ on the domain.} \\
\text{2. } \textit{Partition the domain into } M \textit{ regions for each process.} \\
\quad : \ \mathbf{C}_0 \textit{ is partitioned into } \mathbf{C}_0^{(0)}, \cdots, \mathbf{C}_0^{(M)}. \\
\text{3. } \textit{For } i = 0 : N-1 \\
\quad \begin{cases} \textit{Calculate } \mathbf{K}_1^{(j)} \textit{ for } j = 1 : M \\ \textit{Exange boundary values with neighboring processes.} \end{cases} \\
\quad \begin{cases} \textit{Calculate } \mathbf{K}_2^{(j)} \textit{ for } j = 1 : M \\ \textit{Exange boundary values with neighboring processes.} \end{cases} \\
\quad \begin{cases} \textit{Calculate } \mathbf{K}_3^{(j)} \textit{ for } j = 1 : M \\ \textit{Exange boundary values with neighboring processes.} \end{cases} \\
\quad \begin{cases} \textit{Calculate } \mathbf{K}_4^{(j)} \textit{ for } j = 1 : M \\ \textit{Exange boundary values with neighboring processes.} \end{cases} \\
\quad \textit{Get } \mathbf{C}_i^{(j)} \textit{ from } \mathbf{K}_1^{(j)}, \mathbf{K}_2^{(j)}, \mathbf{K}_3^{(j)}, \mathbf{K}_4^{(j)} \textit{ for } j = 1 : M \\
\text{4. } \textit{Merge the solutions from all the processes at the final time } t = t_N. \\
\quad : \ \mathbf{C}_N^{(0)}, \cdots, \mathbf{C}_N^{(M)} \textit{ is merged into } \mathbf{C}_N.
\end{cases}
\tag{4.2.8}
$$

4.3 Computational Results

The first set of computations are conducted to discover the order of convergence of the immersed DG solutions on a problem with two medium separated by a linear interface. We conduct similar experiments on a second interface problem involves a circular interface. In our computations we used the classical fourth-order Runge-Kutta method to integrate in time with local and global time-stepping.

Example 4.3.1.

Let us consider the acoustic interface problem (3.1.2) on the domain $\Omega = (0, 20)^2$ divided by the linear interface $\Gamma = \{(x, y) \mid y = -5x + 70.05555\}$ into $\Omega_1 = \{(x, y) \in \Omega \mid y < -5x + 70.05555\}$ and $\Omega_2 = \{(x, y) \in \Omega \mid y > -5x + 70.05555\}$. For this test problem we assume that for the medium occupying Ω_1, $c_1 = 1m/s,\ \rho_1 = 1kg/m^3$ and for the medium occupying Ω_2, $c_2 = 2m/s,\ \rho_2 = 1.5kg/m^3$. Moreover, the problem is subjected to the initial

condition (3.4.2) with $t_0 = 13.6649$, $\omega_c = 1$, $(\alpha, \beta) = (2, 1)/\sqrt{5}$ and the inflow boundary condition on $\partial\Omega$ computed using the true solution.

We solve the problem on uniform non fitted meshes having $N = 100^2, 150^2, 200^2, 250^2, 300^2, 350^2, 400^2$ square elements with bilinear and biquadratic IFE spaces. We integrate in time from $t = 0$ to $t = 5$ using a local time-stepping algorithm for the classical fourth-order Runke-Kutta scheme where $\Delta t_1 = 10^{-3}$ on all non interface elements in Ω_1 and $\Delta t_2 = 5\ 10^{-4}$ on the remaining elements using bilinear IFE spaces. Similarly, we used $\Delta t_1 = 5\ 10^{-4}$ on non interface elements in Ω_1 and $\Delta t_2 = 2.5\ 10^{-4}$ on the remaining elements for the biquadratic IFE spaces.

We selected the time steps so that the temporal discretization errors are negligible compared to the spatial errors. We present the L^2 errors for the pressure and velocity and their orders of convergence at $t = 5$ in Table 4.3.1 which suggest optimal convergence rates. The true and IDGFE solutions on a uniform mesh having $N = 200^2$ square elements with bilinear IFE spaces shown in Figure 4.3.1 are in full agreement.

Bilinear						
N	$\frac{\|p-p_h\|_{L^2}}{\|p\|_{L^2}}$	Order	$\frac{\|u-u_h\|_{L^2}}{\|u\|_{L^2}}$	Order	$\frac{\|v-v_h\|_{L^2}}{\|v\|_{L^2}}$	Order
100^2	9.8756e-2	NA	1.2630e-1	NA	1.0784e-1	NA
150^2	3.6146e-2	2.4789	4.7827e-2	2.3949	3.9816e-2	2.4574
200^2	1.6665e-2	2.6914	2.2561e-2	2.6119	1.8556e-2	2.6539
250^2	9.0260e-3	2.7479	1.2462e-2	2.6599	1.0186e-2	2.6880
300^2	5.4571e-3	2.7600	7.6776e-3	2.6566	6.2598e-3	2.6702
350^2	3.5465e-3	2.7956	5.0913e-3	2.6648	4.1607e-3	2.6498
400^2	2.4605e-3	2.7378	3.5972e-3	2.6015	2.9468e-3	2.5833
Biquadratic						
N	$\frac{\|p-p_h\|_{L^2}}{\|p\|_{L^2}}$	Order	$\frac{\|u-u_h\|_{L^2}}{\|u\|_{L^2}}$	Order	$\frac{\|v-v_h\|_{L^2}}{\|v\|_{L^2}}$	Order
100^2	2.2097e-3	NA	3.6015e-3	NA	2.8021e-3	NA
150^2	4.3217e-4	4.0245	8.3734e-4	3.5981	6.5505e-4	3.5846
200^2	1.5662e-4	3.5282	3.3199e-4	3.2157	2.7044e-4	3.0751
250^2	7.6276e-5	3.2242	1.6776e-4	3.0589	1.4107e-4	2.9164
300^2	4.4142e-5	2.9999	9.7195e-5	2.9937	8.1990e-5	2.9765
350^2	2.9907e-5	2.5255	6.2999e-5	2.8128	5.3348e-5	2.7879
400^2	1.8926e-5	3.4266	4.0707e-5	3.2706	3.5404e-5	3.0705

Table 4.3.1: L^2 errors and orders of convergence at $t = 5$ for Example 4.3.1 using bilinear and biquadratic IFE spaces and IDGFE method.

Tables 4.3.2, 4.3.3 are L^2 errors and their orders of convergence for IDG method applied to the scaled problem and IDPGFE method with inflow boundary condition. Two times smaller

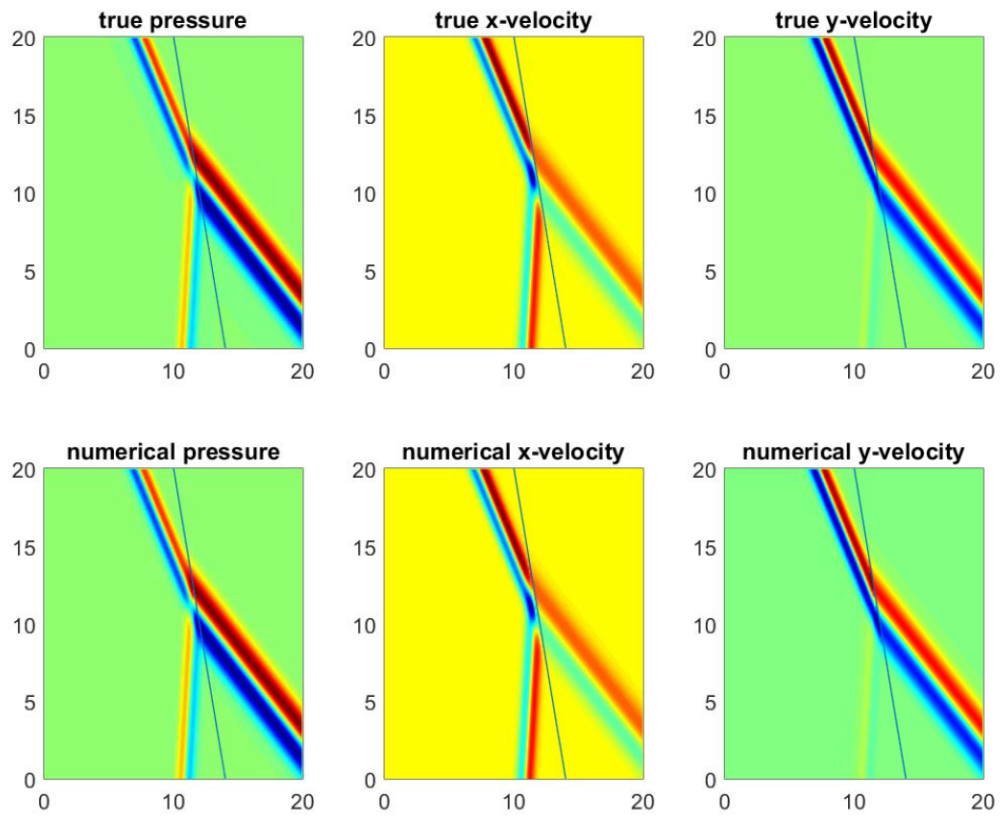

Figure 4.3.1: True (top) and IDGFE (bottom) solutions at $t = 5$ for Example 4.3.1 with $N = 200^2$ elements and bilinear IFE spaces.

time step is used for IDG method applied to the scaled problem in order to make temporal error very small compared to spatial error because it has small stability region compared to IDGFE method and IDPGFE methods. Here we note that linear interpolation is used for Table 4.3.1 and cubic interpolation is used for Tables 4.3.2, 4.3.3 as an interpolation function for local time-stepping.

We will compute the true pressure by first recalling that the pressure satisfies the wave equation (3.2.1) and using the initial wave pulse (3.4.3) to write the incident pressure wave before it hits the interface as

$$p_i(x, y, t) = \psi\left(\frac{\omega_c \alpha}{c_1} x + \frac{\omega_c \beta}{c_1} y - \omega_c (t + t_0)\right), \tag{4.3.1}$$

where $(\alpha, \beta) = (\cos\theta_1, \sin\theta_1)$, $x = x_0 + r\cos\phi, y = y_0 + r\sin\phi$ in polar coordinates with respect to (x_0, y_0). If $\hat{\psi}(\omega) = \frac{i}{8\sqrt{\pi}}\left(e^{-\frac{(1+\omega)^2}{16}} - e^{-\frac{(1-\omega)^2}{16}}\right)$ is the Fourier transform of ψ then the incident pressure can be written as

$$p_i(x, y, t) = \int_{-\infty}^{\infty} \hat{\psi}(\omega) e^{i\omega\left(\frac{\omega_c \alpha}{c_1} x + \frac{\omega_c \beta}{c_1} y - \omega_c (t+t_0)\right)} d\omega. \tag{4.3.2}$$

Letting $\theta = \phi - \theta_1$ and J_n be Bessel function of the first kind we use the Jacobi-Anger

Bilinear						
N	$\frac{\|p-p_h\|_{L^2}}{\|p\|_{L^2}}$	Order	$\frac{\|u-u_h\|_{L^2}}{\|u\|_{L^2}}$	Order	$\frac{\|v-v_h\|_{L^2}}{\|v\|_{L^2}}$	Order
100^2	9.8456e-2	NA	1.2383e-1	NA	1.0785e-1	NA
150^2	3.5575e-2	2.5106	4.6363e-2	2.4230	3.9850e-2	2.4556
200^2	1.6183e-2	2.7380	2.1629e-2	2.6504	1.8553e-2	2.6574
250^2	8.6280e-3	2.8187	1.1810e-2	2.7116	1.0160e-2	2.6986
300^2	5.1387e-3	2.8423	7.2084e-3	2.7079	6.2345e-3	2.6785
350^2	3.3169e-3	2.8398	4.7714e-3	2.6767	4.1538e-3	2.6342
Biquadratic						
N	$\frac{\|p-p_h\|_{L^2}}{\|p\|_{L^2}}$	Order	$\frac{\|u-u_h\|_{L^2}}{\|u\|_{L^2}}$	Order	$\frac{\|v-v_h\|_{L^2}}{\|v\|_{L^2}}$	Order
100^2	2.1401e-3	NA	3.5199e-3	NA	2.7411e-3	NA
150^2	4.2232e-4	4.0024	8.4404e-4	3.5219	6.9506e-4	3.3840
200^2	1.5549e-4	3.4733	3.4240e-4	3.1362	2.9974e-4	2.9237
250^2	7.5961e-5	3.2102	1.7279e-4	3.0648	1.5086e-4	3.0767
300^2	4.2996e-5	3.1215	9.7480e-5	3.1397	8.2198e-5	3.3305
350^2	2.6727e-5	3.0842	5.9619e-5	3.1896	5.0041e-5	3.2195

Table 4.3.2: L^2 errors and orders of convergence at $t = 5$ for Example 4.3.1 using bilinear and biquadratic IFE spaces and IDG method applied to the scaled problem.

Bilinear						
N	$\frac{\|p-p_h\|_{L^2}}{\|p\|_{L^2}}$	Order	$\frac{\|u-u_h\|_{L^2}}{\|u\|_{L^2}}$	Order	$\frac{\|v-v_h\|_{L^2}}{\|v\|_{L^2}}$	Order
100^2	9.5963e-2	NA	1.2288e-1	NA	1.0574e-1	NA
150^2	3.4740e-2	2.5059	4.5990e-2	2.4238	3.8978e-2	2.4613
200^2	1.5833e-2	2.7314	2.1437e-2	2.6532	1.8078e-2	2.6707
250^2	8.4567e-3	2.8106	1.1692e-2	2.7168	9.8547e-3	2.7191
300^2	5.0458e-3	2.8323	7.1269e-3	2.7151	6.0190e-3	2.7041
350^2	3.2630e-3	2.8278	4.7111e-3	2.6853	3.9932e-3	2.6620
Biquadratic						
N	$\frac{\|p-p_h\|_{L^2}}{\|p\|_{L^2}}$	Order	$\frac{\|u-u_h\|_{L^2}}{\|u\|_{L^2}}$	Order	$\frac{\|v-v_h\|_{L^2}}{\|v\|_{L^2}}$	Order
100^2	2.1435e-3	NA	3.5089e-3	NA	2.7061e-3	NA
150^2	4.2452e-4	3.9935	8.3785e-4	3.5323	6.6751e-4	3.4521
200^2	1.5646e-4	3.4696	3.3828e-4	3.1526	2.8148e-4	3.0015
250^2	7.6393e-5	3.2129	1.7082e-4	3.0619	1.4278e-4	3.0419
300^2	4.3221e-5	3.1239	9.6874e-5	3.1111	7.9973e-5	3.1789
350^2	2.6865e-5	3.0848	5.9371e-5	3.1761	4.9050e-5	3.1712

Table 4.3.3: L^2 errors and orders of convergence at $t = 5$ for Example 4.3.1 using bilinear and biquadratic IFE spaces and IDPGFE method.

expansion

$$e^{izcos\theta} = J_0(z) + 2\sum_{n=1}^{\infty} i^n J_n(z)\cos n\theta, \tag{4.3.3}$$

to write the incident pressure in polar coordinates as

$$p_i(r,\theta,t) = \int_{-\infty}^{\infty} \hat{\psi}(\omega) e^{i\frac{\omega}{c_1}\omega_c(\alpha x_0+\beta y_0)} \sum_{n=0}^{\infty} \varepsilon_n i^n \cos n\theta J_n\left(\frac{\omega}{c_1}\omega_c r\right) e^{-i\omega\omega_c(t+t_0)} d\omega. \tag{4.3.4}$$

Next, we write the reflected and transmitted pressure waves as

$$\begin{aligned} p_r(r,\theta,t) &= \int_{-\infty}^{\infty} \sum_{n=0}^{\infty} R_n H_n\left(\frac{\omega}{c_1}\omega_c r\right) d\omega, \\ p_t(r,\theta,t) &= \int_{-\infty}^{\infty} \sum_{n=0}^{\infty} T_n J_n\left(\frac{\omega}{c_2}\omega_c r\right) d\omega, \end{aligned} \tag{4.3.5}$$

where H_n are Hankel functions of the first kind and R_n and T_n are determined by the interface jump conditions

$$p_i(a^+,\theta,t) + p_r(a^+,\theta,t) = p_t(a^-,\theta,t), \tag{4.3.6}$$

$$\frac{1}{\rho_1}\frac{\partial p_i(a^+,\theta,t)}{\partial r} + \frac{1}{\rho_1}\frac{\partial p_r(a^+,\theta,t)}{\partial r} = \frac{1}{\rho_2}\frac{\partial p_t(a^-,\theta,t)}{\partial r}. \tag{4.3.7}$$

In our computations we truncate the infinite series and infinite domain for the integral to obtain an approximation of the true pressure.

Example 4.3.2.

Next we consider the acoustic problem subjected to the initial condition (3.4.2) with $t_0 = 4$, $w_c = 1$, and $(\alpha,\beta) = (1,0)$ on the domain $[0,20]^2$ with the circular interface centered at $(x_0,y_0) = (10.01111, 10.01111)$ and radius $a = 4$. Here the speeds and densities are the same as in Example 4.3.1 and the true solution is used on the boundary $\partial\Omega$ to compute the inflow boundary condition. A planar wave starts in Ω_1 and moves with speed c_1 in the direction of the vector $(1,0)^T$ until it hits the circular interface.

We use the IFE bilinear spaces and integrate in time from $t = 0$ to $t = 3$ using the step sizes $\Delta t_1 = 10^{-4}$ on all non interface elements in Ω_1 and $\Delta t_2 = 5\ 10^{-5}$ on the remaining elements. For biquadratic IFE spaces we use $\Delta t_1 = 5\ 10^{-5}$ on all non interface elements in Ω_1 and $\Delta t_2 = 2.5\ 10^{-5}$ on the remaining elements.

We present in Table 4.3.4 the true L^2 errors and their average orders of convergence on uniform square meshes having $N = 100^2$, 150^2, 200^2, 250^2, 300^2, 350^2, 400^2 square elements for bilinear and biquadratic IFE spaces. The results of Table 4.3.4 show that IFE spaces are optimal. Finally, we plot in Figure 4.3.2 the true and numerical pressures at $t = 3$ on a 200^2-element uniform mesh with bilinear IFE spaces which are in full agreement.

Bilinear			Biquadratic	
N	$\| p - p_h \|_{L^2}$	Order	$\| p - p_h \|_{L^2}$	Order
100^2	1.2623e-1	NA	4.0609e-3	NA
150^2	4.6750e-2	2.4498	9.2822e-4	3.6400
200^2	2.1738e-2	2.6618	3.6163e-4	3.2767
250^2	1.1877e-2	2.7089	1.8081e-4	3.1063
300^2	7.2392e-3	2.7155	1.0510e-4	2.9757
350^2	4.7864e-3	2.6839	6.5772e-5	3.0407
400^2	3.3743e-3	2.6181	4.4082e-5	2.9965

Table 4.3.4: L^2 errors and orders of convergence at $t = 3$ for Example 4.3.2 using bilinear and biquadratic IFE spaces and IDGFE method.

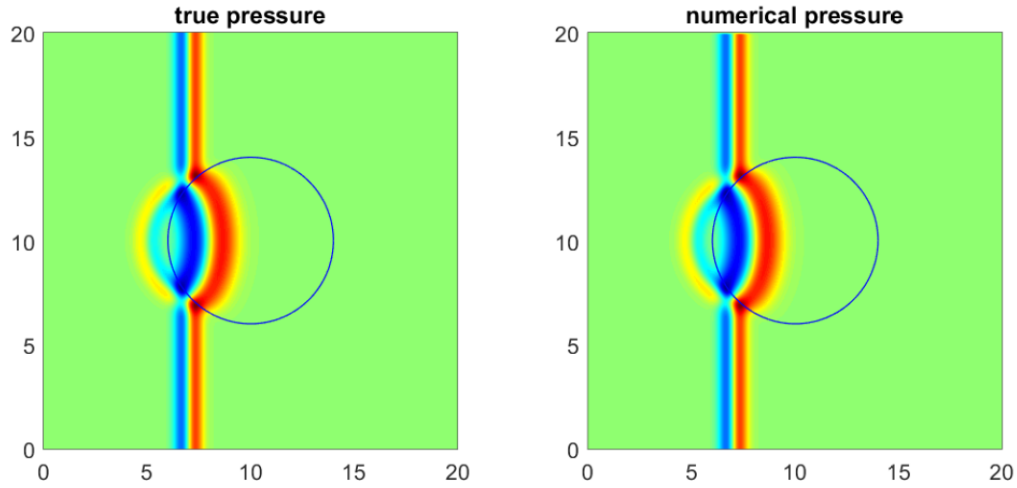

Figure 4.3.2: True (left) and IDGFE (right) pressures at $t = 3$ for Example 4.3.2 using bilinear IFE spaces and $N = 200^2$ elements.

Figure 4.3.3 is L^2 errors and their average orders of convergence for IDG method applied to the scaled problem and IDPGFE method with periodic boundary conditions. Two times smaller time step size for bilinear IFE spaces and 1.25 smaller time step size for biquadratic IFE spaces are used for IDG method applied to the scaled problem. Again we note that linear interpolation is used for Table 4.3.4 and cubic interpolation is used for Figure 4.3.3 as an interpolation function for local time-stepping.

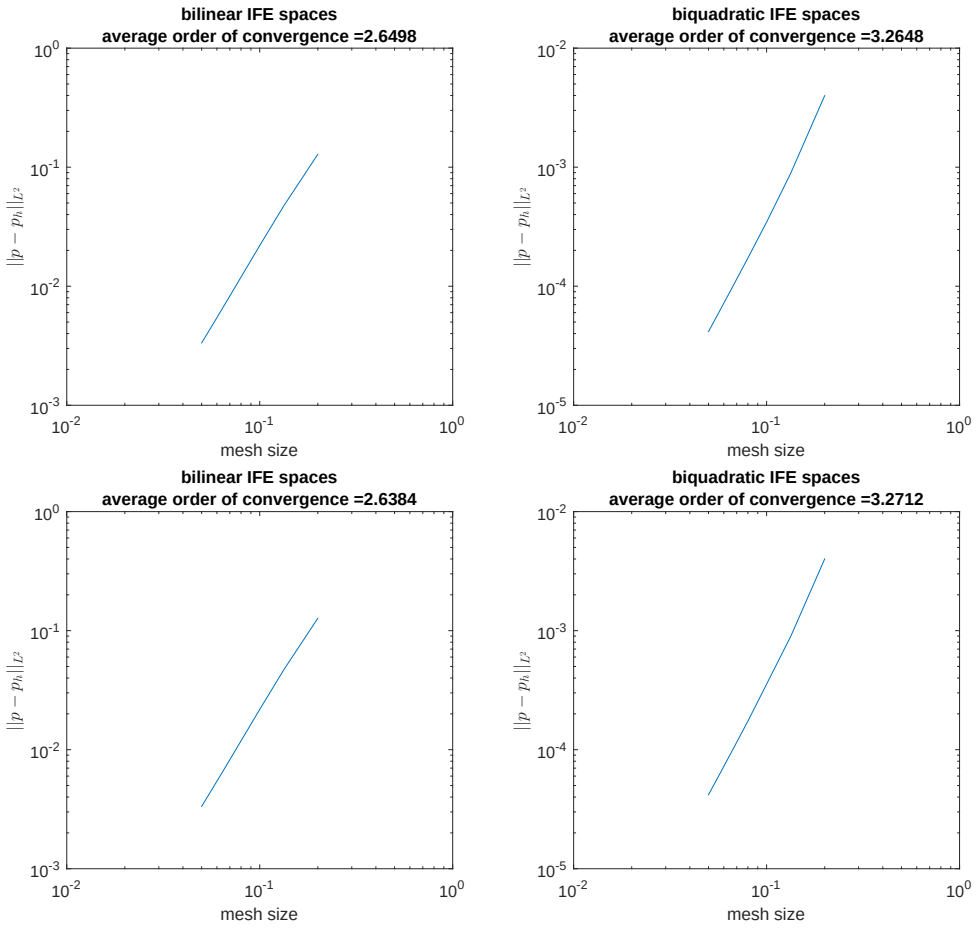

Figure 4.3.3: L^2 errors for pressure and average orders of convergence at $t = 3$ for Example 4.3.2 using bilinear (left) and biquadratic (right) IFE spaces and IDG method applied to the scaled problem (top) and IDPGFE method (bottom).

Example 4.3.3.

Now we consider an interface acoustic problem (3.1.2) on the domain $\Omega = [0, 200] \times [0, 200]$ with a circular interface centered at $(x_0, y_0) = (115.01111, 110.01111)$ with radius $a = 40$ where Ω_1 is occupied by ether with $c_1 = 985m/s$, $\rho_1 = 713.5kg/m^3$ and Ω_2 is occupied by glycerol with $c_2 = 1920m/s$, $\rho_2 = 1126kg/m^3$. The initial condition is given by (3.4.2) with

$t_0 = 0.06$, $\omega_c = 100$ and $(\alpha, \beta) = (1, 0)$ and periodic boundary conditions. A planar initial wave starts in Ω_1 and propagates with speed c_1 in the direction of $(1, 0)^T$ until it hits the circular interface.

We solve this problem using the IFE bilinear spaces on a uniform Cartesian mesh having 200^2 square elements and integrate in time from $t = 0$ to $t = 0.08$ with a global time step size $\Delta t = 2\ 10^{-6}$. The true and bilinear IDGFE pressures at $t = 0.08$ plotted in Figure 4.3.4 are in full agreement.

Example 4.3.4.

We solve the acoustic interface problem defined on the same domain as in Example 4.3.3 where Ω_1 is occupied by water with $c_1 = 1500m/s$, $\rho_1 = 1000kg/m^3$ and Ω_2 is occupied by methyl-alcohol with $c_2 = 1100m/s$, $\rho_2 = 800kg/m^3$. With all parameters kept except initial time $t_0 = 0.04$ the same as in Example 4.3.3, we solved this problem using the bilinear IFE spaces on a uniform mesh having 200^2 square elements and plot the true and IDGFE pressures at $t = 0.05$ in Figure 4.3.5. Again we observe that the true and numerical pressures are in agreement.

Example 4.3.5.

The final problem in this section consists of the water/air acoustic interface problem with a ratio of 1/1000 in the densities on the domain and interface in Example 4.3.4 with $\rho_1 = 1000kg/m^3$ and $\rho_2 = 1.3$, $c_1 = 1500m/s$ and $c_2 = 340m/s$. With all parameters kept except time step size $\Delta t = 10^{-7}$ the same as in Example 4.3.4.

When we apply the IDGFE method described in section 4.1.1 we observe spurious oscillations which show that this method is unstable for interface problems with high jumps of physical parameters. Furthermore, extensive numerical experiments suggest that for ratio higher that 10 we are not able to solve this problem. This stability issue is solved by IDPGFE method described in section 4.1.3. This is the air bubble occupied by water. When the acoustic pressure wave passes through the air bubble, most of the wave is reflected backward because of the low density of air. We observe that the true and numerical solutions are in full agreement as shown in Figure 4.3.6.

We note that when the interface points E and D in Figure 4.1.1 are very close to a vertex A, we observed that small time step size is needed. In this case, we may assume that $E = D = A$ to have non interface element. We didn't use this in Examples 4.3.1, 4.3.2, 4.3.3, 4.3.4 and 4.3.5 because such elements are rare. Instead we used small time steps.

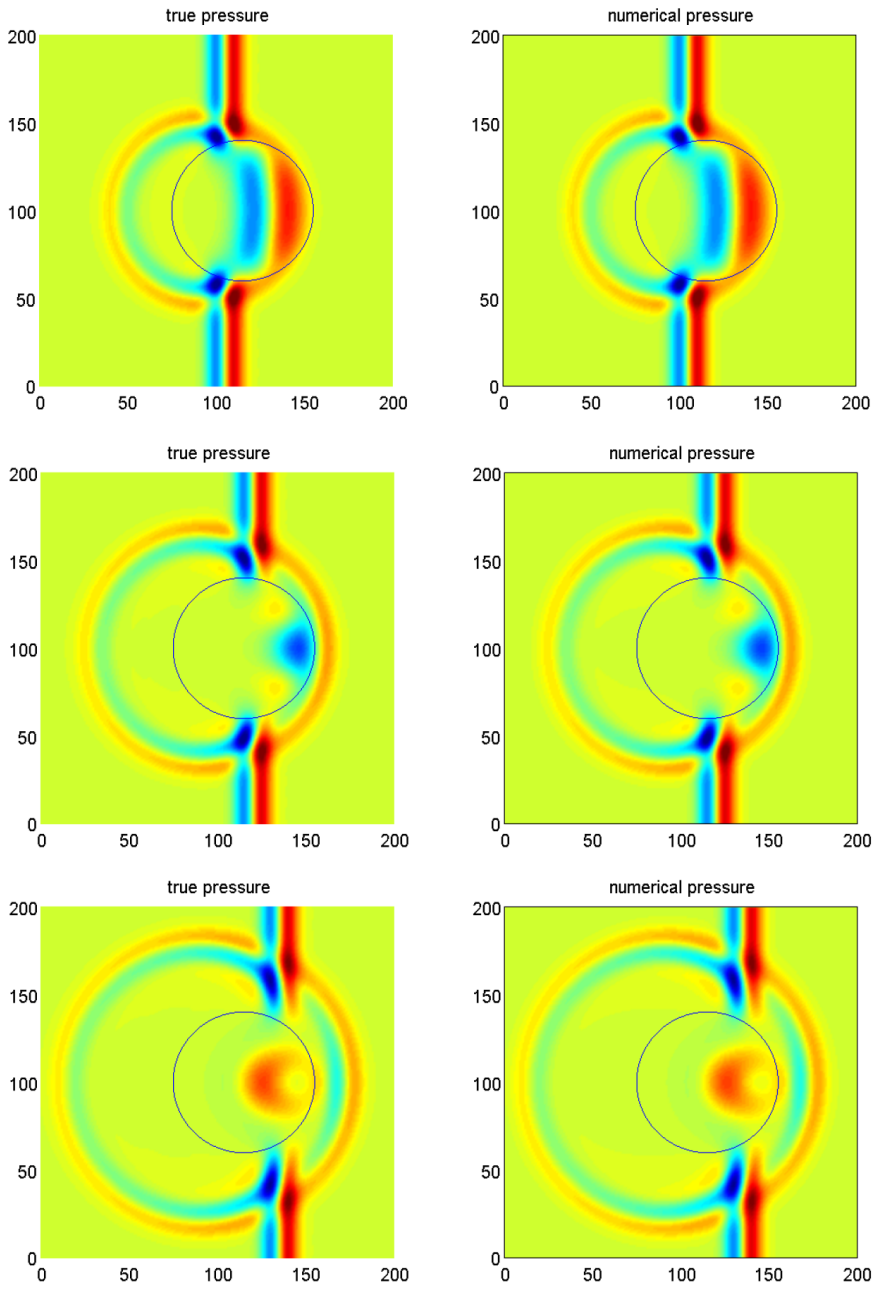

Figure 4.3.4: True (left) and IDGFE (right) pressures for Example 4.3.3 at $t = 0.04, 0.06, 0.08$ (top to bottom) using bilinear IFE spaces.

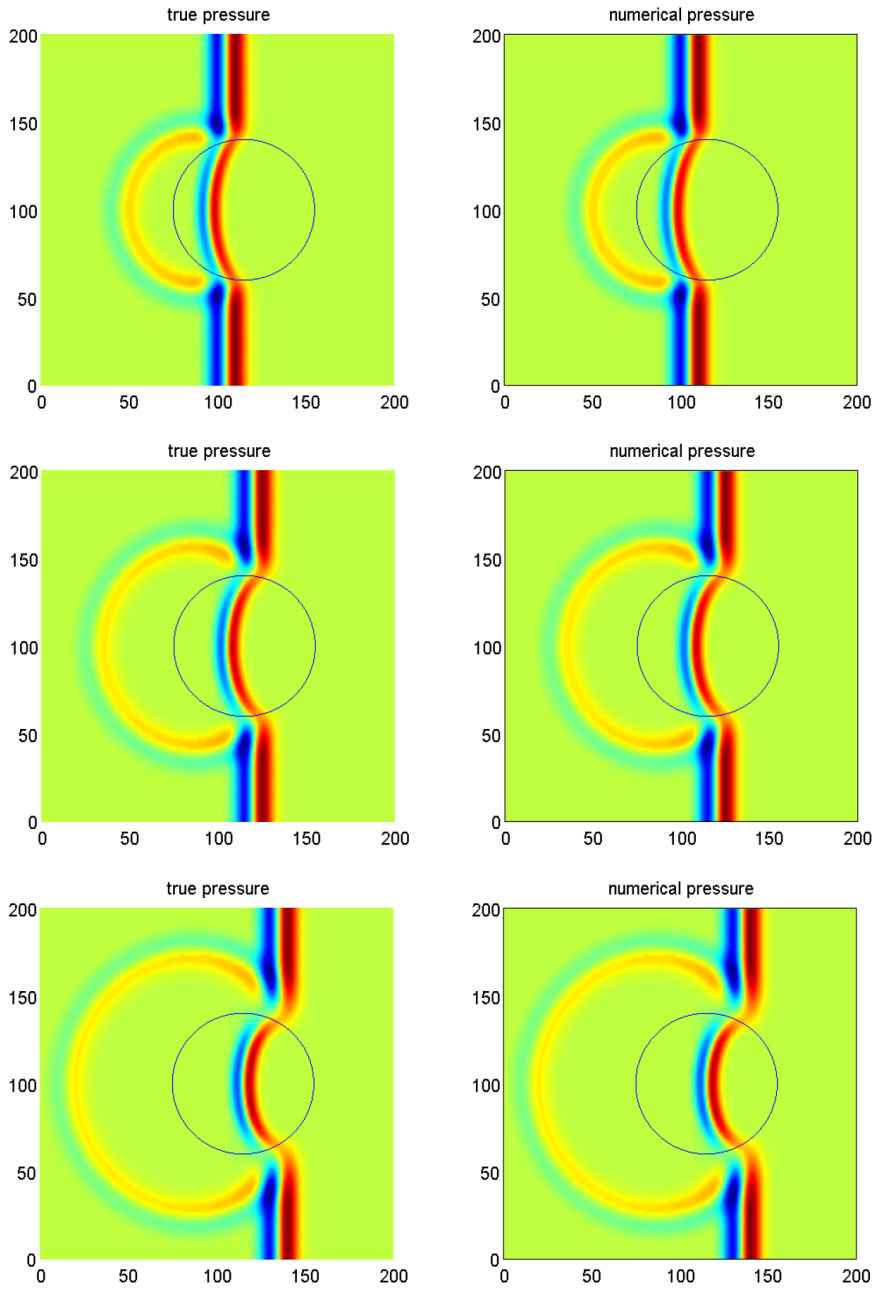

Figure 4.3.5: True (left) and IDGFE (right) pressures for Example 4.3.4 at $t = 0.03, 0.04, 0.05$ (top to bottom) using bilinear IFE spaces.

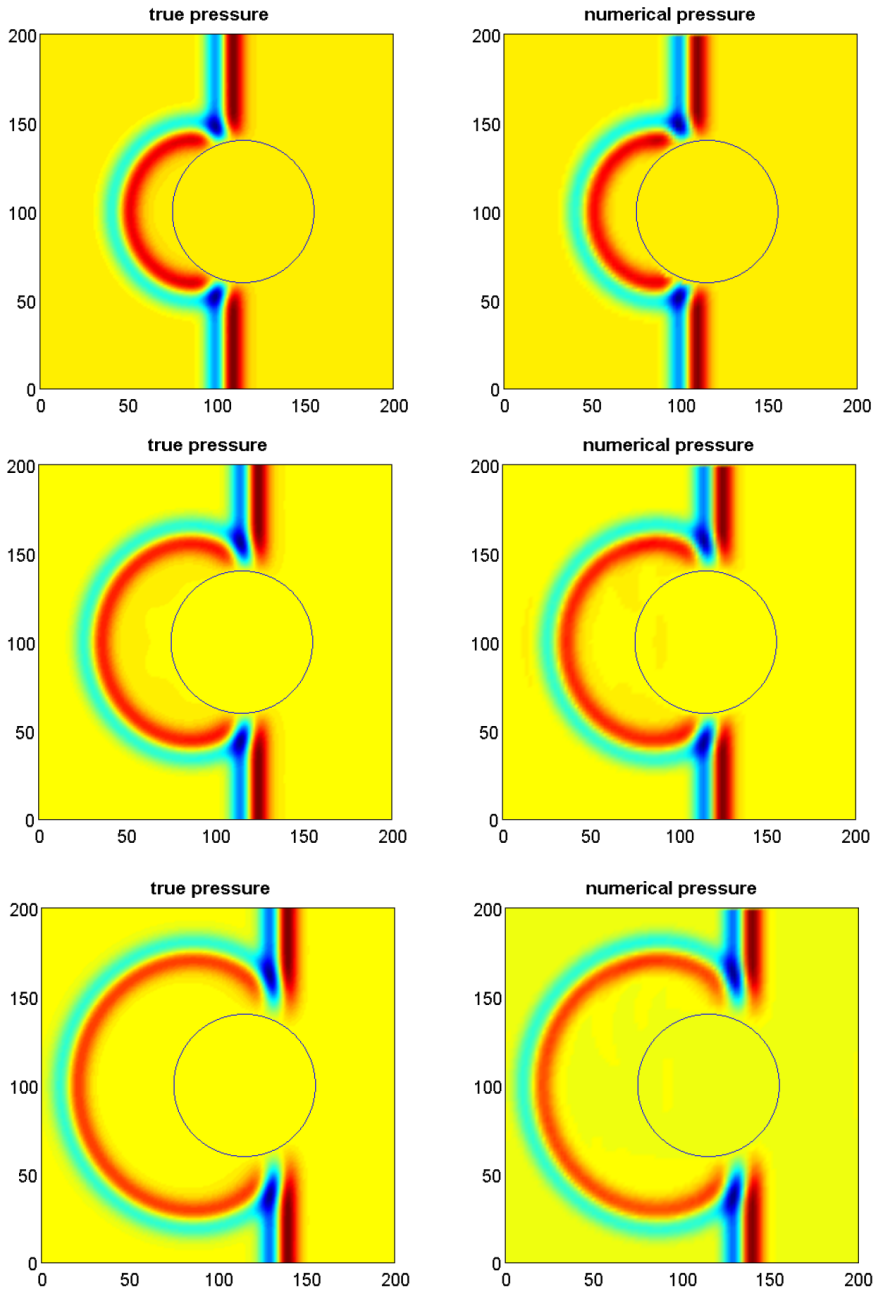

Figure 4.3.6: True (left) and IDPGFE (right) pressures for Example 4.3.5 at $t = 0.03, 0.04, 0.05$ (top to bottom) using bilinear IFE spaces.

Chapter 5

Stability for 2D Immersed DG Methods

Computational results show that the IDGFE method is unstable. Thus, here we only prove the stability of the IDG method applied to the scaled problem and the IDPGFE method. We also prove that the bilinear form $\mathcal{A}(\mathbf{V}_h, \mathbf{U}_h)$ for both methods is skew symmetric when using centered flux. Since stability proofs for the IDG method applied to the scaled problem and IDPGFE method are similar, we only show the stability of the IDPGFE method.

5.1 Stability Analysis

We have the numerical flux defined as

$$\mathbf{F}(\mathbf{U}^+, \mathbf{U}^-) = \frac{1}{2}\mathbf{D}(\mathbf{U}^+ + \mathbf{U}^-) - \frac{1}{2}\left((1-\beta)|\mathbf{D}| + \frac{C}{h}\mathbf{I}\right)(\mathbf{U}^- - \mathbf{U}^+), \qquad (5.1.1)$$

where $\mathbf{D} = n_x\mathbf{A} + \boldsymbol{n}_y\mathbf{B}$ and $\boldsymbol{n} = (n_x, n_y)^T$ is the outward unit normal vector at a point $\mathbf{x}$ on the boundary of T and $\mathbf{U}_h^{\pm}(\mathbf{x}) = \lim_{\epsilon\to 0^{\pm}} \mathbf{U}_h(\mathbf{x} - \epsilon\boldsymbol{n})$. $\mathbf{I}$ is the identity matrix, C is a non negative constant, h is the mesh size. The parameter values $\beta = 1$, 0.5, 0 yield centered, partially upwind and fully upwind fluxes, respectively.

Theorem 5.1.1. *Let* $\mathbf{U}$ *be the solution of the acoustic problem (3.1.2a) defined on* Ω *which split into* Ω_1 *and* Ω_2 *such that* $\overline{\Omega} = \overline{\Omega_1 \cup \Omega_2}$ *satisfying the periodic boundary conditions (4.1.36) on* $\partial\Omega$ *and jump condition (3.1.1b), (3.1.1c). Then the following holds.*

$$\epsilon(t) = \epsilon(t_0) \text{ for all } t \geq t_0, \qquad (5.1.2a)$$

where

$$\begin{aligned}\epsilon(t) &= \int_{\Omega} \mathbf{U}^T(x,y,t)\mathbf{S}\mathbf{U}(x,y,t)dxdy \\ &= \sum_{i=1}^{2} \int_{\Omega_i} \mathbf{U}_i^T(x,y,t)\mathbf{S}_i\mathbf{U}_i(x,y,t)dxdy, \end{aligned} \tag{5.1.2b}$$

where $\mathbf{S}_i$ *is defined in (4.1.8).*

Proof. Multiplying (3.1.2a) by $\mathbf{S}_i\mathbf{U}_i$ and integrating over Ω_i for $i = 1, 2$, we get

$$\begin{aligned}&\int_{\Omega_1} \mathbf{U}_1^T\mathbf{S}_1\frac{\partial \mathbf{U}_1}{\partial t}dxdy + \int_{\Omega_2} \mathbf{U}_2^T\mathbf{S}_2\frac{\partial \mathbf{U}_2}{\partial t}dxdy + \int_{\Omega_1} \mathbf{U}_1^T\tilde{\mathbf{A}}\frac{\partial \mathbf{U}_1}{\partial x}dxdy \\ &+ \int_{\Omega_1} \mathbf{U}_1^T\tilde{\mathbf{B}}\frac{\partial \mathbf{U}_1}{\partial y}dxdy + \int_{\Omega_2} \mathbf{U}_2^T\tilde{\mathbf{A}}\frac{\partial \mathbf{U}_2}{\partial x}dxdy + \int_{\Omega_2} \mathbf{U}_2^T\tilde{\mathbf{B}}\frac{\partial \mathbf{U}_2}{\partial y}dxdy = 0, \end{aligned} \tag{5.1.3}$$

where

$$\tilde{\mathbf{A}} = \mathbf{S}_i\mathbf{A}_i = \begin{pmatrix} 0 & 1 & 0 \\ 1 & 0 & 0 \\ 0 & 0 & 0 \end{pmatrix}, \ \tilde{\mathbf{B}} = \mathbf{S}_i\mathbf{B}_i = \begin{pmatrix} 0 & 0 & 1 \\ 0 & 0 & 0 \\ 1 & 0 & 0 \end{pmatrix}, \text{ for } i = 1, 2. \tag{5.1.4}$$

We can rewrite the equation as

$$\begin{aligned}&\frac{1}{2}\frac{\partial}{\partial t}\int_{\Omega_1} \mathbf{U}_1^T\mathbf{S}_1\mathbf{U}_1dxdy + \frac{1}{2}\frac{\partial}{\partial t}\int_{\Omega_2} \mathbf{U}_2^T\mathbf{S}_2\mathbf{U}_2dxdy \\ &+\frac{1}{2}\int_{\Omega_1}\left(\frac{\partial}{\partial x}\mathbf{U}_1^T\tilde{\mathbf{A}}\mathbf{U}_1 + \frac{\partial}{\partial y}\mathbf{U}_1^T\tilde{\mathbf{B}}\mathbf{U}_1\right)dxdy + \frac{1}{2}\int_{\Omega_2}\left(\frac{\partial}{\partial x}\mathbf{U}_2^T\tilde{\mathbf{A}}\mathbf{U}_2 + \frac{\partial}{\partial y}\mathbf{U}_2^T\tilde{\mathbf{B}}\mathbf{U}_2\right)dxdy = 0. \end{aligned} \tag{5.1.5}$$

By the divergence theorem, we get

$$\begin{aligned}&\frac{1}{2}\frac{\partial}{\partial t}\int_{\Omega_1} \mathbf{U}_1^T\mathbf{S}_1\mathbf{U}_1dxdy + \frac{1}{2}\frac{\partial}{\partial t}\int_{\Omega_2} \mathbf{U}_2^T\mathbf{S}_2\mathbf{U}_2dxdy + \frac{1}{2}\int_{\partial\Omega_1\setminus\Gamma} \mathbf{U}_1^T(n_{1x}\tilde{\mathbf{A}} + n_{1y}\tilde{\mathbf{B}})\mathbf{U}_1ds \\ &+\frac{1}{2}\int_{\partial\Omega_2\setminus\Gamma} \mathbf{U}_2^T(n_{2x}\tilde{\mathbf{A}} + n_{2y}\tilde{\mathbf{B}})\mathbf{U}_2ds + \frac{1}{2}\int_{\Gamma} \mathbf{U}_1^T(n_{1x}\tilde{\mathbf{A}} + n_{1y}\tilde{\mathbf{B}})\mathbf{U}_1ds \\ &+\frac{1}{2}\int_{\Gamma} \mathbf{U}_2^T(n_{2x}\tilde{\mathbf{A}} + n_{2y}\tilde{\mathbf{B}})\mathbf{U}_2ds = 0, \end{aligned} \tag{5.1.6}$$

where $\boldsymbol{\nu}_1 = (n_{1x}, n_{1x})^T$ and $\boldsymbol{\nu}_2 = (n_{2x}, n_{2x})^T$, respectively, are outward unit normal vectors on the boundary of Ω_1, Ω_2 or on the interface Γ. Since $\boldsymbol{\nu}_1$ is the opposite direction of $\boldsymbol{\nu}_2$ on

the interface Γ, we obtain

$$\frac{1}{2}\frac{\partial}{\partial t}\int_{\Omega_1}\mathbf{U}_1^T\mathbf{S}_1\mathbf{U}_1dxdy+\frac{1}{2}\frac{\partial}{\partial t}\int_{\Omega_2}\mathbf{U}_2^T\mathbf{S}_2\mathbf{U}_2dxdy+\frac{1}{2}\int_{\partial\Omega_1\backslash\Gamma}\mathbf{U}_1^T(n_{1x}\tilde{\mathbf{A}}+n_{1y}\tilde{\mathbf{B}})\mathbf{U}_1ds$$
$$+\frac{1}{2}\int_{\partial\Omega_2\backslash\Gamma}\mathbf{U}_2^T(n_{2x}\tilde{\mathbf{A}}+n_{2y}\tilde{\mathbf{B}})\mathbf{U}_2ds+\frac{1}{2}\int_{\Gamma}\mathbf{U}_1^T(n_{1x}\tilde{\mathbf{A}}+n_{1x}\tilde{\mathbf{B}})\mathbf{U}_1ds$$
$$-\frac{1}{2}\int_{\Gamma}\mathbf{U}_2^T(n_{1x}\tilde{\mathbf{A}}+n_{1x}\tilde{\mathbf{B}})\mathbf{U}_2ds=0. \tag{5.1.7}$$

By the interface conditions (3.1.1b) and (3.1.1c)

$$\mathbf{U}_1^T(n_{1x}\tilde{\mathbf{A}}+n_{1y}\tilde{\mathbf{B}})\mathbf{U}_1\mid_\Gamma-\mathbf{U}_2^T(n_{1x}\tilde{\mathbf{A}}+n_{1y}\tilde{\mathbf{B}})\mathbf{U}_2\mid_\Gamma$$
$$=2p_1\mid_\Gamma(\mathbf{v}_1\cdot\boldsymbol{\nu}_1\mid_\Gamma)-2p_2\mid_\Gamma(\mathbf{v}_2\cdot\boldsymbol{\nu}_1\mid_\Gamma)=0, \tag{5.1.8}$$

which yields

$$\frac{1}{2}\int_{\Gamma}\mathbf{U}_1^T(n_{1x}\tilde{\mathbf{A}}+n_{1y}\tilde{\mathbf{B}})\mathbf{U}_1ds-\frac{1}{2}\int_{\Gamma}\mathbf{U}_2^T(n_{1x}\tilde{\mathbf{A}}+n_{1y}\tilde{\mathbf{B}})\mathbf{U}_2ds=0. \tag{5.1.9}$$

Since $\mathbf{U}$ satisfies periodic boundary conditions, we have

$$\frac{1}{2}\int_{\partial\Omega_1\backslash\Gamma}\mathbf{U}_1^T(n_{1x}\tilde{\mathbf{A}}+n_{1y}\tilde{\mathbf{B}})\mathbf{U}_1ds+\frac{1}{2}\int_{\partial\Omega_2\backslash\Gamma}\mathbf{U}_2^T(n_{2x}\tilde{\mathbf{A}}+n_{2y}\tilde{\mathbf{B}})\mathbf{U}_2ds=0. \tag{5.1.10}$$

Thus (5.1.7) becomes

$$\frac{1}{2}\frac{\partial}{\partial t}\int_{\Omega_1}\mathbf{U}_1^T\mathbf{S}_1\mathbf{U}_1dxdy+\frac{1}{2}\frac{\partial}{\partial t}\int_{\Omega_2}\mathbf{U}_2^T\mathbf{S}_2\mathbf{U}_2dxdy=0, \tag{5.1.11}$$

which implies

$$\frac{\partial}{\partial t}\epsilon(t)=0. \tag{5.1.12}$$

Integrating over $[t_0,t]$ completes the proof. □

The IDPGFE formulation with the penalty term

$$-\frac{1}{2}\int_{\Gamma_j}\mathbf{V}_{1,h}^T(n_{1,x}\tilde{\mathbf{A}}+n_{1,y}\tilde{\mathbf{B}})\mathbf{U}_{1,h}ds-\frac{1}{2}\int_{\Gamma_j}\mathbf{V}_{2,h}^T(n_{2,x}\tilde{\mathbf{A}}+n_{2,y}\tilde{\mathbf{B}})\mathbf{U}_{2,h}ds, \tag{5.1.13}$$

on $\Gamma_j=\Gamma\cap T_j$ using centered flux $\beta=1$ in (5.1.1) satisfies

$$\sum_{j=1}^{N}\int_{T_j}\mathbf{V}_h^T\mathbf{S}\frac{\partial\mathbf{U}_h}{\partial t}dxdy+\mathcal{A}(\mathbf{V}_h,\mathbf{U}_h)=0, \tag{5.1.14}$$

where

$$\mathcal{A}(\mathbf{V}_h,\mathbf{U}_h)=-\sum_{j=1}^{N}\int_{T_j}\left(\frac{\partial\mathbf{V}_h^T}{\partial x}\tilde{\mathbf{A}}\mathbf{U}_h+\frac{\partial\mathbf{V}_h^T}{\partial y}\tilde{\mathbf{B}}\mathbf{U}_h\right)dxdy$$
$$+\sum_{j=1}^{N}\int_{\partial T_j\setminus\partial\Omega}\mathbf{V}_h^{+T}(n_x\tilde{\mathbf{A}}+n_y\tilde{\mathbf{B}})\frac{\mathbf{U}_h^{+}+\mathbf{U}_h^{-}}{2}ds \tag{5.1.15}$$
$$+\frac{1}{2}\sum_{j=1}^{N}\int_{\Gamma_j}\mathbf{V}_{1,h}^T(n_{1,x}\tilde{\mathbf{A}}+n_{1,y}\tilde{\mathbf{B}})\mathbf{U}_{1,h}ds+\frac{1}{2}\sum_{j=1}^{N}\int_{\Gamma_j}\mathbf{V}_{2,h}^T(n_{x,2}\tilde{\mathbf{A}}+n_{2,y}\tilde{\mathbf{B}})\mathbf{U}_{2,h}ds,$$

where $\boldsymbol{\nu}_i=(n_{ix},n_{iy})$ is the outward unit normal vector on the boundary of T_j on Ω_i for $i=1,2$ and $\boldsymbol{\nu}=(n_x,n_y)$ indicates both $\boldsymbol{\nu}_1,\boldsymbol{\nu}_2$.

Theorem 5.1.2. *Let $\mathbf{U}_h$ and $\mathbf{V}_h$ be two periodic IFE functions in $\mathcal{U}_h^k$ defined on Ω such that $\overline{\Omega}=\overline{\Omega_1\cup\Omega_2}$ which is partitioned into $T_1,\cdots,T_N$. Then $\mathcal{A}(\mathbf{V}_h,\mathbf{U}_h)$ is skew-symmetric.*

Proof. By switching $\mathbf{V}_h$ and $\mathbf{U}_h$ in (5.1.15), we have

$$\mathcal{A}(\mathbf{U}_h,\mathbf{V}_h)=-\sum_{j=1}^{N}\int_{T_j}\left(\frac{\partial\mathbf{U}_h^T}{\partial x}\tilde{\mathbf{A}}\mathbf{V}_h+\frac{\partial\mathbf{U}_h^T}{\partial y}\tilde{\mathbf{B}}\mathbf{V}_h\right)dxdy$$
$$+\sum_{j=1}^{N}\int_{\partial T_j}\mathbf{U}_h^{+T}(n_x\tilde{\mathbf{A}}+n_y\tilde{\mathbf{B}})\frac{\mathbf{V}_h^{+}+\mathbf{V}_h^{-}}{2}ds \tag{5.1.16}$$
$$+\frac{1}{2}\sum_{j=1}^{N}\int_{\Gamma_j}\mathbf{U}_{1,h}^T(n_{1,x}\tilde{\mathbf{A}}+n_{1,y}\tilde{\mathbf{B}})\mathbf{V}_{1,h}+\frac{1}{2}\sum_{j=1}^{N}\int_{\Gamma_j}\mathbf{U}_{2,h}^T(n_{x,2}\tilde{\mathbf{A}}+n_{2,y}\tilde{\mathbf{B}})\mathbf{V}_{2,h}ds.$$

Letting $\tilde{\mathbf{D}}(\boldsymbol{\nu})=n_x\tilde{\mathbf{A}}+n_y\tilde{\mathbf{B}}$ where $\boldsymbol{\nu}=(n_x,n_y)$, the above equation is

$$\mathcal{A}(\mathbf{U}_h,\mathbf{V}_h)=-\sum_{j=1}^{N}\int_{T_j}\left(\frac{\partial\mathbf{U}_h^T}{\partial x}\tilde{\mathbf{A}}\mathbf{V}_h+\frac{\partial\mathbf{U}_h^T}{\partial y}\tilde{\mathbf{B}}\mathbf{V}_h\right)dxdy \tag{5.1.17}$$
$$+\sum_{j=1}^{N}\int_{\partial T_j}\mathbf{U}_h^{+T}\tilde{\mathbf{D}}(\boldsymbol{\nu})\frac{\mathbf{V}_h^{+}+\mathbf{V}_h^{-}}{2}ds+\frac{1}{2}\sum_{j=1}^{N}\int_{\Gamma_j}\mathbf{U}_{1,h}^T\tilde{\mathbf{D}}(\boldsymbol{\nu}_1)\mathbf{V}_{1,h}+\frac{1}{2}\sum_{j=1}^{N}\int_{\Gamma_j}\mathbf{U}_{2,h}^T\tilde{\mathbf{D}}(\boldsymbol{\nu}_2)\mathbf{V}_{2,h}ds.$$

Applying integration by parts,

$$\mathcal{A}(\mathbf{U}_h,\mathbf{V}_h)=\sum_{j=1}^{N}\int_{T_j}\left(\mathbf{U}_h^T\tilde{\mathbf{A}}\frac{\partial\mathbf{V}_h}{\partial x}+\mathbf{U}_h^T\tilde{\mathbf{B}}\frac{\mathbf{V}_h}{\partial y}\right)dxdy-\sum_{j=1}^{N}\int_{\partial T_j}\mathbf{U}_h^{+T}\tilde{\mathbf{D}}(\boldsymbol{\nu})\mathbf{V}_h^{+}ds$$
$$-\sum_{j=1}^{N}\int_{\Gamma_j}\mathbf{U}_{1,h}^T\tilde{\mathbf{D}}(\boldsymbol{\nu}_1)\mathbf{V}_{1,h}ds-\sum_{j=1}^{N}\int_{\Gamma_j}\mathbf{U}_{2,h}^T\tilde{\mathbf{D}}(\boldsymbol{\nu}_2)\mathbf{V}_{2,h}+\sum_{j=1}^{N}\int_{\partial T_j}\mathbf{U}_h^{+T}\tilde{\mathbf{D}}(\boldsymbol{\nu})\frac{\mathbf{V}_h^{+}+\mathbf{V}_h^{-}}{2}ds$$
$$+\frac{1}{2}\sum_{j=1}^{N}\int_{\Gamma_j}\mathbf{U}_{1,h}^T\tilde{\mathbf{D}}(\boldsymbol{\nu}_1)\mathbf{V}_{1,h}ds+\frac{1}{2}\sum_{j=1}^{N}\int_{\Gamma_j}\mathbf{U}_{2,h}^T\tilde{\mathbf{D}}(\boldsymbol{\nu}_2)\mathbf{V}_{2,h}ds. \tag{5.1.18}$$

Simplifying the above equation (3, 4, 6, 7-terms and 2, 5-th terms), we obtain

$$\mathcal{A}(\mathbf{U}_h, \mathbf{V}_h) = \sum_{j=1}^{N} \int_{T_j} \left(\mathbf{U}_h^T \tilde{\mathbf{A}} \frac{\partial \mathbf{V}_h}{\partial x} + \mathbf{U}_h^T \tilde{\mathbf{B}} \frac{\mathbf{V}_h}{\partial y} \right) dxdy - \frac{1}{2} \sum_{j=1}^{N} \int_{\partial T_j} \mathbf{U}_h^{+T} \tilde{\mathbf{D}}(\boldsymbol{\nu}) \mathbf{V}_h^+ ds$$
$$+ \frac{1}{2} \sum_{j=1}^{N} \int_{\partial T_j} \mathbf{U}_h^{+T} \tilde{\mathbf{D}}(\boldsymbol{\nu}) \mathbf{V}_h^- ds - \frac{1}{2} \sum_{j=1}^{N} \int_{\Gamma_j} \mathbf{U}_{1,h}^T \tilde{\mathbf{D}}(\boldsymbol{\nu}_1) \mathbf{V}_{1,h} ds - \frac{1}{2} \sum_{j=1}^{N} \int_{\Gamma_j} \mathbf{U}_{2,h}^T \tilde{\mathbf{D}}(\boldsymbol{\nu}_2) \mathbf{V}_{2,h} ds. \tag{5.1.19}$$

On two adjacent elements T_j and T_j' with a common edge e as illustrated in Figure 5.1.1, integration is computed twice. The directions of outward normal vector for e are opposite to each other on T_j and T_j'.

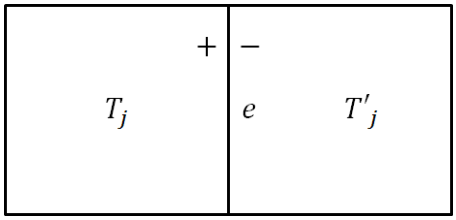

Figure 5.1.1: Two adjacent elements.

Thus, with periodic boundary conditions on $\partial\Omega$

$$\int_{\partial\Omega} \mathbf{V}_h^T (n_x \tilde{\mathbf{A}} + n_y \tilde{\mathbf{B}}) \mathbf{U}_h ds = \int_{\partial\Omega} \mathbf{V}_h^T \tilde{\mathbf{D}}(\boldsymbol{\nu}) \mathbf{U}_h ds = 0, \tag{5.1.20}$$

the second and third terms in (5.1.19) is

$$-\frac{1}{2} \sum_{j=1}^{N} \int_{\partial T_j \setminus \partial\Omega} \mathbf{U}_h^{+T} \tilde{\mathbf{D}}(\boldsymbol{\nu}) \mathbf{V}_h^+ ds + \frac{1}{2} \sum_{j=1}^{N} \int_{\partial T_j \setminus \partial\Omega} \mathbf{U}_h^{+T} \tilde{\mathbf{D}}(\boldsymbol{\nu}) \mathbf{V}_h^- ds$$
$$= -\frac{1}{2} \sum_{e \in \boldsymbol{\varepsilon}_0} \left(\int_e \mathbf{U}_h^{+T} \tilde{\mathbf{D}}(\boldsymbol{\nu}) \mathbf{V}_h^+ ds + \int_e \mathbf{U}_h^{-T} \tilde{\mathbf{D}}(-\boldsymbol{\nu}) \mathbf{V}_h^- ds \right)$$
$$+ \frac{1}{2} \sum_{e \in \boldsymbol{\varepsilon}_0} \left(\int_e \mathbf{U}_h^{+T} \tilde{\mathbf{D}}(\boldsymbol{\nu}) \mathbf{V}_h^- ds + \int_e \mathbf{U}_h^{-T} \tilde{\mathbf{D}}(-\boldsymbol{\nu}) \mathbf{V}_h^+ ds \right)$$
$$= -\frac{1}{2} \sum_{\boldsymbol{\varepsilon}_0} \left(\int_e \mathbf{U}_h^{+T} \tilde{\mathbf{D}}(\boldsymbol{\nu}) \mathbf{V}_h^+ ds - \int_e \mathbf{U}_h^{-T} \tilde{\mathbf{D}}(\boldsymbol{\nu}) \mathbf{V}_h^- ds \right)$$
$$+ \frac{1}{2} \sum_{e \in \boldsymbol{\varepsilon}_0} \left(\int_e \mathbf{U}_h^{+T} \tilde{\mathbf{D}}(\boldsymbol{\nu}) \mathbf{V}_h^- ds - \int_e \mathbf{U}_h^{-T} \tilde{\mathbf{D}}(\boldsymbol{\nu}) \mathbf{V}_h^+ ds \right) \tag{5.1.21}$$

$$= -\sum_{e\in\boldsymbol{\varepsilon}_0}\left(\int_e \frac{\mathbf{U}_h^{+T}+\mathbf{U}_h^{-T}}{2}\tilde{\mathbf{D}}(\boldsymbol{\nu})\mathbf{V}_h^{+}ds - \int_e \frac{\mathbf{U}_h^{+T}+\mathbf{U}_h^{-T}}{2}\tilde{\mathbf{D}}(\boldsymbol{\nu})\mathbf{V}_h^{-}ds\right)$$
$$= -\sum_{e\in\boldsymbol{\varepsilon}_0}\left(\int_e \frac{\mathbf{U}_h^{+T}+\mathbf{U}_h^{-T}}{2}\tilde{\mathbf{D}}(\boldsymbol{\nu})\mathbf{V}_h^{+}ds + \int_e \frac{\mathbf{U}_h^{-T}+\mathbf{U}_h^{+T}}{2}\tilde{\mathbf{D}}(-\boldsymbol{\nu})\mathbf{V}_h^{-}ds\right),$$

where $\boldsymbol{\varepsilon}_0$ is the set of all interior edges in the mesh.

For the same reason illustrated in Figure 5.1.1, the above equation is

$$-\sum_{j=1}^{N}\int_{\partial T_j\setminus\partial\Omega}\frac{\mathbf{U}_h^{+T}+\mathbf{U}_h^{-T}}{2}\tilde{\mathbf{D}}(\boldsymbol{\nu})\mathbf{V}_h^{+}ds. \tag{5.1.22}$$

Thus (5.1.19) becomes

$$\mathcal{A}(\mathbf{U}_h,\mathbf{V}_h) = \sum_{j=1}^{N}\int_{T_j}\left(\mathbf{U}_h^T\tilde{\mathbf{A}}\frac{\partial\mathbf{V}_h}{\partial x}+\mathbf{U}_h^T\tilde{\mathbf{B}}\frac{\mathbf{V}_h}{\partial y}\right)dxdy - \sum_{j=1}^{N}\int_{\partial T_j\setminus\partial\Omega}\frac{\mathbf{U}_h^{+T}+\mathbf{U}_h^{-T}}{2}\tilde{\mathbf{D}}(\boldsymbol{\nu})\mathbf{V}_h^{+}ds$$
$$-\frac{1}{2}\sum_{j=1}^{N}\int_{\Gamma_j}\mathbf{U}_{1,h}^T\tilde{\mathbf{D}}(\boldsymbol{\nu}_1)\mathbf{V}_{1,h}ds - \frac{1}{2}\sum_{j=1}^{N}\int_{\Gamma_j}\mathbf{U}_{2,h}^T\tilde{\mathbf{D}}(\boldsymbol{\nu}_2)\mathbf{V}_{2,h}ds. \tag{5.1.23}$$

Since $\tilde{\mathbf{A}}$, $\tilde{\mathbf{B}}$, and $\tilde{\mathbf{D}}$ are symmetric, we obtain

$$\mathcal{A}(\mathbf{U}_h,\mathbf{V}_h) = \sum_{j=1}^{N}\int_{T_j}\left(\frac{\partial\mathbf{V}_h^T}{\partial x}\tilde{\mathbf{A}}\mathbf{U}_h+\frac{\mathbf{V}_h^T}{\partial y}\tilde{\mathbf{B}}\mathbf{U}_h\right)dxdy - \sum_{j=1}^{N}\int_{\partial T_j\setminus\partial\Omega}\mathbf{V}_h^{+T}\tilde{\mathbf{D}}(\boldsymbol{\nu})\frac{\mathbf{U}_h^{+}+\mathbf{U}_h^{-}}{2}ds$$
$$-\frac{1}{2}\sum_{j=1}^{N}\int_{\Gamma_j}\mathbf{V}_{1,h}^T\tilde{\mathbf{D}}(\boldsymbol{\nu}_1)\mathbf{U}_{1,h}ds - \frac{1}{2}\sum_{j=1}^{N}\int_{\Gamma_j}\mathbf{V}_{2,h}^T\tilde{\mathbf{D}}(\boldsymbol{\nu}_2)\mathbf{U}_{2,h}ds$$
$$= \sum_{j=1}^{N}\int_{T_j}\left(\frac{\partial\mathbf{V}_h^T}{\partial x}\tilde{\mathbf{A}}\mathbf{U}_h+\frac{\mathbf{V}_h^T}{\partial y}\tilde{\mathbf{B}}\mathbf{U}_h\right)dxdy - \sum_{j=1}^{N}\int_{\partial T_j\setminus\partial\Omega}\mathbf{V}_h^{+T}(n_x\tilde{\mathbf{A}}+n_y\tilde{\mathbf{B}})\frac{\mathbf{U}_h^{+}+\mathbf{U}_h^{-}}{2}ds$$
$$-\frac{1}{2}\sum_{j=1}^{N}\int_{\Gamma_j}\mathbf{V}_{1,h}^T(n_{1,x}\tilde{\mathbf{A}}+n_{1,y}\tilde{\mathbf{B}})\mathbf{U}_{1,h}ds - \frac{1}{2}\sum_{j=1}^{N}\int_{\Gamma_j}\mathbf{V}_{2,h}^T(n_{x,2}\tilde{\mathbf{A}}+n_{2,y}\tilde{\mathbf{B}})\mathbf{U}_{2,h}$$
$$= -\mathcal{A}(\mathbf{V}_h,\mathbf{U}_h) \tag{5.1.24}$$

which completes the proof. □

Theorem 5.1.3. *Let $\mathbf{U}_h$ be the IDPGFE solution of the acoustic problem (3.1.2a) defined on Ω such that $\overline{\Omega} = \overline{\Omega_1\cup\Omega_2}$ which is partitioned into $T_1,\cdots,T_N$. The problem satisfies periodic boundary conditions (4.1.36) on $\partial\Omega$ and jump condition (3.1.1b), (3.1.1c) across the interface Γ. Then the following is true.*

$$\epsilon_h(t) \le \epsilon_h(t_0) \text{ for all } t \ge t_0, \tag{5.1.25a}$$

where

$$\epsilon_h(t) = \int_\Omega \mathbf{U}_h^T(x,y,t)\mathbf{S}\mathbf{U}_h(x,y,t)dxdt$$
$$= \sum_{j=1}^{N} \int_{T_j} \mathbf{U}_h^T(x,y,t)\mathbf{S}\mathbf{U}_h(x,y,t)dxdy, \tag{5.1.25b}$$

where $\mathbf{S}$ *is defined in (4.1.8).*

Proof. By multiplying (3.1.2a) by a test function $\mathbf{SV}$, applying integration by parts, summing over all the elements on Ω, and applying numerical flux (5.1.1), the IDPGFE formulation consists of finding $\mathbf{U}_h$ satisfying

$$\sum_{j=1}^{N} \int_{T_j} \mathbf{V}_h^T \mathbf{S} \frac{\partial \mathbf{U}_h}{\partial t} dxdy + \mathcal{A}(\mathbf{U}_h, \mathbf{V}_h)$$
$$-\frac{1}{2}\sum_{j=1}^{N} \int_{\partial T_j \setminus \partial\Omega} \mathbf{V}_h^{+T} \left((1-\beta)\mathbf{S}|\mathbf{D}(\boldsymbol{\nu})| + \frac{C}{h}\mathbf{S} \right) (\mathbf{U}_h^- - \mathbf{U}_h^+) ds = 0, \tag{5.1.26}$$

where $\mathbf{D}(\boldsymbol{\nu}) = n_x\mathbf{A} + n_y\mathbf{B}$ and $\boldsymbol{\nu} = (n_x, n_y)$.

Since $\mathcal{A}(\mathbf{V}_h, \mathbf{U}_h)$ is skew-symmetry by Theorem 5.1.2, we have

$$\mathcal{A}(\mathbf{U}_h, \mathbf{U}_h) = 0. \tag{5.1.27}$$

Thus setting $\mathbf{V}_h = \mathbf{U}_h$ and using (5.1.27), we obtain

$$\sum_{j=1}^{N} \int_{T_j} \mathbf{U}_h^T \mathbf{S} \frac{\partial \mathbf{U}_h}{\partial t} dxdy - \frac{1}{2}\sum_{j=1}^{N} \int_{\partial T_j \setminus \partial\Omega} \mathbf{U}_h^{+T} \left((1-\beta)\mathbf{S}|\mathbf{D}(\boldsymbol{\nu})| + \frac{C}{h}\mathbf{S} \right) (\mathbf{U}_h^- - \mathbf{U}_h^+) ds = 0. \tag{5.1.28}$$

Again, on two adjacent elements T_j and T_j' with a common edge e as illustrated in Figure 5.1.1, integration is computed twice. The directions of outward normal vector for e are opposite to each other on T_j and T_j'.

Thus, the second term of the above equation is

$$-\frac{1}{2}\sum_{j=1}^{N} \int_{\partial T_j \setminus \partial\Omega} \mathbf{U}_h^{+T} \left((1-\beta)\mathbf{S}|\mathbf{D}(\boldsymbol{\nu})| + \frac{C}{h}\mathbf{S} \right) (\mathbf{U}_h^- - \mathbf{U}_h^+) ds$$
$$= -\frac{1}{2}\sum_{e\in\boldsymbol{\varepsilon}_0} \int_e \mathbf{U}_h^{+T} \left((1-\beta)\mathbf{S}|\mathbf{D}(\boldsymbol{\nu})| + \frac{C}{h}\mathbf{S} \right) (\mathbf{U}_h^- - \mathbf{U}_h^+) ds$$
$$-\frac{1}{2}\sum_{e\in\boldsymbol{\varepsilon}_0} \int_e \mathbf{U}_h^{-T} \left((1-\beta)\mathbf{S}|\mathbf{D}(-\boldsymbol{\nu})| + \frac{C}{h}\mathbf{S} \right) (\mathbf{U}_h^+ - \mathbf{U}_h^-) ds. \tag{5.1.29}$$

where $\boldsymbol{\varepsilon}_0$ is the set of all interior edges in the mesh.

By using $|\mathbf{D}(-\boldsymbol{\nu})| = |-\mathbf{D}(\boldsymbol{\nu})| = |\mathbf{D}(\boldsymbol{\nu})|$ and the notation $[\mathbf{U}_h] = (\mathbf{U}_h^+ - \mathbf{U}_h^-)|_e$, $e \in \boldsymbol{\varepsilon}_0$, the above term is

$$\begin{aligned}
&-\frac{1}{2}\sum_{e\in\boldsymbol{\varepsilon}_0}\int_e \mathbf{U}_h^{+T}\left((1-\beta)\mathbf{S}|\mathbf{D}(\boldsymbol{\nu})| + \frac{C}{h}\mathbf{S}\right)(\mathbf{U}_h^- - \mathbf{U}_h^+)ds \\
&-\frac{1}{2}\sum_{e\in\boldsymbol{\varepsilon}_0}\int_e \mathbf{U}_h^{-T}\left((1-\beta)\mathbf{S}|\mathbf{D}(\boldsymbol{\nu})| + \frac{C}{h}\mathbf{S}\right)(\mathbf{U}_h^+ - \mathbf{U}_h^-)ds \\
&= \frac{1}{2}\sum_{e\in\boldsymbol{\varepsilon}_0}\int_e (\mathbf{U}_h^+ - \mathbf{U}_h^-)^T\left((1-\beta)\mathbf{S}|\mathbf{D}(\boldsymbol{\nu})| + \frac{C}{h}\mathbf{S}\right)(\mathbf{U}_h^+ - \mathbf{U}_h^-)ds \\
&= \frac{1}{2}\sum_{e\in\boldsymbol{\varepsilon}_0}\int_e [\mathbf{U}_h]^T\left((1-\beta)\mathbf{S}|\mathbf{D}(\boldsymbol{\nu})| + \frac{C}{h}\mathbf{S}\right)[\mathbf{U}_h]ds. \qquad (5.1.30)
\end{aligned}$$

Thus (5.1.28) becomes

$$\begin{aligned}
&\sum_{j=1}^{N}\int_{T_j}\mathbf{U}_h^T\mathbf{S}\frac{\partial\mathbf{U}_h}{\partial t}dxdy \\
&+\frac{1}{2}\sum_{e\in\boldsymbol{\varepsilon}_0}\int_e [\mathbf{U}_h]^T\left((1-\beta)\mathbf{S}|\mathbf{D}(\boldsymbol{\nu})| + \frac{C}{h}\mathbf{S}\right)[\mathbf{U}_h]ds = 0. \qquad (5.1.31)
\end{aligned}$$

Since C is nonnegative, h is mesh size, $0 \le \beta \le 1$, $\mathbf{S}$ and $\mathbf{S}|\mathbf{D}(\boldsymbol{\nu})|$ are positive definite, we have

$$[\mathbf{U}_h]^T\frac{1}{2}((1-\beta)\mathbf{S}|\mathbf{D}(\boldsymbol{\nu})| + \frac{C}{h}\mathbf{S})[\mathbf{U}_h] \ge 0. \qquad (5.1.32)$$

Thus we obtain

$$\sum_{j=1}^{N}\frac{1}{2}\frac{\partial}{\partial t}\int_{T_j}\mathbf{U}_h^T\mathbf{S}\mathbf{U}_h dxdy \le 0, \qquad (5.1.33)$$

which implies

$$\frac{\partial}{\partial t}\epsilon_h(t) \le 0. \qquad (5.1.34)$$

Integrating over $[t_0, t]$ completes the proof. □

5.2 A Computational Stability Study

Next we provide a numerical stability study for three methods defined earlier. In order to investigate the advantages and disadvantages of each method, we present eigenvalues of $\mathbf{A}_{h,q}^G$,

$\mathbf{A}_{h,q}^{GS}$ and $\mathbf{A}_{h,q}^{PG}$ in (4.1.7), (4.1.21) and (4.1.32), respectively, with various parameters, radii of circular interface, fluxes and orders of IFE spaces. Centered, partially upwind and fully upwind fluxes are used to study the distribution of the eigenvalues with penalty term in (5.1.1). Graphs are presented for three methods with centered ($\beta = 1$), partially upwind ($\beta = 0.5$) and fully upwind flux ($\beta = 0$), respectively, with the maximum real part of eigenvalues.

We note that we use 28 points for straight-edge triangles and 42 points for curved-edge triangles to apply Gaussian quadrature shown in Figure 4.1.2.

We consider the acoustic interface problem (3.1.1) using interface jump and consistency conditions (3.2.26) for pressure and (3.2.29) for velocity, and periodic boundary conditions (4.1.36) with various c_1, ρ_1, c_2, ρ_2. A circular interface centered at $(x_0, y_0) = (20.1111, 20.1111)$ with radius $r = 10$ is used on the domain $[0, 40]^2$. Bilinear and biquadratic IFE spaces are used on a 10×10 square element mesh.

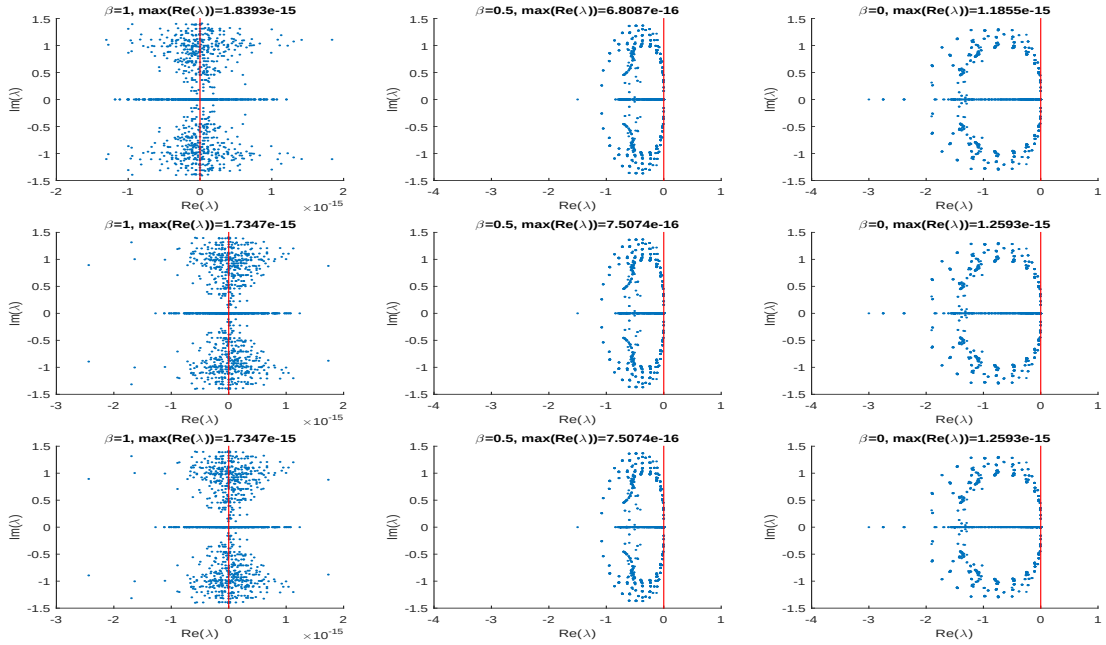

Figure 5.2.1: Eigenvalues of $\mathbf{A}_{h,q}^{G}$ (top), $\mathbf{A}_{h,q}^{GS}$ (middle), $\mathbf{A}_{h,q}^{PG}$ (bottom) with $\beta = 1$ (left), $\beta = 0.5$ (center), $\beta = 0$ (right) for bilinear IFE spaces for med1/med1 problem.

In order to see the effect of various c and ρ, and the effect of bilinear IFE and standard bilinear Lagrange spaces for homogeneous media, we consider two media, the first one with $c_1 = 1m/s$, $\rho_1 = 1m/s$ and refer to it by med1 and the second one with $c_2 = 1.5m/s$, $\rho_2 = 2m/s$ and refer to it by med2. For instance, the interface problem where med1 occupies Ω_1 and med2 occupies Ω_2 will be referred to as med1/med2.

We presents the eigenvalues of the matrices $\mathbf{A}_{h,q}^{G}$, $\mathbf{A}_{h,q}^{GS}$ and $\mathbf{A}_{h,q}^{PG}$ for $\beta = 1$, 0.5, 0 for the interface problems med1/med1 with bilinear IFE basis in Figure 5.2.1, med1/med1 with

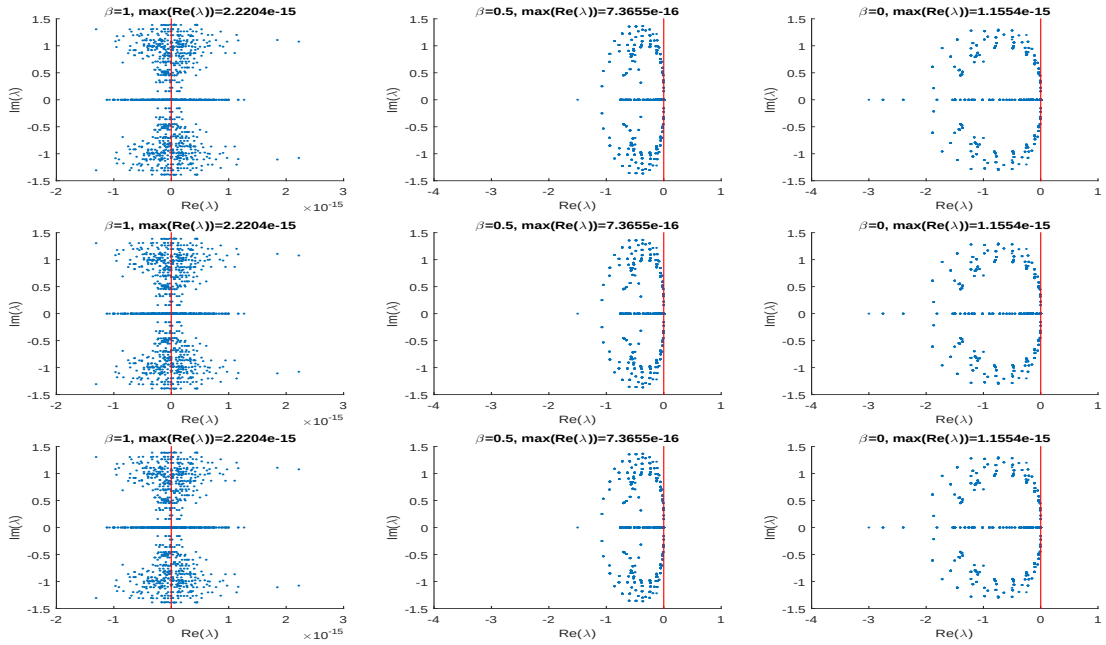

Figure 5.2.2: Eigenvalues of $\mathbf{A}_{h,q}^{G}$ (top), $\mathbf{A}_{h,q}^{GS}$ (middle), $\mathbf{A}_{h,q}^{PG}$ (bottom) with $\beta = 1$ (left), $\beta = 0.5$ (center), $\beta = 0$ (right) for standard bilinear Lagrange spaces for med1/med1 problem.

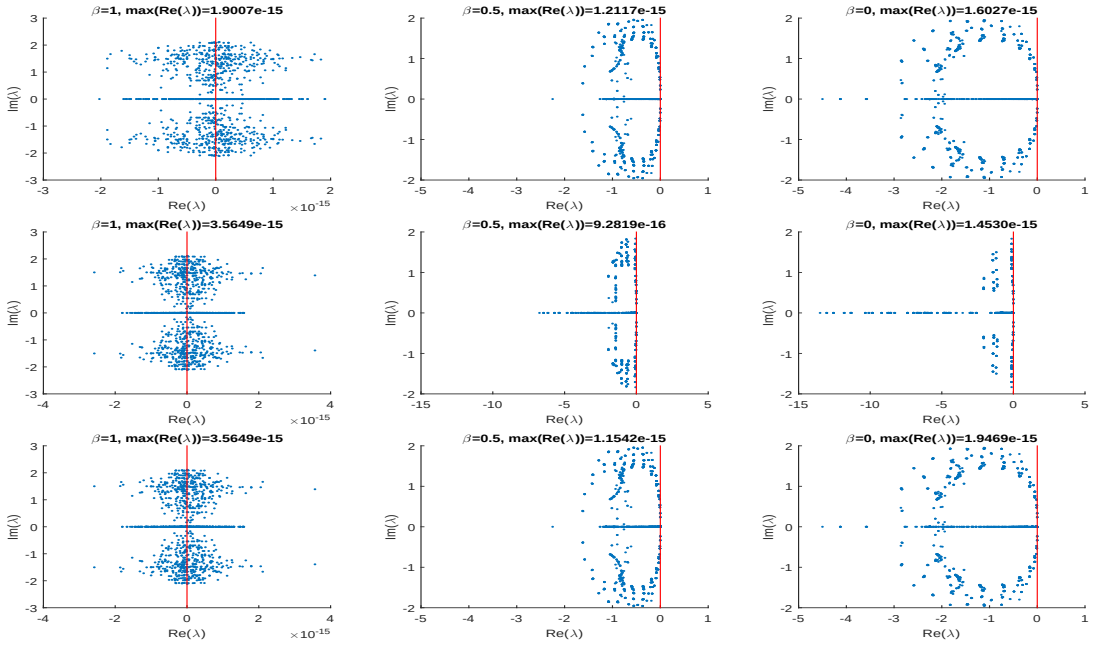

Figure 5.2.3: Eigenvalues of $\mathbf{A}_{h,q}^{G}$ (top), $\mathbf{A}_{h,q}^{GS}$ (middle), $\mathbf{A}_{h,q}^{PG}$ (bottom) with $\beta = 1$ (left), $\beta = 0.5$ (center), $\beta = 0$ (right) for med2/med2 problem.

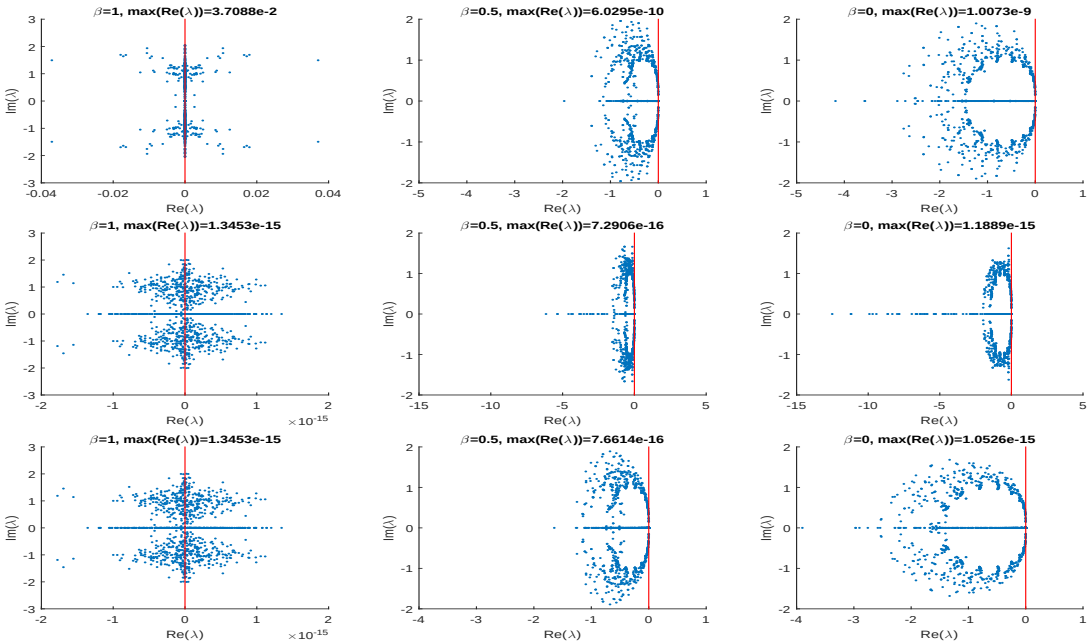

Figure 5.2.4: Eigenvalues of $\mathbf{A}_{h,q}^{G}$ (top), $\mathbf{A}_{h,q}^{GS}$ (middle), $\mathbf{A}_{h,q}^{PG}$ (bottom) with $\beta = 1$ (left), $\beta = 0.5$ (center), $\beta = 0$ (right) for med1/med2 problem.

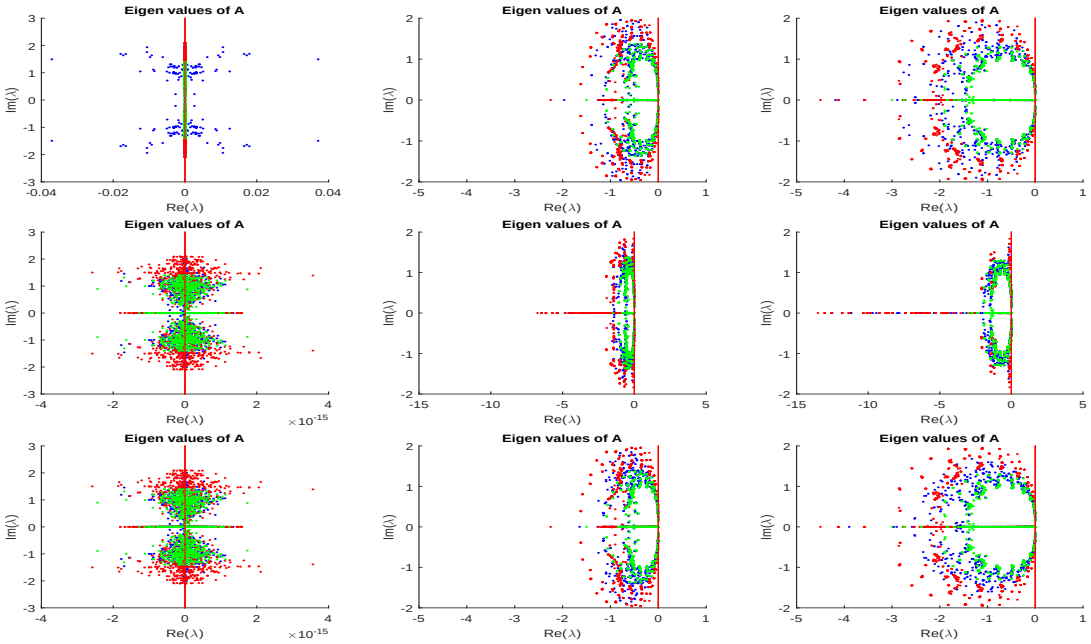

Figure 5.2.5: Eigenvalues of $\mathbf{A}_{h,q}^{G}$ (top), $\mathbf{A}_{h,q}^{GS}$ (middle), $\mathbf{A}_{h,q}^{PG}$ (bottom) with $\beta = 1$ (left), $\beta = 0.5$ (center), $\beta = 0$ (right) for med1/med1 (green), med2/med2 (red), med1/med2 (blue) problems.

standard bilinear Lagrange basis in Figure 5.2.2, med2/med2 with bilinear IFE basis in Figure 5.2.3, med1/med2 with bilinear IFE basis in Figure 5.2.4, and combine the spectrum of all three cases in Figure 5.2.5.

We observe that the IFE spaces for the homogeneous problem lead to the same spectrum as the standard spaces. While we see that the spectrum of the case med1/med2 reflects the spectrum of med1/med1 and med2/med2 as shown in Figure 5.2.5 (According to the Warburton there are analytical formulas for these eigenvalues), we can check with him for references [55]. The spectra of eigenvalues of $\mathbf{A}_{h,q}^{G}$, $\mathbf{A}_{h,q}^{GS}$ and $\mathbf{A}_{h,q}^{PG}$ for two dimensional problems is similar to that for one dimensional problems but it is observed that the values are spread over the plane unlike one dimensional problems as shown in Figures 2.5.1 and 5.2.1. IDGFE method is unstable for the two dimensional problem with high contrast media in Figure 5.2.9.

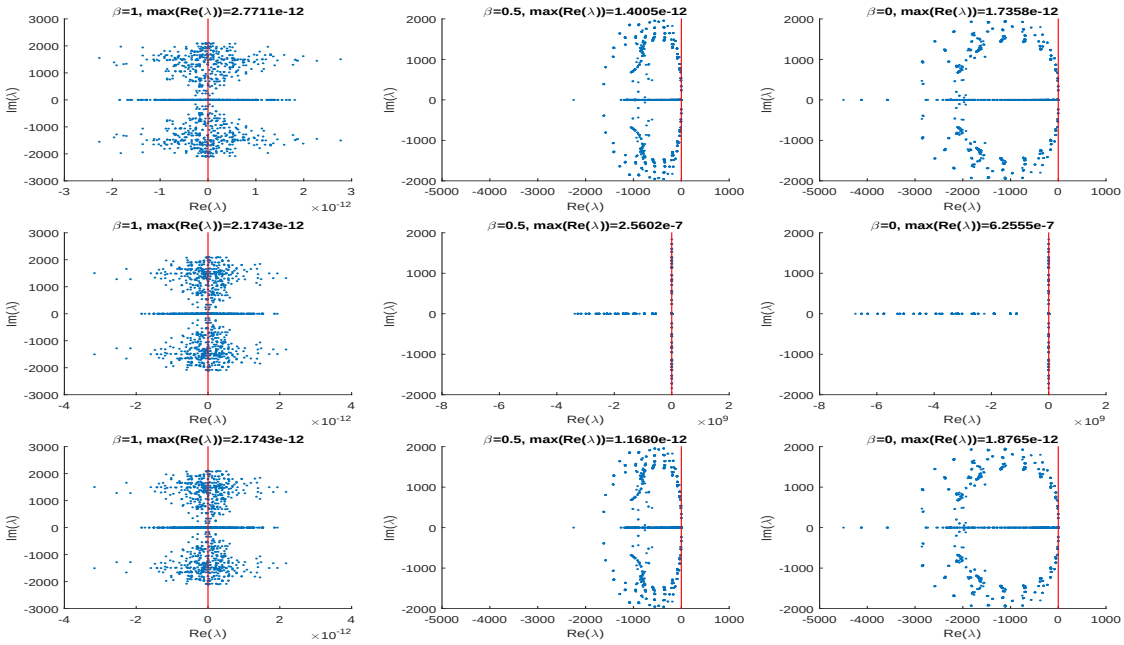

Figure 5.2.6: Eigenvalues of $\mathbf{A}_{h,q}^{G}$ (top), $\mathbf{A}_{h,q}^{GS}$ (middle), $\mathbf{A}_{h,q}^{PG}$ (bottom) with $\beta = 1$ (left), $\beta = 0.5$ (center), $\beta = 0$ (right) for bilinear IFE space for water/water problem.

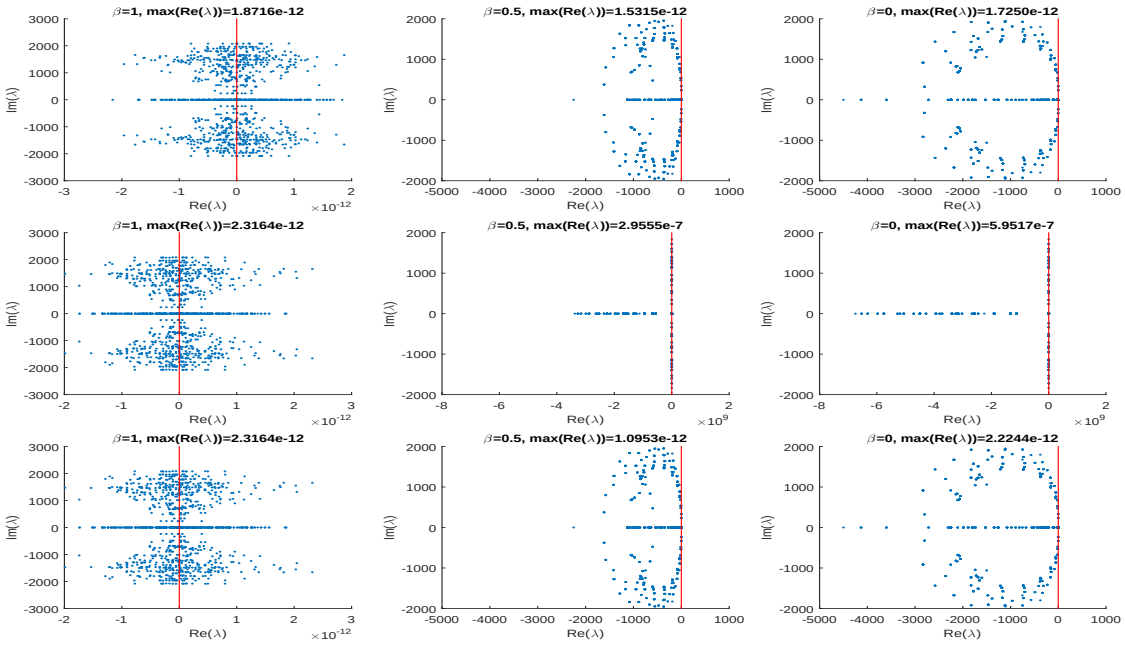

Figure 5.2.7: Eigenvalues of $\mathbf{A}_{h,q}^{G}$ (top), $\mathbf{A}_{h,q}^{GS}$ (middle), $\mathbf{A}_{h,q}^{PG}$ (bottom) with $\beta = 1$ (left), $\beta = 0.5$ (center), $\beta = 0$ (right) for standard bilinear Lagrange space for water/water problem.

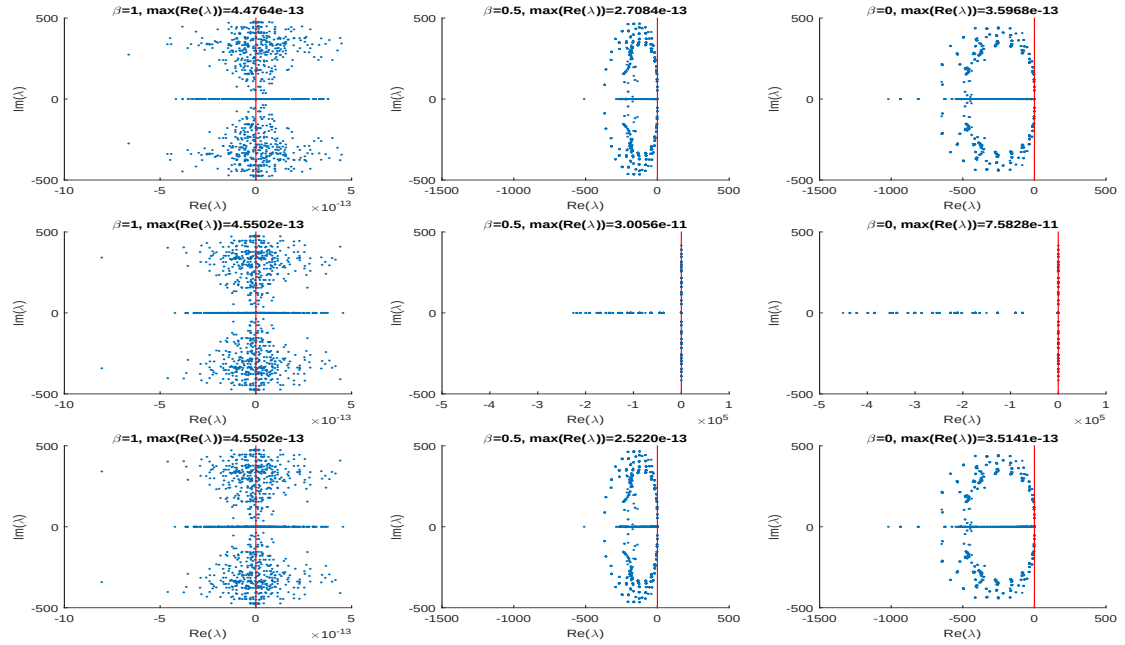

Figure 5.2.8: Eigenvalues of $\mathbf{A}_{h,q}^{G}$ (top), $\mathbf{A}_{h,q}^{GS}$ (middle), $\mathbf{A}_{h,q}^{PG}$ (bottom) with $\beta = 1$ (left), $\beta = 0.5$ (center), $\beta = 0$ (right) for air/air problem.

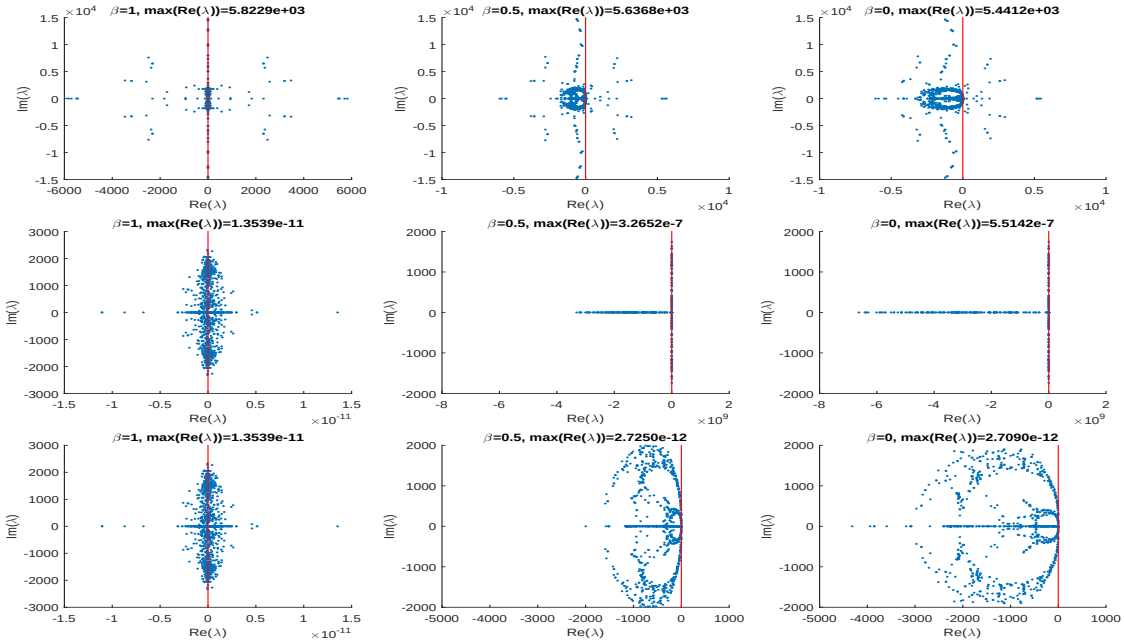

Figure 5.2.9: Eigenvalues of $\mathbf{A}_{h,q}^{G}$ (top), $\mathbf{A}_{h,q}^{GS}$ (middle), $\mathbf{A}_{h,q}^{PG}$ (bottom) with $\beta = 1$ (left), $\beta = 0.5$ (center), $\beta = 0$ (right) for water/air problem.

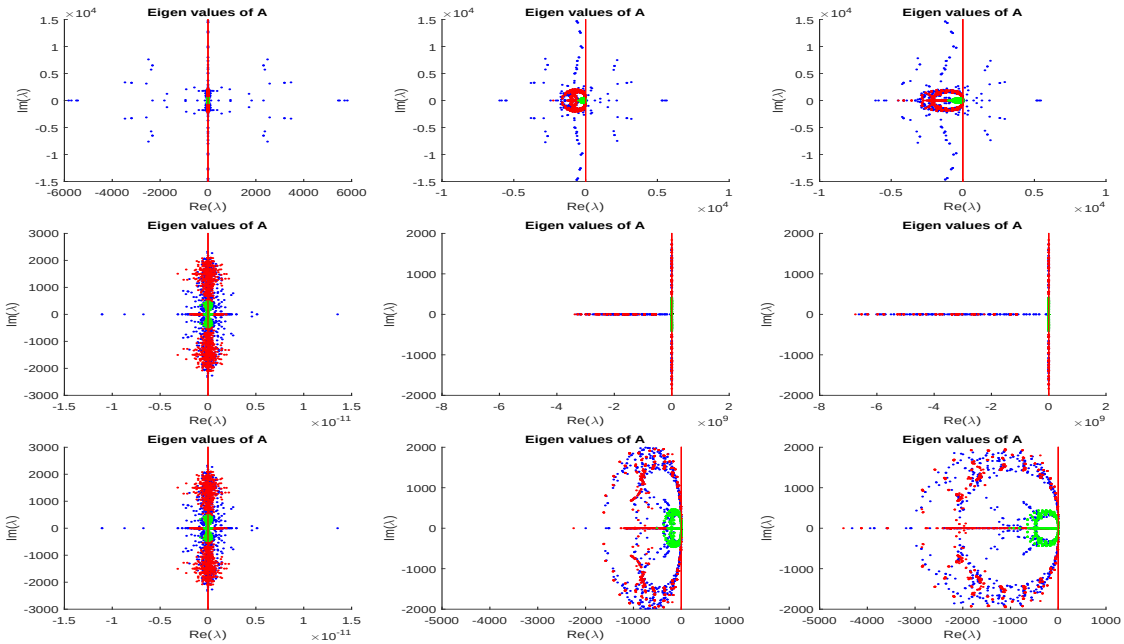

Figure 5.2.10: Eigenvalues of $\mathbf{A}_{h,q}^{G}$ (top), $\mathbf{A}_{h,q}^{GS}$ (middle), $\mathbf{A}_{h,q}^{PG}$ (bottom) with $\beta = 1$ (left), $\beta = 0.5$ (center), $\beta = 0$ (right) for water/water (red), air/air (green), water/air (blue) problems.

We repeat the previous experiments in Figures 5.2.6, 5.2.7, 5.2.8, 5.2.9 and 5.2.10 with realistic media to see the effect of c and ρ. We consider two media, the first one with water $c_1 = 1500m/s$, $\rho_1 = 1000kg/m^3$ and the second one with air $c_2 = 340m/s$, $\rho_2 = 1.3kg/m^3$. We presents the eigenvalues of the matrices $\mathbf{A}_{h,q}^{G}$, $\mathbf{A}_{h,q}^{GS}$ and $\mathbf{A}_{h,q}^{PG}$ for $\beta = 1$, 0.5, 0 for the interface problems water/water with bilinear IFE basis in Figure 5.2.6, water/water with standard bilinear Lagrange basis in Figure 5.2.7, air/air with bilinear IFE basis in Figure 5.2.8, water/air with bilinear IFE basis in Figure 5.2.9, and combine the spectrum of all three cases in Figure 5.2.10.

Again we observe that the IFE spaces for the homogeneous problem lead to the same spectrum as the standard spaces. We see that the spectrum of the case water/air reflects the spectrum of water/water and air/air as shown in Figure 5.2.10. Figure 5.2.9 shows the effect of IFE spaces for inhomogeneous media with water/air. We see that small spectrum is for air and large spectrum is for water.

We see that IDG method applied to the scaled problem is very inefficient especially for the media occupied by water/air. Eigenvalues of $\mathbf{A}_{h,q}^{GS}$ are very large ($-3\ 10^9$ for $\beta = 0.5$, $-7\ 10^9$ for $\beta = 0$) in Figure 5.2.9.

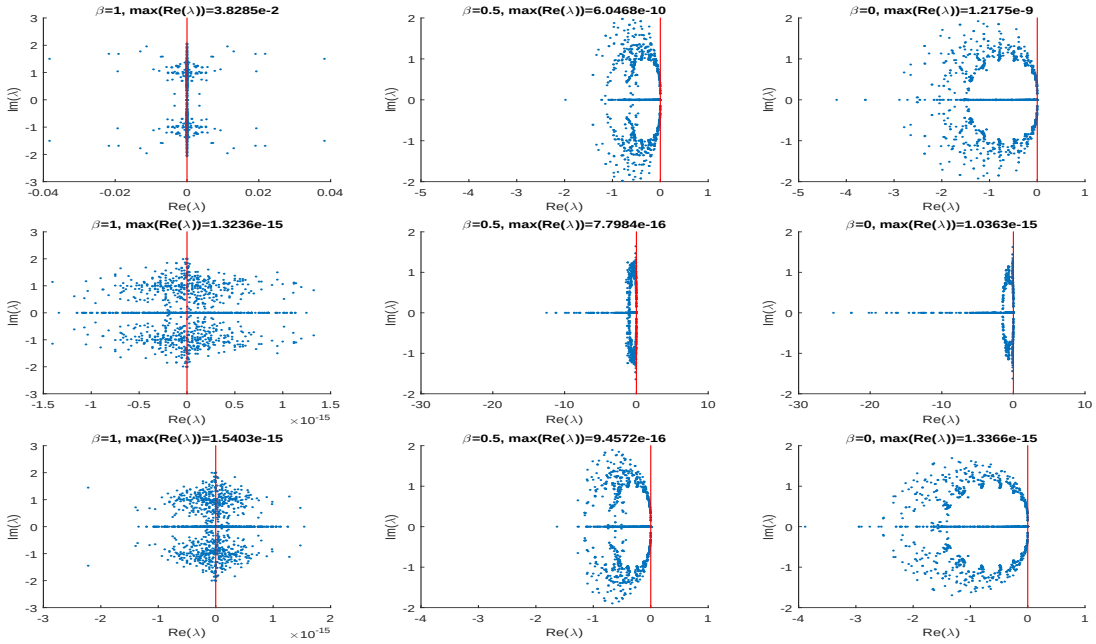

Figure 5.2.11: Eigenvalues of $\mathbf{A}_{h,q}^{G}$ (top), $\mathbf{A}_{h,q}^{GS}$ (middle), $\mathbf{A}_{h,q}^{PG}$ (bottom) with $\beta = 1$ (left), $\beta = 0.5$ (center), $\beta = 0$ (right) and $C = 0$ for med3/med4 problem.

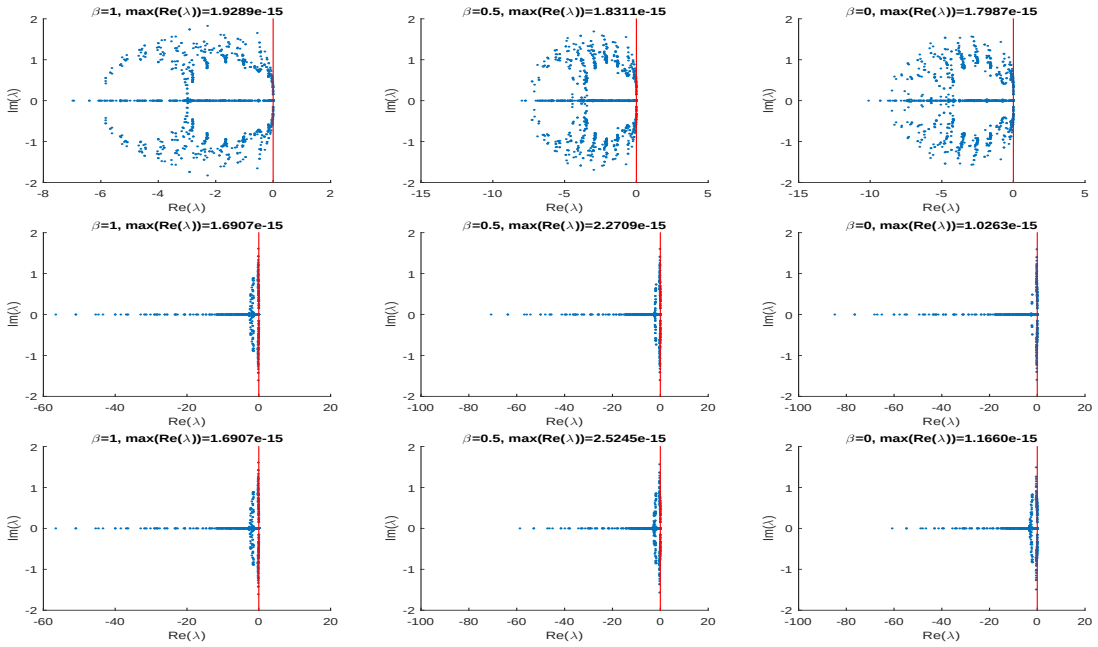

Figure 5.2.12: Eigenvalues of $\mathbf{A}_{h,q}^{G}$ (top), $\mathbf{A}_{h,q}^{GS}$ (middle), $\mathbf{A}_{h,q}^{PG}$ (bottom) with $\beta = 1$ (left), $\beta = 0.5$ (center), $\beta = 0$ (right) and $C = 1$ for med3/med4 problem.

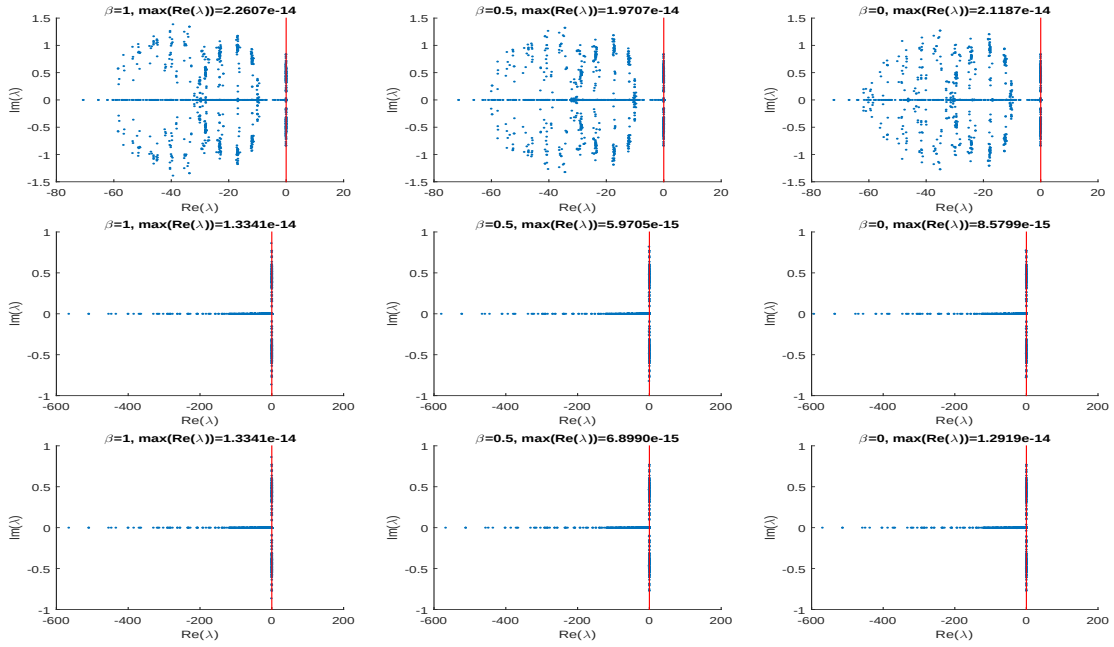

Figure 5.2.13: Eigenvalues of $\mathbf{A}_{h,q}^{G}$ (top), $\mathbf{A}_{h,q}^{GS}$ (middle), $\mathbf{A}_{h,q}^{PG}$ (bottom) with $\beta = 1$ (left), $\beta = 0.5$ (center), $\beta = 0$ (right) and $C = 10$ for med3/med4 problem.

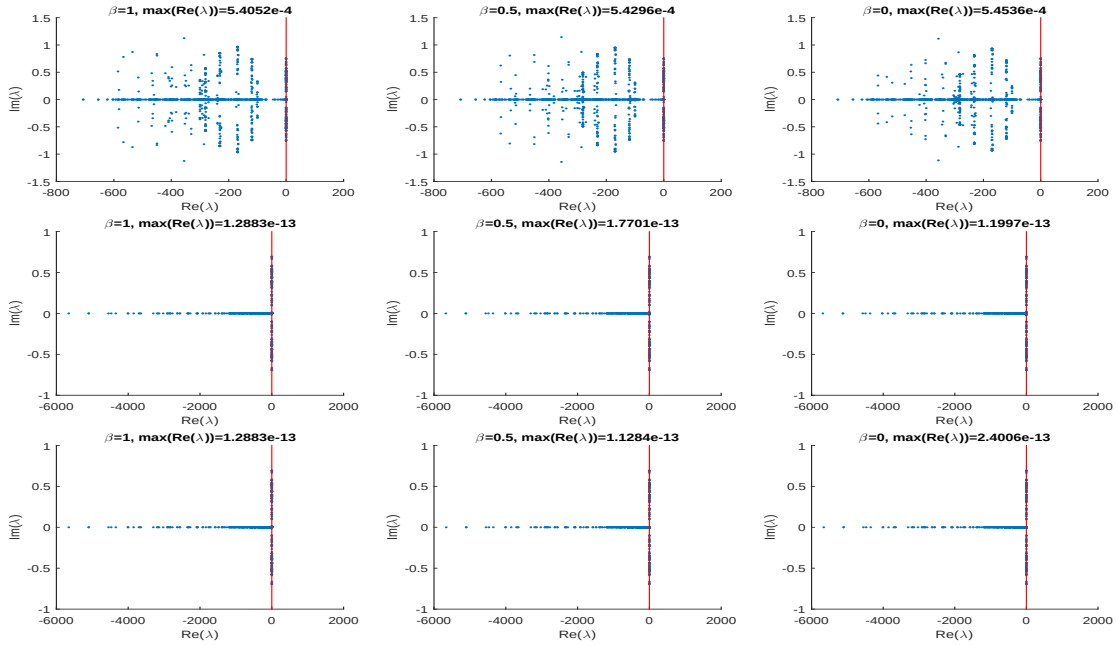

Figure 5.2.14: Eigenvalues of $\mathbf{A}_{h,q}^{G}$ (top), $\mathbf{A}_{h,q}^{GS}$ (middle), $\mathbf{A}_{h,q}^{PG}$ (bottom) with $\beta = 1$ (left), $\beta = 0.5$ (center), $\beta = 0$ (right) and $C = 100$ for med3/med4 problem.

In order to show the effect of the penalty term, we consider two media, the first one with $c_1 = 1m/s$, $\rho_1 = 2kg/m^3$ and refer to it by med3 and the second one with $c_2 = 1.5m/s$, $\rho_2 = 4.5kg/m^3$ refer to it by med4 and circular interface centered at $(x_0, y_0) = (20.1111, 20.1111)$ with radius $r = 10$. We use bilinear IFE spaces and plot the eigenvalues of $\mathbf{A}_{h,q}^{G}$, $\mathbf{A}_{h,q}^{GS}$ and $\mathbf{A}_{h,q}^{PG}$ for $C = 0$, 1, 10, 100, respectively, in Figures 5.2.11, 5.2.12, 5.2.13 and 5.2.14. As expected, the spectra are moved to the left with increasing C which introduces more dissipation.

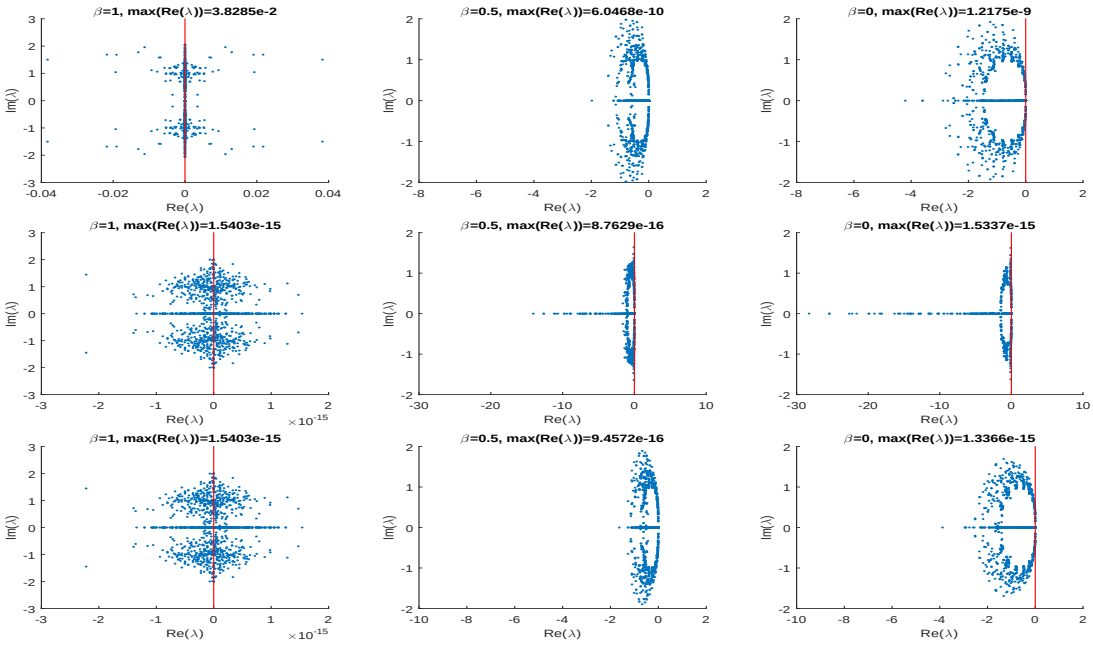

Figure 5.2.15: Eigenvalues of $\mathbf{A}_{h,q}^{G}$ (top), $\mathbf{A}_{h,q}^{GS}$ (middle), $\mathbf{A}_{h,q}^{PG}$ (bottom) with $\beta = 1$ (left), $\beta = 0.5$ (center), $\beta = 0$ (right) and radius $r = 10m$ for med3/med4 problem.

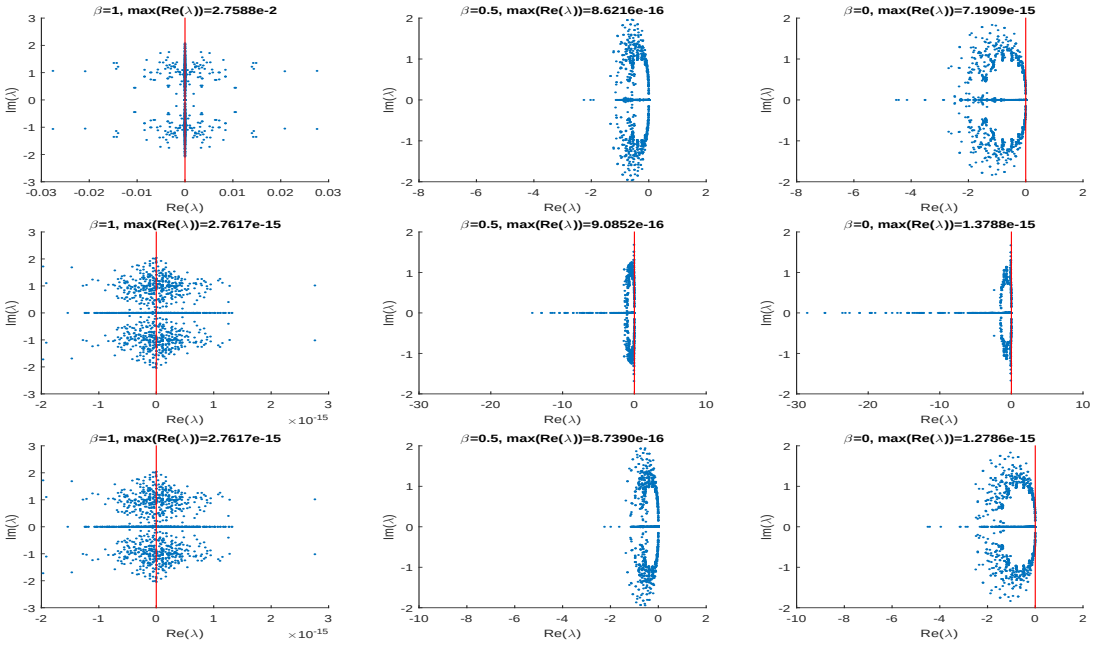

Figure 5.2.16: Eigenvalues of $\mathbf{A}_{h,q}^{G}$ (top), $\mathbf{A}_{h,q}^{GS}$ (middle), $\mathbf{A}_{h,q}^{PG}$ (bottom) with $\beta = 1$ (left), $\beta = 0.5$ (center), $\beta = 0$ (right) and radius $r = 11m$ for med3/med4 problem.

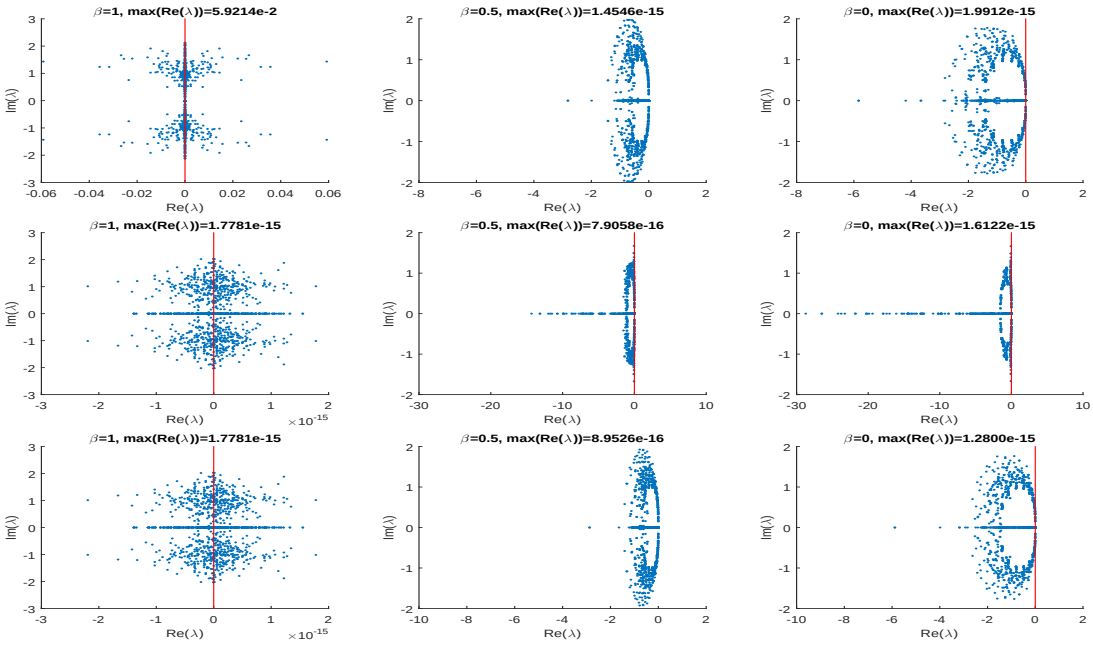

Figure 5.2.17: Eigenvalues of $\mathbf{A}_{h,q}^{G}$ (top), $\mathbf{A}_{h,q}^{GS}$ (middle), $\mathbf{A}_{h,q}^{PG}$ (bottom) with $\beta = 1$ (left), $\beta = 0.5$ (center), $\beta = 0$ (right) and radius $r = 12m$ for med3/med4 problem.

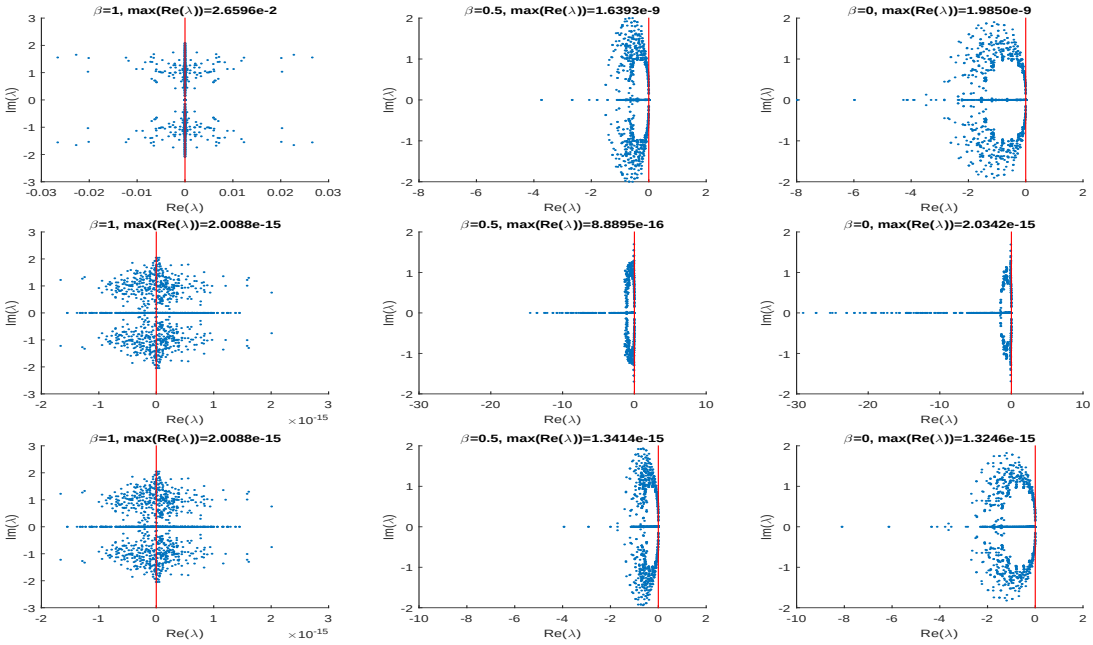

Figure 5.2.18: Eigenvalues of $\mathbf{A}_{h,q}^{G}$ (top), $\mathbf{A}_{h,q}^{GS}$ (middle), $\mathbf{A}_{h,q}^{PG}$ (bottom) with $\beta = 1$ (left), $\beta = 0.5$ (center), $\beta = 0$ (right) and radius $r = 13m$ for med3/med4 problem.

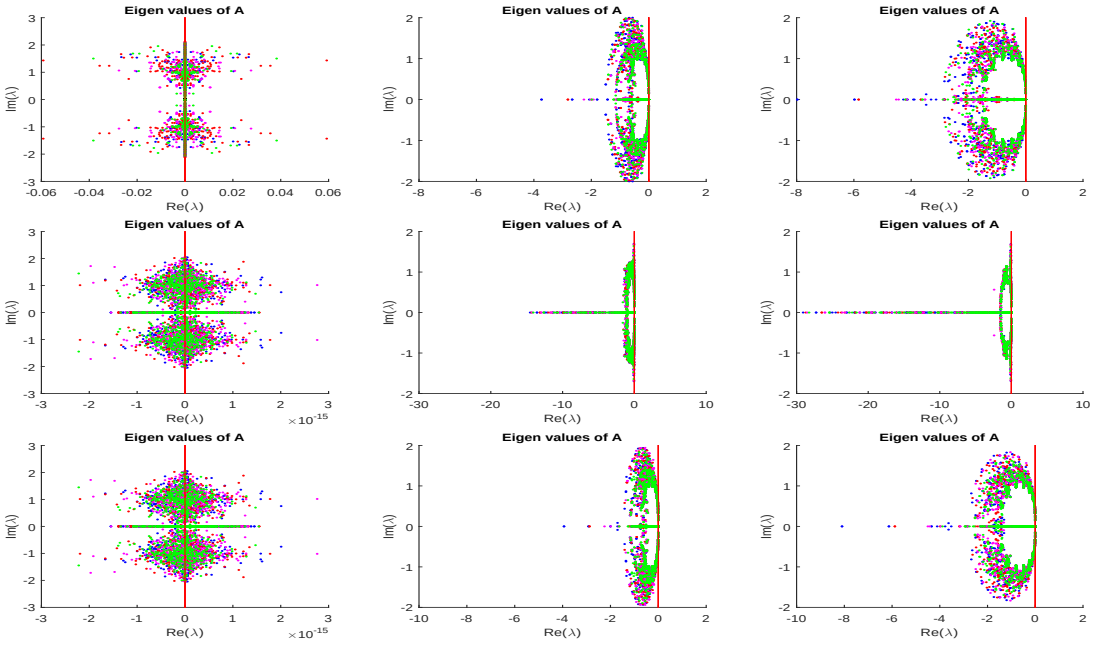

Figure 5.2.19: Eigenvalues of $\mathbf{A}_{h,q}^{G}$ (top), $\mathbf{A}_{h,q}^{GS}$ (middle), $\mathbf{A}_{h,q}^{PG}$ (bottom) with $\beta = 1$ (left), $\beta = 0.5$ (center), $\beta = 0$ (right) and radius $r = 10m$ (green), $11m$ (purple), $12m$ (red), $13m$ (blue) for med3/med4 problem.

We use various radii $r = 10$, 11, 12 and $13m$ in Figures 5.2.15, 5.2.16, 5.2.17 and 5.2.18 to see the effect of the area of the subregions and combine the spectrum of all three cases in Figure 5.2.19. We see that the eigenvalues move outside with increasing radius r which means that the number of elements in medium 1 (region outside) decreases and the number of elements medium 2 (region inside) increases.

We consider the high order IFE spaces in Figures 5.2.20, 5.2.21, 5.2.22 and 5.2.23. We observed that the spectra of all methods are moved to the left with higher degree IFE spaces.

Figures 5.2.24 and 5.2.25 show the eigenvalues of $\mathbf{A}_{h,q}^{PG}$ with and without penalty term (5.1.13) in order to show that penalty term (5.1.13) is needed for stability by especially comparing maximum real part of eigenvalues $\mathbf{A}^{PG}$ with $\beta = 1$. As we proved in Theorem 5.1.3, penalty term is necessary for stability.

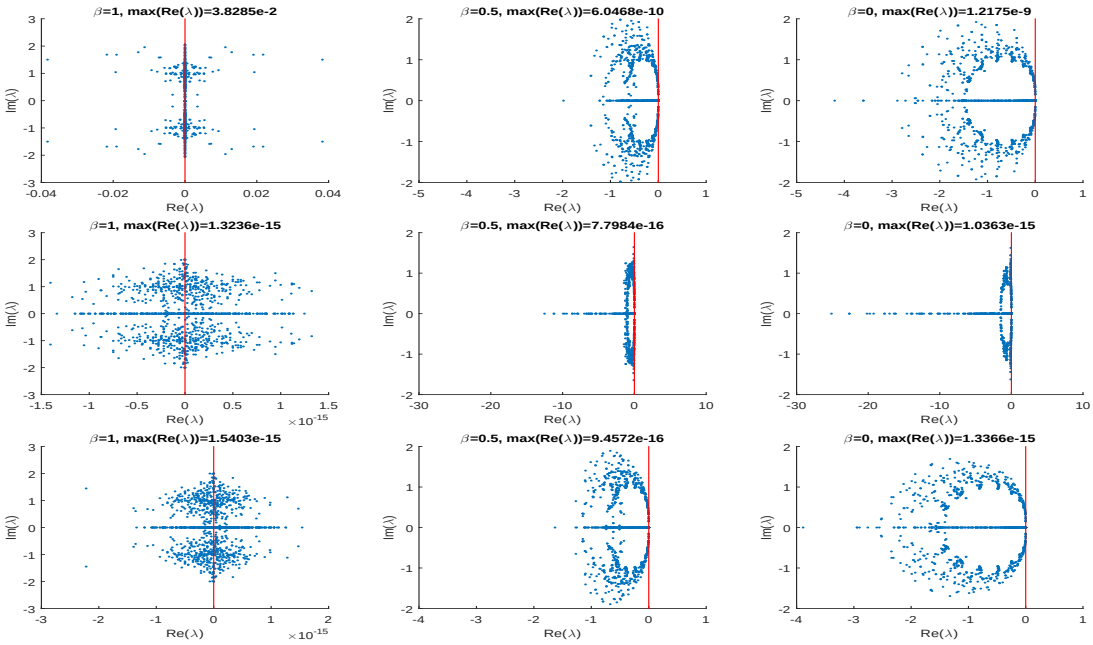

Figure 5.2.20: Eigenvalues of $\mathbf{A}_{h,q}^{G}$ (top), $\mathbf{A}_{h,q}^{GS}$ (middle), $\mathbf{A}_{h,q}^{PG}$ (bottom) with $\beta = 1$ (left), $\beta = 0.5$ (center), $\beta = 0$ (right) for bilinear IFE spaces ($q = 1$) for med3/med4 problem.

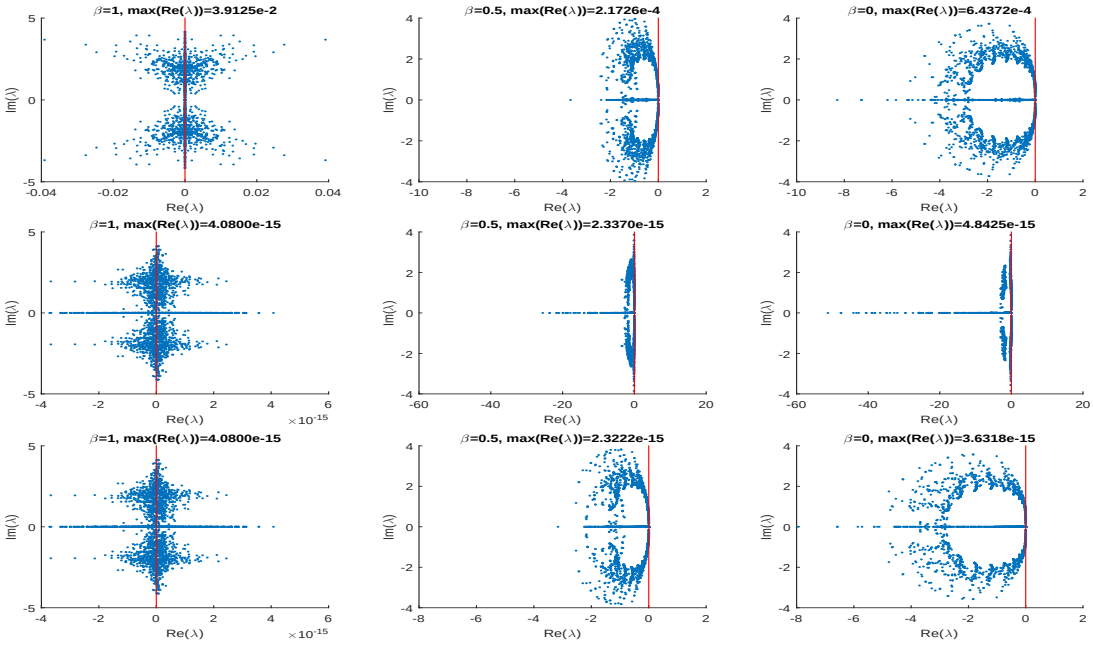

Figure 5.2.21: Eigenvalues of $\mathbf{A}_{h,q}^{G}$ (top), $\mathbf{A}_{h,q}^{GS}$ (middle), $\mathbf{A}_{h,q}^{PG}$ (bottom) with $\beta = 1$ (left), $\beta = 0.5$ (center), $\beta = 0$ (right) for biquadratic IFE spaces ($q = 2$) for med3/med4 problem.

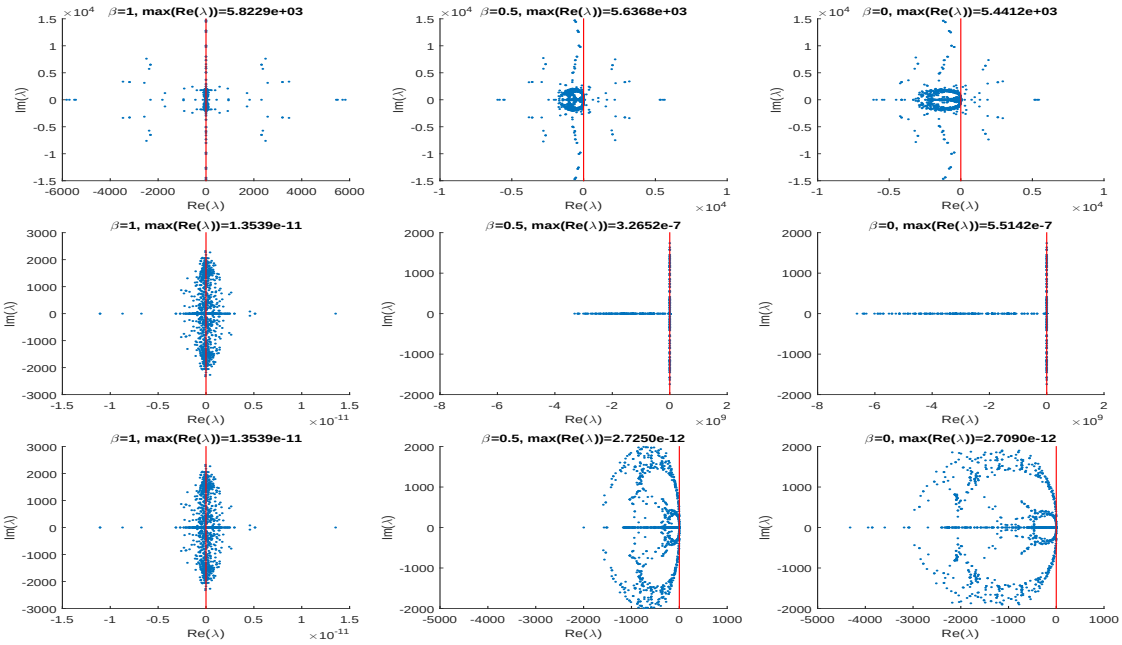

Figure 5.2.22: Eigenvalues of $\mathbf{A}_{h,q}^{G}$ (top), $\mathbf{A}_{h,q}^{GS}$ (middle), $\mathbf{A}_{h,q}^{PG}$ (bottom) with $\beta = 1$ (left), $\beta = 0.5$ (center), $\beta = 0$ (right) for bilinear IFE spaces ($q = 1$) for water/air problem.

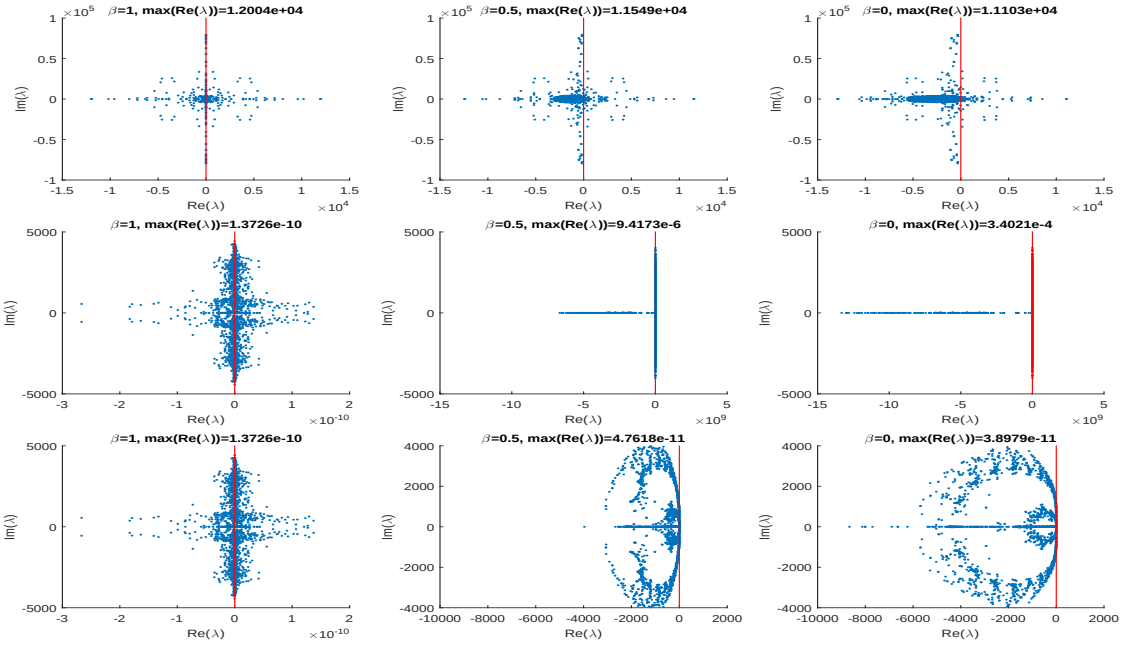

Figure 5.2.23: Eigenvalues of $\mathbf{A}_{h,q}^{G}$ (top), $\mathbf{A}_{h,q}^{GS}$ (middle), $\mathbf{A}_{h,q}^{PG}$ (bottom) with $\beta = 1$ (left), $\beta = 0.5$ (center), $\beta = 0$ (right) for biquadratic IFE spaces ($q = 2$) for water/air problem.

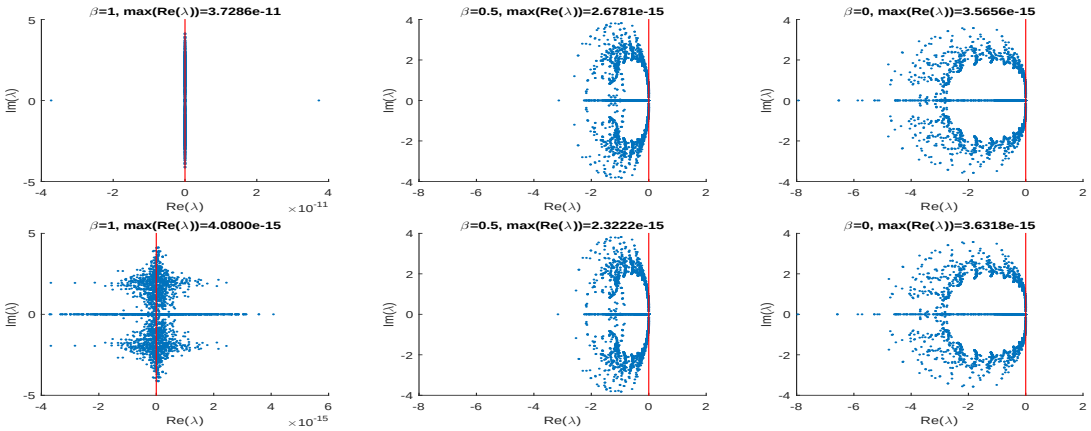

Figure 5.2.24: Eigenvalues of $\mathbf{A}_{h,q}^{PG}$ without the penalty term (5.1.13) (top) and with (bottom) using $\beta = 1$ (left), $\beta = 0.5$ (center), $\beta = 0$ (right) for biquadratic IFE spaces ($q = 2$) for med3/med4 problem.

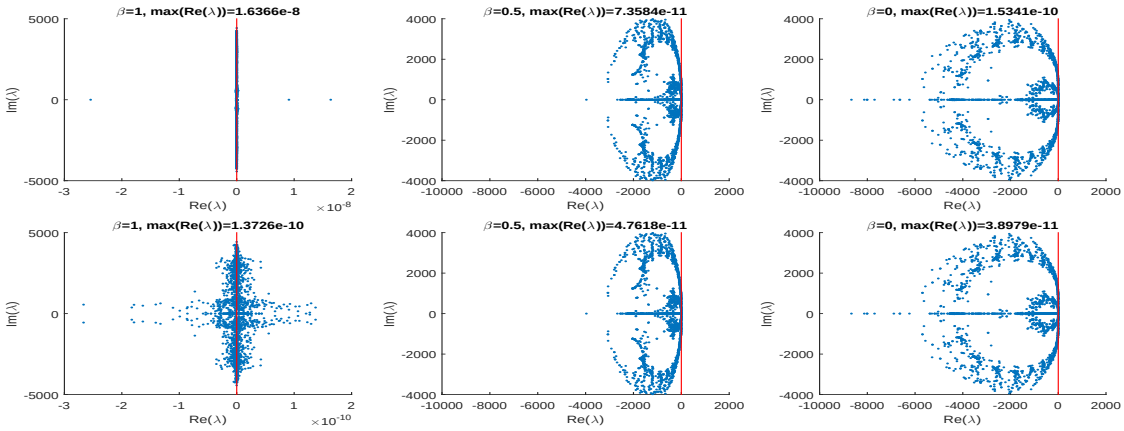

Figure 5.2.25: Eigenvalues of $\mathbf{A}_{h,q}^{PG}$ without the penalty term (5.1.13) (top) and with (bottom) using $\beta = 1$ (left), $\beta = 0.5$ (center), $\beta = 0$ (right) for biquadratic IFE spaces ($q = 2$) for water/air problem.

Chapter 6

Conclusion

6.1 Discussion of Results

In this dissertation we constructed high order immersed discontinuous Galerkin finite element methods for one and two dimensional acoustic interface problems. We developed linear, quadratic, cubic and quartic IFE spaces for one dimensional problems and bilinear and biquadratic IFE spaces for two dimensional problems with standard immersed DG method, immersed DG method applied to a scaled problem and immersed discontinuous Petrov-Galerkin method.

We constructed one and two dimensional IFE spaces by using jump conditions and proved the existence and uniqueness of linear, quadratic, cubic and quartic IFE spaces for one dimensional problems and the existence of bilinear IFE spaces for two dimensional problems. We obtained optimal orders of convergence for one dimensional test problems and water/air problems. We also investigated dispersive and dissipative properties of immersed DG methods.

In order to solve two dimensional acoustic interface problems with high jumps across the interface, we first scaled the problem and applied immersed DG method. The resulting method is stable but has a small stability region. Thus this method is not acceptable for the problems with the real liquid and gas having large densities and sound speeds and acceptable only for test problems having small densities and sound speeds. For this reason, we developed an immersed discontinuous Petrov-Galerkin method where stability region is comparable to standard DG method on fitted meshes.

We achieved optimal orders of convergence for two dimensional acoustic interface problems for the three methods. Extensive numerical experiments show that a ratio less than 10 in densities and sound speeds for liquid/liquid and gas/gas is acceptable for immersed DG method.

We showed that the standard DG method is unstable by presenting numerical computations. Stability of Petrov-Galerkin method is proved for one and two dimensional problems. Here, we recommend the Petrov-Galerkin method on IFE spaces which is stable for one and two dimensional problems with high jumps across the interface.

We also investigated the advantages and disadvantages of three methods by comparing numerical results.

6.2 Future Work

There are several remaining tasks and challenging goals that will follow this dissertation. First, we will investigate conservative local time-stepping methods. Since we have developed bilinear and biquadratic IFE spaces, we can continue to extend IFE spaces for bicubic and biquartic spaces for two dimensional acoustic interface problems. A priori and posteriori error estimates should be carried out. Moving interface and deforming problems will be also considered. We will explore the discontinuous spectrum of the DG formulations.

Since the code is designed to extend to other problems, we can solve other wave propagation problems such as elastic-elastic, acoustic-elastic and electromagnetic interface problems. We will consider three dimensional interface problems. Immersed DG methods will be explored to simulate realistic problems for seismic waves or ultrasonic wave propagation in human body.

Bibliography

[1] S. Adjerid, M. Ben-Romdhane, and T. Lin. Higher degree immersed finite element methods for second-order elliptic interface problems. *International Journal of Numerical Analysis and Modeling*, 11(3):541–556, 2014.

[2] S. Adjerid, M. Ben-Romdhane, and T. Lin. Higher degree immersed finite element methods for second-order elliptic curved-interface problems. in preparation, 2016.

[3] S. Adjerid, N. Chaabane, and T. Lin. An immersed discontinuous finite element method for Stokes interface problems. *Computer Methods in Applied Mechanics and Engineering*, 293:170–190, 2015.

[4] S. Adjerid, N. Chaabane, P. Yue, and T. Lin. An immersed finite element method for the Stokes problem with a moving interface. in preparation, 2016.

[5] S. Adjerid, K.D. Devine, J.E. Flaherty, and L. Krivodonova. A posteriori error estimation for discontinuous Galerkin solutions of hyperbolic problems. *Computer Methods in Applied Mechanics and Engineering*, 191(11-12):1097–1112, 2002.

[6] S. Adjerid and T. Lin. Higher-order immersed discontinuous Galerkin methods. *International Journal of Information and Systems Sciences*, 3(4):555–568, 2007.

[7] S. Adjerid and T. Lin. A p-th degree immersed finite element method for boundary value problems with discontinuous coefficients. *Applied Numerical Mathematics*, 59(6):1303–1321, 2009.

[8] S. Adjerid, M. Ben Romdhane, and T. Lin. Quadratic immersed finite element spaces for elliptic interface problems. In A. Ansari and H. Temimi, editors, *Advances in Applied Mathematics*, volume 18, pages 171–178, New York, 2014. Springer.

[9] M. Ainsworth. Dispersive and dissipative behaviour of high order discontinuous Galerkin finite element methods. *Journal of Computational Physics*, 198:106–130, April 2004.

[10] R.C. Almeida and A.C. Galeão. An adaptive Petrov-Galerkin formulation for the compressible Euler and Navier-Stokes equations. *Computer Methods in Applied Mechanics and Engineering*, 129(1-2):157–176, 1996.

[11] R.C. Almeida and R.S. Silva. A stable Petrov-Galerkin method for convection-dominated problems. *Computer Methods in Applied Mechanics and Engineering*, 140(3-4):291–304, 1997.

[12] D.N. Arnold, F. Brezzi, B. Cockburn, and L.D. Marini. Unified analysis of discontinuous Galerkin methods for elliptic problems. *SIAM Journal on Numerical Analysis*, 39(5):1749–1779, 2002.

[13] R.E. Bank and B.D. Welfert. A comparison between the mini-element and the Petrov-Galerkin formulations for the generalized stokes problem. *Computer Methods in Applied Mechanics and Engineering*, 83(1):61–68, 1990.

[14] F. Bassi and S. Rebay. A high-order accurate discontinuous finite element method for the numerical solution of the compressible Navier-Stokes equations. *Journal of Computational Physics*, 131(2):267–279, 1997.

[15] F. Bassi and S. Rebay. High-order accurate discontinuous finite element solution of the 2D Euler equations. *Journal of Computational Physics*, 138(2):251–285, 1997.

[16] C. Baumann and J. Oden. A discontinuous *hp*-finite element method for the solution of the Euler equation of gas dynamics. *Proceedings of the 10th International Conference on Finite Element in Fluids*, 1998.

[17] C. Baumann and J. Oden. A discontinuous *hp*-finite element method for convection-diffusion problems. *Computer Methods in Applied Mechanics and Engineering*, 175(3-4):311–341, 1999.

[18] R. Becker, P. Hansbo, and M.G. Larson. Energy norm a posteriori error estimation for discontinuous Galerkin methods. *Computer Methods in Applied Mechanics and Engineering*, 192(5-6):723–733, 2003.

[19] K.S. Bey and J.T. Oden. *hp*-version discontinuous Galerkin methods for hyperbolic conservation laws. *Computer Methods in Applied Mechanics and Engineering*, 133(3-4):259–286, 1996.

[20] K.S. Bey, A. Patra, and J.T. Oden. *hp*-version discontinuous Galerkin methods for hyperbolic conservation laws: A parallel adaptive strategy. *Numerical Methods in Engineering*, 38(22):3889–3908, 1995.

[21] R. Biswas, K.D. Devine, and J.E. Flaherty. Parallel, adaptive finite element methods for conservation laws. *Applied Numerical Mathematics*, 14(1-3):255–283, 1994.

[22] A. Bourgeat and B. Cockburn. The TVD-projection method for solving implicit numerical schemes for scalar conservation laws: A numerical study of a simple case. *SIAM Journal on Scientific and Statistical Computing*, 10(2):253–273, 1989.

[23] R. Bustinza, G.N. Gatica, and B. Cockburn. An a posteriori error estimate for the local discontinuous Galerkin method applied to linear and nonlinear diffusion problems. *Journal of Scientific Computing*, 22(1):147–185, 2005.

[24] B. Camp, T. Lin, Y. Lin, and W.W. Sun. Quadratic immersed finite element spaces and their approximation capabilities. *Advances in Computational Mathematics*, 24(1):81–112, 2006.

[25] P. Castillo, B. Cockburn, I. Perugia, and D. Schötzau. An a priori error analysis of the local discontinuous Galerkin method for elliptic problems. *SIAM Journal on Numerical Analysis*, 38(5):1676–1706, 2001.

[26] P. Castillo, B. Cockburn, D. Schötzau, and C. Schwab. Optimal a priori error estimates for the *hp*-version of the local discontinuous Galerkin method for convection-diffusion problems. *Mathematics of Computation*, 71(238):455–478, 2001.

[27] Z. Chen and J. Zou. Finite element methods and their convergence for elliptic and parabolic interface problems. *Numerische Mathematik*, 79(2):175–202, 1998.

[28] Y. Cheng and C.W. Shu. A discontinuous Galerkin finite element method for time dependent partial differential equations with higher order derivatives. *Mathematics of Computation*, 77(262):699–730, 2008.

[29] B. Cockburn, J. Guzman, and H. Wang. Superconvergent discontinuous Galerkin methods for second-order elliptic problems. *Mathematics of Computation*, 78:1–24, 2009.

[30] B. Cockburn, S. Hou, and C.W. Shu. The Runge-Kutta local projection discontinuous Galerkin finite element method for conservation laws IV: The multidimensional case. *Mathematics of Computation*, 54(190):545–591, 1990.

[31] B. Cockburn, G. Kanschat, I. Perugia, and D. Schötzau. Superconvergence of the local discontinuous Galerkin method for elliptic problems on Cartiesian grids. *SIAM Journal on Numerical Analysis*, 39(1):264–285, 2001.

[32] B. Cockburn, G. Kanschat, and D. Schötzau. A locally conservative LDG method for the incompressible Navier-Stokes equations. *Mathematics of Computation*, 74(251):1067–1095, 2005.

[33] B. Cockburn and S. Lin. TVB Runge-Kutta local projection discontinuous Galerkin finite element method for conservation laws III: One-dimentional systems. *Journal of Compututational Physics*, 84(1):90–113, 1989.

[34] B. Cockburn and C.W. Shu. TVB Runge-Kutta local projection discontinuous Galerkin finite element method for conservation laws II: General framework. *Mathematics of Computation*, 52(186):411–435, 1989.

[35] B. Cockburn and C.W. Shu. The local discontinuous Galerkin method for time-dependent convection-diffusion system. *SIAM Journal on Numerial Analysis*, 35(6):2440–2463, 1998.

[36] B. Cockburn and C.W. Shu. The Runge-Kutta discontinuous Galerkin method for conervation laws. V. Multidimensional systems. *Journal of Computational Physics*, 141(2):199–224, 1998.

[37] B. Cockburn and C.W. Shu. Runge-Kutta discontinuous Galerkin methods for convection-dominated problems. *Journal of Scientific Computing*, 16(3):173–261, 2001.

[38] P.A.B. de Sampaio, P.R.M. Lyra, K. Morgan, and N.P. Weatherill. Petrov-Galerkin solutions of the incompressible Navier-Stokes equations in primitive variables with adaptive remeshing. *Computer Methods in Applied Mechanics and Engineering*, 106(1-2):143–178, 1993.

[39] L. Demkowicz and J. Gopalakrishnan. A class of discontinuous Petrov-Galerkin methods. Part I: The transport equation. *Computer Methods in Applied Mechanics and Engineering*, 199(23-24):1558–1572, 2010.

[40] L. Demkowicz and J. Gopalakrishnan. A class of discontinuous Petrov-Galerkin methods. Part II. Optimal test functions. *Numerical Methods for Partial Differential Equations*, 27(1):70–105, 2011.

[41] L. Demkowicz, J. Gopalakrishnan, and A.H. Niemi. A class of discontinuous Petrov-Galerkin methods. Part III: Adaptivity. *Applied Numerical Mathematics*, 62(4):396–427, 2012.

[42] L. Demkowicz and J.T. Oden. An adaptive characteristic Petrov-Galerkin finite element method for convection-dominated linear and nonlinear parabolic problems in one space variable. *Journal of Computational Physics*, 67(1):188–213, 1986.

[43] E.A. Fadlun, R. Verzicco, P. Orlandi, and J. Mohd-Yusof. Combined immersed-boundary finite-difference methods for three-dimensional complex flow simulations. *Journal of Computational Physics*, 161(1):35–60, 2000.

[44] J.E. Flaherty, L. Krivodonova, J. Remacle, and M.S. Shephard. Aspects of discontinuous Galerkin methods for hyperbolic conservation laws. *Finite Elements in Analysis and Design*, 38(10):889–908, 2002.

[45] A.C. Galeão and E.G.D. do Carmo. A consistent approximate upwind Petrov-Galerkin method for convection-dominated problems. *Computer Methods in Applied Mechanics and Engineering*, 68(1):83–95, 1988.

[46] Y. Gong, B. Li, and Z. Li. Immersed-interface finite-element methods for elliptic interface problems with non-homogeneous jump conditions. *SIAM Journal on Numerical Analysis*, 46(1):472–495, 2007.

[47] B.E. Griffith, R.D. Hornung, D.M. McQueen, and C.S. Peskin. An adaptive, formally second order accurate version of the immersed boundary method. *Journal of Computational Physics*, 223(1):10–49, 2007.

[48] R. Hartmann and P. Houston. Adaptive discontinuous Galerkin finite element methods for the compressible Euler equations. *Journal of Computational Physics*, 183(2):508–532, 2002.

[49] X. He. Bilinear immersed finite elements for interface problems. Ph.D Thesis. 2009. Virginia Tech.

[50] X. He, T. Lin, and Y. Lin. Approximation capability of a bilinear immersed finite element space. *Numerical Methods for Partial Differential Equations*, 24(5):1265–1300, 2008.

[51] X. He, T. Lin, and Y. Lin. A bilinear immersed finite volume element method for the diffusion equation with discontinuous coefficient. *Communications in Comutational Physics*, 6(1):185–202, 2009.

[52] X. He, T. Lin, and Y. Lin. Immersed finite element methods for elliptic interface problems with non-homogeneous jump conditions. *International Journals of Numerical Analysis and Modeling*, 8(2):284–301, 2011.

[53] X. He, T. Lin, and Y. Lin. A selective immersed discontinuous Galerkin method for elliptic interface problems. *Mathematical Methods in the Applied Sciences*, 37(7):983–1002, 2014.

[54] X. He, T. Lin, Y. Lin, and X. Zhang. Immersed finite element methods for parabolic equations with moving interface. *Numerical Methods for Partial Differential Equations*, 29(2):619–646, 2013.

[55] J.S. Hesthaven and T. Warburton. High-order nodal discontinuous Galerkin methods for the Maxwell eigenvalue problem. *Philosophical Transactions. Series A, Mathematical, Physical, and Engineering Sciences*, 362(1816):493–52, 2004.

[56] J.S. Hesthaven and T. Warburton. *Nodal Discontinuous Galerkin Methods*. Texts in Applied Mathematics. Springer, 2008.

[57] T.Y. Hou, Z. Li, S. Osher, and H. Zhao. A hybrid method for moving interface problems with application to the Hele-Shaw flow. *Journal of Computational Physics*, 134(2):236–252, 1997.

[58] F.Q. Hua, M.Y. Hussaini, and P. Rasetarinera. An analysis of the discontinuous Galerkin method for wave propagation problems. *Journal of Computational Physics*, 151(2):921–946, 1999.

[59] H. Huang and Z. Li. Convergence analysis of the immersed interface method. *IMA Journal of Numerical Analysis*, 19(4):583–608, 1999.

[60] W. Huang, C.B. Chang, and H.J. Sung. An improved penalty immersed boundary method for fluid-flexible body interaction. *Journal of Computational Physics*, 230(12):5061–5079, 2011.

[61] W. Huang, C.B. Chang, and H.J. Sung. Three-dimensional simulation of elastic capsules in shear flow by the penalty immersed boundary method. *Journal of Computational Physics*, 231(8):3340–3364, 2012.

[62] A. Idesman, R. Niekamp, and E. Stein. Continuous and discontinuous Galerkin methods with finite elements in space and time for parallel computing of viscoelastic deformation. *Computer Methods in Applied Mechanics and Engineering*, 190(8-10):1049–1063, 2000.

[63] G.B. Jacobs and J.S. Hesthaven. High-order nodal discontinuous Galerkin particle-in-cell method on unstructured grids. *Journal of Compututational Physics*, 214(1):96–121, 2006.

[64] R. Kafafy, T. Lin, Y. Lin, and J. Wang. Three-dimensional immersed finite element methods for electric field simulation in composite materials. *International Journal for Numerical Methods in Engineering*, 64:904–972, 2005.

[65] V. Kalro and T.E. Tezduyar. A parallel 3D computational method for fluid-structure interactions in parachute systems. *Computer Methods in Applied Mechanics and Engineering*, 109(3-4):321–332, 2000.

[66] J. Kim, D. Kim, and H. Choi. An immersed-boundary finite-volume method for simulations of flow in complex geometries. *Journal of Computational Physics*, 171(1):132–150, 2001.

[67] Y. Kim and M. Lai. Simulating the dynamics of inextensible vesicles by the penalty immersed boundary method. *Journal of Computational Physics*, 229(10):4840–4853, 2010.

[68] D.A. Kopriva. *Implementing Spectral Methods for Partial Differential Equations*. Algorithms for Scientists and Engineers. Springer, 2009.

[69] D.A. Kopriva. Private communication, 2013.

[70] L. Krivodonova. Limiters for high-order discontinuous Galerkin methods. *Journal of Compututational Physics*, 226(1):879–896, 2007.

[71] L. Krivodonova, J. Xin, J.F. Remacle, N. Chevaugeon, and J.E. Flaherty. Shock detection and limiting with discontinuous Galerkin methods for hyperbolic conservation laws. *Applied Numerical Mathematics*, 48(3-4):323–338, 2004.

[72] M. Lai and C.S. Peskin. An immersed boundary method with formal second-order accuracy and reduced numerical viscosity. *Journal of Computational Physics*, 160(2):705–719, 2000.

[73] P. Lesaint and P.A. Raviart. On a finite element method for solving the neutron transport equation. *Mathematical Aspects of Finite Elements in Partial Differential Equations*, (CdeBoor, ed.), Academic Press, New York:89–123, 1974.

[74] R.J. Leveque and Z. Li. The immersed interface method for elliptic equations with discontinuous coefficients and singular sources. *SIAM Journal on Numerical Analysis*, 31(4):1019–1044, 1994.

[75] Z. Li. The immersed interface method - A numerical approach for partial differential equations with interfaces. Ph.D Thesis. 1994. University of Washington.

[76] Z. Li. A note on immersed interface method for three-dimensional elliptic equations. *Computers and Mathematics with Applications*, 31(3):9–17, 1996.

[77] Z. Li. Immersed interface methods for moving interface problems. *Numerical Algorithms*, 14(4):269–293, 1997.

[78] Z. Li. The immersed interface method using a finite element formulation. *Applied Numerical Mathematics*, 27(3):253–267, 1998.

[79] Z. Li, T. Lin, and X. Wu. New Cartesian grid methods for interface problems using the finite element formulation. *Numerishe Mathematik*, 96(1):61–98, 2003.

[80] Q. Lin and A. Zhou. Convergence of the discontinuous Galerkin method for a scalar hyperbolic equation. *Acta Mathematica Scientia*, 13:207–210, 1993.

[81] T. Lin, Y. Lin, R. Rogers, and M. Ryan. A rectangular immersed finite element space for interface problems. *Advances in Computations: Theory and Practice*, 7:107–114, 2001.

[82] T. Lin, D. Sheen, and X. Zhang. A locking-free immersed finite element method for planar elasticity interface problems. *Journal of Computational Physics*, 247:228–247, 2013.

[83] T. Lin, Q. Yang, and X. Zhang. Partially penalized immersed finite element methods for parabolic interface problems. *Numerical Methods for Partial Differential Equations*, 31(6):1925–1947, 2015.

[84] T. Lin, Q. Yang, and X. Zhang. A priori error estimates for some discontinuous Galerkin immersed finite element methods. *Journal of Scientific Computing*, 65(3):875–894, 2015.

[85] T. Lin and X. Zhang. Linear and bilinear immersed finite elements for planar elasticity interface problems. *Journal of Computational and Applied Mathematics*, 236(18):4681–4699, 2012.

[86] B. Lombard and J. Piraux. A new interface method for hyperbolic problems with discontinuous coefficients: One-dimensional acoustic example. *Journal of computational Physics*, 168(1):227–248, 2001.

[87] B. Lombard and J. Piraux. Numerical treatment of two-dimensional interfaces for acoustic and elastic waves. *Journal of Computational Physics*, 195(1):90–116, 2004.

[88] F. Lörcher, G. Gassner, and C. Munz. An explicit discontinuous Galerkin scheme with local time-stepping for general unsteady diffusion equations. *Journal of Computational Physics*, 227(11):5649–5670, 2008.

[89] P. Monk and G.R. Richter. A discontinuous Galerkin method for linear symmetric hyperbolic systems in inhomogeneous media. *Journal of Scientific Computing*, 22(1):443–477, 2005.

[90] E. Montseny, S. Pernet, X. Ferriéresc, and G. Cohen. Dissipative terms and local time-stepping improvements in a spatial high order discontinuous Galerkin scheme for the time-domain Maxwell's equations. *Journal of Computational Physics*, 227(14):6795–6820, 2008.

[91] I. Perugia and D. Schötzau. An *hp*-analysis of the local discontinuous Galerkin method for diffusion problems. *Journal of Scientific Computing*, 17,(1):561–571, 2002.

[92] J. Piraux and B. Lombard. A new interface method for hyperbolic problems with discontinuous coefficients: One-dimensional acoustic example. *Journal of Computational Physics*, 168(1):227–248, 2001.

[93] W.H. Reed and T.R. Hill. Triangular mesh methods for the neutron transport equation. *Los Alamos Scientific Laboratory, Report LA-UR*, 1973.

[94] S. Rhebergen, O. Bokhove, and J.J.W. van der Vegt. Discontinuous Galerkin finite element methods for hyperbolic nonconservative partial differential equations. *Journal of Computational Physics*, 227(3):1887–1922, 2008.

[95] B. Rivière. *Discontinuous Galerkin Methods for Solving Elliptic and Parabolic Equations*, volume FR35 of *Frontiers in Applied Mathematics*. SIAM, Philadelphia, 2008.

[96] B. Rivière and M.F. Wheeler. A posteriori error estimates for a discontinuous Galerkin method applied to elliptic problems. Log number: R74. *Computers and Mathematics with Applications*, 46(1):141–163, 2003.

[97] A.M. Roma, C.S. Peskin, and M.J. Berger. An adaptive version of the immersed boundary method. *Journal of Computational Physics*, 153(2):509–534, 1999.

[98] P.A.B. De Sampaio. A Petrov-Galerkin formulation for the incompressible Navier-Stokes equations using equal order interpolation for velocity and pressure. *Numerical Methods in Engineering*, 31(6):1135–1149, 1991.

[99] D. Schötzau and C. Schwab. Time discretization of parabolic problems by the *hp*-version of the discontinuous Galerkin finite element method. *SIAM Journal on Numerial Analysis*, 38(3):837–875, 2001.

[100] A.L.F. L.E Silva, A. Silveira-Neto, and J.J.R. Damasceno. Numerical simulation of two-dimensional flows over a circular cylinder using the immersed boundary method. *Journal of Computational Physics*, 189(2):351–370, 2003.

[101] A. Taube, M. Dumbser, C. Munz, and R. Schneider. A high-order discontinuous Galerkin method with time-accurate local time stepping for the Maxwell equations. *International Journal of Numerical Modelling*, 22(1):77–103, 2009.

[102] C.J. Trahan and C. Dawson. Local time-stepping in Runge-Kutta discontinuous Galerkin finite element methods applied to the shallow-water equations. *Computer Methods in Applied Mechanics and Engineering*, 217-220:139–152, 2012.

[103] C. Tu and C.S. Peskin. Stability and instability in the computation of flows with moving immersed boundaries: A comparison of three methods. *SIAM Journal on Scientific and Statistical Computing*, 13(6):1361–1376, 1992.

[104] M. Uhlmann. An immersed boundary method with direct forcing for the simulation of particulate flows. *Journal of Computational Physics*, 209(2):448–476, 2005.

[105] C. Wu, Z. Li, and M. Lai. Adaptive mesh refinement for elliptic interface problems using the non-conforming immersed finite element method. *International Journal of Numerical Analysis and Modeling*, 8(3):466–483, 2011.

[106] Y. Xu and C.W. Shu. Local discontinuous Galerkin methods for high-order time-dependent partial differential equations. *Communications in Computational Physics*, 7(1):1–46, 2009.

[107] J. Yan and C.W. Shu. Local discontinuous Galerkin methods for partial differential equations with higher order derivatives. *Journal of Compututational Physics*, 17(1):27–47, 2002.

[108] X. Zhang. Nonconforming immersed finite element methods for interface problems. Ph.D Thesis. 2013. Virginia Tech.

[109] J. Zitelli, I. Mugaa, L. Demkowicz, J. Gopalakrishnan, D. Pardo, and V.M. Calo. A class of discontinuous Petrov-Galerkin methods. Part IV: The optimal test norm and time-harmonic wave propagation in 1D. *Journal of Computational Physics*, 230(7):24062432, 2011.